

ALMA MATER STUDIOURUM  
UNIVERSITÀ DI BOLOGNA

---

---

FACOLTÀ DI SCIENZE MATEMATICHE, FISICHE E NATURALI  
DIPARTIMENTO DI ASTRONOMIA

DOTTORATO DI RICERCA IN ASTRONOMIA  
CICLO XIX

MODELING THE SIGNAL OF  
THE COSMIC WEB WITH  
HYDRODYNAMICAL SIMULATIONS

RELATORE: CH.MO PROF. L. MOSCARDINI  
COORDINATORE: CH.MO PROF. L. MOSCARDINI  
DOTTORANDO: MAURO RONCARELLI

---

---

SETTORE SCIENTIFICO DISCIPLINARE: AREA 02 - SCIENZE FISICHE  
FIS/05 ASTRONOMIA E ASTROFISICA



*Alla mia Famiglia*



# Contents

<b>INTRODUCTION</b>	<b>1</b>
<b>1 COSMOLOGICAL BACKGROUND</b>	<b>5</b>
1.1 The Cosmological Principle . . . . .	5
1.2 The Robertson-Walker metric . . . . .	6
1.3 The expansion of the Universe . . . . .	6
1.3.1 Proper and comoving coordinates . . . . .	7
1.3.2 The Hubble law . . . . .	8
1.3.3 The redshift . . . . .	9
1.3.4 Cosmological distances . . . . .	10
1.4 Cosmological models . . . . .	11
1.4.1 The Friedmann models . . . . .	11
1.4.2 The cosmological constant . . . . .	12
1.4.3 The density parameter and the geometrical properties of models . . . . .	13
1.4.4 The big bang . . . . .	14
1.4.5 Evolution of the cosmological parameters in flat models . . . . .	15
1.5 Decoupling and recombination . . . . .	16
1.5.1 The cosmic microwave background (CMB) and the cosmic rest frame . . . . .	17
1.6 The formation of structures . . . . .	18
1.6.1 The Jeans theory . . . . .	18
1.6.2 The perturbation spectrum . . . . .	21
1.6.3 Non-linear evolution . . . . .	22
1.7 Current results on cosmology . . . . .	25
1.7.1 The $\Lambda$ CDM model . . . . .	25
1.7.2 Results on cosmological parameters . . . . .	27
<b>2 THE COSMIC WEB</b>	<b>29</b>
2.1 Clusters of galaxies . . . . .	29

2.1.1	The intracluster medium (ICM) . . . . .	30
2.2	Filaments: the warm-hot intergalactic medium (WHIM) . . . . .	31
2.2.1	The “missing baryons” problem . . . . .	31
2.2.2	The results of cosmological simulations . . . . .	32
2.2.3	Observational data . . . . .	35
<b>3</b>	<b>NUMERICAL METHODS IN COSMOLOGY</b>	<b>37</b>
3.1	The role of simulations in cosmology . . . . .	37
3.2	<i>N</i> -body simulations . . . . .	38
3.2.1	The particle-particle (PP) method . . . . .	39
3.2.2	The particle-mesh (PM) method . . . . .	40
3.2.3	The particle-particle-particle-mesh (P <sup>3</sup> M) method . . . . .	41
3.2.4	The TREE code . . . . .	41
3.3	Hydrodynamical simulations . . . . .	43
3.3.1	Eulerian approach . . . . .	43
3.3.2	Lagrangian approach: the Smoothed Particle Hydrodynamics (SPH) . . . . .	44
3.4	GADGET and GADGET-2 . . . . .	46
3.4.1	Radiative cooling and photoionization . . . . .	47
3.4.2	Star formation . . . . .	48
3.4.3	Extra heating . . . . .	49
3.4.4	Thermal conduction . . . . .	50
3.5	Hydrodynamical simulations used for this Thesis . . . . .	51
3.5.1	The <i>Keyproject</i> simulation . . . . .	51
3.5.2	The <i>Hutt</i> simulation set . . . . .	52
3.5.3	The <i>Salacious</i> constrained simulation . . . . .	53
<b>4</b>	<b>PROPERTIES OF THE DIFFUSE X-RAY BACKGROUND</b>	<b>57</b>
4.1	The missing baryons and the unresolved X-ray background . . . . .	57
4.2	The map construction . . . . .	59
4.3	The soft X-ray background . . . . .	62
4.3.1	The autocorrelation function . . . . .	67
4.4	The contribution in the hard X-ray band . . . . .	68
4.5	Comparison with previous works . . . . .	71
4.6	The contribution of diffuse gas to the soft X-ray background . . . . .	75
4.6.1	Observational estimates . . . . .	76

## CONTENTS

4.6.2	Separating the diffuse soft X-ray emission from galaxy groups and clusters in the simulated maps . . . . .	77
4.6.3	The soft X-ray emission from the cosmic web in the simulated maps . . . . .	78
4.7	Summary and conclusions . . . . .	80
<b>5</b>	<b>THE SUNYAEV-ZEL'DOVICH EFFECTS ON THE LARGE SCALE</b>	<b>83</b>
5.1	The Sunyaev-Zeldovich effects in cosmology . . . . .	83
5.2	Basics of the SZ effects . . . . .	85
5.3	The map construction . . . . .	86
5.4	The distribution of the SZ signals . . . . .	90
5.5	The SZ angular power spectra . . . . .	93
5.6	Cross-correlation between the SZ signals . . . . .	96
5.7	Cross-correlation with the soft X-ray signal . . . . .	98
5.8	Summary and conclusions . . . . .	101
<b>6</b>	<b>GALAXY CLUSTERS AT THE VIRIAL RADIUS</b>	<b>105</b>
6.1	Modeling and observing clusters outskirts . . . . .	105
6.2	The simulated clusters . . . . .	107
6.2.1	Preparation of the dataset . . . . .	108
6.3	Results on the outer slopes of the radial profiles . . . . .	115
6.3.1	Comparison with observational constraints . . . . .	117
6.3.2	Implications on X-ray properties of the cluster virial regions . . . . .	119
6.4	Effects of volume cutting in density and temperature profiles . . . . .	120
6.5	Summary and conclusions . . . . .	121
<b>7</b>	<b>THE SUNYAEV-ZEL'DOVICH EFFECTS OF THE LOCAL SUPERCLUSTER</b>	<b>125</b>
7.1	The low multipoles of the CMB power spectrum and the Local Supercluster . . . . .	125
7.2	The constrained hydrodynamical simulations . . . . .	127
7.3	Full-sky map making . . . . .	128
7.4	Results . . . . .	130
7.4.1	Full-sky maps . . . . .	130
7.4.2	The angular power spectrum . . . . .	134
7.4.3	Alignment of lower multipoles . . . . .	137
7.4.4	Detectability of the local SZ signal with the <i>Planck</i> satellite . . . . .	139
7.5	Summary and conclusions . . . . .	141
	<b>CONCLUSIONS</b>	<b>142</b>



# INTRODUCTION

Cosmology is nowadays going through an era of important successes and discoveries. In the last decade the great effort of the astrophysical community led for the first time to the establishment of a physical description of the Universe that agrees with basically all of the data that we possess.

We now believe that the Universe originated from a singularity, the *big bang*, from which it expanded until the present. The data suggest that its spatial geometry is consistent with flatness. We also know that it is dominated by a form of dark-energy (consistent with a cosmological constant indicated as  $\Lambda$ ) that accounts for about the 70 per cent of the total matter-energy density and that causes the expansion of the Universe to accelerate. Another about 25 per cent is due to non-baryonic dark matter (DM) with low primordial velocity dispersion (cold dark matter, CDM) with the remaining fraction associated to ordinary baryonic matter. This scenario is commonly referred to as the “concordance”  $\Lambda$ CDM model.

From the observational point of view, many independent astronomical projects have put the basis of the *Standard Cosmological Model*. The *Wilkinson Microwave Anisotropy Probe* measured with an unprecedented accuracy the cosmic microwave background (CMB) radiation anisotropies, providing a detailed description of the physical conditions of the early Universe. The *Sloan Digital Sky Survey* in the last years was able to identify and measure the spectra of almost one million extragalactic objects, thus giving precise results on galaxy clustering at different ages. The several observations of high-redshift type-Ia supernovae made it possible to calibrate the distance-redshift relation providing constraints on the geometry of the Universe. Thanks to the recent X-ray satellites like *Chandra* and *XMM-Newton* we are now able to have extended information on galaxy clusters physics.

This large amount of data<sup>1</sup> and their accuracy, together with their theoretical interpretation, have now made cosmology a mature science, in which many questions have precise answers. Besides the matter-energy composition, for example, nowadays we can provide an estimate of the age of the Universe of 13.7 Gyrs, which is accurate within a few percent. For these reasons, many scientist like to say that we now live in the era of *precision cosmology*.

Nevertheless, many questions remain still unanswered. Little is known about the nature of DM and almost nothing about dark-energy. A precise knowledge of these two dominant components is crucial in order to put robust physical basis on

---

<sup>1</sup>Together with others not cited for brevity, like Lyman- $\alpha$  forest observations, galaxy lensing and *Hubble Space Telescope* observations.

the Standard Cosmological Model. For this reason, these aspects, which are strictly connected with fundamental physics, are currently being investigated with several projects going from astronomy to particle physics.

Besides from that, the evolution of the Universe on the late ages has several unresolved aspects. From an initial phase in which the Universe was quasi-homogeneous, the primordial density fluctuations grew generating galaxies first and later clusters of galaxies and structures on larger scales with non-trivial aspects connected with their formation and evolution.

The recent observations of galaxy clusters revealed that the physics of the intracluster medium is much more complex than it was thought. In detail, in the central regions the observed cooling rate of the gas is too high to account for the stability of the system. The solution to this puzzle, which is referred to as the *cooling flows* problem, is probably connected with a self-regulated physical mechanism which is still poorly known. Moreover, we still know little about the regions around the virial radius of galaxy clusters due to the lack of observational data.

On the other side, when analysing the aspects connected with the large scale structure (LSS) formation, it is now clear that the “baryon census” in the present-day Universe, provided by observations currently available, accounts for only about a half of the baryons observed at high redshift and predicted by standard cosmology. This aspect, also known as the “*missing baryons*” problem, highlights the fact that we are still missing important cosmological information about the structures on large scales, connected with non-virialized objects.

From the theoretical point of view the dynamics of the LSS formation at low redshift is highly non-linear and, therefore, very difficult to study with analytical models. Furthermore, if the physics that regulates the evolution of the DM component is simple, baryons are also influenced by the energy feedback due to stars and galaxies and by other physical processes that are difficult to model.

For these reasons, the study of all of these problems requires the use of *hydrodynamical simulations*, that are able to describe the evolution of structures formation at low redshift on the basis of the physical model assumed. In the last years the use of these methods in cosmology is becoming more and more important, and provided several results in different fields: this was possible thanks both to the improvement in the physical knowledge of the problems and to the rapid development of computer technology.

The general picture of the LSS that arises from these numerical models is quite clear: at present a large amount of matter resides in non-virialized filamentary structures that connects the gravitationally bound haloes. These filaments, together with the clusters themselves constitute the so-called *cosmic web*, and its physical and phenomenological description on the basis of hydrodynamical models is the subject of this Thesis.

From the observational point of view there are two main ways to obtain informations on the cosmological baryons. The first and most studied one is given by the emission in the X-ray band mainly due to the free-free interaction

between electrons and ions of the ionized plasma. The other one is constituted by the Sunyaev-Zel'dovich (SZ) effect, which is the distortion of the CMB black-body spectrum due to the interaction between the photons and the electrons of the gas. Thanks to the development of new microwave instruments this last aspect is providing the first important results and will likely receive a significant boost in the near future.

For the work of this Thesis we used several high-resolution hydrodynamical simulations to describe the properties of the X-ray and SZ signals of galaxy clusters and of the cosmic web, focusing on the aspects connected with the different physical models adopted. This allowed us to make comparisons with current available observational data in order to test the validity of the physical prescriptions. Furthermore, with the use of hydrodynamical simulations we provided predictions on the expected signals of currently unobserved objects.

This Thesis is organized as follows.

- In Chapter 1 we present the cosmological background that constitutes the basis of this Thesis work. We provide a brief but complete introduction to the main concepts of modern cosmology, starting from the basic principles and definitions and going to the main aspects of structure formation theory.
- In Chapter 2 we focus on the description of the cosmic web, presenting the main physical and observational properties of galaxy clusters and filaments. In all these aspects, we pay particular attention to the connections with the results of cosmological simulations.
- In Chapter 3 we provide an overview about the numerical models used in cosmology, with particular attention to hydrodynamical models. At the end we describe the code GADGET-2 and the three sets of simulations used for our work.
- Chapter 4 is devoted to the presentation of our study on the diffuse X-ray background associated to the cosmic web. We compare our results with the up-to-date X-ray observations.
- In Chapter 5 we analyse the large-scale properties of the SZ effect. We provide a statistical description of both its thermal and kinetic component and we also study their correlation with the expected X-ray signal.
- Chapter 6 provides a detailed analysis on the physical and observational properties of galaxy clusters in the external regions. We concentrate in studying the behaviour of the density, temperature and X-ray surface brightness profiles in the regions around and above the virial radius.
- Finally, in Chapter 7 we present our study on the SZ effect associated to the large scale structures of the local Universe. We compare this signal with the available observations of primary CMB anisotropies and we provide predictions on its detectability with the future *Planck* mission.



# Chapter 1

## COSMOLOGICAL BACKGROUND

**T**his chapter aims at providing an introduction to the basics of modern cosmology. We will briefly describe some concepts of General Relativity, the mathematical and physical basics of the Friedmann models and their connections with the formation of the structures in the Universe. In the final part we will describe the basis of the “concordance”  $\Lambda$ CDM model and present some of the most updated observational data that support this model. For more detailed analysis of cosmological concepts see “*Introduzione alla Cosmologia*”, Lucchin F., 1998 and “*Cosmology: The Origin and Evolution of Cosmic Structure*”, Coles P. and Lucchin F., 2002.

### 1.1 The Cosmological Principle

The great majority of modern cosmological theories assume that on sufficiently large scales (e.g.  $\geq 100$  Mpc, beyond the typical length of the structures traced by galaxy distributions) the Universe is homogeneous and isotropic, which means that there is not any preferential position or direction: this idea is called the *Cosmological Principle*.

During the 20th Century there have been several different approaches that lead theorists to formulate this principle. It was Einstein who first introduced it *ad hoc* in 1917 to solve the field equation of General Relativity. More recently the Cosmological Principle was adopted also to solve the *Cosmological Horizon Problem*.

From the historical point of view also a philosophical approach was of great importance: first of all the *Perfect Cosmological Principle*, proposed by Bondi, Gold and Hoyle in the 1940s, states that the Universe is the same not only in all places and directions, but also at all times. This line of reasoning led to the development of the *steady-state* theory which was abandoned in the 1960s, together the Perfect Cosmological Principle itself, because it failed in providing easy explanations of several observational results: therefore, nowadays it is only of historical interest.

Anyway, the most convincing approach to this idea is probably the empirical one: we accept the Cosmological Principle because it agrees with basically all of the observational data that we possess nowadays, most importantly with the isotropy

and (almost perfect) homogeneity of the cosmic microwave background.

## 1.2 The Robertson-Walker metric

The geometry of space in General Relativity depends on matter distribution. If we assume the Cosmological Principle, then we can define a universal space-time metric, the so-called *Robertson-Walker metric*, in which the interval between two events is given by

$$ds^2 = (cdt)^2 - a(t)^2 \left[ \frac{dr^2}{1 - Kr^2} + r^2(d\theta^2 + \sin^2\theta d\phi^2) \right], \quad (1.1)$$

where  $c$  is the vacuum light-speed,  $a(t)$  is the *expansion parameter* or *cosmic scale factor* (we will describe its meaning more deeply in Section 1.3) which has the dimension of a length,  $t$  is the proper time and  $r$ ,  $\theta$  and  $\phi$  are the polar *comoving coordinates*, with  $r$  dimensionless. The terms  $K$  is the *curvature parameter* of the hypersurface  $\Sigma$ . It is a constant that can assume three possible values:

- $K = +1 \implies \Sigma$  is an hyperspherical space and the Universe is closed;
- $K = 0 \implies \Sigma$  is an Euclidean space and the Universe is flat;
- $K = -1 \implies \Sigma$  is an hyperbolic space and the Universe is open.

This concept is represented in Fig. 1.1. It can be also demonstrated that the Universe has an infinite volume when  $K \leq 0$  and a finite volume in the case of closed geometry.

The geometry of the space-time can substantially influence the evolution of the Universe and the distribution of its structures, thus it constitutes the most important aspect of any cosmological model. The geometrical properties of the hyperspherical and hyperbolic spaces are more complex than the Euclidean one, but since all of the current observational evidences are consistent with a flat Universe, the work of this Thesis we will be mainly focused on the properties of flat cosmological models.

## 1.3 The expansion of the Universe

Another fundamental point of modern cosmology is the *expansion of the Universe*, which is also connected with the Cosmological Principle: every observer, independently of its location, sees a systematic receding of the observed galaxies. Although it can be explained also as a simple Doppler-shift caused by a proper velocity of the observed objects, this phenomenon is not connected to a true dynamical origin but can be interpreted as a consequence of the expansion of space.

This idea is supported by both theoretical and observational considerations. For what concerns theory, it is again General Relativity that provides stationary

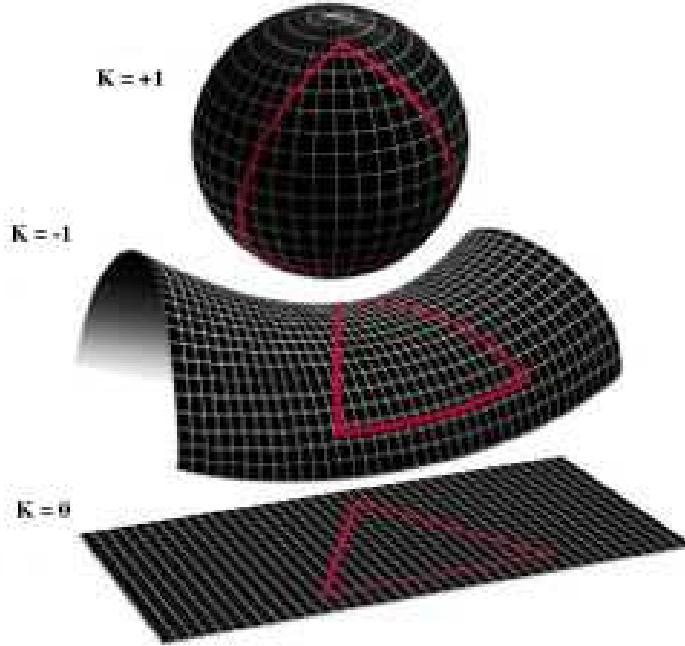


**Figure 1.1.** Representation of the three possible cases for the geometry of the Universe depending on the curvature parameter  $K$ . With a closed hyperspherical geometry,  $K = +1$ , two initially parallel paths tend to converge, while in a hyperbolic space,  $K = -1$ , they diverge. The case of Euclidean geometry corresponds to  $K = 0$ . As a consequence, the sum of the internal angles of a triangle is different depending on the geometry of space.

non-static solutions for the Einstein equations, while the first important experimental evidence of the expansion of the Universe comes from Edwin Hubble's observations in the 1920s, who measured the systematic redshift in the light of distant galaxies.

Therefore when considering the properties of the Universe on large scales, it is homogeneous, isotropic and it follows a homogeneous and isotropic expansion which, as we will see in this section, can be described by the Hubble law.

### 1.3.1 Proper and comoving coordinates

The *proper distance*,  $d_{\text{pr}}$ , of a point  $P$  from another point  $O$ , defined as the origin of a set of polar coordinates  $r$ ,  $\theta$  and  $\phi$ , is defined as the distance measured by a chain of rulers held by observers which connect  $O$  to  $P$  at a given time  $t$ . If we consider the Robertson-Walker metric, given by equation (1.1), with  $dt = 0$ , then the distance becomes

$$d_{\text{pr}} = \int_0^r \frac{a}{(1 - Kr'^2)^{1/2}} dr' = a(t) f_K(r), \quad (1.2)$$

where  $a(t)$  is the expansion parameter, already introduced in Section 1.2, and  $f_K(r)$  is a function that depends on the curvature  $K$ :

$$f_{-1}(r) = \sinh^{-1} r, \quad f_0(r) = r, \quad f_{+1}(r) = \arcsin r. \quad (1.3)$$

Given its definition, the proper distance has no operational meaning because it is impossible to measure simultaneously all the distance elements that connect  $O$  with  $P$ . It is also clear that the proper distance between the two points changes with time: for instance, the relation between the proper distances measured at a generic time  $t$  and at present time  $t_0$  is

$$d_{\text{pr}}(t_0) = a_0 f_K(r) = \frac{a_0}{a} d_{\text{pr}}(t), \quad (1.4)$$

where  $a_0 = a(t_0)$ . The proper distance measured at  $t_0$  is also called *comoving distance*,  $d_c$ , and we have that

$$d_c = \frac{a_0}{a} d_{\text{pr}}. \quad (1.5)$$

Since the proper distances of objects changes with time because of the expanding space, in this framework it is useful to use the comoving distances in order to define a reference frame fixed to themselves, in which the coordinates, called *comoving coordinates*, do not depend on the expansion itself. The positions in this reference frame will vary only due to proper dynamical motions.

The relation between the physical and the comoving coordinates can be expressed using the time-dependent scale factor  $a(t)$ . The relation is

$$\vec{r}(t) = a(t) \vec{x}(t), \quad (1.6)$$

where the vector  $\vec{r}(t)$  represents the proper coordinates and  $\vec{x}(t)$  the comoving ones. Since the Universe is expanding, we have that  $a(t)$  grows with  $t$ .

### 1.3.2 The Hubble law

In 1929 Edwin Hubble observed that distant galaxies are receding from the Milky Way with a velocity proportional to their distance given by

$$v = H_0 d, \quad (1.7)$$

where  $d$  is the proper distance of the galaxy and  $H_0$  is the *Hubble constant* or, more accurately, the *Hubble parameter* because it is not constant with time, as we will see in Section 1.4.5. This idea can be extended with the Cosmological Principle stating that every observer measures a receding of the galaxies proportional to their distance and given by equation (1.7): this statement is called the *Hubble law*.

The Hubble parameter is one of the most important physical quantities that can be measured with observations. According to the most recent estimates by Spergel et al. (2006), who measured the cosmic microwave background anisotropies (see Section 1.5.1), its value is  $H_0 = 73.2^{+3.1}_{-3.2} \text{ km s}^{-1} \text{ Mpc}^{-1}$ . This result is consistent with the one of  $H_0 = (73 \pm 4 \pm 5) \text{ km s}^{-1} \text{ Mpc}^{-1}$  obtained by Riess et al. (2005) by observing distant Cepheids variables and type-Ia supernovae (SN-Ia), while other measurements obtained with similar methods seem to indicate a lower value (see e.g. Sandage et al., 2006). Since this parameter is of great importance and since it is not known exactly, it is conventional to account for the uncertainties in its measurement by using the dimensionless parameter  $h$  defined

as  $h \equiv H_0/(100 \text{ km s}^{-1} \text{ Mpc}^{-1})$ .

From the theoretical point of view the Hubble law can be easily deduced using comoving coordinates: deriving equation (1.6) we obtain

$$\vec{v} = \frac{d\vec{r}}{dt} = \dot{a}(t)\vec{x}(t) + a(t)\frac{d\vec{x}}{dt}. \quad (1.8)$$

The second term, called *peculiar velocity*, represents the true dynamical component and dominates for small distances. On the contrary, in the approximation of large distances it can be neglected and, when defining  $H(t) \equiv \dot{a}(t)/a(t)$ , the resulting equation is

$$\vec{v} = H(t)\vec{r}, \quad (1.9)$$

which is the vectorial expression of the Hubble law at time  $t$ .

### 1.3.3 The redshift

The receding of a galaxy from the observer is related to an observable parameter called *redshift*. This variable is not only a directly measurable parameter but it is also useful to describe several laws that assume a simple form when expressed using this variable.

The redshift,  $z$ , of a luminous source is the increase of the measured radiation wavelength with respect to the emitted one. It is defined as

$$z \equiv \frac{\lambda_o - \lambda_e}{\lambda_e}, \quad (1.10)$$

where  $\lambda_e$  is the wavelength of the radiation emitted by the source and  $\lambda_o$  is the observed one.

The physical explanation of the redshift, of course, is a direct consequence of the expansion of the Universe and must not be interpreted as a Doppler effect due to a true velocity of the object. In fact, we can demonstrate that the expansion of space causes also an increase of the wavelength of the emitted photon from the source to the observer.

Using equation (1.1) applied to light rays that travel along a geodesic of the space-time defined by  $ds^2 = 0$ , if we fix  $t_e$  and  $t_0$  as the times when the radiation is emitted and observed, respectively, we have

$$\int_{t_e}^{t_0} \frac{cdt}{a(t)} = \int_0^r \frac{dr'}{(1-Kr'^2)^{1/2}} = f_K(r). \quad (1.11)$$

The light emitted from the source at the time  $t_e + \delta t_e$  is seen by the observer at  $t_0 + \delta t_0$  and since the two objects are following the cosmological expansion we have that

$$f_K(r) = \int_{t_e + \delta t_e}^{t_0 + \delta t_0} \frac{cdt}{a(t)}, \quad (1.12)$$

because their comoving distance does not change. Then, comparing the two integrals of equations (1.11) and (1.12) and considering that  $\delta t_0$  and  $\delta t_e$  are very

small, we obtain

$$\frac{\delta t_0}{a_0} = \frac{\delta t_e}{a(t_e)}, \quad (1.13)$$

where we have put  $a_0 = a(t_0)$ , or equivalently

$$\frac{a(t_e)}{\lambda_e} = \frac{a_0}{\lambda_0}. \quad (1.14)$$

From this relation it is clear that the redshift and the expansion parameter are connected. For a generic instant  $t$  we have, in fact,

$$1 + z = \frac{a_0}{a(t)}, \quad (1.15)$$

which shows that the objects at the present time have  $z = 0$  and that the redshift grows at lower expansion factors.

### 1.3.4 Cosmological distances

It is clear that in astrophysics an observer cannot measure directly the distances of cosmological objects but he can only consider the properties of the light they emit. This means that the definition of distance is different according to the method adopted to measure it. We have shown in Section 1.3.1 the concept of comoving coordinates and its connection with the proper distance in spaces described by a Robertson-Walker metric and in this Section we will define other useful distances and the simple relations that connect them with the comoving distance.

First of all, the relation between comoving and proper distance of equation (1.5) can be expressed in terms of the redshift when considering also equation (1.15) obtaining

$$d_{\text{pr}} = \frac{d_c}{1 + z}. \quad (1.16)$$

Another important distance is the *luminosity distance*  $d_L$  which is defined in such a way to preserve the Euclidean inverse-square law for the diminishing with distance of the flux of the light coming from a point source. If we consider a source of luminosity  $L$  at time  $t$  at the radial comoving coordinate  $r$  and let  $l$  be the flux per unit surface measured by an observer at time  $t_0$ , we have that

$$d_L \equiv \left( \frac{L}{4\pi l} \right)^{1/2}. \quad (1.17)$$

The luminosity distance is different from the proper one because, as we have seen in Section 1.3.3, the energy of a photon diminishes from the source to the observer by a factor  $(1 + z)$  or equivalently  $(a/a_0)$ . Moreover photons emitted within a given interval of time  $\delta t$  will be detected by the observer in an interval  $\delta t_0 = (a_0/a)\delta t$ . Thus, being the proper distance from the observer  $d_{\text{pr}}(t_0) = a_0 r$ , we have that

$$l = \frac{L}{4\pi a_0^2 r^2} \left( \frac{a}{a_0} \right)^2, \quad (1.18)$$

therefore

$$d_L = a_0^2 \frac{r}{a} . \quad (1.19)$$

If we conveniently assume that at present time  $a_0 = 1$ , we obtain the relation

$$d_L = d_c(1 + z) . \quad (1.20)$$

The *angular diameter distance*  $d_A$  is defined to preserve the geometrical variation of the angular size of an object with distance in an Euclidean space. Let  $D_p$  be the proper diameter of a source placed at the comoving coordinate  $r$  at the time  $t$ . If the angle subtended by  $D_p$  as seen by the observer is  $\Delta\theta$ , then we have that

$$D_p = ar\Delta\theta . \quad (1.21)$$

Therefore  $d_A$  is

$$d_A \equiv \frac{D_p}{\Delta\theta} = ar , \quad (1.22)$$

or equivalently

$$d_A = \frac{d_c}{1 + z} . \quad (1.23)$$

It is clear from these relations that in the limit  $r \rightarrow 0$  of small distances (redshift), when the cosmological effects are negligible, we have that

$$d_c \simeq d_{pr} \simeq d_L \simeq d_A , \quad (1.24)$$

so that we recover the Euclidean behaviour.

Another important effect that must be taken into account when considering objects at cosmological distances is the *K-correction*, which is an effect due to the spectral distortion associated to the shift of the wavelength of the emitted light. In fact, the radiation emitted in a given frequency interval  $[\nu_1, \nu_2]$  at redshift  $z$  is observed at  $z = 0$  in the interval  $[\nu_1/(1+z), \nu_2/(1+z)]$  corresponding to higher wavelengths. This implies that, for a given total emitted flux, two objects at different redshifts with a non-flat spectrum are observed with different flux in the same band. The *K-correction* is usually defined as the ratio of the two fluxes: in order to calculate it one needs to know the true spectrum of the source.

## 1.4 Cosmological models

### 1.4.1 The Friedmann models

As already said, the development of all modern cosmological theories is based on General Relativity. More precisely the *Einstein equations* describe the relationships between the metric of the space-time  $g_{ij}(x_k)$  with the energy-momentum tensor  $T_{ij}(x_k)$  ( $i, j=0, 1, 2, 3$ , with 0 indicating the time coordinate):

$$R_{ij} - \frac{1}{2}g_{ij}R = -\frac{8\pi G}{c^4}T_{ij} , \quad (1.25)$$

where  $R_{ij}$  is the Ricci tensor and  $R$  the Ricci scalar.

The energy-momentum tensor with greater relevance in cosmology is that of a perfect fluid:

$$T_{ij} = -p g_{ij} + (p + \rho c^2) U_i U_j, \quad (1.26)$$

where  $p$  is the pressure,  $\rho c^2$  is the energy density, including also the rest-mass energy, and  $U_k$  is the four-velocity of the fluid. When considering the conditions for which the Robertson-Walker metric is valid, the Einstein equations (1.25) then yield

$$\ddot{a} = -\frac{4\pi}{3} G \left( \rho + 3 \frac{p}{c^2} \right) a \quad (1.27)$$

for the time-time component ( $i = 0, j = 0$ ) and

$$\dot{a}^2 + K c^2 = \frac{8\pi}{3} G \rho a^2 \quad (1.28)$$

for the space-space components ( $i, j = 1, 2, 3$ ). The space-time components give rise to the identity  $0 = 0$ , which is of no use. These last two equations are called *Friedmann equations* and it is easy to demonstrate that they are not independent: the second one can be derived from the first when considering the adiabatic expansion of the Universe, described by

$$d(\rho a^3) = -3 \frac{p}{c^2} a^2 da. \quad (1.29)$$

Then resolving these equations we obtain

$$\left( \frac{\dot{a}}{a_0} \right)^2 - \frac{8\pi}{3} G \rho \left( \frac{a}{a_0} \right)^2 = -\frac{Kc}{a_0}, \quad (1.30)$$

that can be integrated to derive  $a(t)$ .

The simplest solutions of equations (1.28) and (1.27) are called *Friedmann models*; these models describe the matter-energy of the Universe as a fluid with an equation of state

$$p = w \rho c^2, \quad (1.31)$$

with the parameter  $w$  in the range

$$0 \leq w \leq 1, \quad (1.32)$$

called *Zel'dovich interval*. The case of  $w = 0$  corresponds to a pressureless fluid or dust and  $w = 1/3$  represents a gas of photons. A perfect gas is well described by a dust fluid in a non-relativistic regime ( $k_B T \ll m_p c^2$ ).

### 1.4.2 The cosmological constant

When Friedmann models were developed, the first cosmologists followed the idea, that has now proven to be wrong, that since the Universe is must be stable, than it has also to be static. A static model implies that the value of  $\ddot{a}$  is null, which, from equation (1.27) means that

$$p = -\frac{c^2}{3} \rho, \quad (1.33)$$

indicating that either pressure or density must be negative. Since this concept did not seem to have a solid physical basis, Einstein in 1927 introduced the *cosmological constant*  $\Lambda$  in his equations:

$$R_{ij} - \frac{1}{2}g_{ij}R - \Lambda g_{ij} = -\frac{8\pi G}{c^4}T_{ij}, \quad (1.34)$$

which arises as an integration constant and allows to obtain static solutions with suitable values of  $\Lambda$ . These kind of models are called *Einstein universes*.

Friedmann equations have, of course, different forms and solutions when adding a constant  $\Lambda \neq 0$  but they can be written with the same shape by substituting to  $p$  and  $\rho$  the *effective pressure* and the *effective density*, respectively, defined as

$$\tilde{p} = p - \frac{\Lambda c^4}{8\pi G} \quad \text{and} \quad \tilde{\rho} = \rho + \frac{\Lambda c^2}{8\pi G}. \quad (1.35)$$

This applies to all the equations derived from (1.27) and (1.28).

Since the expansion Universe has been firmly established in the last decades, nowadays there is no need to find static solutions to the Friedmann equations. However, in the last years several observational data indicated the presence of a dark energy component that dominates with respect to the other ones and that accelerates the expansion of the Universe: this kind of energy can be associated to the presence of a cosmological constant  $\Lambda \neq 0$ , which corresponds to a medium with  $w = -1$  in the equation of state (1.31). Although the physical motivation of this constant is still far from being understood, the presence of a cosmological constant is believed to be the most realistic explanation of current observational results.

### 1.4.3 The density parameter and the geometrical properties of models

We define the *critical density* of the Universe at a generic instant and at the present time  $t = t_0$

$$\rho_{\text{cr}}(t) \equiv \frac{3H(t)^2}{8\pi G} \quad \text{and} \quad \rho_{0,\text{cr}} \equiv \frac{3H_0^2}{8\pi G}, \quad (1.36)$$

respectively. Then, if we substitute these values in equation (1.30) and fix the time  $t = t_0$  we obtain

$$H_0^2 \left( 1 - \frac{\rho_0}{\rho_{0,\text{cr}}} \right) = -\frac{Kc^2}{a_0^2}, \quad (1.37)$$

where  $H_0 = \dot{a}_0/a_0$  and the suffix '0' is used to denote the values at the present epoch,  $t = t_0$ . This equation shows how the value of  $K$  and, consequently, the geometrical structure of the space-time depend only on the density.

Therefore we can define the *density parameter* at  $t_0$

$$\Omega_0 \equiv \frac{\rho_0}{\rho_{0,\text{cr}}} = \frac{8\pi G \rho_0}{3H_0^2}, \quad (1.38)$$

which is related to the value of the curvature, after a suitable renormalization of the value of  $K$ , by the relation

$$\Omega_0 \begin{cases} < 1 \Rightarrow K = -1 \\ = 1 \Rightarrow K = 0 \\ > 1 \Rightarrow K = +1 . \end{cases} \quad (1.39)$$

Moreover, generalizing the definition of the density parameter to a generic instant  $t$

$$\Omega(t) \equiv \frac{\rho(t)}{\rho_{\text{cr}}(t)} = \frac{8\pi G\rho}{3H(t)^2} , \quad (1.40)$$

it also possible to demonstrate using Friedmann equations that the value of the density parameter  $\Omega(t)$  remains either greater, equal or lower than 1 in every instant  $t$ , so that the geometry of the Universe cannot change with time.

#### 1.4.4 The big bang

All models considering a single fluid with a value for  $w$  inside the Zel'dovich interval ( $0 \leq w \leq 1$ ) have the property that they possess a time where the value of  $a$  vanishes and the density diverges. This instant is called the *big bang singularity* and its existence arises directly from Friedmann equations.

Putting together the condition of adiabatic expansion of the Universe (1.29) and the equation of state (1.31) with constant  $w$  we obtain

$$\rho a^{3(1+w)} = \text{const} = \rho_{w,0} a_0^{3(1+w)} , \quad (1.41)$$

that substituted into equation (1.30) gives the following law that holds for models with only one component:

$$\left( \frac{\dot{a}(t)}{a_0} \right)^2 = H_0^2 \left[ \Omega_{w,0} \left( \frac{a_0}{a(t)} \right)^{1+3w} + (1 - \Omega_{w,0}) \right] , \quad (1.42)$$

or, equivalently, considering the definition  $H(t) \equiv \dot{a}/a$  of the Hubble parameter at a generic time  $t$ ,

$$H^2(t) = H_0^2 \left( \frac{a_0}{a(t)} \right)^2 \left[ \Omega_{w,0} \left( \frac{a_0}{a(t)} \right)^{1+3w} + (1 - \Omega_{w,0}) \right] ; \quad (1.43)$$

In the hypothesis of a fluid with  $w$  in the Zel'dovich interval, or also in the less restrictive condition of  $-\frac{1}{3} < w \leq 1$ , from equation (1.27) we can see that  $\ddot{a}(t) < 0$  for all  $t$ , since  $a(t) > 0$  by definition. Provided that there exists an instant (for example the present time  $t_0$ ) at which the Universe expands,  $\dot{a}(t) > 0$ , this establishes that the graph of  $a(t)$  must necessarily be concave. This implicates the existence of an instant called *big bang* at a finite time in the past, usually denoted with  $t = 0$ , when  $a(0) = 0$  and when, necessarily, the density and the Hubble parameter diverge, as it can be seen from equations (1.41) and (1.43). This instant of singularity, called *big bang*, is not due to an effect of pressure that has instead an effect of decelerating the expansion, as it is clear from equation (1.28), but it is a direct consequence of the homogeneity and isotropy of the Universe.

### 1.4.5 Evolution of the cosmological parameters in flat models

We have already seen in Section 1.4.3 that the density parameter remains constant with time when  $\Omega_0 = 1$ . It is worth to analyse more deeply the properties of flat models since nowadays the value of the density parameter has been determined accurately (see Section 1.7.2) and it is consistent with the case of flatness.

The solution of equation (1.42) in the case of  $\Omega_w = 1$  provides the evolution of cosmological parameters in models dominated by just one component. After putting the value of the density parameter in this equation we obtain

$$\left(\frac{\dot{a}}{a_0}\right)^2 = H_0^2 \left(\frac{a_0}{a}\right)^{1+3w} = H_0^2 (1+z)^{1+3w}, \quad (1.44)$$

also taking into account the relationship between the scale factor and the redshift of equation (1.15). This can be integrated to obtain the evolution of the scale factor with time:

$$a(t) = a_0 \left(\frac{t}{t_0}\right)^{2/3(1+w)}, \quad (1.45)$$

which corresponds to

$$t = t_0 (1+z)^{-3(1+w)/2}, \quad (1.46)$$

that connects time with redshift.

Using equations (1.41), (1.44) and (1.46), we also obtain the evolution of the Hubble parameter:

$$H \equiv \frac{\dot{a}}{a} = \frac{2}{3(1+w)t} = H_0 \frac{t_0}{t} = H_0 (1+z)^{3(1+w)/2}, \quad (1.47)$$

$$t_0 = \frac{H}{H_0} t = \frac{2}{3(1+w)H_0}, \quad (1.48)$$

$$\rho_w = \rho_{w,0} \left(\frac{t}{t_0}\right)^{-2} = \frac{1}{6(1+w)^2 \pi G t^2}. \quad (1.49)$$

Putting together equations (1.46), (1.47) and (1.49), it also possible to note that

$$\Omega(t) \equiv \frac{8\pi G \rho_w(t)}{3H^2(t)} = \left(\frac{8\pi G}{3}\right) \left(\frac{\rho_{w,0} t_0^2}{t^2}\right) \left(\frac{t^2}{H_0^2 t_0^2}\right) = \frac{8\pi G \rho_{w,0}}{3H_0^2} \equiv \Omega_{w,0} = 1, \quad (1.50)$$

as already said at the beginning of this section.

The case of a flat universe where pressureless matter dominates ( $w = 0$ ) is called *Einstein-de Sitter (EdS)* model and it constitutes a good approximation of the actual Universe behaviour in the epoch when matter dominates. In this case we have that

$$H_{\text{EdS}} = \frac{\dot{a}}{a} = \frac{2}{3t} = H_0 (1+z)^{3/2}, \quad (1.51)$$

$$t_{0,\text{EdS}} = \frac{2}{3H_0} \quad (1.52)$$

and

$$\rho_{\text{EdS}} = \rho_{0,\text{EdS}} \left( \frac{t}{t_0} \right)^{-2} = \frac{1}{6\pi G t^2} . \quad (1.53)$$

The solutions in the case where two or more components influence the evolution of the Universe cannot be obtained analytically. When considering, for example, a model with matter ( $w = 0$ ), radiation ( $w = 1/3$ ) and a cosmological constant ( $w = -1$ ) equation (1.44) assumes the general form of

$$\left( \frac{\dot{a}}{a} \right)^2 = H_0^2 \left[ \Omega_{\text{m},0} \left( \frac{a_0}{a} \right) + \Omega_{\text{r},0} \left( \frac{a_0}{a} \right)^2 + \Omega_{\Lambda,0} \left( \frac{a_0}{a} \right)^{-2} + (1 - \Omega_0) \right] , \quad (1.54)$$

that does not have analytical solutions. When considering a flat model ( $\Omega_0 = \Omega_{\text{m},0} + \Omega_{\text{r},0} + \Omega_{\Lambda,0} = 1$ ) with radiation negligible, that constitutes a good approximation of the Universe at the present epoch, equation (1.54) becomes

$$\left( \frac{\dot{a}}{a} \right) = H_0 [\Omega_{\text{m},0} (1+z)^3 + \Omega_{\Lambda,0}]^{1/2} , \quad (1.55)$$

that can be solved with numerical methods. Qualitatively it is possible to see from this equation how the cosmological constant term contributes to accelerate the expansion.

For what concerns the density parameter we have that as  $t$  grows,  $\Omega_{\text{m}}(t)$  diminishes,  $\Omega_{\Lambda}(t)$  grows while their sum remains equal to 1. The redshift at which the two components are equal can be calculated from their value at the present epoch in the following way:

$$z = \sqrt[3]{\frac{\Omega_{\Lambda,0}}{\Omega_{\text{m},0}}} - 1 . \quad (1.56)$$

## 1.5 Decoupling and recombination

In the first phases of the evolution of the Universe matter and radiation were coupled, which means that their tight interaction kept them with the same temperature. This important result is a consequence of the evolution of their thermodynamical properties.

The matter temperature  $T_{\text{m}}$  evolves following an adiabatic expansion; if we consider for simplicity a fluid constituted by only hydrogen atoms we have

$$d \left[ \left( \rho_{\text{m}} c^2 + \frac{3}{2} \rho_{\text{m}} \frac{k_{\text{B}} T_{\text{m}}}{m_{\text{p}}} \right) a^3 \right] = - \rho_{\text{m}} \frac{k_{\text{B}} T_{\text{m}}}{m_{\text{p}}} da^3 , \quad (1.57)$$

where  $m_{\text{p}}$  is the proton rest-mass. Since the matter conservation implies that  $\rho_{\text{m}} a^3 = \rho_{\text{m},0} a_0^3$  this equation provides a relation for the evolution of particles temperature

$$T_{\text{m}} = T_{\text{m},0} \left( \frac{a_0}{a} \right)^2 = T_{\text{m},0} (1+z)^2 , \quad (1.58)$$

which is another form of the Poisson law for adiabatic expansion  $TV^{\gamma-1} = \text{const}$  written for a monoatomic gas ( $\gamma = 5/3$ ).

When calculating the evolution of a gas of photons, the adiabatic expansion is equivalent to the conservation of the energy of a black body. Thus, given  $\rho_r c^2$  the energy density of radiation and  $T_r$  its temperature, we have that

$$\rho_r c^2 = \sigma T_r^4, \quad (1.59)$$

where  $\sigma \cong 5.6 \times 10^{-5} \text{ erg cm}^{-2} \text{ K}^{-4}$  is the Stefan-Boltzmann constant, which considering equations (1.49) and (1.46) with  $w = 1/3$  allows to obtain the law of temperature evolution for the radiation:

$$T_r = T_{r,0} \frac{a_0}{a} = T_{r,0}(1+z). \quad (1.60)$$

It is also possible to demonstrate that the typical collision time  $\tau_{\text{coll}}$  between atoms and photons decreases with redshift more rapidly than the characteristic expansion time  $\tau_{\text{exp}}$  of the Universe. In fact, assuming a flat model we have that

$$\tau_{\text{coll}} \propto \rho_m^{-1} \propto (1+z)^{-3} \quad (1.61)$$

while, assuming matter domination and EdS model,

$$\tau_{\text{exp}} \equiv \frac{1}{H} \propto (1+z)^{-3/2}. \quad (1.62)$$

From these relations it is clear that there must be an instant  $t_{\text{dec}}$  of *decoupling* before which the interactions between matter and radiation were so frequent that the two components were tightly coupled: the evolution of the temperature was mainly driven by radiation, due to its higher heat capacity, and approximately followed the law described by equation (1.60). For  $t > t_{\text{dec}}$  the two components follow the two different thermodynamical evolutions described above.

Since the matter temperature grows indefinitely with redshift there exists a time  $t_{\text{rec}}$  before which the temperature was so high that the atoms were fully ionized, and after which the degree of ionization becomes very small. Only after this epoch the Universe becomes transparent to radiation and the photons are free to travel without significant interaction with matter.

This instant is called epoch of *recombination* and it can be demonstrated that it happened at  $z_{\text{rec}} \approx 10^3$ . This era of the Universe is very important in modern cosmology since it corresponds to the period of emission of the *cosmic microwave background* (CMB) radiation that has been object of an intense observational effort and that provided important information about cosmology.

### 1.5.1 The cosmic microwave background (CMB) and the cosmic rest frame

As already said in Section 1.1, at the present epoch it is possible to observe a diffuse radiation in the microwave band, the CMB, that corresponds to a black-body emission at the present temperature  $T_{\text{CMB}} \cong 2.73 \text{ K}$ . This radiation, that as

already said was emitted at  $z_{\text{rec}} \approx 10^3$ , presents small local anisotropies of the order of

$$\frac{\Delta T}{T_{\text{CMB}}} \approx 10^{-5}, \quad (1.63)$$

after removing the much higher dipole anisotropy due to the peculiar motion of the Earth.

The CMB, therefore, allows one to define an absolute cosmic rest frame in every position of the Universe, that can be fixed to be the one where the CMB does not show any dipole anisotropy.

## 1.6 The formation of structures

One of the main goal of cosmology is the understanding of the formation of the structures that we observe in the Universe nowadays. The Jeans theory of *gravitational instability*, that is able to explain the formation of stars from a quasi-homogeneous fluid, can also be used in the framework of the expanding Universe in order to describe, at first order, the formation of galaxies.

The standard model predicts the existence of small fluctuations in the density field, originated in the first instants after the big bang by quantum oscillations of the scalar field driving the expansion in the inflationary epoch. The CMB observations measured the amplitude of the fluctuations of the primordial Universe and it is possible to show how their gravitational amplification can explain the formation of the large scale structures (LSS) of the Universe. As we will see in Section 1.7.1, according to the standard model the scenario of formation predicts that galaxies are the first objects to form while the structures on larger scale (e.g. clusters and superclusters) are generated via merging of smaller objects: therefore, this picture is called hierarchical clustering.

### 1.6.1 The Jeans theory

We describe now the basis of the Jeans theory that is able to explain the growth of small density fluctuations: the basic concept is that the perturbations of a uniform fluid are able to grow if self-gravity is able to dominate the stabilizing effect of pressure.

The basic laws that describe the dynamics of a self-gravitating fluid are the continuity, the Euler and the Poisson equations:

$$\frac{\partial \rho}{\partial t} + \vec{\nabla} \cdot (\rho \vec{u}) = 0 \quad (1.64a)$$

$$\frac{\partial \vec{u}}{\partial t} + (\vec{u} \cdot \vec{\nabla}) \vec{u} = -\frac{1}{\rho} \vec{\nabla} p - \vec{\nabla} \Phi \quad (1.64b)$$

$$\nabla^2 \Phi = 4\pi G \rho, \quad (1.64c)$$

where  $\rho$ ,  $\vec{u}$  and  $p$  are the density, the velocity and the pressure of the fluid element and  $\Phi$  is the gravitational potential. In this analysis we neglect the effects of thermal conduction and viscosity. This means that we are assuming the conservation of entropy per unit of mass  $S$ , described by the following equation

$$\frac{\partial \vec{S}}{\partial t} + \vec{u} \cdot \vec{\nabla} S = 0. \quad (1.64d)$$

The system composed by the last 4 equations admits a static solution of the kind  $\rho = \rho_0$ ,  $\vec{u} = 0$ ,  $S = S_0$ ,  $p = p_0$ ,  $\vec{\nabla} \Phi = 0$ . However this is not compatible with the Cosmological Principle, because from the Poisson equation a uniform density implies that  $\Phi$  varies spatially. In other words this means that a fluid with homogeneous density distribution cannot be stationary and must be globally expanding or contracting. For what concerns cosmology, we must consider the solution corresponding to the expansion (or contraction) of a homogeneous and isotropic distribution of matter:

$$\rho(t) = \left[ \frac{a_0}{a(t)} \right]^3 \rho(t_0) \quad (1.65a)$$

$$\vec{u} = \frac{\dot{a}(t)}{a(t)} \vec{r} \quad (1.65b)$$

$$\Phi = \frac{2\pi G}{3} \rho r^2 \quad (1.65c)$$

$$p = p(\rho, S) \quad (1.65d)$$

$$S = \text{const}, \quad (1.65e)$$

written in physical coordinates. This solution also has the problem that both  $u$  and  $\Phi$  diverge for  $r \rightarrow \infty$  that can be solved adopting the more accurate relativistic solution, that we do not describe in this Thesis. If now we introduce small perturbations  $\delta$ ,  $\vec{v}$ ,  $\phi$ ,  $dp$  and  $dS$  to all the physical variables, so that

$$\rho = \rho_0 + \delta\rho_0 = \rho_0(1 + \delta) \quad (1.66a)$$

$$\vec{u} = \vec{u}_0 + \vec{v} \quad (1.66b)$$

$$\Phi = \Phi_0 + \phi \quad (1.66c)$$

$$p = p_0 + dp \quad (1.66d)$$

$$S = S_0 + dS, \quad (1.66e)$$

where the index '0' represents the zeroth-order solutions, and put these new values into the system, neglecting the second-order terms, we obtain the new system of equations:

$$\dot{\delta} + 3\frac{\dot{a}}{a}\delta + \frac{\dot{a}}{a}(\vec{r} \cdot \vec{\nabla})\delta + (\vec{\nabla} \cdot \vec{v}) = 0 \quad (1.67a)$$

$$\dot{\vec{v}} + \frac{\dot{a}}{a}\vec{v} + \frac{\dot{a}}{a}(\vec{r} \cdot \vec{\nabla})\vec{v} = -\frac{1}{\rho}\nabla dp - \nabla\phi \quad (1.67b)$$

$$\nabla^2\phi - 4\pi G\rho_0\delta = 0 \quad (1.67c)$$

$$dS + \frac{\dot{a}}{a}(\vec{r} \cdot \vec{\nabla})dS = 0 . \quad (1.67d)$$

We now look for the solutions corresponding to perturbations in the form of small plane-wave departures by the unperturbed one:

$$du_i = u_i(t)e^{i\vec{k} \cdot \vec{r}} , \quad (1.68)$$

where the variables  $u_i$  ( $i=1, 2, 3, 4, 5$ ) correspond to the small perturbations in the different variables and the wavevector  $\vec{k}$  corresponds to a wavelength  $\lambda$  that varies with time following the Hubble expansion:

$$k = \frac{2\pi}{\lambda} = \frac{2\pi}{\lambda_0} \frac{a_0}{a} = k_0 \frac{a_0}{a} . \quad (1.69)$$

We can derive the evolution with time of the amplitudes  $u_i$  of the perturbations obtaining

$$\dot{\delta} + 3\frac{\dot{a}}{a}\delta + i\vec{u} \cdot \vec{k}\delta + i\vec{k} \cdot \vec{v} = 0 \quad (1.70a)$$

$$\dot{\vec{v}} + \frac{\dot{a}}{a}\vec{v} + iv_s^2\vec{k}\delta + i\frac{\vec{k}}{\rho} \left( \frac{\partial p}{\partial S} \right)_\rho dS + i\vec{k}\phi = 0 \quad (1.70b)$$

$$k^2\phi + 4\pi G\rho\delta = 0 \quad (1.70c)$$

$$dS = 0 , \quad (1.70d)$$

being  $v_s$  the sound speed defined as  $v_s^2 \equiv (\partial\rho/\partial p)_S$ .

This system admits a static solution of entropic type, in which  $dS \neq 0$  with its amplitude varying constantly with time ( $\dot{dS} = 0$ ) and another solution of vortical type can be obtained by putting  $\delta = \phi = dS = 0$  and  $\vec{v} \perp \vec{k}$ : both of these solutions lead to have no density perturbations and, therefore, no gravitational instability.

From the cosmological point of view the most interesting solution is the adiabatic one with  $dS = 0$  and  $\vec{v} \parallel \vec{k}$  that describes matter falling inside the potential well without vorticity ( $\vec{\nabla} \times \vec{v} = 0$ ) generated by the density perturbation. In this case the system is simplified into

$$\dot{\delta} + 3\frac{\dot{a}}{a}\delta + ikv = 0 \quad (1.71a)$$

$$\dot{v} + \frac{\dot{a}}{a}v + ik \left( v_s^2 - \frac{4\pi G\rho_0}{k^2} \right) \delta . \quad (1.71b)$$

Deriving equation (1.71a) we have

$$\ddot{\delta} + ik \left( \dot{v} - \frac{\dot{a}}{a}v \right) = 0 \quad (1.72)$$

and substituting in this equation the values of  $v$  and  $\dot{v}$  obtained by equation (1.71b) we obtain

$$\ddot{\delta} + 2\frac{\dot{a}}{a}\dot{\delta} + (v_s^2 k^2 - 4\pi G\rho_0)\delta = 0 . \quad (1.73)$$

This equation represents the evolution with time of the density contrast  $\delta$  and is called *dispersion relation*. This equation shows that the behaviour of the density

perturbations depends on their wavelength. More precisely, if we can define the *Jeans length* as

$$\lambda_J \equiv v_s \left( \frac{\pi}{G\rho_0} \right)^{1/2}, \quad (1.74)$$

we have that for fluctuations with  $\lambda < \lambda_J$  the pressure term  $\propto v_s^2$  in equation (1.71b) dominates and we have oscillating solutions, while for  $\lambda > \lambda_J$  the gravity term  $\propto 4\pi G\rho$  dominates leading to gravitational instability.

Under these hypotheses, in the case of  $\lambda \gg \lambda_J$ , the solutions in the EdS model (see Section 1.4.5), that well represents the epoch of the growth of density fluctuation, have the two forms

$$\delta_-(t) \propto t^{-1} \quad (1.75)$$

$$\delta_+(t) \propto t^{2/3}. \quad (1.76)$$

The first solution can be neglected because it vanishes with time. The second one represents the growing mode and its the only one that has cosmological relevance. This result suggests that the amplitudes of the fluctuations in this regime grow with time in the same way as the scale factor  $a(t)$ , as it can be seen from equation (1.45) with  $w = 0$ .

### 1.6.2 The perturbation spectrum

We analyse now the statistical properties of the primordial perturbations that constitute the “seeds” for the formation of the structures. In any given position  $\vec{x}$  of space it is possible to define the density contrast, already introduced in Section 1.6.1, as

$$\delta(\vec{x}) \equiv \frac{\rho(\vec{x}) - \langle \rho \rangle}{\langle \rho \rangle}, \quad (1.77)$$

where  $\langle \rho \rangle$  is the average density. It is useful to consider its Fourier components

$$\tilde{\delta}(\vec{k}) \equiv \int \delta(\vec{x}) e^{i\vec{k}\cdot\vec{x}} d^3\vec{x}, \quad (1.78)$$

where  $\vec{k}$  is the wavevector, so that the density contrast can be written in the form

$$\delta(\vec{x}) = \frac{1}{(2\pi)^3} \int \tilde{\delta}(\vec{k}) e^{-i\vec{k}\cdot\vec{x}} d^3\vec{k}. \quad (1.79)$$

If we consider a sample volume of the Universe  $V_u = l_u^3$ , with  $l_u$  much larger than the maximum scale at which there is significant structure, then the mean value of the perturbation  $\delta(\vec{x})$  inside this volume must be zero by definition. However its mean square value is not zero, in fact, it can be demonstrated that its *variance*  $\sigma_u^2$  over that sample is

$$\sigma_u^2 \equiv \langle \delta^2(\vec{x}) \rangle_u = \frac{1}{V_u} \int_{V_u} |\tilde{\delta}(\vec{k})|^2 d^3k. \quad (1.80)$$

If we assume that the Universe is homogeneous and isotropic, then there is no dependence on the direction of the wavevector but only on its modulus  $k = |\vec{k}|$ . Thus, in the limit  $V_u \rightarrow \infty$ , we find

$$\sigma^2 = \frac{1}{2\pi^2} \int_0^\infty P(k) k^2 dk, \quad (1.81)$$

where we put  $P(k) \propto \tilde{\delta}^2(k)$ . The quantity  $P(k)$  is called *power spectrum* of the density fluctuations. The quantity  $\sigma^2$  does not depend on spatial positions but on time, since  $\tilde{\delta}(k)$  evolves with time, therefore it represents a measure of the amplitudes of the perturbations it but does not carry information about their spatial structure.

It is usual to assume that the perturbation power spectrum, at least in a limited interval for  $k$ , is given by a power law

$$P(k) = Ak^n, \quad (1.82)$$

with  $n$  usually called *spectral index*. The convergence of the variance in equation 1.81 requires that  $n > -3$  for  $k \rightarrow 0$  and  $n < -3$  for  $k \rightarrow \infty$ . For various physical arguments, the most 'natural' choice for the shape of the primordial power spectrum is believed to be the *Harrison-Zel'dovich* or *scale-invariant*, for which  $n = 1$  in equation (1.82). A convincing physical motivation for this form can be found in the inflationary models (not discussed in this Thesis): these theories usually predict a power spectrum of the scale-invariant form arising from quantum oscillations of the scalar field driving the inflationary epoch.

For what concerns the value  $A$  of the power spectrum normalization in equation (1.82), it can be demonstrated that it is proportional to the variance of the density contrast on a given scale. As a reference, it is usual to adopt  $\sigma_8$  defined as

$$\sigma_8^2 \equiv \frac{1}{(2\pi)^3} \int_0^\infty P(k) |\hat{W}(kR_8)|^2 k^2 dk, \quad (1.83)$$

where  $R_8 = 8h^{-1}$  Mpc and  $\hat{W}(x)$  is the top hat window function defined as having the constant value of 1 for  $x \leq 1$  and 0 otherwise. The scale of  $8 h^{-1}$  Mpc has been chosen taking into account the results of Davis & Peebles (1983) that found that at this radius the variance on galaxy counts is equal to unity.

### 1.6.3 Non-linear evolution

The evolution of structure formation after recombination requires a more complicated mathematical treatment. The Jeans theory described in Section 1.6.1 is valid only for  $|\delta| \ll 1$ , while the structures observed nowadays correspond to overdensities  $|\delta| \gg 1$ , for example a cluster of galaxies correspond to a value of  $\delta$  of several hundred.

In Chapter 3 we will talk in detail about the several possible numerical approaches that are currently used to describe the evolution of the structure

formation in the non-linear regime. Here we will briefly review two simple analytical approximations that are able to describe in a simple and approximate way some characteristics of clusters of galaxies and the formation of the *cosmic web*, that we will describe in detail in Chapter 2.

### The spherical collapse

The simplest approach to follow the non-linear evolution is to study a perturbation which has a particularly simple form. Here we show without going into detail the basis of the *spherical collapse* model and its predictions for the properties of galaxy clusters.

The basic hypothesis is consider a spherical perturbation with a constant density that at the initial time  $t_i \simeq t_{\text{rec}}$  has a density contrast in the range  $0 < \delta_p \ll 1$ . This sphere is expanding with the background in such a way that that the peculiar velocity at the edge of the perturbation is null. With the assumption of symmetry this perturbation can be treated as a separate universe and in the hypothesis that the whole Universe is following the evolution described by the EdS model ( $\Omega_m=1$ ), which is a good approximation at  $t \simeq t_{\text{rec}}$ , then the corresponding density parameter  $\Omega_p$  of the perturbation must be

$$\Omega_p(t_i) = \frac{\rho(t_i)(1 + \delta_p)}{\rho_{\text{cr}}(t_i)} = 1 + \delta_p, \quad (1.84)$$

where  $\rho$  and  $\rho_{\text{cr}}$  correspond to the unperturbed universe. Therefore we can use equation (1.54) in the case of a closed universe ( $\Omega_p > 1$ ) and imposing the boundary conditions to the velocity, it is possible to calculate the time  $t_c$  at which the perturbation collapses to a single point. This, of course, is possible only if we neglect the effects of gas pressure. When taking this into account, this results in a shock-heating of the gas and in a final extended spherical configuration of radius  $R_{\text{vir}}$  that reaches the virial equilibrium. It can be shown that the density contrast enclosed by  $R_{\text{vir}}$ , the virial radius, in the case of the EdS model is

$$\Delta_{\text{EdS}}(t_c) = \frac{\rho_p(t_c)}{\rho(t_c)} = 18\pi^2 \simeq 180. \quad (1.85)$$

This result can be generalized in the cases of the other Friedmann models, also with the presence of the cosmological constant, obtaining the approximate relations (Lacey & Cole, 1993; Eke et al., 1996):

$$\Delta(t_c) \simeq 18\pi^2 \begin{cases} \Omega_m^{0.30} & \text{if } \Omega_\Lambda = 0 \\ \Omega_m^{0.45} & \text{if } \Omega_m + \Omega_\Lambda = 1. \end{cases} \quad (1.86)$$

However we will see that, although it is able to describe many general properties of halo formation, this simple picture does not fully apply to observed galaxy clusters: this is because the assumptions made are not realistic and because this picture neglects different effects like merging, mass dissipation and other processes that affect the baryons during the collapse.

### The Zel'dovich approximation

The main limitations of the spherical collapse model are in its too simple initial conditions that do not apply to true perturbations in the early Universe. Moreover, even if this was the case, such a symmetrical configuration for the collapse makes it very unstable to the growth of non-radial motions. In fact, it can be demonstrated that in the more general case of a triaxial perturbation, the collapse does occur to a point, but to a flattened, quasi-two-dimensional structure that is usually called with the descriptive term of *pancake*.

As we will see in Chapter 2 the formation of filaments and sheet-like structures on very large scales is a standard result of cosmological numerical simulations. However it is possible to understand the growth of these structures also analytically using the *Zel'dovich approximation* (Zel'dovich, 1970) applied to the density perturbations. If we take a Lagrangian approach to the linear evolution of initial perturbations and define  $\vec{q}$  as the unperturbed comoving coordinates of a particle, in the assumption that the position and time dependence between initial and final positions of the particles can be separated, the perturbed position at the time  $t$  can be approximated as

$$\vec{r}(t, \vec{q}) \simeq a(t)[\vec{q} - b(t)\nabla_{\vec{q}} \Phi_0(\vec{q})], \quad (1.87)$$

where  $\vec{r} = a(t)\vec{x}$ , with  $\vec{x}$  comoving coordinate, and  $b(t)$  is a dimensionless function that describes the evolution of a perturbation in the linear regime and therefore solves the equation

$$\ddot{b} + 2\frac{\dot{a}}{a}\dot{b} - 4\pi G\rho b = 0. \quad (1.88)$$

This equation is equivalent to the dispersion relation (1.73) obtained for the gravitational instability of a universe dominated by pressureless matter; as already said at the end of Section 1.6.1, in the case of the EdS model we have that  $b(t) \propto a(t)$ , therefore we can substitute it in the next equations. The quantity  $\Phi_0(\vec{q})$  is proportional to a peculiar velocity potential: in fact, from equations (1.87) and (1.8)

$$\vec{v}_p = \frac{d\vec{r}}{dt} - H\vec{r} = a\frac{d\vec{x}}{dt} = -a\dot{a}\nabla_{\vec{q}} \Phi_0(\vec{q}), \quad (1.89)$$

which means that the velocity field is irrotational. The potential  $\Phi_0(\vec{q})$  is related to the density by the relation

$$\delta = a\nabla_{\vec{q}}^2 \Phi_0(\vec{q}). \quad (1.90)$$

For times close to the initial state, when the displacements between  $\vec{r}$  and  $a(t)\vec{q}$  are small, it is possible to recover the result of the Eulerian linear regime, since equation (1.87) constitutes a unique mapping between the two coordinates; this means that  $\rho(\vec{r}, t)d^3r = \langle\rho(t)\rangle d^3q$  or

$$\rho(\vec{r}, t) = \frac{\langle\rho(t)\rangle}{|J(\vec{r}, t)|}, \quad (1.91)$$

where  $|J(\vec{r}, t)|$  is the determinant of the Jacobian of the mapping  $\partial\vec{r}/\partial\vec{q}$ . Since the flow is irrotational, the matrix  $J$  is symmetric and can therefore be locally

diagonalised, so that

$$\rho(\vec{r}, t) = \langle \rho(t) \rangle \prod_{i=1}^3 [1 + a(t)\alpha_i(\vec{q})]^{-1}, \quad (1.92)$$

where  $1 + b(t)\alpha_i(\vec{q})$  are the eigenvalues of the matrix  $J$ , with the values of  $\alpha_j$  that quantify the expansion or contraction (if negative or positive, respectively) of the fluid in the three dimensions. If the approximation of small displacements ( $|b(t)\alpha_i| \ll 1$ ) holds, we have that, from equation (1.92)

$$\delta \simeq -(\alpha_1 + \alpha_2 + \alpha_3)a(t), \quad (1.93)$$

recovering the law of perturbation growth in the linear regime.

From equation (1.92) it is possible to see that if in a given direction the fluid contracts,  $\alpha_j < 0$ , there exists an instant  $t_{sc}$  at which  $b(t_{sc}) = -1/\alpha_j$ : this instant is called *shell crossing* and leads to a singularity because the density becomes formally infinite: this corresponds to a situation at which two different Lagrangian points have the same Eulerian coordinates. In other words, the mapping becomes not unique because the particle trajectories have crossed: a region where the shell crossing occurs is called *caustic*. Of course, in reality this does not happen because, when the density increases, the effects of pressure become important and are able to stop the collapse while shock-heating the gas.

It is important to note that, if there is no special symmetry, then for every given fluid element the values of  $\alpha_i$  will not be all negative or positive, indicating that the collapse of a fluid element does not occur necessarily in three dimensions. If the three eigenvalues are negative then the collapse will occur first along the axis corresponding to the most negative one giving rise to a sheet or pancake; then the sheet will collapse to a filament along another direction and finally to a point. A condition similar to the spherical collapse occurs only in the unlikely situation when the three values are negative and comparable: therefore the formation of sheets and filaments must be a generic result of structure collapse.

## 1.7 Current results on cosmology

### 1.7.1 The $\Lambda$ CDM model

Current observational data suggest as a favorite scenario the so-called “*concordance*”  $\Lambda$ -Cold Dark Matter ( $\Lambda$ CDM) model. In this picture the Universe is flat with the energy density at the present epoch dominated by a cosmological constant and the remaining fraction mainly due to non-baryonic, non-collisional dark matter (DM) with low primordial velocity dispersion. The fraction of density due to standard baryonic matter  $\Omega_b$  is only of few percent.

After the radiation epoch ( $z \gtrsim 10^4$ ), the DM component starts to dominate driving the growth of the density fluctuations up to the epoch of recombination when

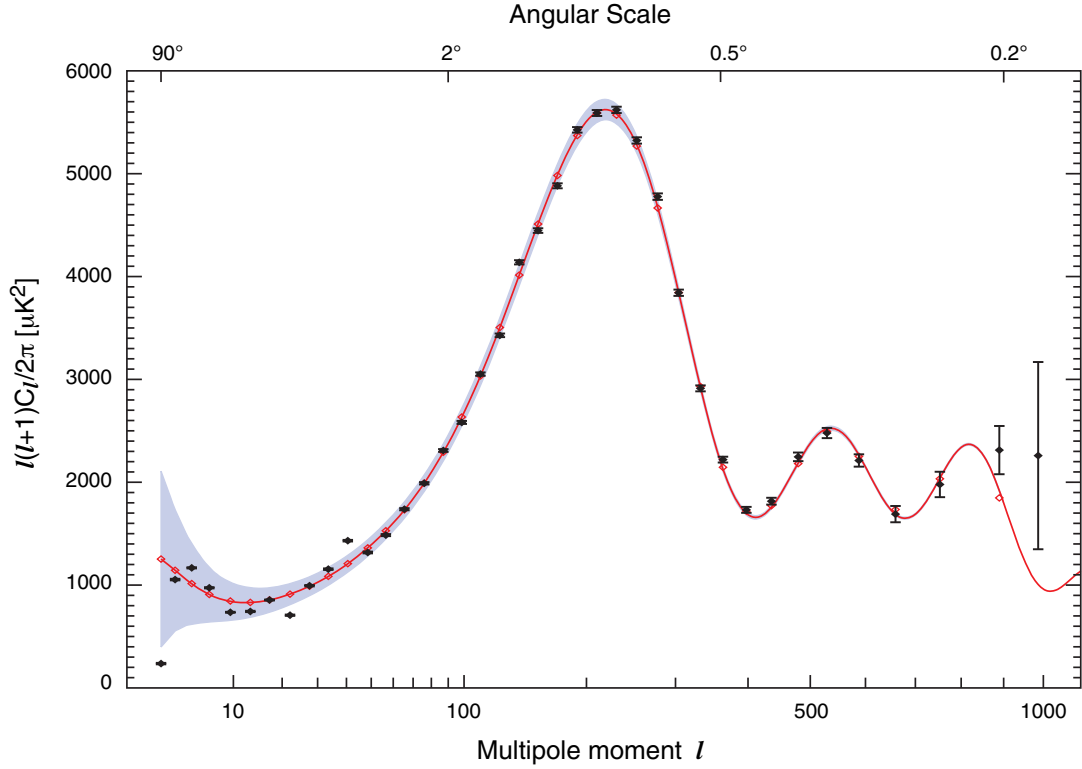


**Figure 1.2.** Power spectrum of the CMB temperature fluctuations as a function of the multipole moment (picture taken from Hinshaw et al., 2006). On the top the corresponding angular scale is shown. The black dots are the binned data measured by the WMAP satellite (3-year results, Spergel et al., 2006) with the error-bars corresponding to noise-errors. The red curve represents the best-fit to the data assuming a  $\Lambda$ CDM model with flat geometry and the shaded band is the  $1\sigma$  error due to the cosmic variance. The red diamonds show the model points when binned in the same way as the data.

they become observable as gas temperature fluctuations imprinted in the CMB anisotropies. Since the CDM particles have a low velocity dispersion, the typical perturbations that survive to the effect of free-streaming correspond to masses of the order of  $M \simeq M_{\text{J}}(z_{\text{rec}}) \simeq 10^5 M_{\odot}$ , thus to the typical scales of protogalaxies. Therefore, in this scenario galaxies form first while clusters are created via merging of smaller objects: this picture is called *hierarchical clustering* of structure formation.

The dark energy component starts to dominate the expansion at  $z \lesssim 0.5$  and, as already noted in the comments on equation (1.55), it has the effect of accelerating the expansion of the Universe. The main problem with the existence of this energy component is that, as already said in Section 1.4.2, its physical origin is still unknown: the most natural explanation is the vacuum energy but the energy density  $\epsilon_{\Lambda}$  currently estimated is of the order of

$$\epsilon_{\Lambda} = \Omega_{\Lambda}(\rho_{0,\text{cr}}c^2) \approx 5 \times 10^{-9} \text{ erg cm}^{-3}, \quad (1.94)$$

which is several order of magnitude below the estimates for the vacuum energy

**Table 1.1.** Main cosmological parameters as estimated by Spergel et al. (2006) using the data of the WMAP satellite together with other results from CMB data, galaxy clustering, SN-Ia and weak lensing analysis. These values have been obtained assuming a flat  $\Lambda$ CDM model. Errors correspond to  $1\sigma$ .

$\Omega_m$	$0.268 \pm 0.018$
$\Omega_\Lambda = 1 - \Omega_m$	$0.732 \pm 0.018$
$10^2 \Omega_b h^2$	$2.186 \pm 0.068$
$h$	$0.704^{+0.015}_{-0.016}$
$\sigma_8$	$0.776^{+0.031}_{-0.032}$
$n_s$	$0.947 \pm 0.015$

density of standard field theories. However, despite of the lack of strong physical motivation for the existence of this form of dark energy, the  $\Lambda$ CDM model is able to explain the great majority of observational data available today.

### 1.7.2 Results on cosmological parameters

The concordance  $\Lambda$ CDM cosmology is currently supported by many observations which allow a precise estimate of the cosmological parameters. These data include results from the  $d_L - z$  relation of high-redshift supernovae (see, e.g., Astier et al., 2006; Wood-Vasey et al., 2007), weak lensing (see, e.g., Heymans et al., 2005; Massey et al., 2005; Hettterscheidt et al., 2006; Semboloni et al., 2006; Hoekstra et al., 2006) and galaxy clustering (see, e.g., Cole et al., 2005; Eisenstein et al., 2005; Tegmark et al., 2006; Sánchez et al., 2006).

The most important and complete dataset comes from the CMB anisotropies observations made by the *Wilkinson Microwave Anisotropy Probe* satellite (*WMAP*, Spergel et al., 2003, 2006). As said in Section 1.5.1, the CMB temperature presents intrinsic primordial fluctuations of the order of  $\Delta T/T_{\text{CMB}} \approx 10^{-5}$ : by measuring their power spectrum it is possible to obtain constraints on many cosmological parameters.

In Fig. 1.2 we show the power spectrum of the CMB temperature anisotropies measured by Spergel et al. (2006), together with the best-fit obtained assuming a flat ( $\Omega_\Lambda = 1 - \Omega_m$ )  $\Lambda$ CDM model: although some points are outside the expected  $1\sigma$  error due to the cosmic variance (see Section 7.1 for a discussion about this topic), we can see that the agreement between data and theory predictions is remarkable.

As a reference, we also quote in Table 1.1 the estimates on the main cosmological parameters coming from this dataset together other observational results (Spergel et al., 2006).

The cosmological parameters of the models used for our work are compatible to the ones shown in this table. Although some difference is present, this does not change the main results obtained. In the next chapters we will also discuss the

dependence on cosmological parameters of the results shown in this Thesis.

## Chapter 2

# THE COSMIC WEB

**T**his chapter is devoted to the analysis of the structures of the Universe on the largest scales: we will describe the main properties of the structures that constitute the so-called *cosmic web*. In the first part we will describe clusters of galaxies concentrating on the properties of the baryonic component. In the final part we will talk about the “missing baryons” problem concentrating on its connections with the filamentary structures.

### 2.1 Clusters of galaxies

*Clusters of galaxies* are ensembles of 100–1000 galaxies and represent the largest gravitationally bound objects observed. Their typical mass is of the order of  $10^{14}$ – $10^{15}M_{\odot}$  of which more than 80 per cent is due to DM (see e.g. Ettori et al., 2004, for an estimate of the baryon fraction in clusters), about 15 per cent constituted by hot gas and the remaining fraction is concentrated in galaxies. The smaller virialized haloes of masses  $M \sim 10^{14}M_{\odot}$ , are usually referred to as *galaxy groups*.

As described in Section 1.6.3 adopting a simple analytical approximation, clusters of galaxies form in correspondence of the highest peaks of density fluctuation field due to the non-linear collapse of the perturbation. At the first order, this process brings the material to a virial equilibrium with the halo reaching the typical overdensity of about 100 while the gas is adiabatically shock-heated up to temperatures of several million degrees.

There are several reasons to consider clusters of galaxies as ideal objects for cosmological studies. First, their peculiar velocities are small, assuring that their current environment corresponds to the primordial one, from which they originated. Their mass function and their abundance depend on  $\Omega_m$  and  $\sigma_8$  and their thermodynamical properties can provide constraints on the baryon density  $\Omega_b$ . Moreover, clusters are young systems, since they formed mainly at  $z \lesssim 2$ , and their formation history can allow to discriminate between different cosmological models: in fact, at high redshift all the cosmological scenarios tend to the EdS model, while in the recent epochs the differences between their properties are larger, especially for what concerns the dynamic effect of the cosmological constant, as already said

in Section 1.4.5.

The formation and evolution of galaxy clusters is mainly driven by the non-baryonic DM component that does not emit and is therefore difficult to study. DM haloes can be probed only with gravitational lensing observations, with the study of the velocity fields and by studying the observational properties of the baryons that fall inside their gravitational potential.

### 2.1.1 The intracluster medium (ICM)

As already said, the main process driving the formation of galaxy clusters is the gravitational collapse. The evolution of the baryonic component is determined by the DM one, since it dominates in mass. The baryons that constitute the intracluster medium (ICM) fall inside the gravitational wells generated by DM haloes, they follow an adiabatic compression and, consequently, they heat also due to shock processes. For a typical cluster the ICM reaches a temperature of  $10^7$ – $10^8$  K, it becomes completely ionized and it emits in the X-ray band via free-free interaction between electrons and ions.

This process puts galaxy clusters among the most luminous objects in the X-ray band ( $L_X \approx 10^{45}$  erg/s), making them detectable also at high distances: thanks to the recent development of X-ray satellites like *Chandra* and *XMM-Newton*, observations in this band nowadays constitute the most important dataset to study cluster physics. As we will see in detail in Sections 5.1 and 5.2, the hot ionized gas of the ICM also interacts with the CMB photons via Thomson scattering giving rise to the Sunyaev-Zel'dovich (SZ) effect: therefore, the properties of the ICM can also be studied with microwave observations.

The simple picture of the spherical collapse described in Section 1.6.3, together with the assumptions that the gas is in hydrostatic equilibrium with the DM component, leads to the important conclusion that the basic physical and observational properties of galaxy clusters are connected one with each other and depend only on one parameter (e.g. the mass). This scenario is called *self-similar* model and predicts that, since gravity has no preferential scales, haloes with different masses are scaled copies one of each other (Kaiser, 1986).

The connection between the different properties of galaxy clusters can be expressed with the *scaling relations*:

- i* -  $M_{\text{gas}} \propto M_{\text{vir}} \propto T^{3/2}$ , that connects gas mass, total virialized mass and gas temperature;
- ii* -  $L_X \propto T^2 \propto M^{4/3}$ , that describes the dependence of the X-ray luminosity  $L_X$ , in the hypothesis that bremsstrahlung dominates the emission;
- iii* -  $y_0 \propto M$  and  $y_{\text{int}} \propto M^{5/3}$  for the thermal SZ effect, where  $y_0$  and  $y_{\text{int}}$  are the value of the Compton  $y$ -parameter at the cluster centre and integrated in its angular surface, respectively.

Besides gravitational heating, there are also several physical processes that affect the baryonic component, the physics of which is very complicated: these non-gravitational phenomena are responsible of deviations from the scaling relations and are of great importance in the study of cluster physics, especially in their internal regions.

Radiation emission influences the thermodynamics of the ICM acting as a cooling process, particularly at the centre where the emission is higher. Moreover, this mechanism is at the basis of the creation of cool and dense ( $T < 10^5$  K,  $\delta > 1000$ ) regions, that condense to create stars. Then the most massive stars can create a feedback mechanism by injecting energy in the ICM with supernova (SN) explosion and also influence the gas chemical composition by metal diffusion. Other non-gravitational processes that can influence significantly the thermodynamics of the gas are the presence of turbulence connected with merging events, the thermal conduction, the feedback from active galactic nuclei (AGNs) and the presence of magnetic fields.

## 2.2 Filaments: the warm-hot intergalactic medium (WHIM)

The amount of gas mass that constitutes galaxy clusters, together with the mass concentrated in stars and galaxies at the present epoch accounts for only about 20 per cent of the total baryonic mass of the Universe. In fact, the majority of baryons is believed to be in the form of non-virialized structures, like filaments and sheets, that constitute the so-called *cosmic web*.

Even if these structures have not been observed yet, we will see in this Section that this picture of the LSS agrees with the theoretical pancake scenario suggested by the Zel'dovich approximation (see Section 1.6.3), with the results of cosmological hydrodynamical simulations and is also the most natural explanation of the “missing baryons” problem.

### 2.2.1 The “missing baryons” problem

The cosmological baryon density can be inferred from the big bang nucleosynthesis (BBN) theory associated to the measurements of light elements abundances (e.g. the deuterium-to-hydrogen ratio as measured by Kirkman et al., 2003) and also from CMB data (Spergel et al., 2003, 2006). Both datasets agree in fixing a value of  $\Omega_b$  around 4 per cent. This result is also in agreement with the lower limits imposed by observations at  $z \gtrsim 2$  of Lyman- $\alpha$  absorption systems (see Weinberg et al., 1997; Rauch, 1998). Since all these measurements gave precise and independent results and given the remarkable agreement between them and the theory predictions, this result on the value of  $\Omega_b$  can be considered very robust.

However, when summing up all of the mass components coming from different observed contributions in the present-day Universe, only about a half of the total baryon budget is accounted for, thus leaving a big fraction of the baryons still undetected. This issue, which is summarized in Table 2.1, is known as the “*missing baryons*” problem (see e.g. Cen & Ostriker, 1999; Nicastro et al., 2005a) and

**Table 2.1.** Census of observed baryons in the high-redshift and low-redshift Universe. The reference in the right column are the following: Data taken from Nicastro et al. (2005a). For these results it is assumed the value of the parameter  $h = 0.7$ .

Inferred from	$10^2 \Omega_b$	References
BBN and D-to-H ratio	(4.4±0.4)	Kirkman et al. (2003)
CMB anisotropies	(4.6±0.2)	Bennett et al. (2003b); Spergel et al. (2003)
Lyman- $\alpha$ forest ( $z > 2$ )	>3.5	Weinberg et al. (1997); Rauch (1998)
Observed at $z < 2$ :		
Stars	(0.26±0.08)	Fukugita (2004)
HI + HeI + H <sub>2</sub>	(0.080±0.016)	Fukugita (2004)
Gas in clusters (X-ray)	(0.21±0.06)	Fukugita (2004)
Lyman- $\alpha$ forest	(1.34±0.23)	Penton et al. (2004)
Warm+warm-hot gas (OVI)	(0.6 <sup>+0.4</sup> <sub>-0.3</sub> )	Tripp et al. (2000); Savage et al. (2002)
Total at $z < 2$	(2.5 <sup>+0.5</sup> <sub>-0.4</sub> )	
Missing at $z < 2$	(2.1 <sup>+0.5</sup> <sub>-0.4</sub> )	

constitutes one of the most important and debated problems of modern cosmology.

The study of this issue from the theoretical point of view is very difficult. In fact, the large-scale dynamics at the late epochs is highly non-linear and the physics affecting the baryons when the first condensed structures are formed is very complicated due to the presence of feedback processes.

The main approach to the study of the missing baryons problem comes from numerical methods applied to the LSS formation, that we will describe in detail in Chapter 3.

## 2.2.2 The results of cosmological simulations

As we will see in Chapter 3, the “missing baryons” problem is a typical kind of study that requires the use of numerical methods, since it is connected with the non-linear dynamics of structure formation. Cen & Ostriker (1999) and later Davé et al. (2001) investigated the LSS formation in the low-redshift Universe using cosmological hydrodynamical simulations. The picture arising from this kind of works is that at the present epoch the gas can be roughly divided into 4 different phases (see Fig. 2.1), according to its density and temperature:

- i - diffuse:* with  $\delta < 1000$  and  $T < 10^5$  K, of mainly photoionized gas that gives rise to Lyman- $\alpha$  absorption systems;
- ii - condensed:* with  $\delta > 1000$  and  $T < 10^5$  K, of cold and dense gas associated to the regions of star formation;
- iii - hot:* with  $T > 10^7$  K, that corresponds to the gas inside galaxy clusters and large groups;

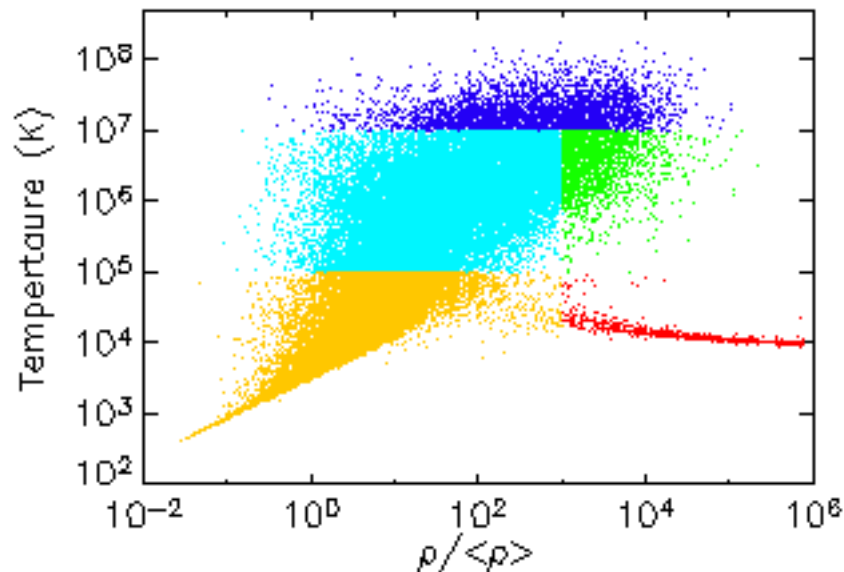


**Figure 2.1.** Phase-diagram (temperature versus density) of the gas at  $z = 0$  as obtained from the *Keyproject* cosmological hydrodynamical simulation (see its detailed description in Section 3.5.1) by Borgani et al. (2004). Each dot corresponds to a gas element. According to their temperature and density the gas has been separated into different phases: hot (blue), WHIM (cyan, for the diffuse WHIM and green for the dense WHIM), diffuse (yellow) and condensed (red).

*iv - warm-hot:*  $10^5 \text{ K} < T < 10^7 \text{ K}$ , the *warm-hot intergalactic medium (WHIM)* that corresponds mainly to the gas residing in groups, in the external regions of clusters (the *dense WHIM*) and in filaments (the *diffuse WHIM*).

Numerical simulations estimate that the WHIM constitutes an important fraction of the total amount of baryons. The exact percentage varies depending on the physical prescriptions adopted (e.g. considering/neglecting the effects of the reionization and feedback from SN and galactic winds): the most realistic models predict that about a half of the baryons at  $z = 0$  are in this phase. This gas is mainly located in filaments connecting virialized objects that create the characteristic picture of the LSS at low-redshift called *cosmic web*, as shown in Fig. 2.2.

In fact, as the massive haloes collapse and merge to create galaxy clusters and groups at  $z \lesssim 2$ , a large fraction of baryons and DM is not involved in this process and remains outside virialized regions. This matter creates filaments that constitute the preferential directions for accretion into clusters. The gas inside these structures reaches high temperatures due to shock-heating processes caused by large-scale perturbation waves. The temperature reached with this process can be calculated analytically in an approximate way (Cen & Ostriker, 1999; Davé et al., 2001): if we imagine a large-scale perturbation that becomes non-linear at the scale  $L_{\text{nl}}$  and that collapses in approximately a Hubble time  $t_{\text{H}} = H(t)^{-1}$ , then

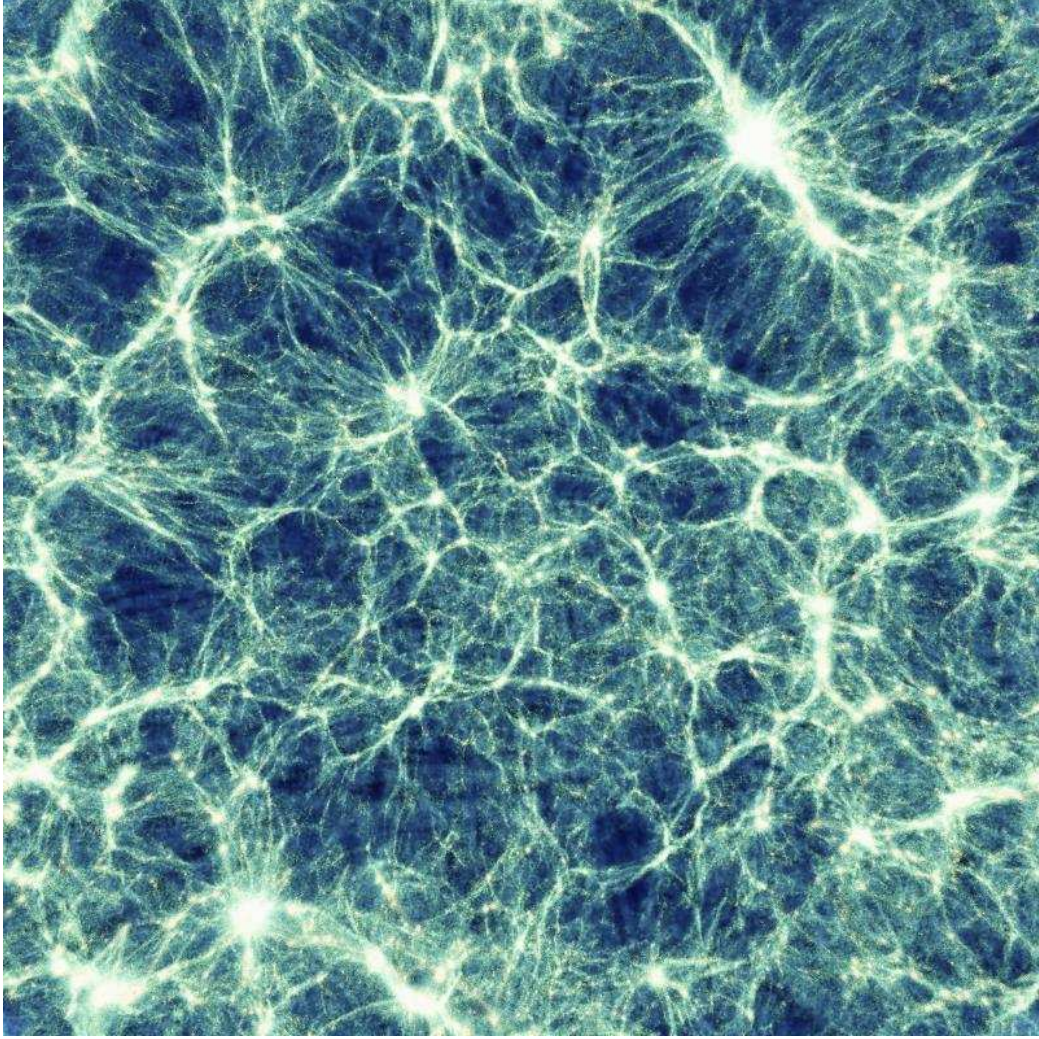


**Figure 2.2.** The LSS of the Universe at  $z = 0$  creating the cosmic-web. This picture corresponds to the projected density of both DM and gas of a volume of  $(192 \times 192 \times 10) h^{-3} \text{ Mpc}^3$  obtained from the *Keyproject* cosmological hydrodynamical simulation (see its detailed description in Section 3.5.1) by Borgani et al. (2004).

the temperature after the shock process is

$$T_{\text{nl}} \propto c_{\text{nl}}^2 = k(HL_{\text{nl}})^2, \quad (2.1)$$

where  $c_{\text{nl}}$  is the speed of the perturbation wave and  $k$  is a constant estimated by Davé et al. (2001) to be about 0.3, which corresponds to the postshock sound speed of a strong shock. With this process the gas that creates filaments can heat up to temperatures of  $10^5$ – $10^7$  K.

Given its temperature, the WHIM is fully ionized for what concerns the hydrogen and helium component, therefore it does not produce any Lyman- $\alpha$  absorption feature. Its main emitting process is the bremsstrahlung emission, but since it depends on the square of the density, only the most dense WHIM regions, constituting mainly galaxy groups, will produce a significant emission making them

detectable in the X-ray band. On the contrary the gas residing in filaments is predicted to be much more diffuse making it very difficult to detect.

The amount of gas residing in filaments at  $z = 0$  as estimated by cosmological hydrodynamical simulations is consistent with the fraction of gas that has not been observed yet. Therefore, the presence of filaments of WHIM in the LSS of the Universe is believed to be the most likely solution to the missing baryons problem.

The chances of detecting a signal coming from filaments are mainly in the X-ray band. In fact, as we will see in Chapter 4, the integrated emission of these structures is expected to contribute to a non-negligible fraction of the X-ray background at the lower energies. However, in order to get significant information about their thermodynamical status, it is necessary to perform high-resolution spectroscopic observations in order to detect emission or absorption lines due to the metals that are not completely ionized at the WHIM temperatures.

### 2.2.3 Observational data

Even if in the recent years the cosmic X-ray background (XRB) has been investigated deeply using different instruments, a clear detection of a filamentary structure of the LSS has not been made yet, probably due to several difficulties in the detection of the WHIM in this band. In fact, the soft XRB has a significant contribution by local components, namely the Local Bubble and the Galactic Halo, that are poorly known, making it very challenging to disentangle any extragalactic signal from these foregrounds. Moreover, the detection of a single filament is made even more difficult by the projection effects of the signal of the LSS itself (see Fig. 4.3 and the relative discussion).

For these reasons the most promising observational technique to measure this signal is via high-resolution spectroscopic observations of line emission or absorption (the so-called *X-ray forest*) due to the metals present in the WHIM gas. In fact, the detection of an emission/absorption feature can provide a direct information on the redshift of the gas, thus allowing one to distinguish its signal from the background and the local components.

Despite the difficulties, in the last years several possible detections of filaments' emission have been reported by using different techniques. Examining the soft XRB measured by *ROSAT* and *XMM-Newton*, Sołtan et al. (2005) found an excess emission in the 0.3–0.5 keV band consistent with a bremsstrahlung spectrum of warm-hot gas. Zappacosta et al. (2002) detected a diffuse X-ray structure in the *ROSAT* field with properties similar to the ones predicted by simulations for the WHIM gas ( $T \approx 3 \times 10^6$  K). Moreover this structure seems to be associated to a galaxy overdensity as predicted by theoretical models. Recently Mannucci et al. (2007) measured a redshift of  $z = 0.401 \pm 0.02$  for this structure estimated from the photometric observations of its galaxies. Dietrich et al. (2005) studied the double cluster system Abell 222-223 demonstrating the correspondence of a DM filament, detected via weak-lensing analysis, with a diffuse soft X-ray emission between the two objects. This result is in agreement with the picture of the cosmic web, in which filaments constitute bridges between galaxy clusters.

Furthermore, also two claimed detections in absorption have been reported. Mathur et al. (2003) analysed the spectrum of the bright quasar H1821+643 identifying several absorption features at different redshifts associated to O and Ne. They also estimated the density of the gas and obtained values consistent with those of non-virialized objects. Nicastro et al. (2005a) observed the spectrum of the blazar Markarian 421 with *Chandra* and identified two absorption systems at  $z = 0.011 \pm 0.001$  and  $z = 0.027 \pm 0.001$  associated to O and N (see, however, Kaastra et al., 2006). From these data they also estimated the density and the temperature of the gas obtaining, again, values consistent with the WHIM gas predicted by simulations.

All of these results are encouraging and nowadays there are several observational projects aimed at the detection of the cosmic-web signal. The planning of this kind of observations requires a detailed theoretical description of the physical properties of the WHIM gas. We will see in Chapter 3 that hydrodynamical simulations play an important role in this framework, because they constitute the only tool to investigate the evolution of structure formation in the highly non-linear regime.

## Chapter 3

# NUMERICAL METHODS IN COSMOLOGY

In this chapter we will describe the basis of the main simulation techniques adopted in cosmology. We will explain their role in the understanding of structure evolution and we will give examples of different kinds of numerical methods comparing their mathematical approach for solving the equations regulating the dynamics of the structures of the Universe. Finally, we will describe the code GADGET-2 and the three simulations adopted for the work of this Thesis.

### 3.1 The role of simulations in cosmology

In Section 1.6.1 we described the analytical solutions of the equations that regulate the growth of perturbations in the linear regime, when the density contrast is very low,  $\delta \ll 1$ . We gave two examples of possible approximations for the evolution at the non-linear scales in Section 1.6.3 stressing the limits connected with the adopted approximations.

Therefore, a correct description of the dynamical evolution of structure formation requires the use of *numerical methods* or, more precisely, of *hydrodynamical simulations* when the evolution of the baryonic component is accounted for. Thanks to the development of computers and supercomputers, the use of simulations in cosmology has grown massively in the last years and it is now possible to use a large variety of numerical codes that are able to provide realistic descriptions of several physical processes.

However, it is important to note that in order to reproduce the evolution of a given physical system with simulations, there are some basic conditions that this system must satisfy. More precisely it is required that

- i* - the physical properties of the system must be representable by a finite number  $N$  of variables,
- ii* - the initial conditions must be known,

*iii* - the nature of the forces that influence the evolution of the system must be known,

*iv* - the equations that regulate its dynamics must be numerically solvable.

The numerical methods used for hydrodynamical simulations are usually classified in two main groups: the *Lagrangian* and *Eulerian* methods, referring to the two different mathematical approaches to fluid dynamics.

Eulerian simulations study the physical system by describing the evolution of physical quantities at fixed points of space. In the simulation the space is divided in cells to which are associated the physical variables that change with time: the volume of the cell fixes the resolution of the simulation.

Conversely, a Lagrangian analysis consists in connecting the physical quantities of interest to fluid elements and in studying their evolution as a function of time following the change in the position of the fluid elements. Therefore, a Lagrangian simulation assumes that the fluid is divided into discrete particles, usually of the same mass thus fixing the resolution in mass.

## 3.2 *N*-body simulations

The *N*-body problem is a classical mathematical problem that has been studied starting from the XVIII Century. It consists in finding the solutions to the equations of motion for a finite number of massive points that interact only via gravitational force.

The hypothesis is to consider  $N$  bodies of mass  $m_i$ , with initial positions and velocities  $\vec{x}_i(0) = \vec{x}_{0,i}$  and  $\vec{v}_i(0) = \vec{v}_{0,i}$ , respectively. The equations that must be solved are the following:

1. the definition of velocity

$$\frac{d\vec{x}_i}{dt} = \vec{v}_i, \quad (3.1)$$

2. the definition of force

$$\frac{d\vec{v}_i}{dt} = \frac{\vec{F}_i}{m_i}, \quad (3.2)$$

3. and the Poisson equation (1.64c)

$$\nabla^2\Phi = 4\pi G\rho(\vec{x}, t). \quad (3.3)$$

Many mathematical studies of celestial mechanics were focused on this problem and provided a solution for  $N = 2$  (Kepler theory); H. Poincaré (1890) demonstrated that for  $N > 2$  the equations are not solvable in the most general case. For  $N = 3$  it is possible to solve the problem when assuming some particular initial conditions, but these solutions are only of purely mathematical interest or, in the case of a body with negligible mass  $m_3 \ll m_1, m_2$  (*restricted 3-bodies problem*), they provide approximate results valid under very restrictive hypothesis.

The generalization to  $N > 3$  requires the use of Lagrangian numerical techniques called *N-body simulations*. These simulations calculate the evolution of physical systems in which particles interact only by gravity but neglecting all the effects of pressure and other physical processes connected with gas physics. Therefore these models are effective only in describing the evolution of the dark matter component.

This approach consists in calculating the solutions of equations (3.1) and (3.2) with the finite difference method; for example the analytical derivative that defines the velocity is substituted by the numerical counterpart

$$\vec{v} \equiv \frac{\vec{x}(t + \Delta t) - \vec{x}(t)}{\Delta t}, \quad (3.4)$$

where  $\Delta t$  is the finite *timestep* that fixes the time resolution of the simulation.

More precisely, the execution of a timestep in a *N-body* algorithm is constituted by three different phases

1. the length  $\Delta t$  of the timestep is decided: some algorithms require fixed timesteps while other adapt its length according to the physical conditions;
2. the gravitational force acting on every particle is calculated from Newton law

$$\frac{\vec{F}_i}{m_i} = \sum_{j=1}^N \frac{Gm_j}{|\vec{r}_{ij}|^3} \vec{r}_{ij}, \quad (3.5)$$

where  $r_{ij}$  is the vector connecting the  $i$ -th and  $j$ -th particles ( $j \neq i$ );

3. for every particle the new positions  $\vec{x}_{i,N}$  and velocities  $\vec{v}_{i,N}$  are calculated as

$$\vec{x}_{i,N} = \vec{x}_i(t + \Delta t) = \vec{x}_i(t) + \vec{v}_i(t)\Delta t, \quad (3.6)$$

$$\vec{v}_{i,N} = \vec{v}_i(t + \Delta t) = \vec{v}_i(t) + \frac{\vec{F}_i(t)}{m_i}\Delta t. \quad (3.7)$$

The second phase is the most time-consuming one because it requires the calculation of all distances  $r_{ij}$  ( $i, j = 1, \dots, N$ ) between the  $N(N - 1)/2$  different pairs of particles: thus, the *calculation time*  $\tau_c$  is proportional roughly to  $N^2$ . This aspect is particularly important when considering cosmological simulations because a detailed study of structure formation requires the use of a large number of particles. As we will see in the next subsections, the *N-body* algorithms used in cosmology have as a main difference the method of force calculation.

### 3.2.1 The particle-particle (PP) method

The *particle-particle (PP) method* consists in calculating the force acting on each particle simply by summing up the forces due to the remaining particles of the simulation. It uses a slightly modified version of the Newton equation (3.5): the force acting on the  $i$ -th particle is

$$\frac{\vec{F}_i}{m_i} = \sum_{j=1}^N \frac{Gm_j}{(|\vec{r}_{ij}| + \epsilon_s)^3} \vec{r}_{ij}, \quad (3.8)$$

where the term  $\epsilon_s$ , called *softening*, is added in the equation in order to avoid an overflow in the calculation of the force of very close particles: this term acts approximately as a finite size for the particles.

The force calculation with the PP method is extremely accurate but it is also very time consuming ( $\tau_c \propto N^2$ ), making it suitable only for systems representable with a low number of particles.

### 3.2.2 The particle-mesh (PM) method

The *particle-mesh (PM) method* is a hybrid Lagrangian-Eulerian algorithm that both considers the presence of the  $N$ -bodies and divides the volume of the system with a mesh associating to every cell the value of the gravitational potential and of the other field variables. The grid is used in order to quickly solve the Poisson equation (3.3) in the Fourier space.

The space is represented by a cube of side  $L$  with  $N$  particles of mass  $m$  and  $M$  equispaced nodes for every dimension (i.e.  $M^3$  grid points): thus being  $\Delta s = L/M$  the spacing between the grid points, the space is divided into  $M^3$  cells of volume  $\Delta s^3$ . The following step is the calculation of the fluid density in every cell by distributing the masses of each particle with the following formula:

$$\rho(\vec{x}_{ijk}) = m \frac{M^3}{L^3} \sum_{l=1}^N W(\delta\vec{x}_l), \quad (3.9)$$

where  $\delta\vec{x}_l = \vec{x}_l - \vec{x}_{ijk}$  are the coordinate differences between the position  $\vec{x}_{ijk}$  of the centre of every cell and the  $l$ -th particle ( $\vec{x}_l$ ) and  $W$  is a suitable function called *kernel*, normalized in order to conserve the mass. The three forms for the function  $W$  usually adopted are:

1. NGP (Nearest Grid Point),
2. CIC (Cloud In Cell),
3. TSC (Triangular Shaped Cell).

In the first case the whole mass of the particle is assigned to the nearest cell, while in the second and the third it is distributed in the  $2^3 = 8$  and  $3^3 = 27$  nearest cells, respectively, with fractions proportional to the inverse of the square of the distance.

The density in the grid is then used to calculate the gravitational potential by solving the Poisson equation with FFT, since in the Fourier space the Poisson equation becomes algebraic. In fact, if we consider the Fourier transforms of the density and the potential

$$\tilde{\rho}(\vec{k}) = \int \rho(\vec{x}) e^{-i(\vec{k} \cdot \vec{x})} d^3\vec{x} \quad (3.10)$$

and

$$\tilde{\Phi}(\vec{k}) = \int \Phi(\vec{x}) e^{-i(\vec{k} \cdot \vec{x})} d^3\vec{x}, \quad (3.11)$$

respectively, equation (3.3) becomes

$$\tilde{\Phi}(\vec{k}) = G(\vec{k})\tilde{\rho}(\vec{k}), \quad (3.12)$$

where  $G(\vec{k})$  is the Green function of the Laplacian that can be expressed as

$$G(\vec{k}) \propto -\frac{1}{k^2}. \quad (3.13)$$

Finally, the force in every grid point can be computed in the ordinary space from the potential or, equivalently, in the Fourier space as

$$\vec{F}(\vec{k}) = -i\vec{k}\tilde{\Phi}(\vec{k}). \quad (3.14)$$

Finally, the force acting on a particle is obtained with the inverse process of the one used to calculate the density.

The PM method requires much shorter computation times, in fact  $\tau_c \propto N \log N$ . On the other side, the drawbacks of this scheme are given by the explicit approximations introduced, that lower the accuracy, and by the fixed size of the grid that constitutes a spatial resolution limit: in fact, any information on scales lower than  $\Delta s$  is lost.

### 3.2.3 The particle-particle-particle-mesh (P<sup>3</sup>M) method

The *particle-particle-particle-mesh* (P<sup>3</sup>M) method was studied to have a force calculation as accurate as in the case of the PP method but also as fast as the PM. For this purpose the force  $\vec{F}_i$  acting on a given particle is separated into two components: a short-distance term,  $\vec{F}_i^{\text{PP}}$ , computed with the PP method, and a long-distance term,  $\vec{F}_i^{\text{PM}}$ , computed with the PM one, so that the final force is

$$\vec{F}_i = \vec{F}_i^{\text{PP}} + \vec{F}_i^{\text{PM}}. \quad (3.15)$$

Therefore in the P<sup>3</sup>M algorithms there is a critical distance  $d_{\text{cr}}$  that separates the two regimes. The choice of  $d_{\text{cr}}$  depends on the compromise between accuracy and speed that one wants to adopt.

The most recent P<sup>3</sup>M codes use adaptive meshes that increase the grid points in regions corresponding to higher densities: with this method the calculation time is focused in the volumes that contain most of the mass, thus more relevant for the final results. The drawbacks of the P<sup>3</sup>M method are basically in the adaptive mesh that complicates significantly the algorithm. Moreover the refinement introduced in the running time is not able to reconstruct the power on scales lower than  $\Delta s$  that is not contained in the initial conditions.

### 3.2.4 The TREE code

The TREE code (Barnes & Hut, 1986) is an algorithm that adopts a hierarchical tree to classify the particles: this classification is used in order to optimize the speed and the accuracy of the force calculation. This is obtained by introducing specific

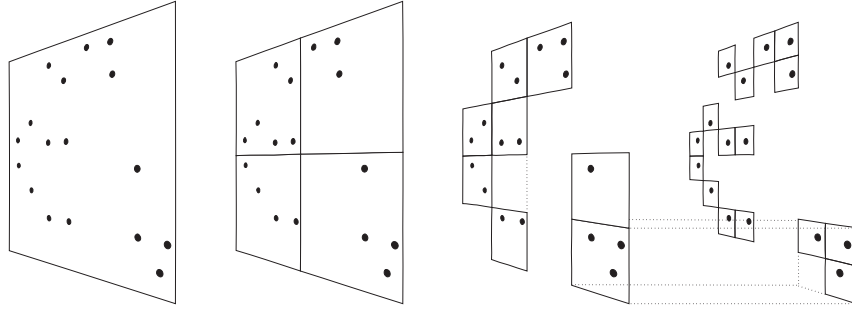


**Figure 3.1.** Sketch of the TREE code scheme in two dimensions (picture taken from Springel et al., 2001). The particles on the left are enclosed in a first level cell (main node) that is iteratively split into 4 squares (8 cubes for the three-dimensional case) until only one particle remains (the “leaf” of the tree). Empty cells are not considered.

approximations that are calibrated according to the distance in order to improve the efficiency.

The scheme of the TREE code is sketched in Fig. 3.1. The particles are divided into groups by splitting the initial volume into  $2^3 = 8$  cubes that constitute the main nodes: for each node the gravitational potential multipoles are calculated up to a fixed precision limit. Then the cell-splitting is iteratively refined into lower hierarchical elements until each cell contains at most one particle. The acceleration acting on each particle is then calculated with different methods according to the hierarchical element, which is determined according to the distance from the particle itself. This procedure neglects the actual distribution of particles inside the hierarchical elements and approximates the calculation of the potential using the barycentre theorem and multipole expansion.

In detail, the force arising from the nearest particles is calculated with the PP method, while for particles at larger distances the contribution is computed considering the total contribution of the hierarchical cell to which they belong: the refinement in the cell-splitting and the consequent accuracy in the multipole calculations decreases with increasing distance. The accuracy parameters that determines at which level a cell must be split is given by an angle  $\theta$ , that determines the precision and the velocity of the algorithm: a cell is refined until its size  $s_{\text{cell}}$  satisfies the relation

$$s_{\text{cell}} < d \theta , \quad (3.16)$$

being  $d$  the distance of the cell from the particles.

With this method the number of elements that contribute to the force acting on a particle is of the order of  $\log N$ , therefore for the TREE code we have that  $\tau_c \propto N \log N$ , like for the PM method, but with higher precision.

### 3.3 Hydrodynamical simulations

A numerical approach to the study of the evolution of structure formation cannot rely only on  $N$ -body simulations. In fact, if it is true that DM can be considered non-collisional and interacts only via gravitational force, the baryonic component is subject to a variety of complex physical processes that are not considered in  $N$ -body algorithms. Since the baryons are responsible of basically all of the observational phenomena that we observe, a detailed comparison between simulations and observations requires the use of codes which can model the evolution of the gas.

In more detail, the study of the evolution of the baryons in the Universe requires numerical methods capable of describing mainly

- i* - thermodynamics,
- ii* - radiative and absorption properties of the gas,
- iii* - galaxy/star formation and consequent feedback.

The accuracy required for the description of the baryon physics depends on the system that one wants to study. For example, the formation of galaxy clusters can be approximated using only thermodynamics while a description of gas clouds responsible for the line absorption in the quasar spectra requires also the second point. An accurate description of galaxies and of their observational properties needs also the modelization of star formation. Other more complicated physical phenomena may require also the addition of magnetic fields, thermal conduction and other processes.

Since the basis of all of this kind of phenomena is the dynamics of fluids, these models are generally referred to as *hydrodynamical simulations* and in this Section we will review the main types of codes used in this field, focusing on the thermodynamical part. A description of some specific algorithms for the other physical processes will be given in the following Sections.

#### 3.3.1 Eulerian approach

As already said in Section 3.1, in Eulerian algorithms the physical quantities are described in the form of field variables defined in discretized (usually cubic) cells. The main quantities necessary to follow the thermodynamics of the fluid are temperature, pressure and gravitational potential that follow equations (1.64). For a given generic field  $f(x, t)$  we can obtain its evolution from the continuity equation expressed in terms of the flux of the field  $F$ :

$$\frac{\partial f}{\partial t} = -\vec{\nabla} \cdot \vec{F} . \quad (3.17)$$

If we perform a Taylor expansion of the field at the time  $t + dt$  we obtain

$$f(\vec{x}, t + dt) = f(\vec{x}, t) + \frac{\partial f}{\partial t} dt + \frac{1}{2} \frac{\partial^2 f}{\partial t^2} dt^2 + O(dt^3) \quad (3.18)$$

and combining the two previous equations we have

$$f(\vec{x}, t + dt) = f(\vec{x}, t) - (\vec{\nabla} \cdot \vec{F})dt + \frac{1}{2} \vec{\nabla} \cdot \left[ (\vec{\nabla} \cdot \vec{F}) \frac{\partial \vec{F}}{\partial f} \right] dt^2 + O(dt^3), \quad (3.19)$$

that describes the time evolution of the field at the second order. In Eulerian codes this equation is discretized with timesteps and meshes and solved at the first or second order.

This description is valid only for algorithms that analyse ideal fluids, while the treatment of shocks and entropy production requires the addition of *artificial viscosity* terms in the equations. This introduces a minimum scale under which the effects of shocks can be neglected, but also reduces the resolution of the code. Other more accurate techniques have been implemented, like Riemann solvers that include the exact solution of a simple non-linear problem (the ‘‘Riemann shock tube’’) into the algorithm. Examples of these algorithms are the Total Variation Diminishing (TVD, Ryu et al., 1993) and the Piecewise Parabolic Method (PPM, Bryan et al., 1995).

### 3.3.2 Lagrangian approach: the Smoothed Particle Hydrodynamics (SPH)

The Lagrangian methods, like  $N$ -body simulations, represent the fluid by dividing it into discrete particles: the physical quantities necessary to describe the fluid are associated to every Lagrangian particle and their evolution is computed considering also the equations of motion of the particles. The main advantage of this approach is that the spatial resolution of the code can be very high in dense regions without the need of including additional implementations. On the other side the resolution can become very poor in low-density regions.

Starting from the 1970’s many different Lagrangian techniques have been developed. The most important one is the *Smoothed Particle Hydrodynamics* (SPH; Lucy, 1977; Gingold & Monaghan, 1977). This algorithm solves the equations of hydrodynamics at every position of the particles by substituting the true physical quantities by the estimates obtained from the closest particles: this process requires the definition of a function  $W(x, h)$ , called *smoothing kernel*. Being  $\vec{r}$  the position in the space and  $\vec{r}'$  a position of a given particle, the kernel depends on the distance  $x \equiv |\vec{r} - \vec{r}'|$  and on a parameter  $h$  called *smoothing length*. Usually this function  $W$  is similar to a Gaussian function with null values for distances larger than a multiple of  $h$ : this allows one to define a maximum interaction distance between the particles thus reducing the execution time of the code.

In order to have physical sense,  $W$  must be peaked around 0,

$$\lim_{h \rightarrow 0} W(x, h) = \delta_D(x), \quad (3.20)$$

where  $\delta_D$  is Dirac delta, and must be normalized to 1 when integrated in the volume,

$$\int W(x, h) d^3x = 1. \quad (3.21)$$

Then, for a given field function  $f(\vec{r})$  it is possible to define  $\langle f(\vec{r}) \rangle_a$  as the convolution of the function with the smoothing kernel

$$\langle f(\vec{r}) \rangle_a \equiv \int W(|\vec{r} - \vec{r}'|, h) f(\vec{r}') d^3 \vec{r}' . \quad (3.22)$$

The numerical counterpart  $\langle f(\vec{r}_i) \rangle_n$  of this function is used to estimate the values of the field functions at the positions occupied by the particles. Being  $\vec{r}_i$  the position of the  $i$ -th particle, the value of the function in that position is calculated as

$$\langle f(\vec{r}_i) \rangle_n \equiv \sum_{j=1}^N W(|\vec{r}_i - \vec{r}_j|, h) f(\vec{r}_j) d^3 \vec{x}_j , \quad (3.23)$$

where  $d^3 \vec{x}_j$  is the volume occupied by the  $j$ -th particle that is usually obtained from density  $\rho_j$  and the mass  $m_j$ :

$$d^3 \vec{x}_j = \frac{m_j}{\rho_j} . \quad (3.24)$$

This allows one to calculate the value of all physical quantities. For example, for the density the expression simplifies to

$$\rho_i = \sum_{j=1}^N m_j W(|\vec{r}_i - \vec{r}_j|, h) . \quad (3.25)$$

The SPH formalism is useful also to calculate the gradient of the field functions, providing an easy way to resolve the differential equations that contain spatial gradients. In fact, from equation (3.22) we have that

$$\langle \vec{\nabla} f(\vec{r}) \rangle_a = \int W(|\vec{r} - \vec{r}'|, h) \vec{\nabla} f(\vec{r}') d^3 \vec{r}' . \quad (3.26)$$

Integrating the second term by parts, applying the divergence theorem one obtains

$$\langle \vec{\nabla} f(\vec{r}) \rangle_a = \int \vec{\nabla} W(|\vec{r} - \vec{r}'|, h) f(\vec{r}') d^3 \vec{r}' , \quad (3.27)$$

that can be approximated with the numeric expression

$$\langle \vec{\nabla} f(\vec{r}) \rangle_n = \sum_{j=1}^N \frac{m_j}{\rho_j} \vec{\nabla} W(|\vec{r} - \vec{r}'|, h) f(\vec{r}') . \quad (3.28)$$

Equation (3.28) provides a way to evaluate the gradient of the field function directly from the gradient of the smoothing kernel. An appropriate choice of the kernel function (e.g. a differentiable function) can lead to a significant shortening of the calculation time, because the function  $\vec{\nabla} W(|\vec{r} - \vec{r}'|, h) f(\vec{r}')$  can be calculated once and inserted in the code avoiding the computation of the gradients of the different field functions that would be highly time consuming.

Two examples of functions that can be used in SPH codes are

1. the Gaussian kernel (Gingold & Monaghan, 1977)

$$W(x, h) = \frac{1}{\pi^{3/2} h^3} e^{-x^2/h^2} , \quad (3.29)$$

2. the cubic-spline kernel (Monaghan & Lattanzio, 1985)

$$W(x, h) = \frac{8}{\pi h^3} \begin{cases} 1 - 6(x/h)^2 + 6(x/h)^3 & 0 \leq x \leq h/2 \\ 2(1 - x/h)^3 & h/2 \leq x \leq h \\ 0 & x \geq h \end{cases} \quad (3.30)$$

The Gaussian kernel allows one to obtain more accurate estimates but, since it is larger than 0 for every distance value, it does not define a maximum length for the particles interaction with a consequent increase of calculation time. For this reason kernel functions like the second one are more suitable for long integrations.

The number of interactions that occur between particles in a given timestep depends also on the value of  $h$ . The choice of the value of the smoothing length is usually the result of the compromise between accuracy and computation time: usually this value is chosen to be variable with particles and time in order to keep the number of interactions constant (typically a number in the range 30–50).

In every timestep the SPH code must solve the fluid equations: the mass conservation is implicit in (3.21), while in the adiabatic regime the Euler and the energy conservation equations become

$$\left(\frac{d\vec{v}_i}{dt}\right)_n = - \sum_{j=1}^N m_j \left[ \frac{p_i}{\rho_i^2} + \frac{p_j}{\rho_j^2} \right] \vec{\nabla} W(|\vec{r}_i - \vec{r}_j|, h) \quad (3.31)$$

and

$$\left(\frac{d\epsilon_i}{dt}\right)_n = \frac{p_i}{\rho_i^2} \sum_{j=1}^N m_j (\vec{v}_i - \vec{v}_j) \cdot \vec{\nabla} W(|\vec{r}_i - \vec{r}_j|, h), \quad (3.32)$$

respectively.

The description of non-conservative physical systems, e.g. a radiative gas, can be implemented by modifying equation (3.32). On the contrary the description of phenomena like shock-heating requires the addition of artificial viscosity terms.

### 3.4 GADGET and GADGET-2

The TREE-SPH code GADGET (“*Galaxies with Dark matter and Gas intEract*”, Springel et al., 2001) is a Lagrangian algorithm where the gravitational force is computed with a TREE method, while the hydrodynamical equations are solved with the SPH technique. Its high flexibility makes it suitable for the study of many astrophysical problems ranging from planetary physics, galaxy formation and cosmology. For what concerns LSS formation GADGET can follow the evolution of both DM and baryonic component and has proven to be successful in describing the main characteristics of clusters of galaxies.

The main qualities of the code are the full adaptivity of the force calculation and time-stepping and its accuracy in solving equation, with force symmetry guaranteed

by the kernel averaging technique. Moreover several additional implementations of different physical process affecting the baryonic component, like radiative cooling and star formation, are nowadays available. Recently a new version of the code, called GADGET-2 (Springel, 2005), has been developed: it contains improvements of the time integration scheme and of the “entropy conserving” formulation of SPH and also in the gravitational computation algorithm. This resulted in a reduction of computation time and memory requirements compared to the original version.

All of the simulations used for the works presented in this Thesis were performed with GADGET-2. In the next Sections we will focus on the description of the main physical processes affecting the baryonic component implemented in the new version of the code.

### 3.4.1 Radiative cooling and photoionization

The most important processes that influence the thermodynamics of the baryons are the radiative cooling and the heating due to the interactions with the ultraviolet (UV) photons responsible of the re-ionization of the Universe. The effects of these two processes are implemented by modifying the equation of energy conservation adding a term

$$\frac{du_i}{dt} \propto \frac{H_i - \Lambda_i}{\rho_i}, \quad (3.33)$$

where  $u_i$  is the thermal energy associated to the  $i$ -th particle and  $H_i$ ,  $\Lambda_i$  and  $\rho_i$  represent the heating function, the cooling function and the density associated to the particle, respectively.

The radiative cooling is usually implemented in the hypothesis of primordial composition of the gas, ionization equilibrium, optically thin gas and spatially uniform radiation field. Only the two-body processes are considered, since at densities typical of astrophysical environments three-body interactions are negligible. The various processes are followed considering the different ionization species of hydrogen and helium and are summarized in Table 3.1. For high-temperature ( $T > 10^6$  K) the gas is fully ionized, therefore the most important cooling process is the free-free or *bremstrahlung* emission, while the other processes become important for neutral gas. Besides from these processes, at high redshift also the inverse-Compton cooling due to the interaction with the CMB is important and, therefore, implemented in GADGET, assuming an emissivity

$$\Lambda_C = 5.41 \times 10^{-36} n_e T(1+z)^4 \text{ erg s}^{-1} \text{ cm}^{-3}, \quad (3.34)$$

being  $n_e$  the electron number density and  $T$  the temperature of the gas.

The computation of the heating function  $H_i$  is done considering a uniform, time dependent, photoionizing UV background expected from a population of quasars. A more accurate description of the model adopted can be found in Haardt & Madau (1996).

PHYSICAL PROCESS	CHEMICAL SPECIES	EMISSIVITY $T_n = T/(10^n \text{K})$ $\text{erg s}^{-1} \text{cm}^{-3}$
Collisional excitation .....	H <sup>0</sup>	$7.50 \times 10^{-19} e^{-118384.0/T} (1 + T_5^{1/2})^{-1} n_e n_{\text{H}^0}$
	He <sup>+</sup>	$5.54 \times 10^{-17} T^{0.397} e^{-473638.0/T} (1 + T_5^{1/2})^{-1} n_e n_{\text{He}^+}$
Collisional ionization .....	H <sup>0</sup>	$1.27 \times 10^{-21} T^{1/2} e^{-157809.1/T} (1 + T_5^{1/2})^{-1} n_e n_{\text{H}^0}$
	He <sup>0</sup>	$9.38 \times 10^{-22} T^{1/2} e^{-285335.4/T} (1 + T_5^{1/2})^{-1} n_e n_{\text{He}^0}$
	He <sup>+</sup>	$4.95 \times 10^{-22} T^{1/2} e^{-631515.0/T} (1 + T_5^{1/2})^{-1} n_e n_{\text{He}^+}$
Recombination .....	H <sup>+</sup>	$8.70 \times 10^{-27} T^{1/2} T_3^{-0.2} (1 + T_6^{0.7})^{-1} n_e n_{\text{H}^+}$
	He <sup>+</sup>	$1.55 \times 10^{-26} T^{0.3647} n_e n_{\text{He}^+}$
	He <sup>++</sup>	$3.48 \times 10^{-26} T^{1/2} T_3^{-0.2} (1 + T_6^{0.7})^{-1} n_e n_{\text{He}^{++}}$
Dielectric recombination	He <sup>+</sup>	$1.24 \times 10^{-13} T^{-1.5} e^{-4.7/T_5} (1 + 0.3e^{-9.4/T_4}) n_e n_{\text{He}^+}$
Free-free interaction .....	ions	$1.42 \times 10^{-27} g_{ff} T^{1/2} n_e (n_{\text{H}^+} + n_{\text{He}^+} + 4n_{\text{He}^{++}})$

**Table 3.1.** Radiative cooling processes. For the free-free interaction  $g_{ff}$  is the Gaunt factor assumed to be  $g_{ff} = 1.1 + 0.34e^{-(5.5 - \log T)^2/3.0}$ .

### 3.4.2 Star formation

The amount of mass in stars in cluster-sized systems is much smaller than the corresponding amount in gas and DM ( $\sim 10$  per cent of the total baryonic mass, at  $z = 0$ ). Nevertheless a treatment of star formation in cosmological hydrodynamical codes is important not only because stars are directly observable, but also because, since they are basically collisionless, they behave in a different way with respect to gas, affecting mergers rates and ram pressure stripping.

In GADGET star particles are generated subtracting the equivalent mass to gas particles. This happens when a gas particle satisfies some dynamical and thermodynamical conditions:

*i* - the particle must correspond to a locally convergent flow,

$$\vec{\nabla} \cdot \vec{v}_i < 0 ; \quad (3.35)$$

*ii* - it must be Jeans-unstable, which means that the crossing time  $\tau_c$  must be higher than the dynamical time  $\tau_d$ ,

$$\tau_s = \frac{h_i}{v_{s,i}} > \frac{1}{\sqrt{4\pi G \rho_{g,i}}} = \tau_d , \quad (3.36)$$

where  $v_{s,i}$  is the local sound speed,  $h_i$  is the smoothing length and  $\rho_{g,i}$  is the gas density;

*iii* - gas overdensity must exceed a fixed threshold,

$$\frac{\rho_{g,i}}{\bar{\rho}_g} > 55 ; \quad (3.37)$$

*iv* - hydrogen number density must be higher than a fixed limit (for more detail see Katz et al., 1996; Tornatore et al., 2003),

$$n_{h,i} > 0.1 \text{ cm}^{-3}. \quad (3.38)$$

The rate of gas mass which is turned into star is then computed using the formula

$$\frac{d(\log \rho_g)}{dt} = -\frac{c_\star}{\tau_g}, \quad (3.39)$$

where  $c_\star$  is an adimensional parameter and  $\tau_g$  is a characteristic time connected with the flow of the gas and estimated from the dynamical cooling times. When a particle is forming stars it is actually split into two components: the gaseous one and the stellar one, which is treated in a non-collisional way. When the gaseous component is below a given threshold, it is distributed to the near particles with adopting smoothing kernel and the particle becomes stellar.

### 3.4.3 Extra heating

When including only cooling and star formation in simulation, the resulting amount of cool gas and star mass is more than three times higher than the observed one (Lewis et al., 2000; Borgani et al., 2001; Yoshida et al., 2002). This is known as the problem of *overcooling*: gas cooling tends to produce high density region where the cooling efficiency is higher, leading to a runaway process. This clearly indicates that in real clusters a source of non-gravitational heating is acting to reduce the amount of gas that reaches very high densities.

The simplest scenario is the implementation in the code of the heating action of type-II supernovae (SN-II) associated to star-forming particles: in GADGET this is obtained by assuming the initial mass function (IMF) of Miller & Scalo (1979) and associating to every star with  $M > 8M_\odot$  an instantaneous energy injection of  $10^{51}$  erg that is distributed between the nearest particles with the smoothing kernel. Anyway this process resulted to be not efficient in preventing the gas cooling because the energy is injected in dense regions where the cooling time is very short and, therefore, quickly radiated away.

Other possible sources of heating have been suggested like heating processes from star formation (Bower et al., 2001), active galactic nuclei (AGNs) feedback, buoyant radio bubbles (Churazov et al., 2001; Ensslin & Heinz, 2002), acoustic waves (Fujita et al., 2004) and turbulent mixing (Kim & Narayan, 2003). These kinds of feedback mechanisms are generally modelled following two different approaches:

- i* - *impulsive heating*, i.e. the energy is transferred instantaneously to all the particles at a given redshift by fixing an entropy floor (all the particles must have a minimum value of entropy) or by adding to each particle a fixed amount of energy ( $\approx 1$  keV);
- ii* - *semi-analytic models*, i.e. the algorithm tries to follow directly the physical process considered by using simulation variables and analytical models.

The second approach (see Tornatore et al., 2003, for an example on star-formation feedback) is, of course, more complex but also more realistic.

Simulations including sources of extra heating result in a significant reduction of the amount of cold gas in galaxy clusters and are also able to reproduce other important observational properties, like some of the scaling relations. However, the fraction of cold gas remains too high and there still exist some discrepancies between simulations and observations of galaxy clusters that still need to be explained.

### 3.4.4 Thermal conduction

One of the most important aspects which is still a matter of tension between observed clusters is the physics of the clusters' inner regions. In fact, hydrodynamical simulation failed to reproduce some observed features expected by the standard cooling-flow model (Fabian, 1994): simulations including cooling and star formation find an increase of the gas temperature in the central regions due to the lack of pressure support generated by cooling and the consequent infall of the gas (Tornatore et al., 2003). This lead to the counterintuitive result that cooling generates a steepening of central temperature profiles (Lewis et al., 2000; Borgani et al., 2004). On the contrary, several observational results (e.g. De Grandi & Molendi, 2002; Pratt & Arnaud, 2002) indicate that the gas is almost isothermal on scales below one fourth of the virial radius.

Narayan & Medvedev (2001) proposed thermal conduction as a possible heating mechanism for the cores of galaxy clusters: this process, in fact, could transport thermal energy from the outer cluster regions to the slightly cooler central gas, thereby largely reducing its cooling losses and stabilizing the intracluster medium (ICM). Heat conduction depends strongly on temperature and magnetic fields. Spitzer (1962) derived the result of heat conductivity due to electrons in a non magnetized plasma

$$\kappa_{\text{sp}} = 1.31 n_e \lambda_e \left( \frac{k_B T_e}{m_e} \right)^{1/2}, \quad (3.40)$$

where  $n_e$  is the electron density,  $\lambda_e$  is the electron mean free path and  $T_e$  is the electron temperature. It is important to note that since the product  $n_e \lambda_e$  depends only on  $T_e$ , the Spitzer conductivity in the case of the hot gas of galaxy clusters can be expressed as

$$\kappa_{\text{sp}} = 8.2 \times 10^{20} \left( \frac{k_B T_e}{10 \text{ keV}} \right)^{5/2} \text{ erg s}^{-1} \text{ cm}^{-1} \text{ keV}^{-1}. \quad (3.41)$$

The presence of magnetic fields suppresses significantly the conductivity of the gas: however Narayan & Medvedev (2001) showed that for a chaotically tangled magnetic field, which is the expected condition for clusters of galaxies, conductivities in the range  $\kappa \sim (0.2 - 0.5)\kappa_{\text{sp}}$  can be reached, making thermal conduction an important physical mechanism acting on the ICM.

The energy transfer due to heat conduction can be computed using the simple relation

$$\frac{du}{dt} = \frac{1}{\rho} \nabla \cdot (\kappa \nabla T), \quad (3.42)$$

where  $u$  is the thermal energy per unit mass of the gas. However, even if one assumes a fixed constant value for  $\kappa$ , the implementation of equation (3.42) in the SPH formalism presents several problems due, for example, to the presence of the second derivative of the temperature. Recently Jubelgas et al. (2004) implemented heating transfer in GADGET-2 and Dolag et al. (2004) performed the first cosmological hydrodynamical simulation including a self-consistent modelization of heat transfer. This simulation showed that the inclusion of this physical process is able to affect significantly the thermodynamics of the inner regions of galaxy clusters, producing isothermal cores for the most massive systems. However, this model was not able to significantly reduce the overcooling and also the temperature profiles of low-mass systems do not match the observed ones.

### 3.5 Hydrodynamical simulations used for this Thesis

The goal of this Thesis is the study of the physics and emission properties of the baryons of the LSS of the Universe. For this purpose we used the results of 3 different hydrodynamical simulations: the *Keyproject* simulation, the *Hutt* simulation set and the *Salacious* constrained simulation. In this Section we describe their main characteristics.

#### 3.5.1 The *Keyproject* simulation

The *Keyproject* simulation (Borgani et al., 2004, see the image displayed in Fig. 2.2) is a hydrodynamical simulation of the LSS of the Universe developed with the main aim of describing in detail the X-ray and Sunyaev-Zeldovich (SZ) properties of the baryonic intergalactic medium (IGM) in groups and clusters of galaxies and within large-scale filaments, using the most updated physical implementations present in GADGET-2 in 2003. It considers the concordance cosmological model, i.e a flat  $\Lambda$ CDM model dominated by the presence of the cosmological constant ( $\Omega_m = 0.3$ ,  $\Omega_\Lambda = 0.7$ ), with a Hubble constant  $H_0 = h$  100 km s<sup>-1</sup>Mpc<sup>-1</sup> with  $h = 0.7$ , and a baryon density  $\Omega_b = 0.04$ . The initial conditions were set by the cold dark matter power spectrum and were normalized by assuming  $\sigma_8 = 0.8$ . The comoving volume was filled with 480<sup>3</sup> DM Lagrangian particles and as many gas particles followed in their evolution from  $z = 49$  to  $z = 0$ . The cubic box is 192 $h^{-1}$  Mpc on a side, and the DM and gas particles have mass  $m_{\text{DM}} = 4.62 \times 10^9 h^{-1} M_\odot$  and  $m_{\text{gas}} = 6.93 \times 10^8 h^{-1} M_\odot$ , respectively. The (Plummer-equivalent) gravitational softening is  $\epsilon = 7.5 h^{-1}$  kpc at  $z = 0$ , fixed in physical units between  $z = 2$  and  $z = 0$ , and fixed in comoving units at earlier times.

Besides gravity and non-radiative hydrodynamics, the *Keyproject* simulation includes a treatment of several physical processes described in this Chapter: star formation, by adopting a sub-resolution multiphase model for the interstellar

medium (Springel & Hernquist, 2003), feedback from SNe with the effect of weak galactic outflows, radiative gas cooling and heating by a uniform, time-dependent, photoionizing UV background (Haardt & Madau, 1996). This run produced about one hundred outputs, equally spaced in the logarithm of the expansion factor, between  $z = 9$  and  $z = 0$ .

The results of this simulation have been used for several works on different topics (see, e.g., Murante et al., 2004; Ettori et al., 2004; Cheng et al., 2005; Rasia et al., 2005). Diaferio et al. (2005) used the whole sample of galaxy clusters extracted from this simulation at  $z = 0$  to find a good agreement with the observed scaling relations between X-ray and SZ properties and to evaluate the lower limit (about  $200 \text{ km s}^{-1}$ ) to the systematic errors that will affect future measurements of cluster peculiar velocities with the SZ effect.

For the work of this Thesis the *Keyproject* simulation has been used to study the characteristics of the diffuse X-ray background, as described in Chapter 4 and also to study the SZ effects of the LSS as shown in Chapter 5.

### 3.5.2 The *Hutt* simulation set

The *Hutt* simulation set includes 9 high-resolution re-simulations of galaxy clusters taken from a large-size cosmological simulation and carried out with GADGET-2 adopting 4 different physical prescriptions. The aim of this project is to provide a description of cluster physics adopting different physical models and considering different mass ranges. This is done to study the effects on cluster formation of both environmental properties and different processes affecting the baryonic component.

The parent simulation is a DM-only simulation of a comoving box of  $479h^{-1}$  Mpc per side, followed in the framework of a  $\Lambda$ CDM model with  $\Omega_m = 0.3$  and  $\Omega_\Lambda = 0.7$ . The Hubble parameter was set to  $h = 0.7$  and the baryon fraction is  $\Omega_b = 0.04$ . The initial conditions of the parent simulation were set considering a CDM power spectrum normalized by assuming  $\sigma_8 = 0.9$  (see Yoshida et al., 2001).

In the volume of the parent simulation 9 different haloes were identified, spanning different mass ranges: 4 of them with the typical size of clusters and 5 of small clusters or group-like objects. Then using the "Zoomed Initial Conditions" (ZIC) technique (Tormen et al., 1997) they have been resimulated by identifying their corresponding Lagrangian regions in the initial domain and populating them with more particles (of both DM and gas), while appropriately adding high-frequency modes. At the same time the volume outside the region of interest was resimulated using low-resolution (LR) particles in order to follow the tidal effects of the cosmological environment. The setup of initial conditions of all the resimulations was optimized to guarantee a volume around the clusters of  $\sim 5R_{\text{vir}}$  free of contamination from LR particles. This was obtained using an iterative process as follows. Starting from a first guess of the high-resolution (HR) region that one wants to resimulate, a DM-only re-simulation is run. Analysing its final output, all the particles that are at distances smaller than  $5R_{\text{vir}}$  from the cluster centre are selected in order to identify the corresponding Lagrangian region in the initial domain. Applying ZIC, new initial conditions at higher resolution are

generated and one more DM-only resimulation is performed. This procedure is iteratively repeated until none of the LR particles enters the HR region, which could be possible because of the introduction of low-scale modes. At the end of this process these resimulations can be considered as faithful results of the chosen model also in the external regions of the clusters without any spurious numerical effect.

In detail, these resimulations were set to have a mass resolution of  $m_{\text{DM}} = 1.13 \times 10^9 h^{-1} M_{\odot}$  for DM particles and  $m_{\text{gas}} = 1.69 \times 10^8 h^{-1} M_{\odot}$  for baryons, so that every resimulated cluster is resolved with between  $2 \times 10^5$  and  $4 \times 10^6$  particles (both DM and gas) depending on its final mass. All the simulations have a (Plummer-equivalent) softening-length kept fixed at  $\epsilon = 30 h^{-1}$  kpc comoving at  $z > 5$  and switched to a physical softening length  $\epsilon = 5 h^{-1}$  kpc at lower redshifts.

For the purpose of this Thesis, the *Hutt* simulation set was used to study the shape of the density, temperature and X-ray surface brightness profiles of the external regions of galaxy clusters as described in Chapter 6, where we also give more details on the physical models adopted and on the characteristics of the cluster sample.

### 3.5.3 The *Salacious* constrained simulation

*Salacious* is a cosmological constrained simulation of the local Universe (LU) designed to represent the observed local neighborhood out to  $80 h^{-1}$  Mpc. Inside its volume it is possible to identify some of the most prominent haloes corresponding to real observed galaxy clusters: in Fig. 3.2 we show a full-sky map extracted from this simulation in which some of the most important nearby clusters have been marked.

The main goal of this simulation is to study the local properties of the Universe on the large scale considering the true position of the objects and allowing to make direct comparison with observations in different fields. Dolag et al. (2005a) used its outputs to study the evolution of magnetic fields in the LU and their effect in cosmic-rays propagation. For the purpose of this Thesis we used the *Salacious* simulation to study the diffuse signal arising from the WHIM (see Section 2.2.2) and clusters in the nearby Universe.

In more detail, the initial conditions of the *Salacious* simulation are similar to those adopted by Mathis et al. (2002) in a previous study of structure formation in the LU based on a pure N-body simulation. In order to have a representation of the actual matter distribution of the local neighborhood, the galaxy dataset of the IRAS 1.2-Jy (Fisher et al., 1995) galaxy survey is considered: this distribution is first gaussianly smoothed on a scale of 7 Mpc and then linearly evolved back in time up to  $z = 50$  following the method proposed by Kolatt et al. (1996). The resulting field is then used as a Gaussian constraint (Hoffman & Ribak, 1991) for an otherwise random realization of a flat  $\Lambda$ CDM model, for which we assume a present matter density parameter  $\Omega_{\text{m}} = 0.3$ , a Hubble parameter  $h = 0.7$  and a r.m.s. density fluctuation  $\sigma_8 = 0.9$ . The comoving (Plummer-equivalent) softening length was fixed to be 14 kpc, which is comparable to the interparticle separation reached by the SPH particles in the dense centres of the simulated galaxy clusters.

The volume that is constrained by the observational data covers a sphere of

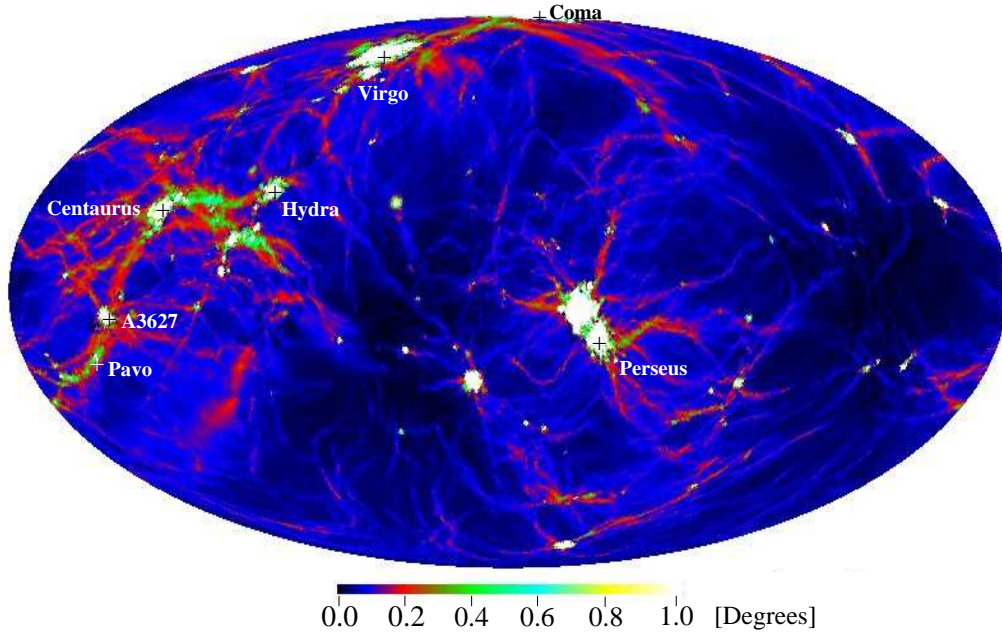


**Figure 3.2.** Full-sky map of the *Salacious* constrained simulation (picture taken from Dolag et al., 2005a). It represents the deflection angles for high-energy protons due to the structures of the LU. The coordinate system is galactic, with the Galactic anti-center in the middle of the map. Some of the most prominent haloes have been marked, with the Coma cluster near the north galactic-pole.

radius  $\sim 110$  Mpc, centred on the Milky Way. This region is sampled with more than 50 million high-resolution DM particles and is embedded in a periodic box of  $\sim 343$  Mpc on a side. The region outside the constrained volume is filled with nearly 7 million low-resolution DM particles, allowing a good coverage of long-range gravitational tidal forces.

The statistical analysis made by Mathis et al. (2002) demonstrated that the evolved state of these initial conditions provides a good match to the large-scale structure observed in the local universe. Using semi-analytic models of galaxy formation built on top of merging history trees extracted from the dark matter distribution in the simulation, they showed that the density and velocity maps obtained from synthetic mock galaxy catalogues have characteristics very similar to their observational counterparts. Moreover many of the most prominent nearby galaxy clusters like Virgo, Coma, Pisces-Perseus and Hydra-Centaurus, can be identified directly with haloes in the simulation, with a good agreement for sky positions and virial masses. In fact the positions of all identified objects differ less than the smoothing radius adopted in the initial conditions (7 Mpc), with the only exception of Centaurus, which is displaced by 9.6 Mpc. The agreement for the masses is within a factor of 2 which can be considered acceptable if one considers the uncertainties in the inferred observational masses, mainly when velocity dispersion is used.

Unlike in the original simulation made by Mathis et al. (2002), where only the DM component is evolved, the *Salacious* simulation follows also the gas

distribution. For this reason the initial conditions are extended by splitting the original high-resolution DM particles into gas and DM particles having masses of  $0.48 \times 10^9 M_\odot$  and  $3.1 \times 10^9 M_\odot$ , respectively; this corresponds to a value of  $\Omega_b = 0.04$ . The total number of particles within the simulation is then slightly more than 108 million and the most massive clusters will be resolved by almost one million particles.

The *Salacious* simulation was carried out with GADGET-2, adopting two different physical prescription for the baryonic matter. In Chapter 7 we will describe in detail the two different models and how we used the results of these simulation to study the properties of the SZ signal due to the structures of the LU.



## Chapter 4

# PROPERTIES OF THE DIFFUSE X-RAY BACKGROUND

According to the results of cosmological simulations, a large amount of gas resides outside virialized structures at the present epoch. This ionized gas emits via free-free interaction and is therefore expected to contribute significantly to the cosmic X-ray background, forming a diffuse component. Using a cosmological hydrodynamical simulation we estimate its emission properties and compare them with the present observational constraints. This chapter is mainly based on: “*Properties of the diffuse X-ray background in a high-resolution hydrodynamical simulation*”, Roncarelli M., Moscardini L., Tozzi P., Borgani S., Cheng L. M., Diaferio A., Dolag K., Murante G., 2006a, MNRAS, 368, 74.

### 4.1 The missing baryons and the unresolved X-ray background

As described in Section 2.2, hydrodynamical simulations predict that about 40-50 per cent of the total amount of baryons are out of virialized objects at the present epoch. In fact, while clusters form, starting from  $z \sim 2$  this gas undergoes a process of shock-heating that heats it to an intermediate temperature between  $10^5$  K and  $10^7$  K and becomes warm-hot intergalactic medium (WHIM, see the definition in Section 2.2.2).

Simulations also show that these baryons are not uniformly distributed: they constitute a filamentary network linking the largest virialized objects, the cosmic web. The existence of these structures is believed to be the solution to the missing baryons problem (see Sections 2.2.1 and 2.2.2): in fact, the density of filaments is expected to be very low and consequently their detection is made difficult by both their extremely low surface brightness and projection effects (see, however, some first claimed detections in X-ray analyses: Zappacosta et al., 2002; Finoguenov et al., 2003; Nicastro et al., 2005b). In any case, the intermediate temperature of the cosmic web gas suggests that it can produce a non-negligible X-ray emission through thermal bremsstrahlung. Given the physical state of the gas, this emission is expected to appear mostly as a diffuse background at soft energies.

It is now generally accepted that some of the observed cluster X-ray properties, like the scaling relations between mass, X-ray luminosity and temperature and their redshift evolution, the temperature profiles, or the entropy excess in the central regions of poor clusters and groups, cannot be reproduced by a simple model of gasdynamics based on gravitational heating alone (see the discussion in Rosati et al., 2002; Voit, 2005, and references therein). In an attempt to explain these discrepancies, new processes like the ones described in Section 3.4 have been included in the models of cluster formation, largely increasing the complexity of the physics of the ICM (see, e.g., Bower, 1997; Cavaliere et al., 1998; Balogh et al., 1999; Pearce et al., 2000; Bryan, 2000; Tozzi & Norman, 2001; Muanwong et al., 2001; Voit & Bryan, 2001b; Babul et al., 2002; Voit et al., 2002; Tornatore et al., 2003; Jubelgas et al., 2004; Dolag et al., 2005a; Di Matteo et al., 2005). All these processes affect the properties of both the gas within virialized objects, like galaxy groups and clusters, and the diffuse gas component which has low density and temperature. Therefore, the expected X-ray emission from the cosmic web can sensitively change when the parameters describing the ICM physics are varied. For these reasons, observational data on the soft X-ray background emitted by diffuse gas can be used as a probe of these physical processes, as suggested by different authors (see, e.g., Voit & Bryan, 2001a; Bryan & Voit, 2001; Xue & Wu, 2003).

Thanks to the latest generation of X-ray satellites (*Chandra* and *XMM-Newton*), the observational picture about the cosmic X-ray background (hereafter XRB) in the soft (0.5–2 keV) energy band has become much clearer. Very deep pointed observations, like the 1-2 Ms *Chandra* Deep Fields (CDFs) (Giacconi et al., 2002; Alexander et al., 2003) and the Lockman Hole *XMM-Newton* data (Worsley et al., 2004), showed that the soft XRB is largely produced by individual discrete sources, mostly AGN. Recent estimates of the percentage of the resolved contribution range between 80 and 95 per cent (see, e.g., Bauer et al., 2004; Worsley et al., 2005; Hickox & Markevitch, 2006).

However, the exact value of the non-resolved flux is still not known with great precision: this is mainly due to the uncertainties in the total value and in the slope of the  $\log N$ - $\log S$  at the lower fluxes. The most conservative estimates provide a value of approximately  $(1.2 \pm 0.3) \times 10^{-12} \text{ erg s}^{-1} \text{ cm}^{-2} \text{ deg}^{-2}$  (Worsley et al., 2005) for the intensity of the still unresolved soft X-ray background (see the discussion in Section 4.6.1): therefore this value can be used to set a stringent upper limit to the background from the diffuse IGM.

The availability of these new observational constraints suggests to re-consider the problem of the soft X-ray emission from the cosmic web and its implications for the ICM physics by updating an analysis made by Croft et al. (2001). The main goal of this work is to check the consistency of our model with the observed limits by using the outputs of the *keyproject* cosmological simulation (Borgani et al., 2004, described in Section 3.5.1), which, besides gravitational and gas dynamics, includes a treatment of the ICM with radiative cooling, star formation and SN feedback. Some previous analyses (Borgani et al., 2004; Ettori et al., 2004; Diaferio et al., 2005) showed that the results of this simulation are in encouraging agreement with some of the most significant observed properties of clusters, such as the

mass-temperature and the X-ray luminosity-temperature relations; however, the feedback mechanism does not appear to be efficient enough to avoid the production of overluminous groups and poor clusters. Therefore adopting this model we expect to overestimate significantly the total contribution of the IGM to the soft XRB due these objects, while it is crucial to separate their contribution from the truly diffuse component (see Section 4.6).

In this Chapter we describe the properties of the X-ray emission of the IGM estimated from the *keyproject* cosmological simulation and we compare them with current observational upper limits. In Section 4.2 we describe the characteristics of our simulation and present the procedure used to create the set of X-ray maps. The general statistical properties of the XRB extracted from these maps are discussed in Sections 4.3 and 4.4 for the soft (0.5–2 keV) and hard (2–10 keV) X-ray bands, respectively. Section 4.5 is devoted to the comparison of our results with previous works. In Section 4.6 we review the observational estimates of the contribution of diffuse gas to the soft XRB and we compare them with the results of our mock maps in order to obtain qualitative constraints on the modeling of the physical processes included in our hydrodynamical simulation. We summarize the results of this work in Section 4.7.

## 4.2 The map construction

In order to create mock maps of the X-ray emission of the structures within the past light-cone from the *keyproject* simulation, we follow the same technique adopted by Croft et al. (2001) (see also similar applications for maps of the Sunyaev-Zel’dovich effect, e.g. da Silva et al., 2001; Springel et al., 2001; White et al., 2002). The method is based on the replication of the original box volume along the line of sight. Since we assume a flat cosmological model, we use the comoving coordinates for the projection because the light trajectory is a straight line in this reference frame. We build past light-cones which extend to  $z = 6$ . Even if this maximum redshift can appear too large to still yield a significant signal in the X-ray band (this will be confirmed by our analysis in Section 4.3), this choice is done to obtain, at the same time, maps for the thermal and kinetic Sunyaev-Zel’dovich effects, that we will discuss in Chapter 5, for which there is a non-negligible contribution from the high-redshift gas.

The extension of the light-cone corresponds to a comoving distance of approximately  $5770h^{-1}$  Mpc, so we need to stack the simulation volume roughly 30 times. However, in order to obtain a better redshift sampling, rather than stacking individual boxes, we adopt the following procedure. We divide the simulated box at each output redshift into three equal slices along the line of sight (each of them with a depth of  $64h^{-1}$  Mpc); for the stacking procedure, we choose the slice extracted from the simulation output that better matches the redshift of the central point of the slice. Our light-cones are thus built with 91 slices extracted from 82 different snapshots.

The necessity of avoiding the repetition of the same structures along the line of sight requires a randomization of the boxes used to build our maps: since our simulation assumes periodic boundary conditions, for each box entering the light-cone we combine a process of random recentring of the coordinates with a 50 per cent probability of reflecting each axis. The slices belonging to the same box undergo the same randomization process to avoid spatial discontinuities between them: this allows to retain the entire information on the structures within the box and strongly reduces the loss of power on larger scales. By varying the initial random seeds we also obtain different light-cone reconstructions: we use this technique to produce ten different realizations that we use to assess the statistical robustness of our results.

In order to have maps covering a larger field of view, we replicate the boxes four times across the line of sight starting at comoving distances larger than half the light-cone extension (i.e. larger than about  $2900h^{-1}$  Mpc, corresponding to  $z > 1.4$ ). The strategy to pile up boxes is shown in Fig. 4.1. In this way we obtain maps  $3.78^\circ$  on a side. Every map contains 8,192 pixel on a side: consequently our resolution is  $1.66''$ , roughly three times the resolution of the CDFs at the aimpoint.

We now need to calculate the contribution, to the X-ray emission, of every gas particle that lies within the light-cone volume. The X-ray luminosity of the  $i$ -th particle in a given energy band  $[E_1, E_2]$ , as measured at  $z = 0$ , is calculated as

$$L_{X,i} = (\mu m_p)^{-2} x_e m_i \rho_i \Lambda(T_i, Z_i, E'_1, E'_2), \quad (4.1)$$

where  $\mu$  is the mean molecular weight in units of the proton mass  $m_p$ ,  $x_e$  represents the ratio between the number density of free electrons and hydrogen nuclei ( $n_e/n_H$ ),  $m_i$  and  $\rho_i$  are the particle mass and density, respectively. Since only the gas with  $T > 10^5$  K gives a significant contribution to the X-ray emission, we can safely assume full ionization of hydrogen and helium for all the particles: therefore the values of  $\mu$  and  $x_e$  depend only on the metallicity (notice that  $\mu = 0.588$  and  $x_e = 1.158$  for zero metallicity). The cooling function  $\Lambda$  is computed by using the plasma emission model by Raymond & Smith (1977) as a function of temperature  $T_i$  and metallicity  $Z_i$  of the particle and depends on the energy interval  $[E'_1, E'_2]$ ; this interval is  $K$ -corrected for redshift:  $E'_{1,2} = E_{1,2}(1+z)$ .

As we will discuss in the following Section, a sizeable contribution to the soft X-ray background comes from relatively warm particles, with temperature below  $10^7$  K. At these temperatures, the emissivity from metal lines becomes non negligible and, therefore, one needs to account for their contribution. In its original implementation, GADGET-2 includes a prescription to generate metals from SN explosions. This model assumes that only SN-II contribute to the chemical enrichment, under the assumption of instantaneous recycling, i.e. metals are released instantaneously when new stars form and the effect of stellar life-times is neglected (see, e.g., Tornatore et al., 2004, for a more detailed implementation of chemical enrichment in GADGET-2). In Eq. (4.1) we adopt the value of metallicity  $Z_i$  yielded by this prescription to compute the luminosity of each gas particle.

We then calculate the contribution of the  $i$ -th gas particle to the X-ray intensity  $I_{X,i}$  as

$$I_{X,i} = L_{X,i}/(4\pi d_L(z)^2 A), \quad (4.2)$$

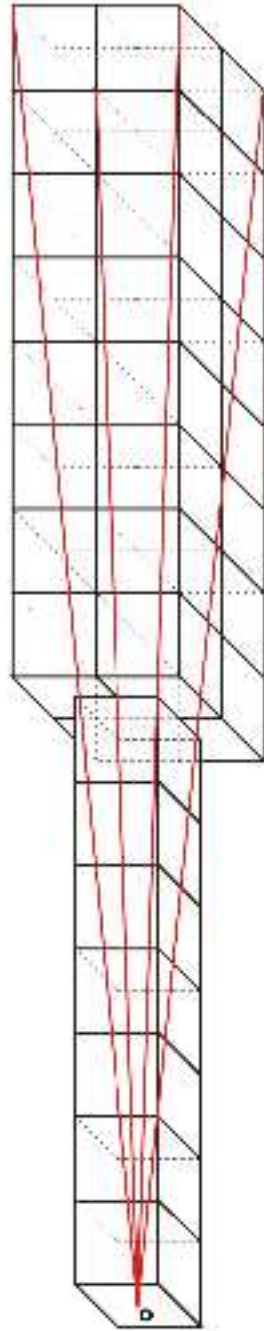


**Figure 4.1.** Sketch of the configuration adopted to realize the light-cone. The observer is located at the position  $O$  at the centre of the lowest side of the first box. The past light-cone is obtained by stacking the comoving volumes of the simulation outputs at the corresponding redshift. In order to obtain a large field of view of size  $3.78^2 \text{ deg}^2$ , starting at  $z = 1.4$  we use four replications of the box at the same redshift. The red lines show the volume in the light cone corresponding to the field of view.

where  $d_L(z)$  is the luminosity distance and  $A$  is the angular area covered by a pixel. This quantity is then distributed over the pixels by using an SPH smoothing kernel given by

$$W(x) \propto \begin{cases} 1 - 6x^2 + 6x^3, & 0 \leq x < 0.5 \\ 2(1-x)^3, & 0.5 < x \leq 1 \\ 0, & x > 1. \end{cases} \quad (4.3)$$

In the previous expressions  $x \equiv \Delta\theta/\alpha_i$ , where  $\Delta\theta$  is the angular distance between the pixel centre and the projected particle position and  $\alpha_i$  is the angle subtended by the particle smoothing length provided by the hydrodynamical code. In order to conserve the total intensity emitted by each particle we normalize to unity the sum of the weights  $W$  over all “touched” pixels. Finally, the intensity for a given pixel is obtained by summing over all the particles inside the light-cone.

To avoid spurious effects in the computation of the X-ray intensity, we exclude the particles having a mean electron density  $n_e > 0.26 h^2 \text{cm}^{-3}$ . According to the model of Springel & Hernquist (2003), these particles are assumed to be composed by a hot ionized phase and a cold neutral phase, whose relative amounts depend on the local temperature and density. Since these particles are meant to account for the multi-phase nature of the interstellar medium, we correctly exclude them from the computation of the X-ray emissivity.

### 4.3 The soft X-ray background

Examples of intensity maps obtained by adopting the method described above are displayed in Figs. 4.2 and 4.3 for the emission in the soft (0.5–2 keV) band. Following Croft et al. (2001), we distinguish two X-ray contributions: the contribution from the intergalactic medium (IGM, Fig. 4.2), i.e. from all the gas particles, and the contribution from the WHIM (Fig. 4.3) as defined in Section 2.2.2, i.e. from the gas particles having a temperature between  $10^5$  and  $10^7$  K. The IGM map is dominated by several extended bright galaxy clusters (with flux in the range  $10^{-12} - 10^{-11} \text{erg s}^{-1} \text{cm}^{-2}$ ) that give significant contributions to the total flux; there is also a large number of smaller structures, corresponding to nearby galaxy groups or distant fainter clusters. These smaller objects give the dominating contribution in the WHIM maps, because the WHIM does not contain the hottest particles; on the contrary, in these maps, the brightest galaxy clusters are much less prominent. Note that neither map shows evident signatures of filamentary structures like in the image of Fig. 2.2: this is because the LSS emission is washed away by projection effects.

The distribution of the values assumed by the intensity (considering the  $1.66''$  pixels) is shown in Fig. 4.4 for both the IGM and the WHIM. The thin lines refer to each of the ten light-cone realizations, while the thick solid line shows their average. A small dispersion between the different realization is evident: this is mainly due to the inclusion, in the maps, of a larger or smaller number of galaxy clusters at relatively low redshifts. In general the two averaged distributions for

**Table 4.1.** Average value of the intensity  $I_X$  in the two different X-ray bands for the IGM and the WHIM. The average is computed over ten different map realizations; the quoted errors are the r.m.s. in fields of  $1 \text{ deg}^2$ .

Energy band	IGM (total) ( $\text{erg s}^{-1} \text{ cm}^{-2} \text{ deg}^{-2}$ )	WHIM ( $\text{erg s}^{-1} \text{ cm}^{-2} \text{ deg}^{-2}$ )
SOFT (0.5 – 2 keV)	$(4.06 \pm 2.19) \times 10^{-12}$	$(1.68 \pm 0.62) \times 10^{-12}$
HARD (2 – 10 keV)	$(1.01 \pm 1.53) \times 10^{-12}$	$(2.92 \pm 2.46) \times 10^{-14}$

$\mathcal{I} \equiv \log I_X$  ( $\text{erg s}^{-1} \text{ cm}^{-2} \text{ deg}^{-2}$ ) are very close to a Gaussian distribution. In particular we find  $\overline{\mathcal{I}} = -12.81$  with a corresponding r.m.s. of 1.05 for the IGM, and  $\overline{\mathcal{I}} = -13.01$  with a corresponding r.m.s. of 0.94 for the WHIM; the skewness is 0.30 and 0.25, for the IGM and the WHIM respectively. Of course the distributions differ for larger fluxes: this is due to the fact that the flux of the brightest structures comes from gas at high temperature ( $T > 10^7 \text{ K}$ ).

The values of the intensity averaged over the ten map realizations are reported in Table 4.1 for both the IGM and the WHIM. The quoted errors are the dispersions computed in fields of  $1 \text{ deg}^2$  to allow a direct comparison with the corresponding results reported in Croft et al. (2001). We find that the mean intensity for the IGM is about  $4 \times 10^{-12} \text{ erg s}^{-1} \text{ cm}^{-2} \text{ deg}^{-2}$ , a factor 1.8 larger than in Croft et al. (2001). The corresponding dispersion is also larger: about 50 per cent compared to about 20 per cent in Croft et al. (2001). Again, we checked that the high map-to-map spread is due to the presence of some bright galaxy clusters very close to the observer and giving a strong contribution to the total emission: this effect is also evident in the pixel distributions of individual maps shown in Fig. 4.4.

By looking at the WHIM contribution, we find that its mean intensity is about 40 per cent of the total bremsstrahlung emission in the soft band (see Table 4.1). Again this value is larger than in the analysis of Croft et al. (2001), who reported a value of  $4.15 \times 10^{-13} \text{ erg s}^{-1} \text{ cm}^{-2} \text{ deg}^{-2}$ , corresponding to about 20 per cent of the total intensity of the IGM. However, we emphasize that we cannot make a direct comparison between these results and those presented in Croft et al. (2001) because the simulation analysed in that paper considers a much smaller box ( $50h^{-1} \text{ Mpc}$  on a side), assumes a slightly different cosmological model (a flat universe with  $\Omega_m = 0.4$  and a primordial spectral index  $n = 0.95$ ) and, most importantly, the included physical processes are not the same (see also the discussion in Section 4.5).

To determine which sources contribute most to the soft X-ray emission, in Fig. 4.5 we show how the mean intensity varies when we include pixels with fluxes above a given threshold. The results show that the bremsstrahlung emission is dominated by very bright objects: pixels having a surface brightness larger than  $10^{-10} \text{ erg s}^{-1} \text{ cm}^{-2} \text{ deg}^{-2}$  (mainly corresponding to galaxy clusters and groups as shown in Section 4.6.2) contribute to more than 50 per cent of the total value, for both the IGM and the WHIM.

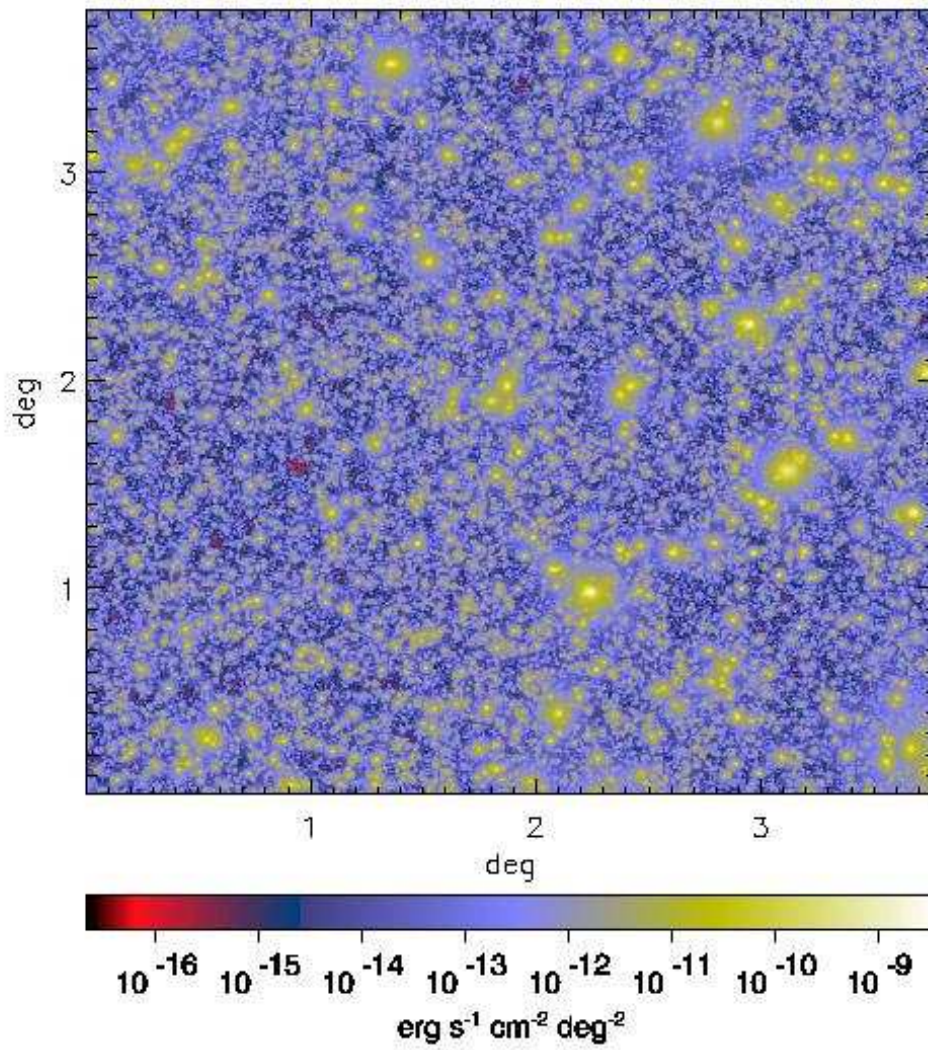


**Figure 4.2.** Map of the soft (0.5–2 keV) X-ray intensity obtained by considering all the gas particles (IGM). This map is  $3.78^\circ$  on a side and the pixel size is  $(1.66'')^2$ .

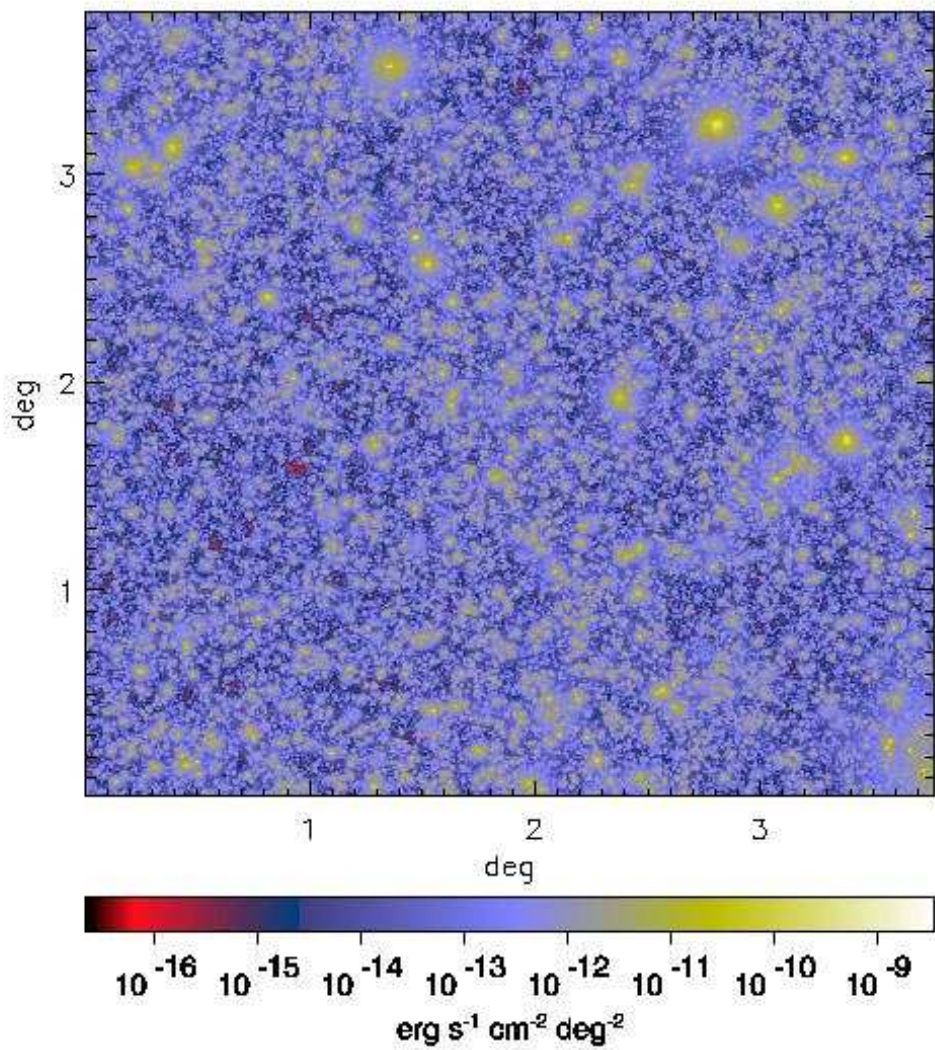


**Figure 4.3.** Map of the soft (0.5–2 keV) X-ray intensity obtained by considering the gas particles with temperature in the range  $10^5 \text{ K} < T < 10^7 \text{ K}$  (WHIM). The map is  $3.78^\circ$  on a side and the pixel size is  $(1.66'')^2$ . This map refers to the same realization of the past light-cone of Fig. 4.2.

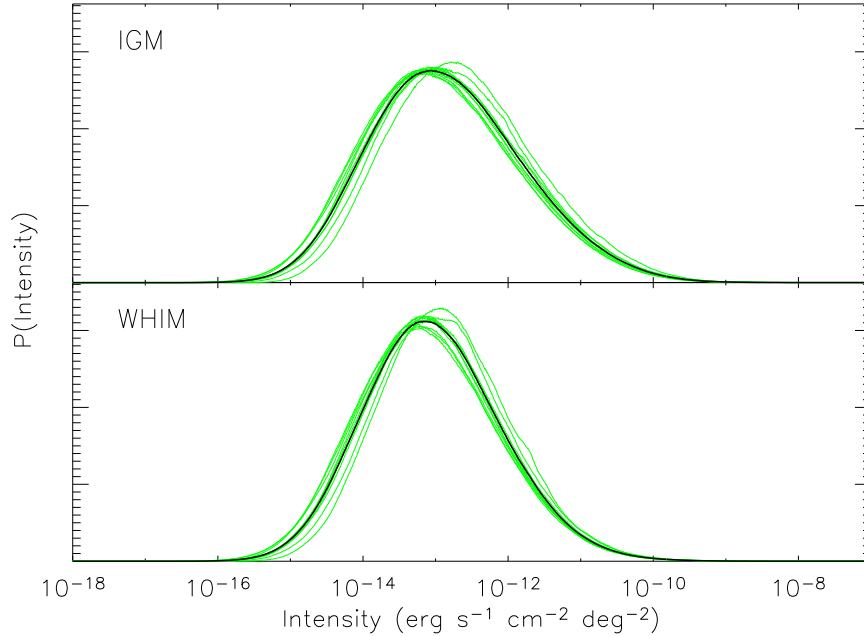


**Figure 4.4.** Distribution of pixel values of the intensity in the soft X-ray band. Upper and lower panels refer to the IGM and the WHIM, respectively. The thin lines show the results of ten different realizations; the thick solid line is the corresponding average.

In order to have an indication of the typical distances of the soft X-ray sources, we follow Croft et al. (2001) and compute, for each pixel, the mean redshift of the particles contributing to the XRB weighted by their fluxes. The resulting map for the same IGM realization shown in Fig. 4.2 is displayed in Fig. 4.6.

Almost all the bright clusters are at low redshift ( $z < 0.15$ ), while the emission from the faintest structures mainly comes from redshifts around unity. This is confirmed by the distributions of the flux-weighted redshifts, shown in Fig. 4.7, computed from the complete set of ten realizations: the shapes of the distributions for the IGM and the WHIM are very similar, with a peak at  $z \approx 0.7$ . Notice that few realizations have an excess of contribution from sources at relatively low redshift ( $z < 0.15$ ): this is the origin of the large spread of the mean intensity previously discussed.

The analysis of the maps also clearly shows how the projection of nearby and distant objects makes it very difficult to see imprints of the filamentary network present in the large-scale structure of the universe. Finally, in Fig. 4.8 we show the integrated soft X-ray intensity as a function of the limiting redshift. The curves for both the IGM and the WHIM reach half the total value at  $z \approx 0.3$ , the 90 per cent level is reached around  $z \approx 0.9$  for the IGM and at  $z \approx 0.8$  for the WHIM. We can also notice that the sources at  $z > 2$  contribute less than 1 per cent of the soft X-ray flux.

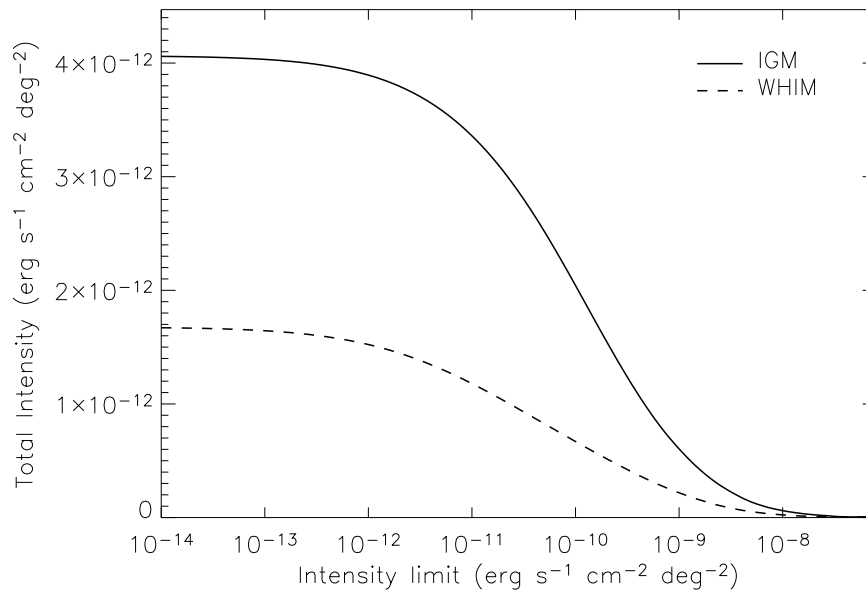


**Figure 4.5.** The value of the mean intensity (averaged over ten different map realizations) as a function of the lower limit of the pixel surface brightness. The solid and dashed lines refer to the IGM and the WHIM, respectively.

### 4.3.1 The autocorrelation function

We analyse the clustering properties of the IGM in the soft X-ray band by estimating the autocorrelation function in our simulated maps. Following Croft et al. (2001), we calculate the contrast  $\delta(\vec{x})$  defined as

$$\delta(\vec{x}) \equiv [I_X(\vec{x})/\overline{\mathcal{I}}] - 1, \quad (4.4)$$

where  $I_X(\vec{x})$  is the surface brightness at the position  $\vec{x}$  and  $\overline{\mathcal{I}}$  is the average of each map. The contrast is then used to compute the angular correlation function as

$$w(\theta) = \langle \delta(\vec{x})\delta(\vec{x} + \vec{\theta}) \rangle. \quad (4.5)$$

The results are shown in Fig. 4.9, where we plot the average of the angular correlation functions calculated by considering the ten different realizations of the light cone; error bars are the error on the mean obtained from the scatter of the maps. We notice that the mean function is always positive up to  $\theta \sim 30'$ , although some of the realizations show negative values for  $\theta \geq 8'$ ; the smallest scale at which  $w(\theta)$  is compatible with a null value is  $20'$ . From the plot it is also evident a slow change of the logarithmic slope. This is confirmed by our analysis: by fitting our mean function under the assumption of a power-law relation,  $w(\theta) \propto \theta^\alpha$ , we find  $\alpha \approx -0.9$  and  $\alpha \approx -2.6$  in the intervals  $0.1' < \theta < 2'$  and  $2' < \theta < 30'$ , respectively.

Our results can be directly compared to those obtained by Croft et al. (2001). In general the autocorrelation function extracted from our maps is larger by a factor of about 6. Moreover we find that at large scales the decrease of their  $w(\theta)$  is slower

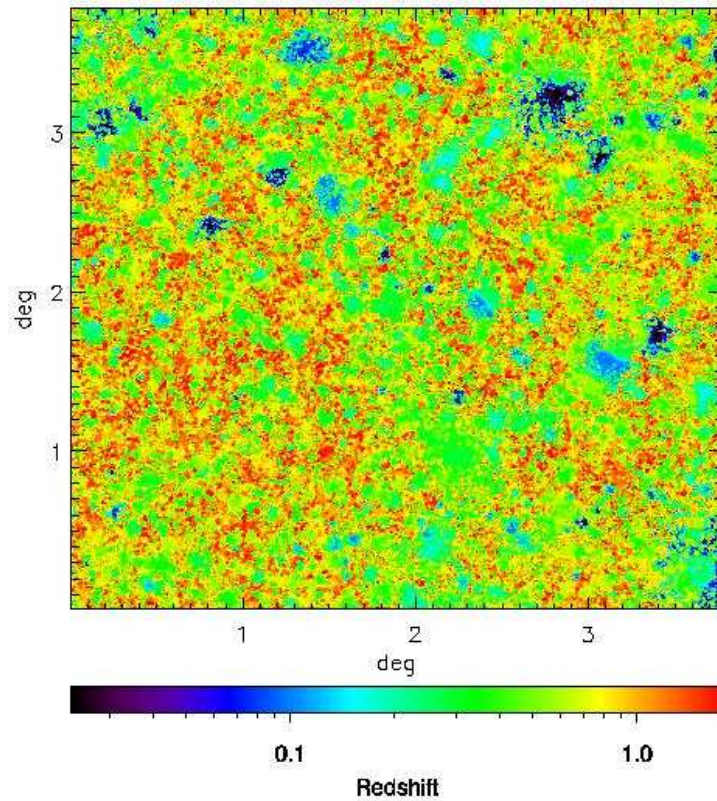


**Figure 4.6.** Map of the flux-weighted redshift, computed for the IGM in the soft X-ray band. The plot refers to the same light-cone realization shown in Fig. 4.2.

(they found  $\alpha = -1.4$ ). These discrepancies can be easily explained by considering the differences between the two simulations. First, and most importantly, the size of the simulation box used by Croft et al. (2001) is about four times smaller than our box size: the resulting lack of large-scale power can lead to a significant underestimate of the clustering strength. Second, the physical processes included in our simulation produce higher values of the soft X-ray signal: as a consequence, the contrast  $\delta$  also tends to be amplified, thus originating a larger autocorrelation function.

#### 4.4 The contribution in the hard X-ray band

It is well known that the hard (2–10 keV) X-ray band is strongly dominated by the emission from AGN. However, a small portion of gas, mainly located within the richest clusters, is at high temperature and also gives some contribution in this band.

The maps presented in Figs. 4.10 and 4.11 show the hard band intensity for

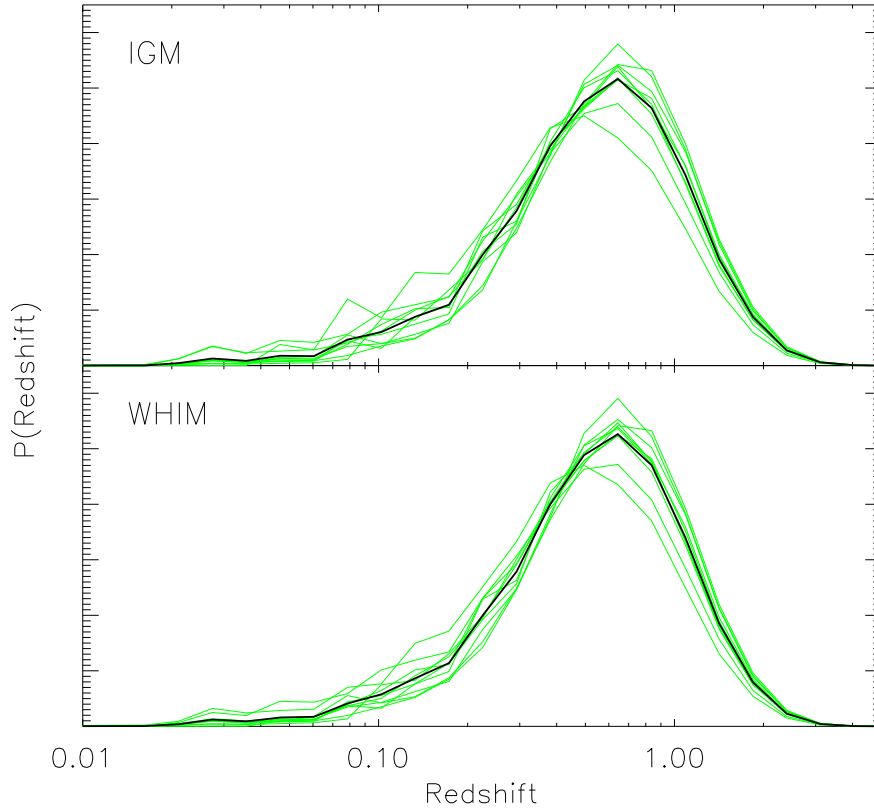


**Figure 4.7.** As in Fig. 4.4, but for the distribution of the flux-weighted redshift in the soft X-ray band.

the IGM and the WHIM, respectively, for the same light-cone realization shown in Fig. 4.2. We note that, even if in some positions, corresponding to the hottest clusters, the intensity can reach values similar to those obtained in the soft X-ray maps ( $10^{-9}$  erg s $^{-1}$  cm $^{-2}$  deg $^{-2}$ ), outside virialized objects the hard X-ray maps are much fainter. In the map for the WHIM the signal is strongly reduced and limited to the cluster atmospheres, with no evident emission from the diffuse gas: this makes the cosmic web not observable in this band because of its very low signal-to-noise ratio and projection effects. However, the high contrast between clusters and diffuse regions in the hard band maps suggests an empirical way to identify the positions of galaxy clusters in our simulated maps. This method will be used in Section 4.6 to separate the emission coming from extended objects from that produced by diffuse gas.

The small contribution of the IGM and the WHIM to the hard XRB is confirmed by the average total intensity reported in Table 4.1, for both components: we find about  $1 \times 10^{-12}$  erg s $^{-1}$  cm $^{-2}$  deg $^{-2}$  and  $3 \times 10^{-14}$  erg s $^{-1}$  cm $^{-2}$  deg $^{-2}$ , for the IGM and the WHIM, respectively. These values account for approximately 25 per cent and 2 per cent of the corresponding mean intensity in the soft band. Note that, while for the WHIM our flux is a factor of two larger than Croft et al. (2001) result, for the IGM there is a substantial agreement. In fact, the lack of large-scale power

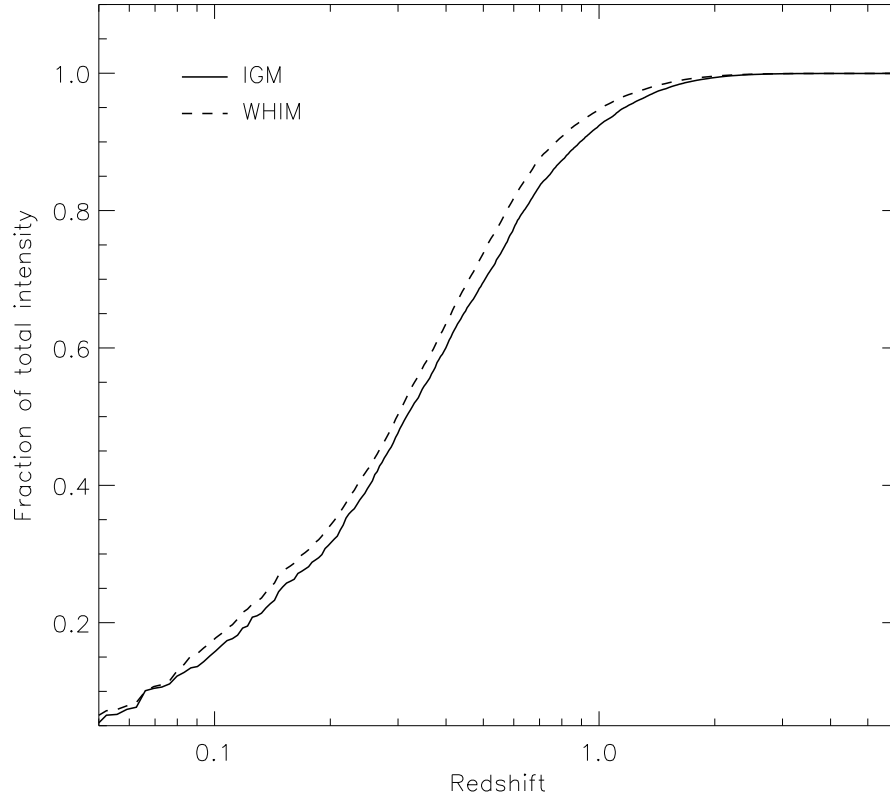


**Figure 4.8.** Integrated soft X-ray intensity (normalized to the total value) as a function of redshift. The solid and dashed lines refer to the IGM and the WHIM, respectively. The values plotted are the mean of ten map realizations.

in the simulation by Croft et al. (2001), due to the small box size, is compensated by the higher dynamical evolution associated to the higher value of  $\Omega_m$ , for a fixed power spectrum normalization  $\sigma_8$  assumed in both analyses. Moreover, the effect of feedback on the hard X-ray emission by rich clusters is expected to be less relevant.

We have to consider, however, that the field-to-field variance is quite large for the hard X-ray band, because most of the signal comes from nearby bright clusters: in fact, the hard X-ray spectrum decreases exponentially and, even for hot objects, the bulk of the signal is rapidly shifted into the soft band at increasing redshifts.

A way to discriminate the AGN signal from that coming from clusters and the cosmic web is based on the energy flux hardness ratio ( $HR$ ), here defined as the ratio between the intensities in the hard and soft bands at each pixel position:  $HR \equiv I_X[2-10 \text{ keV}]/I_X[0.5-2 \text{ keV}]$ . The emission from AGN is in fact expected to have  $HR > 0.5$ , while much lower values are common for galaxy clusters and diffuse gas.

The map for the  $HR$  obtained from the same IGM realization displayed in the previous figures is shown in Fig. 4.12: in the plot it is easy to recognize the position of the richest galaxy clusters, while the connecting filamentary structure is almost completely absent. The distributions of the  $HR$  values for the ten realizations and

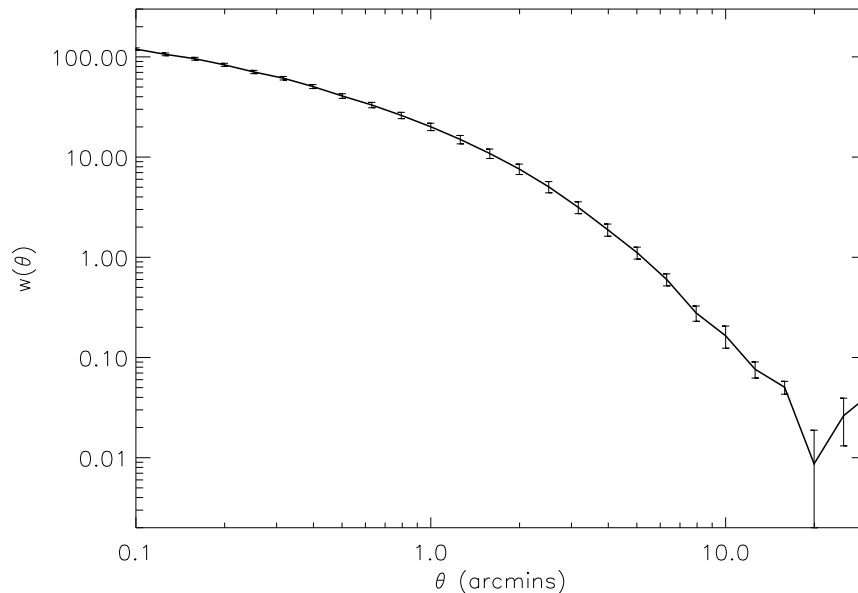


**Figure 4.9.** The angular correlation function of the IGM in the soft (0.5–2 keV) X-ray band. The solid line is the average over ten different maps  $3.78^\circ$  on a side; error bars are the error on the mean calculated from the scatter of the maps.

their average are shown in Fig. 4.13, for both the IGM (upper panel) and the WHIM (lower panel). In the former case the median value is around  $HR = 0.03$ , and less than a few per cent of the pixels have  $HR > 0.5$ ; in the latter case the median is smaller than 0.01 and no pixel has  $HR > 0.1$ .

## 4.5 Comparison with previous works

In our work we study the properties of the X-ray background from the large-scale structure of the universe. In particular we followed the same method to build light-cone realizations applied by Croft et al. (2001), performing then similar statistical tests. From a comparison between our and their analysis, we found that in our soft X-ray maps the mean intensities of the IGM and the WHIM are larger than the intensities obtained by Croft et al. (2001) by a factor of 1.8 and 4, respectively. The autocorrelation function of the signal is also larger by a factor of about 6. As for the hard X-ray band, we find a substantial agreement with Croft et al. (2001) for the IGM contribution, while our contribution from the WHIM is a factor of 2 higher.

These differences can be understood in terms of the different characteristics of the two hydrodynamic simulations on which the analyses are based. The main reason for our higher values is that we followed the evolution of a much larger (almost 60 times) volume. This allows us to obtain a better representation of very massive clusters that contribute to most of the emission (see the discussion in Section 4.3). The larger sampled volume is also the main motivation of our higher

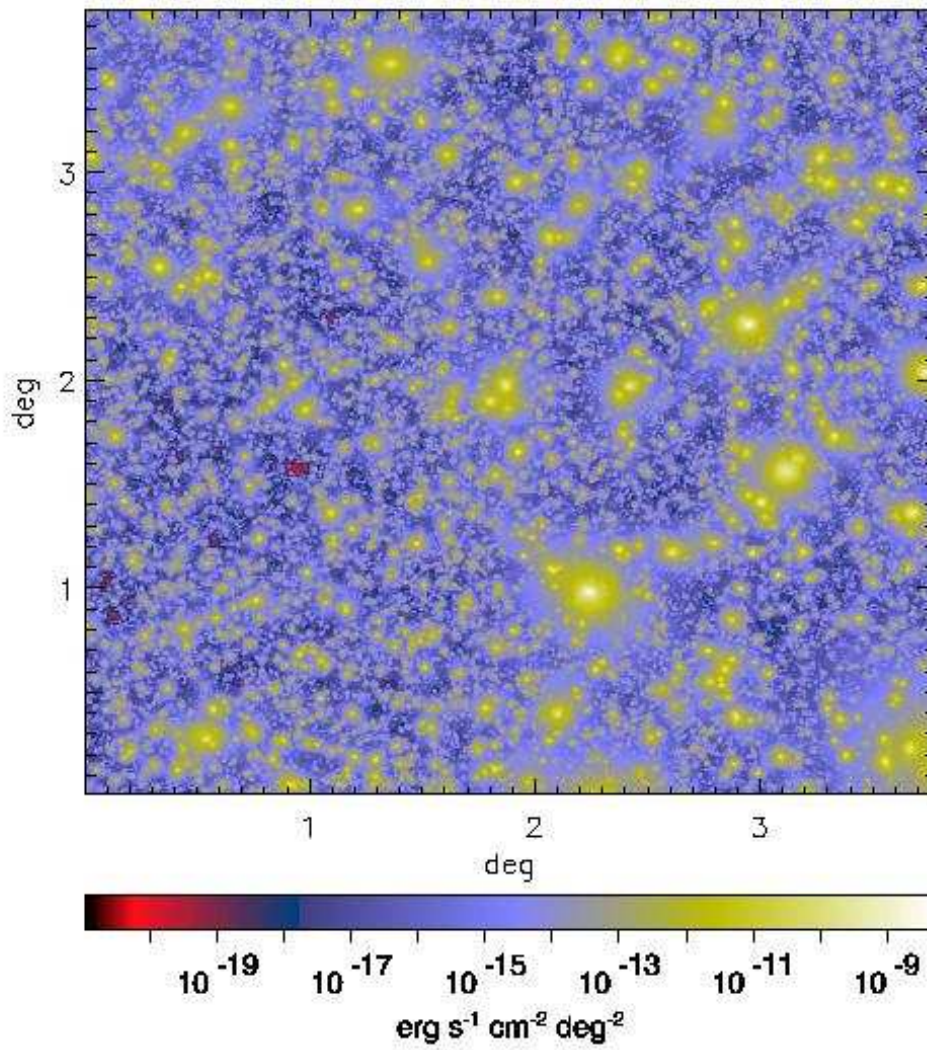


**Figure 4.10.** Map of the hard (2–10 keV) X-ray intensity obtained by considering all the gas particles (IGM). This map is  $3.78^\circ$  on a side and the pixel size is  $(1.66'')^2$ . This map refers to the same realization of the past light-cone of Fig. 4.2.

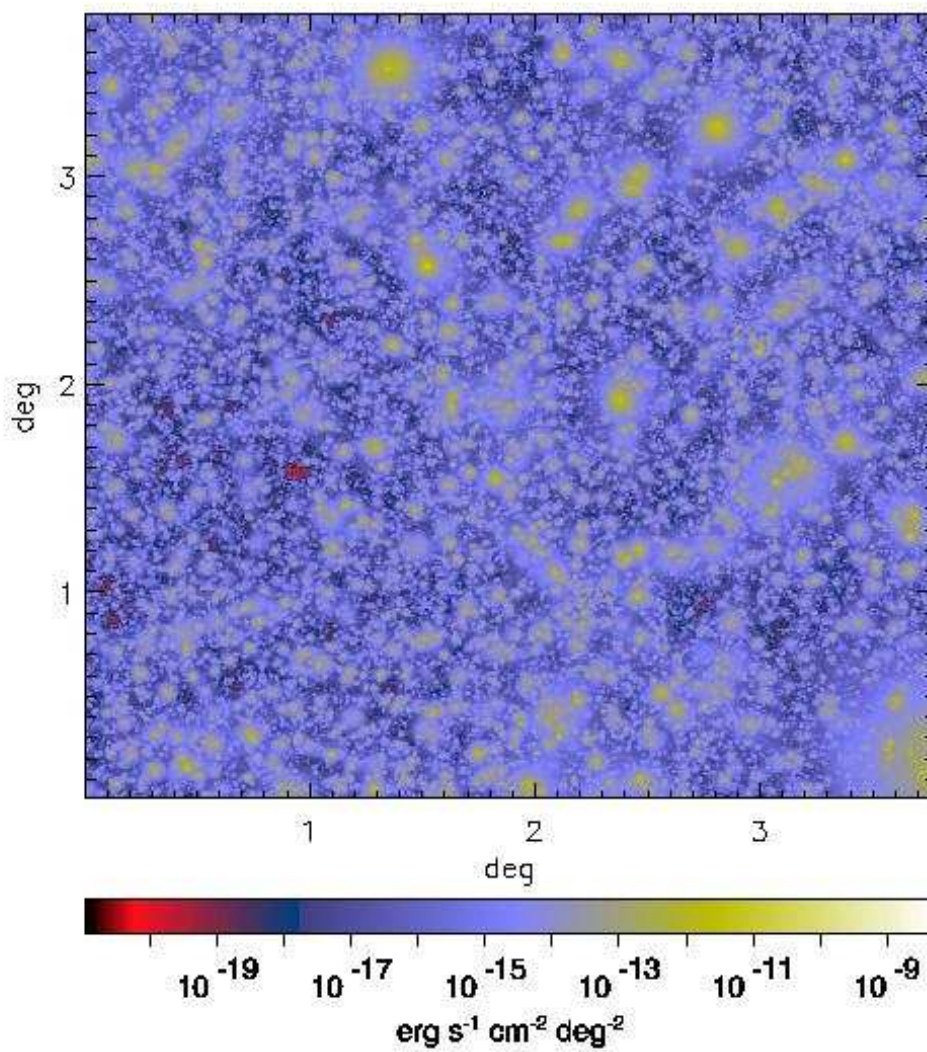


**Figure 4.11.** Map of the hard (2–10 keV) X-ray intensity obtained by considering the gas particles with temperature in the range  $10^5 < T < 10^7$  K (WHIM). The map is  $3.78^\circ$  on a side and the pixel size is  $(1.66'')^2$ . This map refers to the same realization of the past light-cone of Fig. 4.2.

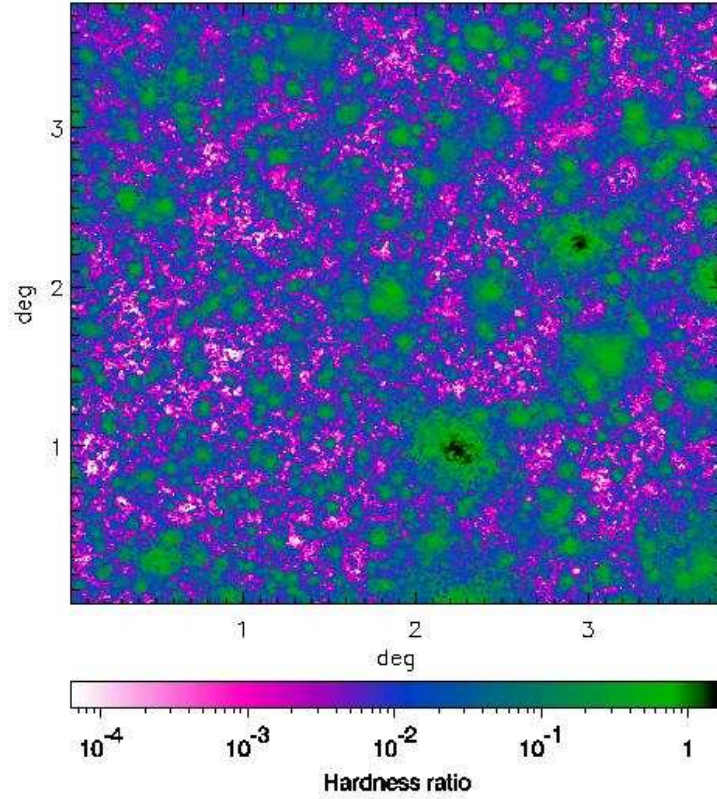


**Figure 4.12.** Map of the hardness ratio (hard band to soft band)  $HR$ . This map refers to the same realization of the past light-cone of Fig. 4.2.

autocorrelation function, which includes the contribution of longer wavelength modes.

However, an important difference between the two hydrodynamic simulations is also related to the treatment of the physical processes affecting the evolution of the baryonic component. The simulation of Croft et al. (2001) did not consider the possible multiphase nature of the starforming gas. For this reason they had to resort *a posteriori* to a correction of their results to account for it. On the contrary, the GADGET-2 code used for our simulation follows the different physical processes (radiative cooling, star formation and supernova feedback) in a self-consistent way. In particular the inclusion of a phenomenological description of galactic winds provides a much more efficient energy feedback than that implemented in the simulation by Croft et al. (2001). Moreover the code directly considers the effect of a photoionizing time-dependent UV background. Globally this gas treatment produces a larger fraction of WHIM. This explains why larger differences are found for the contributions of the WHIM, while less significant differences are found between the signals in the hard X-ray band, which are mostly originated by the hottest objects. We also assumed a cosmological model which is closer to that suggested by the most recent observational data with  $\Omega_m = 0.3$ , while Croft

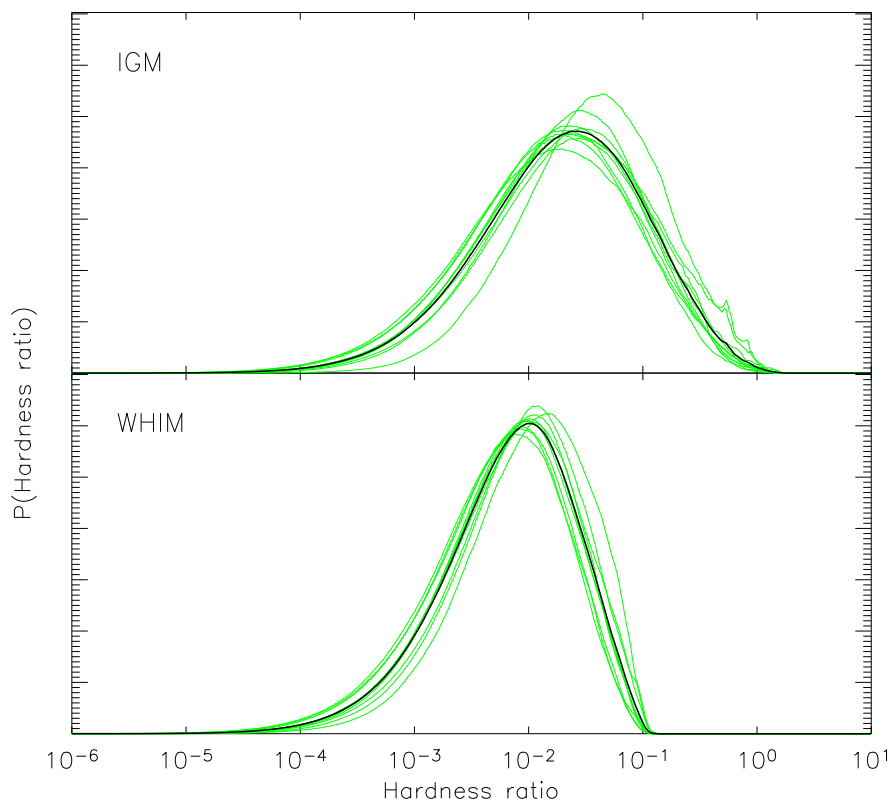


**Figure 4.13.** Distribution of  $HR$  for the IGM (up) and for the WHIM (down). The thin lines show the results for ten different realizations; the thick solid line is the corresponding average.

et al. (2001) adopted  $\Omega_m = 0.4$ : thus we have a higher contribution from baryons at high redshifts due to the slower dynamical evolution of the structures. The apparent agreement of our result for the hard band emission of the IGM with Croft et al. (2001) is due to a combination of all of these factors (see the discussion in Section 4.4).

Finally, a similar result to the one of Croft et al. (2001) has been obtained also by Bryan & Voit (2001) for the soft X-ray emission of the IGM from their AMR simulation which includes a simple feedback model. Again the difference with respect to the present work is mainly due to the relatively small volume sampled by their simulation.

## 4.6 The contribution of diffuse gas to the soft X-ray background

As already said in Section 4.1, the comparison between our simulated maps and observational results on the unresolved XRB requires to define a criterion to separate the contribution arising from the truly diffuse gas from the one due to clusters and groups that correspond to resolved extended sources in real X-ray data.

In this Section we describe our method to extract the contribution produced by

the cosmic web, i.e. the baryons which are not included in the groups and clusters of galaxies currently identified in deep X-ray surveys, from the soft X-ray maps discussed above. In order to check whether the modelling of the physical processes treated by our hydrodynamical simulation (which also influence the low-density gas regions) is reliable, we compare our results with observational estimates (mainly upper limits).

We have to notice that in the literature, as reviewed in the following subsection, there is no robust determination of the contribution of diffuse gas to the soft XRB: the value that we will use later for comparison is based, to some extent, on interpretation of the existing data.

#### 4.6.1 Observational estimates

In recent years, thanks to the availability of new X-ray satellites like *Chandra* and *XMM/Newton*, there have been many efforts to measure the total XRB and to resolve it in its different components (see, e.g. Giacconi et al., 2002; Moretti et al., 2002; Alexander et al., 2003; Worsley et al., 2004; Bauer et al., 2004, and references therein). In fact the possibility of recognizing the discrete sources which give the main contribution opens new windows to study the connection between AGN and galaxy formation and, most importantly for this work, constrains the possible signals from the diffuse gas.

At present, there are several different estimates of the unresolved XRB in the soft (0.5–2 keV). Worsley et al. (2005) estimate an  $\text{XRB}[0.5\text{--}2\text{ keV}] = (8.12 \pm 0.23) \times 10^{-12} \text{ erg s}^{-1} \text{ cm}^{-2} \text{ deg}^{-2}$  by assuming the shape of the XRB in the 1–8 keV band determined by De Luca & Molendi (2004) from *BeppoSAX* data, and by taking into account the steepening of the spectrum below 1 keV as found by Roberts & Warwick (2001). Note that this value is larger than the one adopted by Bauer et al. (2004), who found  $\text{XRB}[0.5\text{--}2\text{ keV}] = (7.52 \pm 0.35) \times 10^{-12} \text{ erg s}^{-1} \text{ cm}^{-2} \text{ deg}^{-2}$ . The discrepancy is originated by the fact that Bauer et al. (2004) extrapolate the hard spectrum in the soft band by assuming a slope of -1.4: of course, this does not take into account the steepening due to the non-AGN contribution, which, by the way, is the one we are most interested in. This total value includes any contribution, namely the Local Hot Bubble, the Galactic halo, unresolved galactic stars, and most importantly, the extragalactic components (both bright and faint) from point sources (AGN), clusters, groups and the truly diffuse gas.

The resolved (to date) XRB in the soft band produced by these extragalactic sources has been recently estimated by Worsley et al. (2005), who found  $(6.9 \pm 0.2) \times 10^{-12} \text{ erg s}^{-1} \text{ cm}^{-2} \text{ deg}^{-2}$ . Similar results for the resolved component are presented by Bauer et al. (2004):  $(6.7 \pm 0.3) \times 10^{-12} \text{ erg s}^{-1} \text{ cm}^{-2} \text{ deg}^{-2}$ . Therefore, by assuming the values found by Worsley et al. (2005) for the total XRB in the soft band, the emission which is still unresolved is approximately  $(1.2 \pm 0.3) \times 10^{-12} \text{ erg s}^{-1} \text{ cm}^{-2} \text{ deg}^{-2}$ .

Recently, Hickox & Markevitch (2006) obtain an higher value by directly measuring the unresolved flux in the 1–2 keV band of the two CDFs and extrapolating the fit down to 0.5 keV. Their final result for the unresolved XRB in the 0.5–2 keV band is  $(1.77 \pm 0.31) \times 10^{-12} \text{ erg s}^{-1} \text{ cm}^{-2} \text{ deg}^{-2}$ .

The amount of unresolved flux which can be ascribed to a truly diffuse WHIM component is very controversial. First of all, these values contain thermal components (e.g. Local Hot Bubble, Galactic Halo) that have never been measured. Moreover Worsley et al. (2006) argue that all of the unresolved fraction of the XRB in the CDFs at the lower energies can be ascribed to the signal of normal galaxies identified by the *Great Observatories Origins Deep Survey (GOODS)* in the optical band (see, however, also the the most recent results of Hickox & Markevitch, 2007, that exclude this hypothesis).

Therefore, it is important to stress that all of these values represent upper limits to the possible contribution from the diffuse gas. Notice also that the local thermal components probably dominate the XRB below 0.5 keV, making highly uncertain the estimate of the extragalactic contribution in the lowest X-ray energy band, where the signal from the cosmic web is expected to be even more significant.

#### **4.6.2 Separating the diffuse soft X-ray emission from galaxy groups and clusters in the simulated maps**

By comparing naively the estimates of the IGM soft X-ray contribution reported in Table 4.1 with the observational data discussed above, we would notice that our simulated XRB accounts for about 50 per cent of the observed value of the XRB, but it is much larger (by a factor of 3-4) than the observed upper limit obtained by removing the discrete sources. Even considering the signal from the WHIM only, i.e. from gas having temperature between  $10^5$  K and  $10^7$  K, the signal in our maps would be too large. However, this comparison is quite misleading, because in the results from the simulation we still include the portion of the warm gas located in groups or in the external atmospheres of galaxy clusters; on the contrary, this gas is not present in the observed values described in the previous Section. For this reason we need a more detailed analysis of our maps, where these objects need to be excluded.

We already know, from the previous analysis of our original hydrodynamical simulation (see, e.g., Borgani et al., 2004), that the modeling of the included physical processes produces overluminous groups and poor clusters of galaxies. As discussed in that paper, additional sources of energy (like feedback from SN-Ia or AGN) would help to solve this discrepancy. This excess is located in high-density regions, whereas we are interested in the soft X-ray emission from the cosmic web: therefore, we need to identify and remove the X-ray extended sources, which correspond to galaxy clusters and groups, from the total intensity of our maps.

The proper procedure would be to identify and remove all the clusters and groups from mock observations of our simulated volumes. In practice, this is unfeasible, because it would require simulating a full wide-area survey with all the related observational aspects, which is far beyond the aim of our work. Therefore, we will remove clusters and groups on the basis of their total flux as it appears on our flux maps. To establish a definition of a cluster or a group to be applied to our two-dimensional maps, we use an identification criterion based on the surface

brightness value. We identify as an X-ray extended source (group or cluster) all the connected regions of pixel above a surface brightness threshold.

To accomplish this, we use the maps in the hard (2–10 keV) band because the emission from the diffuse gas in this band is much lower than in the soft band and therefore it is easier to identify the regions corresponding to virialized haloes (see Fig. 4.10). Then, we choose the value of the surface brightness threshold by inspecting the faintest groups identified in the deepest X-ray observations to date.

Specifically, we consider a group (CDFS-594) identified in the CDF South (Giacconi et al., 2002) at  $z \sim 0.7 - 0.8$ . Its emission is detected with a high signal-to-noise ratio over a circular region of approximately  $2700 \text{ arcsec}^2$ . After fitting its spectrum with a *mekal* model (see, e.g., Liedahl et al., 1995, and references therein) we obtain a temperature of about 2.1 keV. Therefore, the corresponding *average* surface brightness in the hard band is  $3.06 \times 10^{-12} \text{ erg s}^{-1} \text{ cm}^{-2} \text{ deg}^{-2}$ , which will be used as the reference value in the following analysis<sup>1</sup>.

Notice that this average value corresponds to the central part of the group (typically about 3 core radii), which is the region where the emission can be realistically detected, while some emission associated to the X-ray halo is expected to provide sub-threshold contribution up to the virial radius. Since we want to remove all the X-ray emission associated to a given halo, in the following analysis we will also consider smaller, up to 8 times, surface brightness thresholds. We choose these thresholds, because the surface brightness of an isothermal gas in the central region (about 3 core radii) is roughly 8 times larger than at the virial radius.

Finally, we consider a threshold for the minimum angular size of the region that can be identified as a group or a cluster. For this purpose we choose a reference physical length of 100 kpc, that corresponds to a minimum angular size of  $\sim 10 \text{ arcsec}$  (at  $z \sim 1$ ) for the cosmological model assumed in our simulation: this gives a minimum angular surface of  $\sim 310 \text{ arcsec}^2$ . This quantity roughly corresponds to the minimum size of the central detectable regions of X-ray groups (see Willis et al. 2005). This last criterion has a small impact on the final results (i.e. the expected average surface brightness of the cosmic web changes of few percent when doubling the minimum angular size of the haloes).

### 4.6.3 The soft X-ray emission from the cosmic web in the simulated maps

By applying the previously discussed thresholds of the surface brightness and size on the maps produced in the hard (2–10 keV) X-ray band, we create a catalogue of connected regions corresponding to the extended objects like groups and clusters. We use them as a mask on the soft 0.5–2 keV X-ray maps to remove their emission and finally obtain the diffuse contribution.

By averaging over our ten different realizations, we find that the signal from the diffuse gas is  $1.57 \times 10^{-12} \text{ erg s}^{-1} \text{ cm}^{-2} \text{ deg}^{-2}$  which is comparable to the observed upper limits. 69 per cent of the diffuse emission comes from gas with temperature in the range  $10^5 - 10^7 \text{ K}$ , whereas the total contribution of clusters and groups to the XRB is  $2.49 \times 10^{-12} \text{ erg s}^{-1} \text{ cm}^{-2} \text{ deg}^{-2}$ ; this value is larger than the

<sup>1</sup>Similar results are obtained by considering a different galaxy group (CDFS-645), again identified in the CDF South exposure.

**Table 4.2.** Contribution to the soft (0.5–2 keV) XRB of galaxy clusters and groups (Column 2) and of the diffuse gas (Column 3) as a function of the adopted threshold of the surface brightness (Column 1). We also report the percentage of the diffuse contribution coming from the WHIM (Column 4). The quoted errors are the r.m.s. in fields of 1 deg<sup>2</sup>. All values are in units of 10<sup>-12</sup> erg s<sup>-1</sup> cm<sup>-2</sup> deg<sup>-2</sup>.

SOFT (0.5–2 KEV) X-RAY BACKGROUND SURFACE BRIGHTNESS (10 <sup>-12</sup> erg s <sup>-1</sup> cm <sup>-2</sup> deg <sup>-2</sup> )			
THRESHOLD (2–10 KEV)	CONTRIBUTIONS FROM		
	HALOS	DIFFUSE GAS	%WHIM
3.06	2.49±2.04	1.57±0.27	(69±13)%
1.53	2.78±2.10	1.28±0.19	(73±12)%
0.77	3.05±2.14	1.01±0.13	(78±11)%
0.38	3.28±2.17	0.78±0.09	(82±11)%
OBSERVATIONAL UPPER LIMITS			
WORSLEY ET AL. (2005)		1.2±0.3	
HICKOX & MARKEVITCH (2006)		1.77±0.31	

total contribution from clusters and groups estimated from the observed number counts (Rosati et al., 2002, see also the corresponding discussion at the end of this Section).

As noted above, the adopted surface brightness threshold can be considered as an average of the group emission at intermediate redshifts, and then it could be too high to account for all clusters' and groups' emission. In fact we find that 31 per cent of the  $1.57 \times 10^{-12}$  erg s<sup>-1</sup> cm<sup>-2</sup> deg<sup>-2</sup> emission is still produced by gas having a temperature larger than 10<sup>7</sup> K. This is further confirmed by a visual inspection of the masked maps: the external regions of nearby clusters are not excluded.

This is an indication that in general the surface brightness threshold defining high density regions associated to groups and clusters of galaxies is probably lower than the adopted value. For this reason, we repeat the previous analysis by using thresholds which are smaller by factor of 2, 4 and 8. The results, reported in Table 4.2, show a reduction of the contribution of the diffuse gas by a factor of 2 when the surface brightness cut is 8 times smaller; the corresponding fraction of the signal from the WHIM increases up to 82 per cent.

In general we can conclude that the soft X-ray emission from the diffuse gas computed from our simulation is consistent with the upper limit coming from observational data. The feedback model we are assuming is efficient in describing the properties of the WHIM and/or the regions with intermediate density, although it can show problems in the deepest potential wells.

Finally, as a self-consistency check, we compute the log $N$ -log $S$  function (always in the soft X-ray band) for our connected regions. The results are shown in Fig. 4.14 for the four different thresholds reported in Table 4.2.

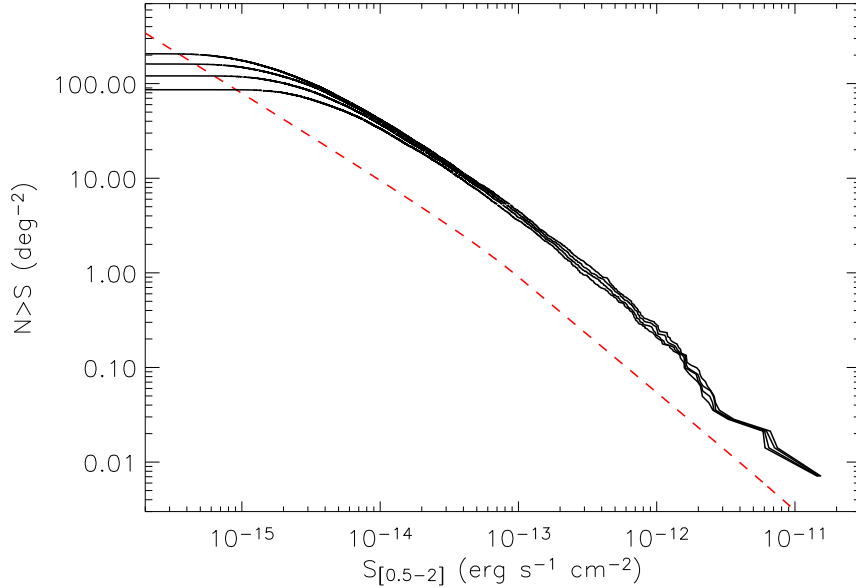


**Figure 4.14.** Number of objects as a function of the limiting flux in the soft (0.5–2 keV) X-ray band. The black solid lines are the results obtained by considering the connected regions with four different surface brightness cuts (see Table 4.2 for the adopted values). For comparison, we show (red dashed line) the observational data obtained by Rosati et al. (2002) by combining the results from the *Rosat* Deep Cluster Survey (Rosati et al., 1998), EMSS (Rosati et al., 1995), BCS (Ebeling et al., 1998) and REFLEX (Bohringer et al., 2001).

Again, we notice the excess with respect to the observational data, represented by a combination of data made by Rosati et al. (2002) and coming from the *Rosat* Deep Cluster Survey (Rosati et al., 1998), EMSS (Rosati et al., 1995), BCS (Ebeling et al., 1998) and REFLEX (Bohringer et al., 2001). This excess is produced by the overluminous objects which are present in our simulation at all relevant redshifts: for this reason, number counts are overestimated over the entire flux range.

Finally, the apparent flattening at low fluxes ( $S \approx 10^{-15} \text{ erg s}^{-1} \text{ cm}^{-2}$ ) is originated by both resolution effects and the surface brightness limit assumed for the identification of the extended sources.

## 4.7 Summary and conclusions

In this chapter we have analysed the results of a cosmological hydrodynamical simulation of a concordance  $\Lambda$ CDM model to discuss the properties of the diffuse XRB. The simulation (Borgani et al., 2004) includes many relevant physical processes affecting the gas component. Indeed the numerical treatment accounts for a time-dependent, photoionizing UV uniform background, radiative cooling processes within an optically thin gas of hydrogen and helium in collisional ionization equilibrium, star formation events, and feedback processes from both SN-II and galactic winds.

Previous analyses (Borgani et al., 2004; Ettori et al., 2004) showed that the results of this simulation are consistent with several observational X-ray properties of galaxy clusters. However, there is also a number of discrepancies that remain unaccounted for: in particular the cluster X-ray luminosity-temperature relation extracted from our simulation appears too high, i.e. there are overluminous groups and small clusters.

As suggested by different authors (see, e.g., Voit & Bryan, 2001a; Bryan & Voit, 2001; Xue & Wu, 2003), an alternative way to constrain the model describing the thermal properties of baryons and their cosmic history is related to the soft X-ray emission from diffuse gas. Indeed, a model of heating and cooling of the intergalactic medium makes predictions in terms of diffuse emission from filaments and unresolved structures. These predictions can be compared with the observational measurements of the XRB, which are now available (in form of upper limits) thanks to the deep *Chandra* data.

In order to test the model included in our simulation, we follow the method of Croft et al. (2001) and, starting from the simulation snapshots, we constructed a set of ten different two-dimensional maps, of size  $(3.78^\circ)^2$ , of the past light-cone back to  $z = 6$ . The present analysis extends Croft et al. (2001) previous work, thanks to a much larger volume sampling, to a more realistic representation of the physical processes affecting the baryon history and to the comparison with the observed XRB data after the *Chandra* era.

The main results obtained by using our set of maps are as follows.

- i* - The mean intensity of the IGM in the soft (0.5–2 keV) X-ray band is about  $4.1 \times 10^{-12} \text{ erg s}^{-1} \text{ cm}^{-2} \text{ deg}^{-2}$ ; when considering the WHIM (defined as gas with temperature between  $10^5$  and  $10^7$  K) the mean intensity reduces to about  $1.7 \times 10^{-12} \text{ erg s}^{-1} \text{ cm}^{-2} \text{ deg}^{-2}$ . The distribution of the intensity in the maps is very similar to a lognormal. 90 per cent of the signal comes from structures at  $z \lesssim 0.9$ .
- ii* - As expected, in the hard (2–10 keV) X-ray band the total mean intensity is smaller (by a factor 4) than in the soft one and becomes almost negligible when considering the WHIM (about  $3 \times 10^{-14} \text{ erg s}^{-1} \text{ cm}^{-2} \text{ deg}^{-2}$ ). The hardness ratio in the maps has a distribution which peaks at low values, with a median close to 0.03, which enables an easy discrimination of the AGN signal.
- iii* - We obtain an estimate of  $(0.8 - 1.6) \times 10^{-12} \text{ erg s}^{-1} \text{ cm}^{-2} \text{ deg}^{-2}$  for the soft X-ray emission from the diffuse gas after removing the regions corresponding to extended objects, like galaxy groups and clusters, from the maps. Our result is consistent with the present upper limits coming from observational data (Worsley et al., 2005; Hickox & Markevitch, 2006) and estimated by removing the contribution of resolved sources (AGN, groups and clusters of galaxies) from the total XRB.

As a conclusion, our results show that the physical processes discussed here are consistent with existing constraints on the X-ray properties of the warm-hot baryons. However, if in the near future the measurements of the possible

contribution from Galactic and local structures (still included in the observational upper limits) will reduce the maximum allowed emission from the diffuse gas by a factor of 2 or more, our predictions will start to conflict with the data. In this case it will be required a more efficient mechanism of feedback acting on the gas with intermediate temperatures and densities: in fact the presence of a stronger feedback would place the gas on a higher adiabat, thereby preventing it from reaching high densities and, on turn, suppressing the diffuse emission.

Our analysis confirms that the comparison between observational constraints on the diffuse emission in the soft X-ray band and results from cosmological hydrodynamical simulations enables us to gain information on the thermodynamical history of the diffuse baryons. In the future it will be interesting to study some detailed simulated observations of the diffuse gas to check its detectability not only through bremsstrahlung emission, but also via emission and/or absorption of oxygen lines (OVI, OVII and OVIII): real observations will probably be provided by some dedicated wide-field high-resolution spectroscopic experiments now in project. It will also be relevant to compare simulated results with observations performed by the next generation of X-ray spectroscopic satellites, like *Constellation-X/XEUS* or *NeXT*, provided that their field of view is large enough to cover the filamentary structure of the cosmic web.

## Chapter 5

# THE SUNYAEV-ZEL'DOVICH EFFECTS ON THE LARGE SCALE

**B**esides from X-ray emission, the other important observational aspect connected with the large-scale structure as traced by the baryons is the Sunyaev-Zel'dovich effect. Using a cosmological hydrodynamical simulation we describe its large-scale properties considering both the thermal and kinetic components, concentrating on their statistical behaviour. We also investigate their correlation with the soft X-ray signal. This chapter is mainly based on "*The Sunyaev-Zel'dovich effects from a cosmological hydrodynamical simulation: large-scale properties and correlation with the soft X-ray signal*", Roncarelli M., Moscardini L., Borgani S., Dolag K., 2007, astro-ph/0701680.

### 5.1 The Sunyaev-Zeldovich effects in cosmology

In the recent years the CMB primordial fluctuations have been measured with high accuracy thanks to the observations made by the *WMAP* (Spergel et al., 2003, 2006), establishing an important step forward in precision cosmology, as discussed in Section 1.7.2). The primary CMB anisotropies, in fact, constitute the most important dataset to obtain information about the physical conditions of the early Universe and, together with other results coming from high-redshift supernovae (see, e.g., Astier et al., 2006; Wood-Vasey et al., 2007), weak lensing (see, e.g., Heymans et al., 2005; Massey et al., 2005; Hettterscheidt et al., 2006; Semboloni et al., 2006; Hoekstra et al., 2006) and galaxy clustering (see, e.g., Cole et al., 2005; Eisenstein et al., 2005; Tegmark et al., 2006; Sánchez et al., 2006), they indicated as a favorite scenario a flat cosmological model dominated by a cosmological constant: the so-called  $\Lambda$ CDM model (see also the discussion in Section 1.7.1).

The dynamical and thermodynamical effects of the LSS formation after the recombination also create secondary anisotropies in the CMB signal. Most importantly, after the epoch of reionization the CMB photons interact with the free electrons of the IGM via Thomson scattering giving rise to the Sunyaev-Zel'dovich (SZ) effect (Sunyaev & Zel'dovich, 1972, 1980): this constitutes both a noise for the primary CMB signal and a probe for the baryon physics.

The SZ effect is usually classified into two components: the dominant one, the thermal SZ (tSZ) effect, is the inverse-Compton scattering caused by the thermal motion of a population of high-temperature electrons, mainly located in the hot plasma of galaxy clusters, which results in a gain in energy for the photons and a consequent distortion of the black-body spectrum of the CMB. Conversely, the kinetic SZ (kSZ) effect is the Doppler shift caused by the bulk motion of the ionized gas and can result either in a gain or in a loss of photon energy, depending on the direction of the gas velocity with respect to the photon.

After its first claimed detection by Parijskij (1973) and the works of Birkinshaw et al. (1991) and Birkinshaw & Hughes (1994), the development of new microwave instruments has now made available a large amount of observational data for the study of the tSZ effect in galaxy clusters, including two-dimensional mapping. In the near future this observational field is believed to receive a significant boost thanks to a new generation of suitable land-based instruments, like *AMI*, *SPT*, *ACT*, *SZA*, *AMiBA* and *APEX*, and the launch of the *Planck* satellite that will provide a full-sky catalogue of galaxy clusters detected via the tSZ. Finally the project of the *Atacama Large Millimeter Array (ALMA)* specifically includes high-resolution imaging of the SZ effect in its scientific goals.

The development of the SZ science for galaxy clusters will be strictly connected with the already available data in the X-ray band that nowadays constitute the most important dataset for cluster physics. In fact, since both the bremsstrahlung emission and the SZ effect depend on the density and temperature of the gas, the two signals are expected to be highly correlated and their comparison will be of great interest in order to understand the systematics of the two observables. In addition to it, while the X-ray signal has proven to be a sensitive probe for the properties of the hot gas in the central regions of nearby clusters, the absence of redshift dimming for the SZ effect and its different dependence on the density will allow one to detect more distant sources and, hopefully, to obtain more information on the physics of the external regions of galaxy clusters where the modelization of the cluster physics has smaller uncertainties, as discussed in Chapter 6.

Besides from cluster physics the tSZ effect arising from the whole LSS, which is expected to be the most important signal at the angular scales of some arcminutes, can also be used to directly constrain cosmology because of the strong dependence of its amplitude on the normalization of the power spectrum  $\sigma_8$ . On the other side a measurement of the kSZ effect can yield information on the peculiar velocity field at high redshift and, consequently, put constraints on different dark energy models (see, e.g., Hernández-Monteagudo et al., 2006); at the second order the kSZ effect is also believed to be marginally affected by the dynamical effects associated with epoch of reionization, even if a future measurement of this signal appears very challenging (Iliev et al., 2006).

In this framework a theoretical analysis of the SZ effect and of its correlation with the X-ray signal is crucial not only for investigating the connections between these observables and the LSS formation, but also for modeling and, possibly,

taking under control the SZ-noise, that is expected to affect high-multipole CMB observations.

This Chapter is devoted to the presentation of our results on the statistical properties of the SZ signal obtained from the *keyproject* cosmological simulation (Borgani et al., 2004, described in Section 3.5.1) that follows the evolution of the structure formation in the framework of the  $\Lambda$ CDM cosmology. Since the thermodynamical evolution of the baryons depends not only on the cosmological parameters but also on different non-thermal processes influencing the gas physics, the numerical model adopted specifically includes several physical effects connected with radiative cooling and star formation that have a significant effect on the shape of the temperature and density profiles of the inner regions of galaxy clusters and, consequently, on their X-ray and SZ properties.

We organize this Chapter as follows. In the next Section we briefly review the basic equations that describe the tSZ and kSZ effects. In Section 5.3 we present the method used to our mock SZ maps from the outputs of the *keyproject* simulation. In Section 5.4 we discuss the average large-scale properties of the SZ effects. In Section 5.5 we analyse the power spectra of the tSZ and kSZ signals and in Section 5.6 we study their cross-correlation. Section 5.7 is devoted to the description of the correlation properties with the soft X-ray signal already studied in Chapter 4. Finally we summarize our conclusions in Section 5.8.

## 5.2 Basics of the SZ effects

Here we review some of the basic equations for both SZ effects in the non-relativistic approximation. More details can be found in several reviews (see, e.g., Rephaeli, 1995; Birkinshaw, 1999; Carlstrom et al., 2002; Rephaeli et al., 2005).

The intensity of the tSZ effect in a given direction is usually expressed in terms of the Compton  $y$ -parameter defined as

$$y \equiv \frac{k_B \sigma_T}{m_e c^2} \int dl n_e (T_e - T_{\text{CMB}}), \quad (5.1)$$

where  $m_e$  is the electron rest mass,  $c$  is the light speed,  $n_e$  and  $T_e$  are the electron number density and temperature, and  $T_{\text{CMB}}=2.726$  K is the CMB temperature (Mather et al., 1994). The resulting change in the latter due to the scattering of the electrons is directly proportional to the value of the  $y$ -parameter and is given by

$$\frac{\Delta T}{T_{\text{CMB}}} = y g_\nu(x), \quad (5.2)$$

where  $x \equiv h\nu/(k_B T_{\text{CMB}})$  is the dimensionless frequency and  $g_\nu(x)$  represents the dependence on the observation frequency:

$$g_\nu(x) = \left( x \frac{e^x + 1}{e^x - 1} - 4 \right). \quad (5.3)$$

It is important to note that in the Rayleigh-Jeans (RJ) limit ( $x \ll 1$ ) this expression reduces to  $g_\nu(x) \simeq -2$  and that for  $\nu \simeq 218$  GHz the tSZ effect is null.

The kSZ effect can be expressed in terms of the Doppler  $b$ -parameter defined as

$$b \equiv \frac{\sigma_T}{c} \int dl n_e v_r, \quad (5.4)$$

where  $v_r$  is the radial component of the peculiar velocity of the gas element (positive if it is moving away from the observer, negative if it is approaching). The resulting measured temperature fluctuation is  $\Delta T/T_{\text{CMB}} = -b$ . Note that, unlike for the tSZ, this is independent of the observation frequency.

### 5.3 The map construction

It is known that the global properties of the tSZ and kSZ effects depend on the physical characteristics of the LSS as a whole. Moreover, as we will discuss in Section 5.4, significant contributions to both SZ effects comes from high-redshift gas. Therefore a theoretical study of their global properties and the comparison with present and future observations require a realistic modelization of the thermodynamical and dynamical history of the gas filling the volume of the past light-cone seen by an observer located at  $z = 0$  out to the epoch of reionization. For this purpose we use the outputs of the *keyproject* simulation at different redshifts to build different realizations of light-cones, which enable the production of simulated maps of the SZ signals.

The method to reconstruct the light-cone used here is the same described in Section 4.2 and sketched in Fig. 4.1, both for the geometry and for the pixel distribution scheme. We also use the same randomization seeds in order to obtain ten light-cone realizations identical to the ones used in Chapter 4 to discuss the properties of the X-ray emission: this allows us to perform a direct comparison between the X-ray and SZ signals and to study their correlations. Therefore, we refer the reader to Section 4.2 for the detailed description of the method, while here we will focus only on the differences that arise when computing the quantities connected with the SZ effects.

To compute the signal produced by the SZ effects we need to convert the line-of-sight integrals of equations (5.1) and (5.4) into expressions suitable for the SPH formalism. First, for the tSZ effect, we calculate the contribution of every gas element that lies inside the light-cone volume. We follow an approach similar to the one proposed by da Silva et al. (2000). Given the  $i$ -th SPH particle, we define

$$\Upsilon_i \equiv \frac{k_B \sigma_T}{m_e c^2} N_{e,i} T_i, \quad (5.5)$$

where  $T_i$  is the gas temperature and  $N_{e,i}$  is the number of electrons associated to the particle, i.e.  $N_{e,i} = n_{e,i} m_i / \rho_i$ , being  $n_{e,i}$ ,  $m_i$  and  $\rho_i$  the electron density, the mass and the gas density of the  $i$ -th particle, respectively.

Since the electron number density in the gas depends almost only on the ionization state of the H and the He component and since the kinetic SZ effects has non-negligible contribution from low-temperature gas, here and in the next calculations  $n_{e,i}$  is computed neglecting the presence of metals and considering the ionization state of gas provided by the GADGET-2 code. This is different from the procedure adopted for the calculation of the X-ray signal described in Section 4.2.

Then, according to the required map resolution, we compute the physical length of the pixel  $L_{\text{pix},i}$  at the particle's distance from the observer and we use it to calculate

$$y_i \equiv \frac{Y_i}{L_{\text{pix},i}^2}, \quad (5.6)$$

which is the total contribution to the  $y$ -parameter from the  $i$ -th particle. This quantity is then distributed over the map pixels by adopting the formula of equation (4.3).

The construction of the maps of the Doppler  $b$ -parameter follows an identical procedure with the only difference that we have to substitute equation (5.5) and (5.6) with

$$B_i \equiv \frac{v_{r,i}}{c} N_{e,i}, \quad (5.7)$$

and

$$b_i \equiv \frac{B_i}{L_{\text{pix},i}^2}, \quad (5.8)$$

where  $v_{r,i}$  is the radial component of the peculiar velocity of the  $i$ -th particle, which can be either negative or positive.

As for the X-ray emission we build past light-cones extending out to  $z = 6$ . As we will discuss in more detail in Section 5.4, this limit is enough to account for almost all of the tSZ signal; on the contrary the kSZ is believed to have a non-negligible contribution from the gas located at  $z > 6$ , out to the epoch of reionization. Anyway, since the reionization model assumed in our simulation considers the gas at  $z \gtrsim 6$  almost neutral, extending the calculation to higher redshifts would not produce a significant change in the kSZ signal. Therefore we stress that the results for the kSZ effect presented in this work *cannot* be considered as the whole signal expected, but rather as the signal arising from the gas in the range  $0 \leq z \leq 6$  which according to the results of Iliev et al. (2006), should constitute the dominating component.

Given the different redshift dependence with respect to the X-ray emission, it is important to take into account the possible systematic errors that the method to pile up boxes (sketched in Fig. 4.1) can introduce on the calculation of the power spectrum (see the corresponding discussion in Section 5.5).

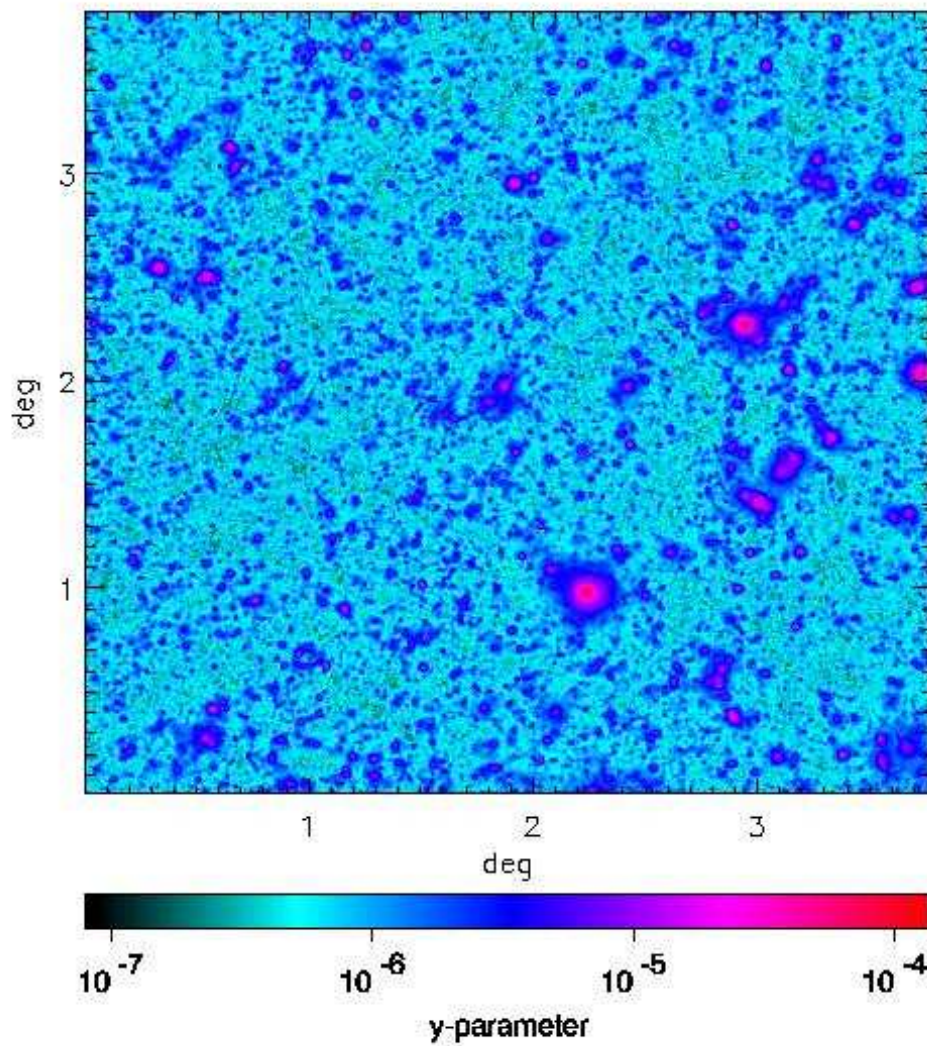


**Figure 5.1.** Map of the tSZ signal expressed in terms of the Compton  $y$ -parameter. The map is  $3.78^\circ$  on a side and the pixel size is  $(1.66 \text{ arcsec})^2$ . This map refers to the same realization of the past light-cone of the of Fig. 4.2.

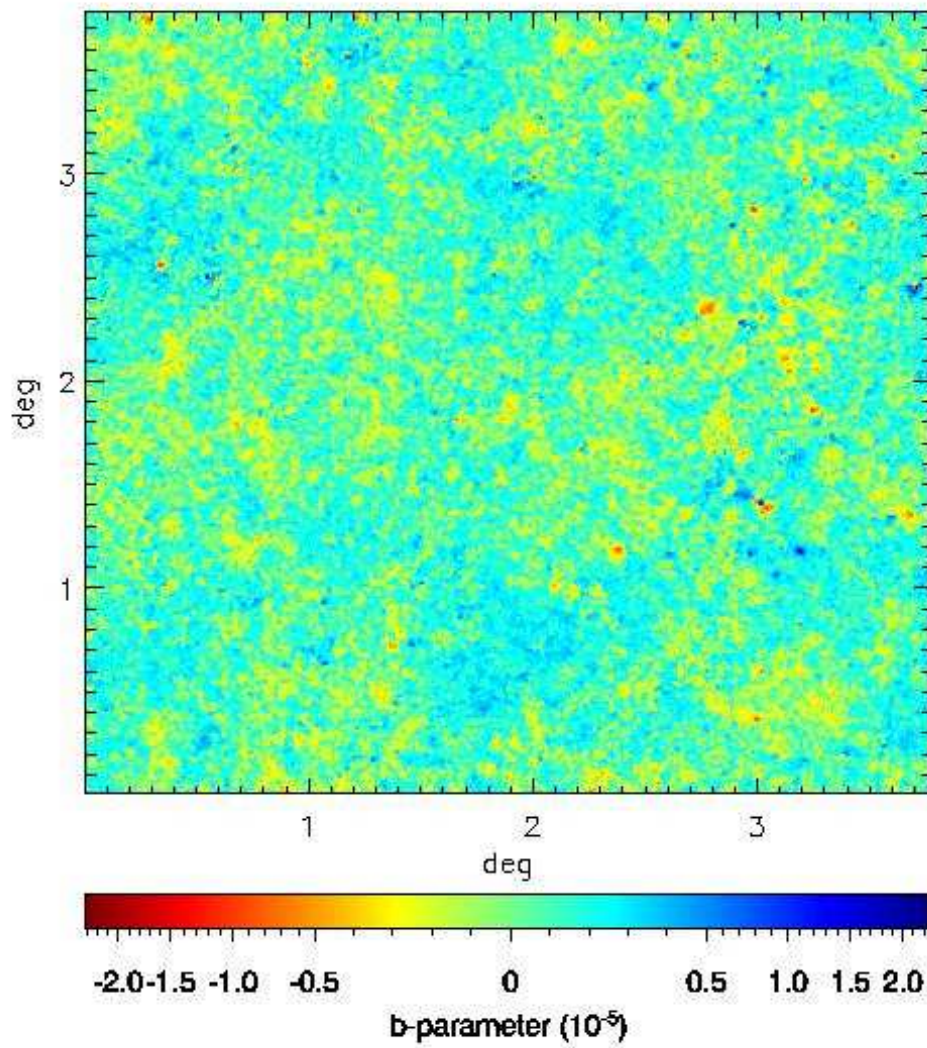


**Figure 5.2.** Map of the kSZ signal expressed in terms of the Doppler  $b$ -parameter (given in units of  $10^{-5}$ ). The map is  $3.78^\circ$  on a side and the pixel size is  $(1.66 \text{ arcsec})^2$ . This map refers to the same realization of the past light-cone of the of Fig. 4.2.

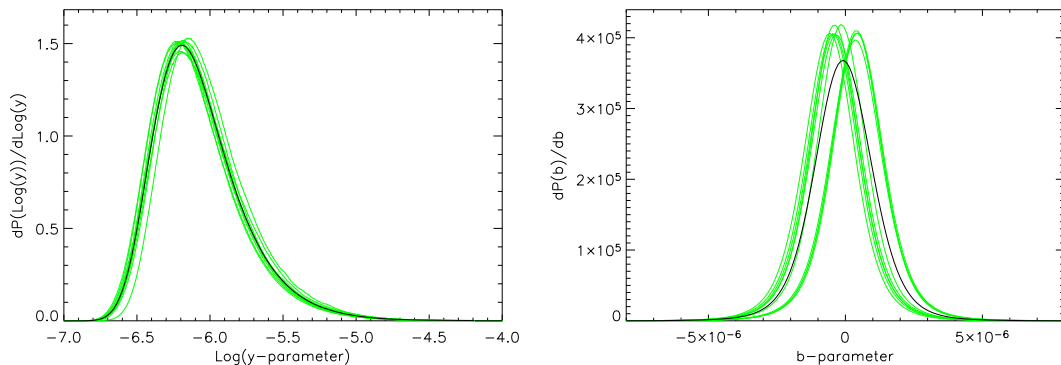


**Figure 5.3.** Probability distribution of pixel values of the logarithm of the  $y$ -parameter (left panel) and the  $b$ -parameter (right panel). The thin lines show the results for 10 different realizations; the thick solid line is the corresponding average.

## 5.4 The distribution of the SZ signals

In Figs. 5.1 and 5.2 we present two examples of the maps of the Compton  $y$ -parameter and Doppler  $b$ -parameter, respectively, obtained with the method described in the previous section; both refer the same light-cone simulation of the maps shown in Chapter 4.

It is evident in the tSZ map that the signal is dominated by galaxy clusters that can reach in their central regions typical intensities close to  $y \sim 10^{-4}$ , which correspond to temperature changes an order of magnitude higher than the primary CMB anisotropies, in the RJ limit. In the map it is also possible to recognize a large number of smaller and fainter structures with  $y \sim 5 \times 10^{-6}$ : they correspond to distant protoclusters or more local galaxy groups. We also note a non-negligible signal arising from regions outside clusters (e.g. filaments and diffuse gas) that can reach at most  $y \sim 10^{-6}$ .

We use the whole set of maps to compute the expected average of the Compton  $y$ -parameter: we obtain a value of  $\langle y \rangle = (1.19 \pm 0.32) \times 10^{-6}$  as the mean of the pixel values in the 10 fields of  $3.78^2 \text{ deg}^2$ ; the reported error represents the r.m.s. in fields of  $1 \text{ deg}^2$ . This value is significantly lower than the results obtained by da Silva et al. (2001b, cooling model) and White et al. (2002, cooling plus feedback model):  $2.3 \times 10^{-6}$  and  $2.1 \times 10^{-6}$ , respectively. The main reason of this discrepancy is the smaller value of  $\sigma_8$  adopted in our simulation ( $\sigma_8 = 0.8$  against their  $\sigma_8 = 0.9$ ): the mean value of the Compton  $y$ -parameter is in fact expected to scale roughly as  $\sigma_8^{\alpha/2}$ , with  $\alpha \approx 4 - 7$  (see, e.g., Sadeh & Rephaeli, 2004; Diego & Majumdar, 2004). For the same set of maps, we also repeat the analysis but considering only the gas particles of the warm-hot intergalactic medium (WHIM, see Cen & Ostriker, 1999; Davé et al., 2001), defined as the gas component having a temperature  $T$  in the range  $10^5 < T < 10^7 \text{ K}$  and we obtain  $\langle y \rangle_{\text{WHIM}} = (6.90 \pm 0.42) \times 10^{-7}$ , which means that about 60 per cent of the total value of the  $y$ -parameter is originated by WHIM gas, while the remaining fraction comes from hotter gas ( $T > 10^7 \text{ K}$ ).

Analysing the kSZ map, we notice that the peaks can reach values of  $|b| \gtrsim 10^{-5}$ ,

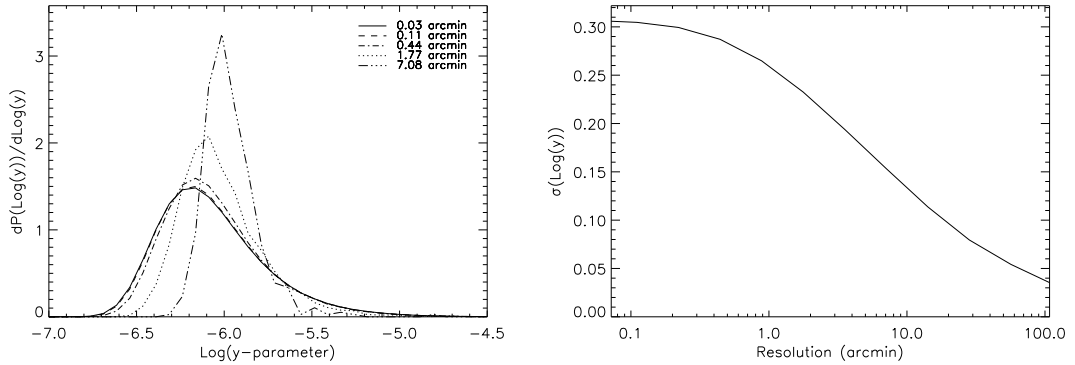


**Figure 5.4.** Left panel: probability distribution functions of the logarithm of the  $y$ -parameter in the 10 maps for different angular resolutions of the maps. Right panel: standard deviation of the distribution of the logarithm of the  $y$ -parameter as a function of the map resolution.

i.e. roughly of the same intensity of the typical  $\Delta T/T$  of the primary CMB signal. These peaks correspond to clusters which are not necessarily massive and/or hot like for the tSZ signal, but that have significant bulk motions. This leads to considerable displacements in the peak positions in the two maps: for example, we note that the brightest source in the tSZ map roughly located in the position  $(2.2^\circ, 1.0^\circ)$ , and corresponding to a cluster at  $z \sim 0.3$ , is completely absent in the kSZ maps, since it is a relaxed object with a small radial component of the peculiar velocity.

In Fig. 5.3 we show the probability distribution function of both SZ signals calculated considering the values in the  $(1.66 \text{ arcsec})^2$  pixels: in particular the thin lines refer to each of the 10 light-cone realizations, while the thick line is the corresponding average. We notice that the tSZ distribution is close to a lognormal function while the kSZ is similar to a gaussian one.

Regarding the average distribution of the tSZ signal we computed the first moments of  $I_y \equiv \log y$ : we find  $\overline{I_y} = -6.07$  with a corresponding r.m.s. of 0.31 and a skewness<sup>1</sup> of 0.96. The odd moments of the kSZ average distributions are close to zero, as expected, and we obtain an r.m.s. of  $1.3 \times 10^{-6}$  and a kurtosis<sup>2</sup> of 5.1.

It is also interesting to analyse the dependence of these statistics on the maps resolution. We show in the left panel of Fig. 5.4 the dependence of the distribution of the logarithm of the  $y$ -parameter: the shape does not change significantly when decreasing the resolution down to 0.44 arcmin (corresponding to  $16^2$  pixels in the original map), while a further reduction of the resolution leads to a change in the shape of the distribution with a resulting absence of the lowest values in the map. On the contrary the probability of obtaining high values remains unchanged also with a resolution of 1.77 arcmin, as a consequence of the fact that the peaks correspond to galaxy clusters which have this typical angular size.

<sup>1</sup>Here we adopt the definition of skewness  $s$  of a population  $\{x_1, \dots, x_n\}$  given by the formula  $s \equiv \frac{1}{(n-1)\sigma^3} \sum_{i=1}^n (x_i - \bar{x})^3$ , where  $\bar{x}$  is the mean of the distribution and  $\sigma$  is its r.m.s.

<sup>2</sup>The kurtosis  $\kappa$  is defined as  $\kappa \equiv \frac{1}{(n-1)\sigma^4} \sum_{i=1}^n (x_i - \bar{x})^4 - 3$ .

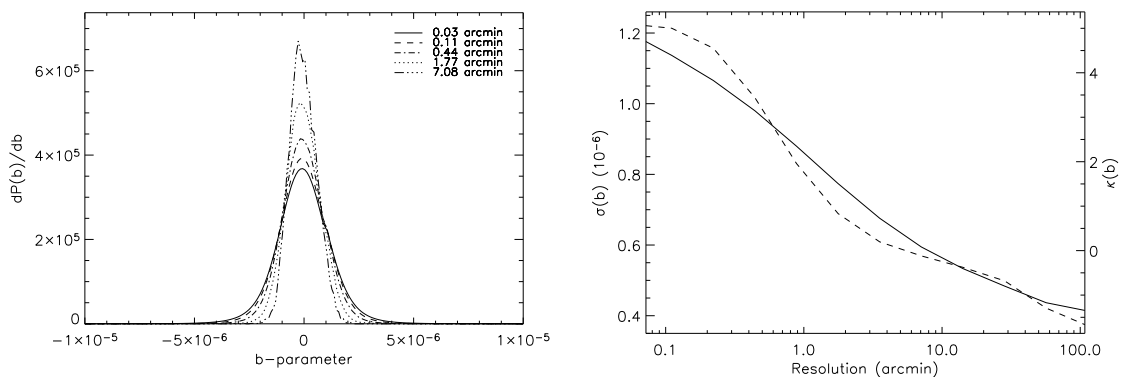


**Figure 5.5.** Left panel: probability distribution functions of the  $b$ -parameter in the 10 maps for different angular resolutions of the maps. Right panel: standard deviation (solid line) and kurtosis (dashed line) of the distribution of the  $b$ -parameter as a function of the map resolution.

At low resolutions the distribution is also more peaked, as it can also be seen in the right panel of Fig. 5.4: the standard deviation of the distribution drops from 0.3 to less than 0.1 when varying the resolution from 0.2 to 20 arcmin, indicating that in order to capture the main features of the fluctuation field of the tSZ effect a resolution better than 1 arcmin is desirable.

We show in Fig. 5.5 the corresponding plots for the distribution of the kSZ values. As expected the tails of the distribution function are strongly affected by the reduction of the resolution (our results are similar to those obtained by da Silva et al., 2001a). The right panel shows that the standard deviation (solid line) increases at higher resolution due to the fact that, as we will discuss more extensively in Section 5.5, the kSZ has a significant contribution from small-scale signal.

The level of non-gaussianity of the distribution can be expressed in terms of the kurtosis  $\kappa$  also plotted in the right panel of Fig. 5.5 (dashed line). The distribution of values is very close to a gaussian (i.e.  $\kappa = 0$ ) for resolutions of  $\sim 1$  arcmin, while at higher resolution the kurtosis increases up to more than 4 thus populating more the tails of distribution. This indicates that the non-gaussianity originated by the kSZ effect must be taken into account when measuring the primordial (i.e. inflationary) non-gaussianity at scales lower than 1 arcmin.

As already mentioned in Section 5.3, unlike the X-ray signal, both the tSZ and the kSZ effects have significant contributions from high-redshift gas. This can be clearly seen in Fig. 5.6, where we show the contribution to the  $y$ -parameter and  $b$ -parameter, divided into equal comoving distance intervals with length of  $10h^{-1}$  Mpc (the corresponding redshifts are indicated on the top of the panels). Note that the curves represent the average value of the 10 different light-cone realizations.

The tSZ signal (left panel) shows several spikes at low redshift ( $z < 0.5$ ), mainly due to the presence of galaxy clusters in the bin. At higher redshifts the distribution is much more regular because the dispersion becomes lower, since the light cones include larger comoving volumes at larger distances. Moreover large collapsed

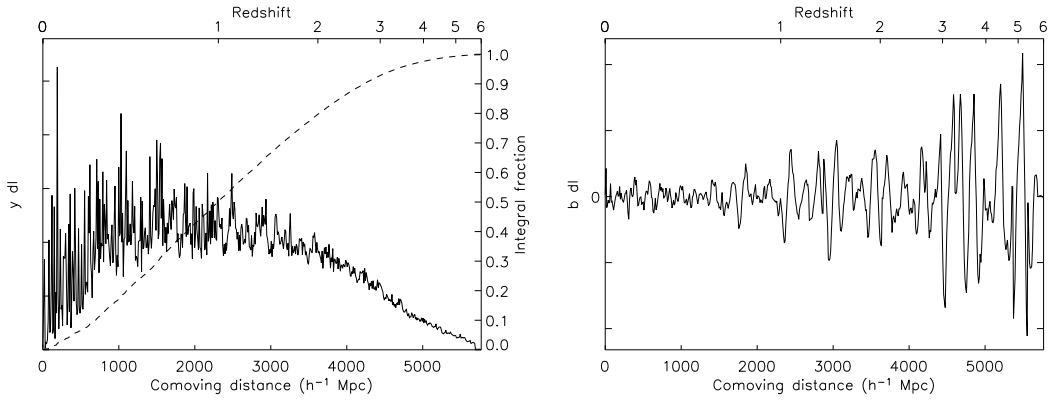


**Figure 5.6.** Differential contributions to the  $y$ -parameter (left panel) and  $b$ -parameter (right panel) as a function of the comoving distance from the observer; the corresponding redshifts are indicated on the top. The values, representing the mean of the 10 map realizations, are computed in equispaced comoving distance intervals with length of  $10h^{-1}$  Mpc. The dashed line in the left panel shows the integral of the distribution as a fraction of the final average value of the  $y$ -parameter.

structures are very rare events at  $z \gtrsim 2$ . Integrating this redshift distribution we obtain, in good agreement with previous analyses (see, e.g., da Silva et al., 2000), that half of the total tSZ signal comes from  $z > 1$ , and only about 20 per cent from  $z > 2$ .

Since in a given redshift bin there are both gas elements approaching and receding from the observer with similar probabilities, the kSZ signal (right panel), which is the algebraic sum of all the contributions, has a vanishing expectation value. Therefore the distribution plotted in the right panel of Fig. 5.6 can be considered as a measurement of the dispersion. The plot clearly shows that, even at very high redshift, the contribution to the kSZ is non-negligible: as suggested by da Silva et al. (2001a), the increase of the contributing gas mass compensates the decrease of its velocities.

## 5.5 The SZ angular power spectra

In order to study the detectability of the SZ effects, it is important to analyse not only the intensity of the signal itself, but also its power at different angular scales. In Fig. 5.7 we compare the angular power spectra for both SZ effects to the primary CMB one. The displayed SZ spectra, which represent the average of the power spectra of the 10 different light-cone realizations, have been obtained in the approximation of flat sky (which well holds for  $\ell > 100$ ) and using a method based on Fast Fourier Transform. We considered a frequency  $\nu = 30$  GHz for the tSZ effect, that corresponds to  $g_\nu(x) = -1.94$ , (see equation 5.3), thus near the RJ limit for which the effect is maximum, while the choice of the frequency does not affect the intensity of the kSZ (see Section 5.2) effect.

As already discussed at the end of Section 5.4, the tSZ effect has a significant contribution from high-redshift gas ( $z > 1$ ). Since our map-making algorithm

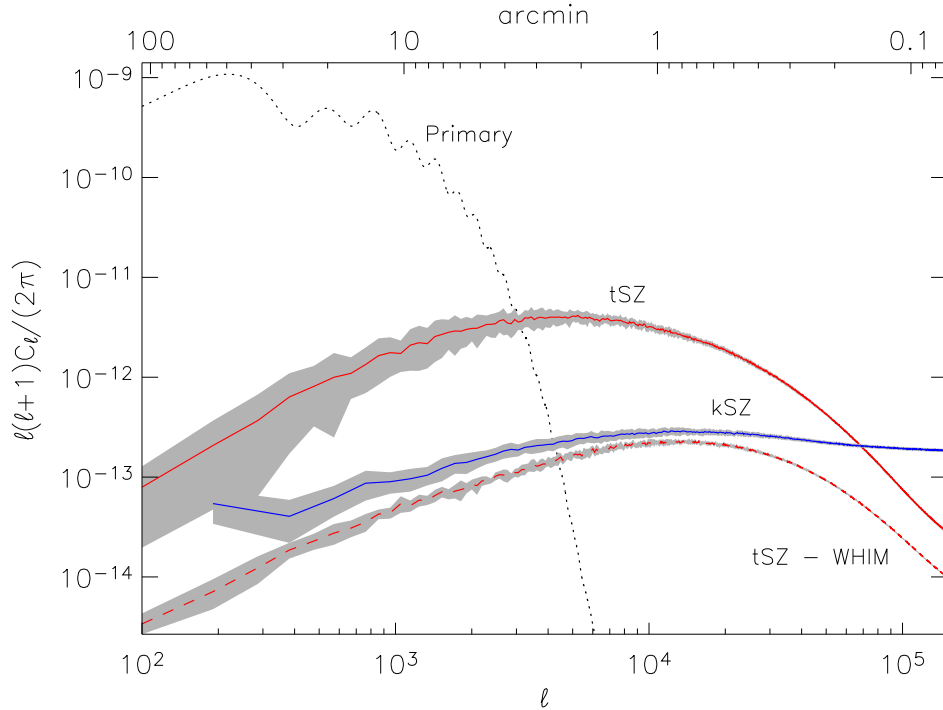


**Figure 5.7.** Angular power spectra of the  $\Delta T/T_{\text{CMB}}$  induced by the different SZ effects as a function of the multipole  $\ell$ . The dotted line represents the primary CMB signal calculated using CMBFAST (Seljak & Zaldarriaga, 1996) and assuming the same cosmological model considered for our hydrodynamical simulation. The solid lines are the tSZ (red) and kSZ (blue) power spectra: they represent the average of the power spectra of different maps (10 light-cones for the tSZ, 40 for the kSZ). The dashed line refers to the tSZ power spectrum for the WHIM. The shaded regions represent the r.m.s. calculated between the 10 (40) maps. The tSZ spectra are computed at the frequency  $\nu = 30$  GHz.

replicates the same volume four times for  $z > 1.4$  (see the comments on Fig. 4.1 at the end of Section 5.3), this could introduce some spurious correlation. We checked that this is not the case for the tSZ signal, while we found that the kSZ maps are affected by this problem: for this reason we decided to split each of the 10 kSZ maps into 4 submaps (thus creating 40 different light cones) and to calculate their power spectra separately.

Given the size and resolution of our maps, in principle this procedure can allow us to compute the power spectra from  $\ell \simeq 95$  ( $\ell \simeq 190$  for the kSZ effect) out to  $\ell \simeq 7.8 \times 10^5$ . However the finite box size of  $192h^{-1}$  Mpc of our simulation makes our results reliable only for  $\ell \gtrsim 400$  (e.g. the angular extension of 1/4 of the box size at  $z = 6$ ). Anyway for the purpose of our work, we are not interested in investigating the properties of the SZ signal at  $\ell \lesssim 1000$ , because in this range the primary CMB anisotropies dominate and because at large scales the tSZ is highly affected by the local structures (see Chapter 7). Since at low angular scales all the signal is coming from small and dense objects, the spatial resolution of our simulation (e.g. the highest smoothing length of the SPH particle in the region) is large enough to have

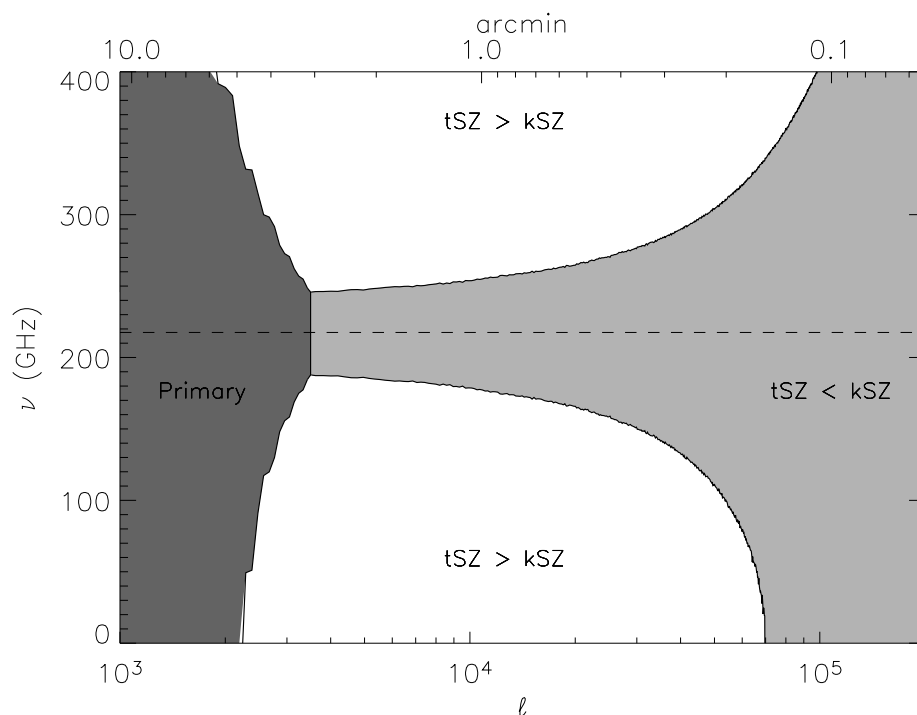


**Figure 5.8.** In the  $\nu - \ell$  (observed frequency-angular scale) plane we show the regions where the power spectra corresponding to different signals are dominant. Dark shaded, light shaded and white regions show where the primary CMB signal, the kSZ effect and the tSZ effect dominate the other components, respectively. The solid lines show where two effects have the same power, the dashed line corresponds to the frequency of 218 GHz, at which the tSZ vanishes.

results reliable out to  $\ell \simeq 2 \times 10^5$ .

The tSZ power spectrum peaks at  $\ell \simeq 5000$  and, in the RJ regime, it starts to dominate the primary CMB signal at scales of about 4 arcmin. The kSZ signal is about one order of magnitude lower at these scales. However, it is interesting to note that while at higher  $\ell$  the tSZ signal loses power significantly, our model predicts an almost flat kSZ power spectrum, that overcomes the tSZ one for  $\ell \gtrsim 7 \times 10^4$  even in the RJ regime. This behaviour, which is similar to the one obtained by Zhang et al. (2004), is a consequence of both the high contribution from distant, and therefore smaller, objects that affect the kSZ effect signal and of the effect of the galactic winds present in our simulation that are able to increase the power of the signal on very small scales.

The tSZ signal arising from the WHIM (also plotted in Fig. 5.7) peaks at the scales of about 1 arcmin, which roughly corresponds to the angular scales of galaxy groups. Even if the total signal of the WHIM contributes to about 60 per cent of the mean value of the  $y$ -parameter (as we already noted in Section 5.4), at the angular scales where the tSZ signal is dominant the amplitude of its power spectrum contributes to less than 10 per cent of the total tSZ one: this shows that the detection of the tSZ signal constitutes a probe almost only for the ICM at temperatures  $T > 10^7$  K, that mainly resides in collapsed structures.

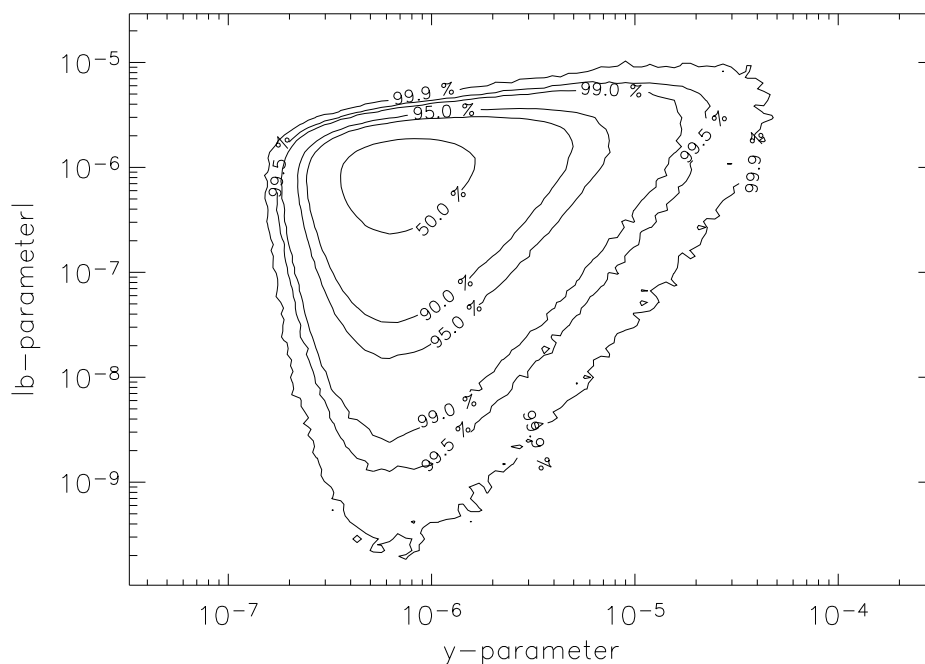


**Figure 5.9.** Distribution of the pixel values for the whole set of 10 maps: the (modulus of the) Doppler  $b$ -parameter vs. the Compton  $y$ -parameter. The 6 contour levels enclose 50, 90, 95, 99, 99.5 and 99.9 per cent of the total amount of pixels, respectively.

As already noted in Section 5.2, the intensity of the kSZ effect does not depend on the observed frequency. On the contrary, when increasing the frequency in the RJ regime, the tSZ effect decreases, so the angular scale at which the kSZ signal dominates over the tSZ becomes higher. Fig. 5.8 shows the dependence on the angular multipole of the frequency of equality between the power spectra of the two effects. It is worth to note that at 150 GHz the kSZ dominates for  $\ell \gtrsim 3 \times 10^4$ .

## 5.6 Cross-correlation between the SZ signals

The two SZ signals both depend linearly on the electron density  $n_e$  and receive the main contribution from the same cosmic structures, so a correlation between the two is expected. However, since temperature and velocity of the gas are not tightly correlated and since the  $b$ -parameter depends only on the radial component of the velocity, a spread is expected also. This can be seen in the contour plot in Fig. 5.9 which represent the distribution of pixel values according to the two SZ effects: a significant scatter is present for low ( $y \lesssim 10^{-6}$ ) values of the  $y$ -parameter to which can correspond  $b$ -parameter from zero almost to the highest possible values. Anyway, considering the contour levels, most of the surface of the sky is expected to have average values of the two signals.

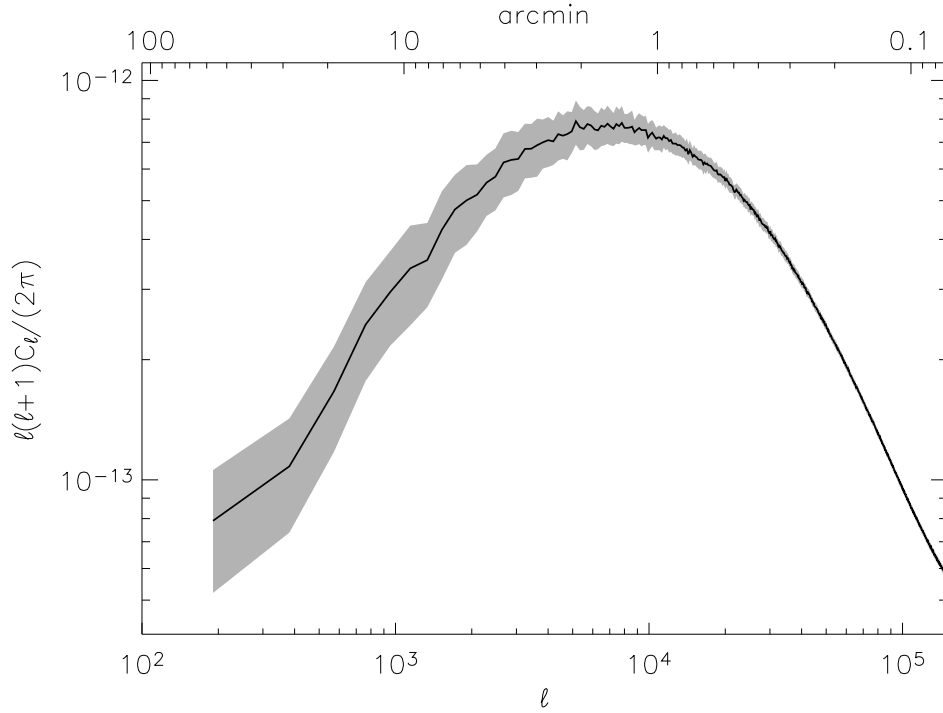


**Figure 5.10.** Power spectrum of the cross-correlation tSZ-kSZ at  $\nu = 30$  GHz as a function of the multipole  $\ell$ . The solid line represents the average of the power spectra of the 40 submaps; the shaded region shows the corresponding r.m.s.

We show in Fig. 5.10 the power spectrum of the cross-correlation between the two SZ signals computed at 30 GHz (the scaling with the frequency  $\nu$  is simply given by the term  $g_\nu(x)$  of equation 5.3). The correlation peaks at 2 arcmin, the typical scale of galaxy clusters and has sharp decrease at higher  $\ell$  due to the lack of power of the tSZ effect.

In order to quantify the strength of the correlation we follow Cheng et al. (2004) and compute the cross-correlation coefficient between the two signals which is defined as

$$r_\ell \equiv \frac{C_\ell^{\text{tSZ-kSZ}}}{\sqrt{C_\ell^{\text{tSZ}} C_\ell^{\text{kSZ}}}}. \quad (5.9)$$

The corresponding results are shown in Fig. 5.11. Globally the tSZ and kSZ present a high correlation ( $r_\ell \simeq 0.78$ ), almost independent of the angular scale, indicating that, as already said in the comments on Fig. 5.9, the average properties of the two signals are similar despite of the different physical dependence. The spread of the correlation in the different light-cones (indicated by the shaded region) is also quite low ( $\sim 0.01$ ); at low  $\ell$  it increases ( $\sim 0.07$ ) due to the lack of statistics and the larger cosmic variance.

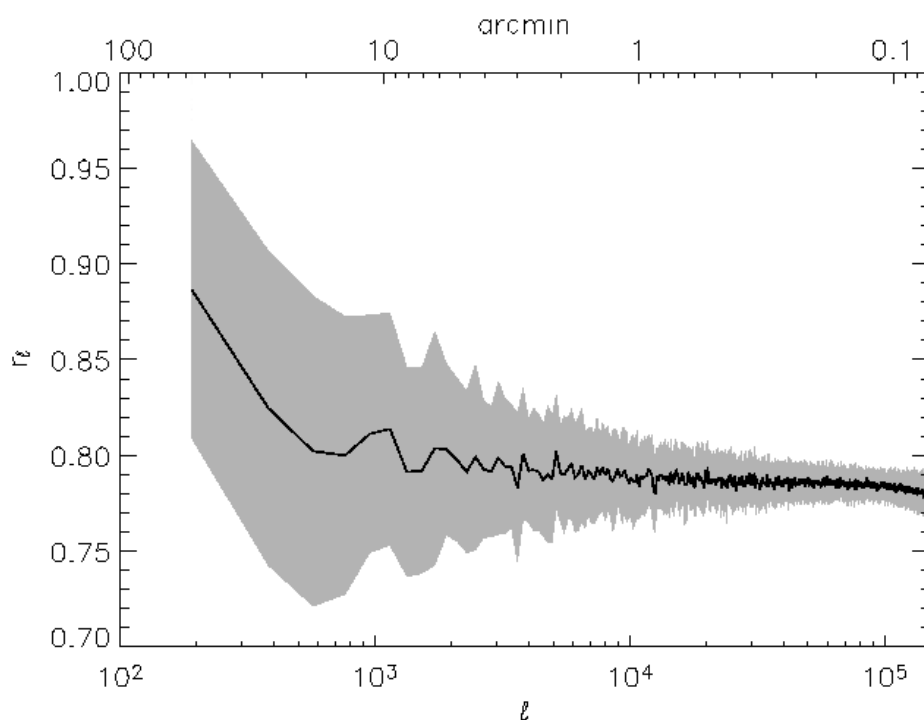


**Figure 5.11.** Cross-correlation coefficient between the tSZ and the kSZ effects as a function of the multipole  $\ell$ . The solid line represents the average of the correlation coefficient of the 40 submaps; the shaded region shows the r.m.s. between them.

## 5.7 Cross-correlation with the soft X-ray signal

The ionized gas responsible of the SZ signal also produces an X-ray emission. However, the dependence on both density/scale and redshift is different. Consequently, the cross-correlation between the two signals can provide information on the scales, masses and redshifts contributing to each signal.

Taking advantage of the X-ray maps presented in Chapter 4 obtained from the same light-cone realizations of the tSZ and kSZ maps studied here, we are able to analyse the properties of the correlation between the X-ray surface brightness and the two SZ signals discussed in this Chapter.

The contours in the left panel of Fig. 5.12 represent the distribution of pixel values according to the soft (0.5–2 keV) X-ray surface brightness (SXR) and the tSZ effect: it is evident that most of the regions in the sky present both a low soft X-ray emission ( $\sim 10^{-14} - 10^{-12} \text{ erg s}^{-1} \text{ cm}^{-2} \text{ deg}^{-2}$ ) and  $y$ -parameter ( $\sim 10^{-6}$ ), as shown by the distributions reported in Figures 4.4 (top panel) and 5.3 (left panel). We also notice that, as expected, the amplitudes of the two signals are correlated, even if a significant scatter is present especially for high intensities.

Using this two-dimensional distribution we calculate the maximum-likelihood relation that for a given value of the X-ray surface brightness provides the corresponding one of the  $y$ -parameter. We proceed in the following way: given

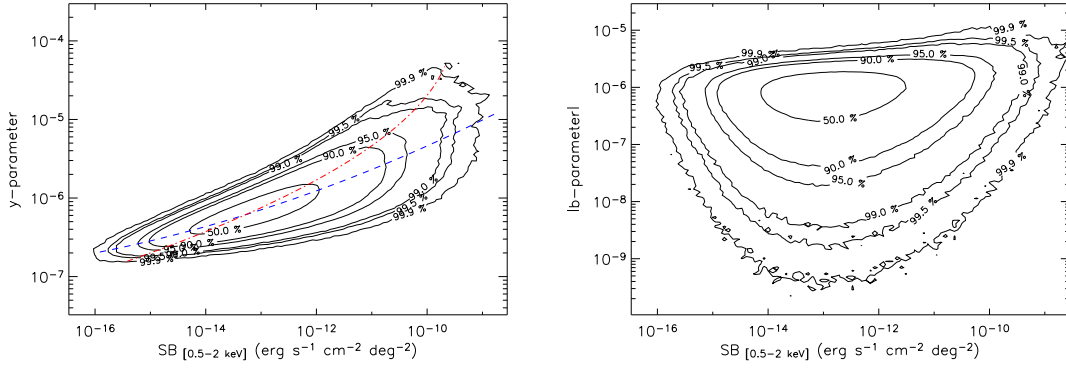


**Figure 5.12.** Left panel: distribution of the pixel values for the whole set of 10 maps: the Compton  $y$ -parameter vs. the soft (0.5–2 keV) X-ray surface brightness. The 6 contour levels enclose 50, 90, 95, 99, 99.5 and 99.9 per cent of the total amount of pixels, respectively. The dashed line represents the maximum-likelihood relation  $Y(X)$ , obtained by fitting the relation in equation (5.10); the dot-dashed line represents the opposite maximum-likelihood relation  $X(Y)$ . Right panel: as the left panel, but for the (modulus of the) Doppler  $b$ -parameter vs. the soft (0.5–2 keV) X-ray surface brightness.

$X \equiv \log_{10}(\text{SB}(\text{erg s}^{-1} \text{ cm}^{-2} \text{ deg}^{-2}))$  and  $Y \equiv \log_{10}(y)$ , we consider separately the distribution associated to all the different values of  $X$  (i.e. the columns of the matrix shown in the left panel of Fig. 5.12); then for a given  $X$  we take the value of  $Y$  corresponding to the maximum point of the distribution and its scatter and we fit these data with a polynomial relation given by the formula

$$Y = a_0 + a_1X + a_2X^2, \quad (5.10)$$

where and  $a_{i=0,2}$  are the free parameters. We also weight the data according to the total amount of points of each distribution. We obtain the best-fit relation of  $Y = -0.72 + 0.61X + 0.015X^2$  represented in the plot by the dashed line. Switching the two variables of equation (5.10) and with the same procedure we obtain also the opposite relation  $X = -21 - 5.8Y - 0.73Y^2$  shown by the dot-dashed line.

We show in Fig. 5.13 the power spectrum of the soft (0.5–2 keV) X-ray surface brightness arising from the hot ionized plasma; this power spectrum has been obtained in the same way described in Section 5.5 for the tSZ, but after dividing the pixel values for their average value corresponding to  $4.06 \times 10^{-12} \text{ erg s}^{-1} \text{ cm}^{-2} \text{ deg}^{-2}$  (see Table 4.1). The amplitude of the r.m.s. is a direct consequence of the large variance between different fields of the soft X-ray emission coming from the LSS already discussed in Chapter 4.

Confronting the soft X-ray power spectrum with the one of the tSZ effect shown in Fig. 5.7 we can see that the former peaks at higher multipoles than the latter. This is due to the fact that the dependence on the square of the gas density of the bremsstrahlung emission makes it more sensitive to the inner parts of collapsed objects.

We show in Fig. 5.14 the power spectrum of the correlation of the tSZ with the soft X-ray emission; again, we computed them following the same methods

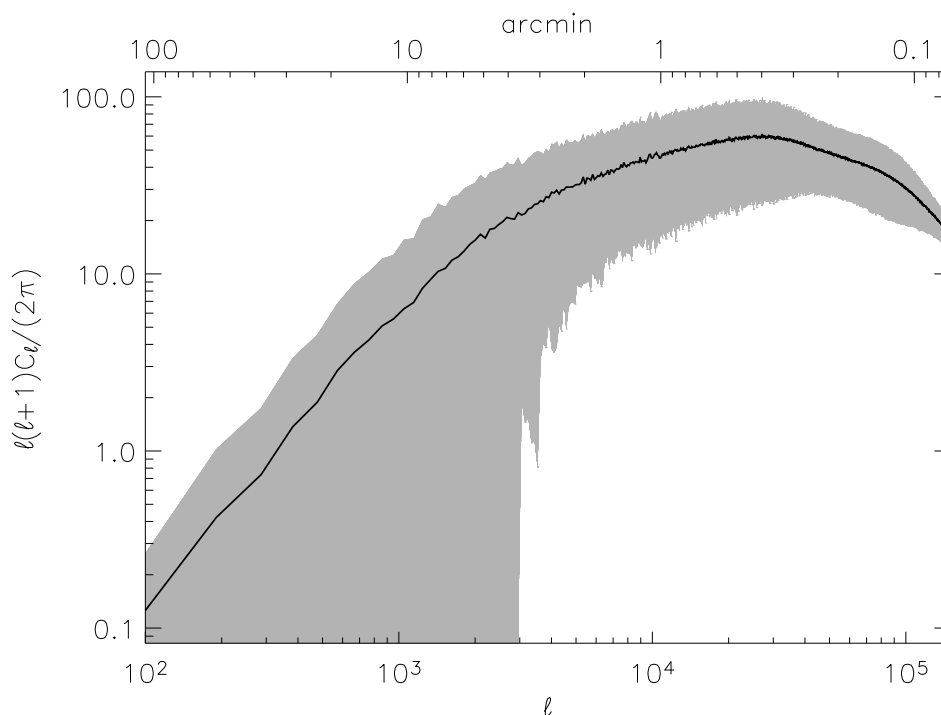


**Figure 5.13.** Power spectrum of the SXRb in the soft (0.5–2 keV) X-ray band as a function of the multipole  $\ell$ : it is obtained after normalizing the pixel values to their average of  $4.06 \times 10^{-12} \text{ erg s}^{-1} \text{ cm}^{-2} \text{ deg}^{-2}$ . The solid line represents the average of the power spectra of the 10 maps; the shaded region shows the corresponding r.m.s.

described in Section 5.5 (using the set of 40 submaps for the tSZ-kSZ correlation) and assuming the frequency<sup>3</sup>  $\nu = 30 \text{ GHz}$ . As expected the cross-correlation peaks at an intermediate scale between the two power spectra, and it remains almost constant in the range between  $\sim 0.5$  and  $\sim 3$  arcmin. Therefore this constitutes the best angular range to study the two signals together.

The right panel of Fig. 5.12 shows the scatter plot between the soft X-ray surface brightness and the (modulus of the)  $b$ -parameter. The dependence of the kSZ effect from the X-ray emission is weaker than the tSZ effect one, however this plot shows that the highest peaks of the kSZ effect ( $|b| > 10^{-5}$ ) are always associated to high surface brightness values (e.g. inner regions of galaxy clusters).

Finally, we also compute the cross-correlation coefficient between the SXRb and the two SZ effects and show our results in Fig. 5.15 (left and right panel, respectively). The correlation with the tSZ is as high as  $\sim 0.9$  at  $\ell \sim 1000$ , slightly decreasing at lower angular scales. This result is in contrast with that obtained by Cheng et al. (2004) that predict a correlation coefficient of about 0.3. The explanation can be found in the different methods used to obtain the results: in fact Cheng et al. (2004) followed an analytical approach using several approximations to account for the cooling of the gas and for the shape of the density profiles.

<sup>3</sup>For these computations we dropped the negative sign arising from  $g_\nu(x) \simeq -1.94$  for  $\nu = 30 \text{ GHz}$ .

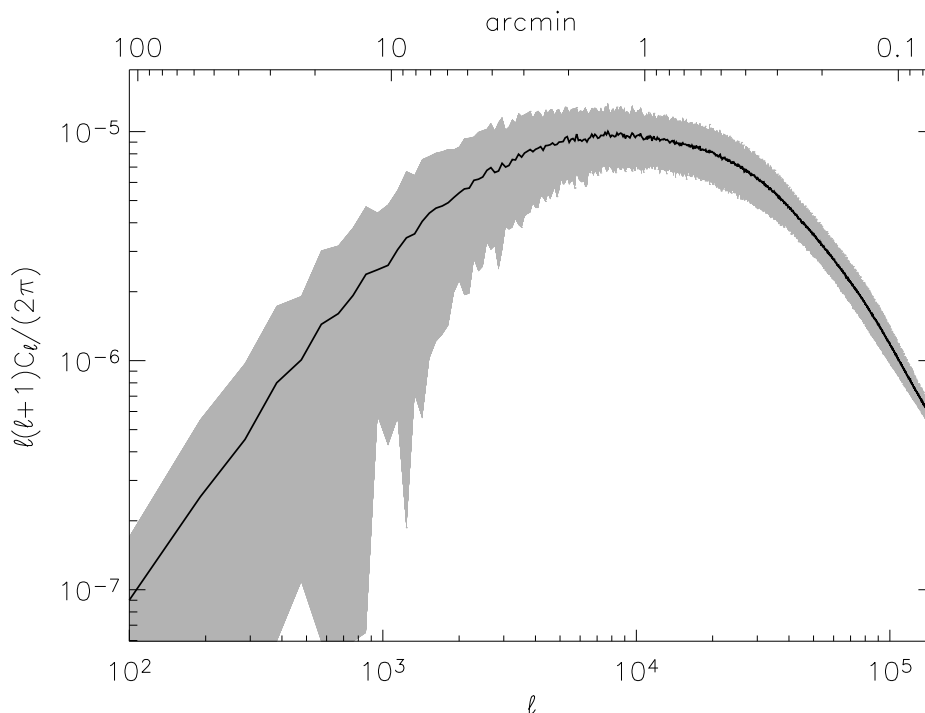


**Figure 5.14.** Power spectrum of the cross-correlation SXRb-tSZ at  $\nu = 30$  GHz as a function of the multipole  $\ell$ . The solid line represents the average of the power spectra of the 10 maps; the shaded region shows the corresponding r.m.s.

The correlation between the SXRb and the kSZ is also very high: in all of our light-cone realizations the values of  $r_\ell$  for  $\ell > 1000$  are around 0.8 with negligible differences between them.

## 5.8 Summary and conclusions

In this chapter we have studied the global properties of the tSZ and kSZ effects using the results of a cosmological hydrodynamical simulation of the  $\Lambda$ CDM model. The simulation (Borgani et al., 2004) follows the evolution of dark matter and baryons accounting for several physical processes that affect the thermodynamical history of the gas: a time dependent photo-ionizing uniform UV background, radiative cooling processes and star formation with consequent feedback processes by SN-II and galactic winds.

We used the outputs of the simulations to construct 10 independent light-cone realizations from  $z = 0$  out to  $z = 6$  and computed associated mock maps, of size  $(3.78^\circ)^2$ , of the Compton  $y$ -parameter and Doppler  $b$ -parameter. Using this dataset we estimated the expected statistical properties of the two SZ effects, we calculated their power spectra and studied their cross-correlations. We also analysed their correlation properties with the soft (0.5–2 keV) X-ray emission obtained with the same light-cone realizations and already studied in a Chapter 4.

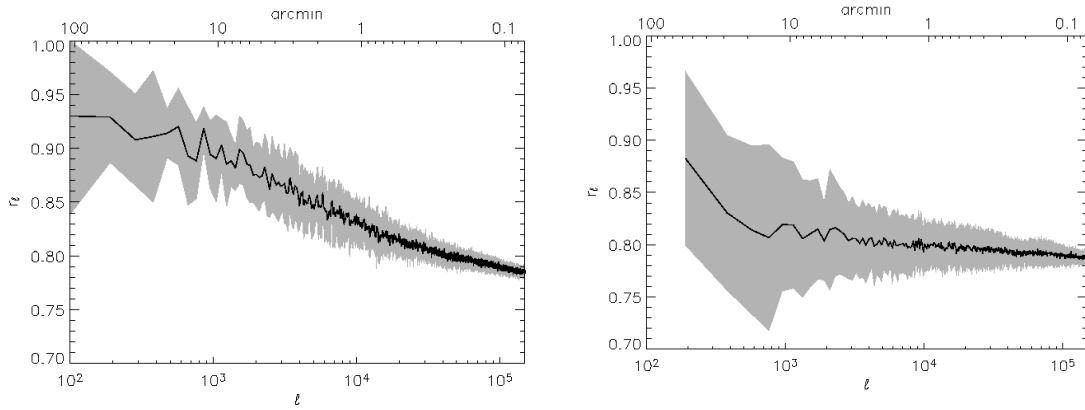


**Figure 5.15.** Cross-correlation coefficient between the SXRb in the 0.5–2 keV band and the tSZ effect (left panel) and between the SXRb and kSZ effect (right panel) as a function of the multipole  $\ell$ . The black line is calculated the average of the 10 (40) maps; the shaded region shows the r.m.s. between them.

Our main results can be summarized as follows.

- i* - The mean intensity of the Compton  $y$ -parameter due to the IGM is  $\langle y \rangle = (1.19 \pm 0.32) \times 10^{-6}$ : almost 60 per cent of this signal comes from WHIM and about half comes from  $z > 1$ . The distribution of the pixel values in the sky is close to a lognormal, with variance increasing at higher resolution up to<sup>4</sup> 0.3 at the scales of 0.1 arcmin.
- ii* - The peaks of the Doppler  $b$ -parameter associated with collapsed objects, are of the order of  $|b| \simeq 10^{-5}$ . This signal presents a nearly gaussian distribution peaked around 0, with a variance that increases with resolution out to the scales of some arcsecond. The kSZ has a significant contribution from high-redshift gas.
- iii* - The power spectrum analysis shows that the tSZ dominates the primary CMB anisotropies for  $\ell > 3000$  and peaks at  $\ell \simeq 5000$ . The kSZ peaks at  $\sim 1$  arcmin and has a flat power spectrum towards high  $\ell$  out to  $\ell > 2 \times 10^5$ . It dominates the tSZ signal for  $\ell \gtrsim 7 \times 10^4$  at all frequencies. The two SZ effect are highly correlated at all scales.
- iv* - The SXRb is highly correlated with the two SZ effects, particularly with the tSZ ( $r_\ell \simeq 0.8 - 0.9$ ). We also calculated a maximum-likelihood analytic formula that connects the values of the two observables.

In conclusion, the work presented in this Chapter further demonstrates the importance of the upcoming measurements of both SZ effects and their complementarity with present-day and future X-ray data. A joint analysis of these signals, in combination with high-resolution hydrodynamical simulations,

<sup>4</sup>In a logarithmic scale.

will allow one to obtain insights on the properties of the baryonic component, and on the physical processes acting on it.



## Chapter 6

# GALAXY CLUSTERS AT THE VIRIAL RADIUS

**T**he physics that affects the gas inside galaxy clusters is much more complex than it was thought some years ago. In fact, some sort of feedback connected with the formation of stars and galaxies acts on the ICM and influences its thermodynamics. However, the external regions of galaxy clusters, where the density is lower, are expected to be less affected by this feedback and, therefore, can provide constraints on the presence of other physical processes, especially in the framework of the forthcoming low-background observational data. This chapter is mainly based on “*Simulated X-ray galaxy clusters at the virial radius: slopes of the gas density, temperature and surface brightness profiles*”, Roncarelli M., Ettori S., Dolag K., Moscardini L., Borgani S., Murante G., 2006b, MNRAS, 373, 1339.

### 6.1 Modeling and observing clusters outskirts

Galaxy clusters form in correspondence of the highest peaks of the fluctuations in the cosmic dark matter density field and collapse under the action of gravitational attraction to define structures with a mean density enhanced with respect to the cosmic value by a factor of few hundreds (see Section 1.6.3). They reach the virial equilibrium over a volume with a typical virial radius that indicates, as a first approximation, the regions where the pristine gas accretes on the dark matter halo through gravitational collapse and is heated up to millions degrees through adiabatic compression and shocks. This ICM, that represents about 80 (15) per cent of the baryonic (total) cluster mass (e.g. Ettori et al., 2004), becomes, then, X-ray emitter mainly through bremsstrahlung processes, thus allowing one to trace and characterize the distribution of the baryonic and dark matter components.

From an observational point of view, the measurement of the properties of the ICM is possible only where the X-ray emission can be well resolved against the background (both instrumental and cosmic). At the present, data permit to firmly characterize observables like surface brightness (see Mohr et al., 1999; Ettori & Fabian, 1999) and gas temperature (see Markevitch et al., 1998; De Grandi & Molendi, 2002; Pointecouteau et al., 2005; Vikhlinin et al., 2006; Zhang et al., 2006)

out to a fraction ( $\sim 0.5-0.6$ ) of the virial radius. Only few examples of nearby X-ray bright clusters with surface brightness estimated out to the virial radius are available, thanks to the good spatial resolution, the large field-of-view and the low instrumental background of the *ROSAT/PSPC* instrument (Vikhlinin et al., 1999; Neumann, 2005).

However, as described in Section 2.1.1 the brightest regions of galaxy clusters are influenced by the presence of self-regulated feedback mechanisms associated to radiative cooling, star formation and to the energy injection from AGNs that are very difficult to model and are not yet well understood. This aspect, which is known as the *cooling flow problem* (see e.g. Fabian, 1994), makes it very complicated to extract direct cosmological informations from cluster cores and it constitutes one of the most challenging issues of modern astrophysics, since its modeling is still matter of tension between the present simulated constraints and the observed counterparts (see e.g. Borgani et al., 2004).

However, when studying the formation of galaxy clusters, it is important to take into account that the regions not-yet resolved occupy almost 80 per cent of the total volume and that they retain most of the information on the processes that characterize the accretion and evolution within the cluster of the main baryonic component (Molendi, 2004). In fact, the ICM in these regions is at a lower density and, therefore, is less affected by the presence of non-gravitational physics. In principle, this makes the outskirts of galaxy clusters ideal tools to understand the haloes formation history, provided the availability of observations capable of probing these low surface brightness regions.

In this Chapter we describe the results of our study of the distribution of the ICM density, temperature and surface brightness in a set of simulated galaxy clusters by looking at their radial profiles in the range between  $0.3R_{200}$ <sup>1</sup> and  $3R_{200}$ . For the reasons described above, we avoid considering the regions where the clusters evolve a core with active cooling and suspected feedback regulation. Therefore, we concentrate our analysis on cluster volumes where the gas density and temperature suggest that radiative processes are not dominant and the main physical driver is just the gravitational collapse, that is expected to be well described in the present numerical N-body simulations.

We consider 9 objects of the *Hutt* simulation set described in Section 3.5.2: these haloes are extracted from a dark matter only cosmological simulation that were resimulated at much higher resolution by including the gas subjected to gravitational heating and other physical treatments like cooling, star formation, feedback, thermal conduction and an alternative implementation of artificial viscosity.

---

<sup>1</sup>In this chapter we adopt the typical physical quantities of clusters as follows:  $R_{200}$  ( $R_{500}$ ) is the radius of a sphere centered in a local minimum of the potential and enclosing an average density of  $\rho = 200(500)\rho_{\text{cr}}$ , with  $\rho_{\text{cr}}$  being the critical density of the Universe. The virial quantities are defined using the density threshold obtained by the spherical collapse model, described in Section 1.6.3, and adopting the cosmological parameters of the simulations. So, following the formula of equation (1.86), the virial radius  $R_{\text{vir}}$  encloses an average density of  $\rho_{\text{vir}} \simeq 104\rho_{\text{cr}}$ . Consequently the virial mass  $M_{\text{vir}}$  is the total mass (DM plus baryons) of the cluster up to  $R_{\text{vir}}$ .

We organize the presentation of this chapter in the following way: in the next Section, we describe our dataset of simulated clusters and their different physical properties; in Section 6.3 we discuss the results on the slopes of the gas temperature, density and surface brightness profiles in the outskirts (i.e.  $r > 0.3R_{200}$ ) of the simulated objects and compare our results with the present constraints obtained from X-ray observations of bright clusters. We summarize and discuss our results in Section 6.5.

## 6.2 The simulated clusters

For the purpose of this work we use the set of 9 resimulated galaxy clusters of the *Hutt* simulation. These haloes span different mass ranges: 4 of them with the typical dimension of clusters and 5 of small clusters or group-like objects. We remand the reader to Section 3.5.2 for a detailed description of the simulation set.

In order to study the impact of different physical processes on the clusters properties, we simulated every cluster using 4 different sets of physical models:

1. Gravitational heating only with an ordinary treatment of gas viscosity (which will be referred as the *ovisc* model).
2. Gravitational heating only but with an alternative implementation of artificial viscosity (*lvisc* model), following the scheme proposed by Morris & Monaghan (1997), in which every gas particle evolves with its own viscosity parameter. With this implementation the shocks produced by gas accretion are as well captured as in the *ovisc* model, while regions with no shocks are not characterized by a large residual numerical viscosity. As already studied in Dolag et al. (2005c), this scheme allows to better resolve the turbulence driven by fluid instabilities, thus allowing clusters to build up a sufficient level of turbulence-powered instabilities along the surfaces of the large-scale velocity structures present in cosmic structure formation.
3. Runs which implement a treatment of cooling, star formation and feedback (*csf* model). The star formation is followed by adopting a sub-resolution multiphase model for the interstellar medium which includes also the feedback from supernovae (SN) and galactic outflows (Springel & Hernquist, 2003). The efficiency of SN to power galactic winds has been set to 50 per cent, which turns into a wind speed of 340 km/s.
4. Runs like *csf* but also including thermal conduction (*csfc* model), adopting the scheme described by Jubelgas et al. (2004). This implementation in SPH, which has been proved to be stable and to conserve the thermal energy even when individual and adaptive time-steps are used, assumes an isotropic effective conductivity parametrized as a fixed fraction of the Spitzer rate (1/3 in our simulations). It also accounts for saturation which can become relevant in low-density regions. For more details on the properties of simulated clusters using this model, see also Dolag et al. (2004).

**Table 6.1.** List of main physical parameters of the 9 clusters taken from the *ovisc* runs. The objects are divided into 2 subsamples according to their virial mass. Note that  $T_{\text{vir}}$  is the average mass-weighted temperature of the gas up to  $R_{\text{vir}}$ , while  $T_{200}$  is the temperature of the gas at  $R_{200}$ .

Cluster	SAMPLE A: $M_{\text{vir}} > 10^{15} M_{\odot}$				SAMPLE B: $M_{\text{vir}} < 10^{15} M_{\odot}$				
	<i>g1</i>	<i>g8</i>	<i>g51</i>	<i>g72</i>	<i>g676</i>	<i>g914</i>	<i>g1542</i>	<i>g3344</i>	<i>g6212</i>
$M_{\text{vir}} (10^{15} M_{\odot})$	2.12	3.39	1.90	1.96	0.15	0.17	0.15	0.16	0.16
$R_{\text{vir}} (\text{Mpc})$	3.37	3.94	3.25	3.28	1.40	1.46	1.40	1.43	1.43
$T_{\text{vir}} (\text{keV})$	6.49	9.89	5.78	5.44	1.25	1.28	1.18	1.26	1.22
$R_{200} (\text{Mpc})$	2.48	2.91	2.39	2.40	1.04	1.08	1.04	1.05	1.05
$T_{200} (\text{keV})$	4.18	7.52	4.18	4.09	0.82	1.03	0.83	0.88	0.84

The masses, radii and temperatures<sup>2</sup> of the 9 clusters for the *ovisc* model are summarized in Table 6.1. The other models have similar results for masses and radii with variation of few percent between the models while temperatures have larger variations with *csf* and *csfc* models having slightly higher temperatures ( $\sim 8$  per cent).

In our following analyses we will separate the clusters into two different samples: sample *A* (4 clusters) and *B* (5) according to their virial mass being larger or smaller than  $10^{15} M_{\odot}$ , respectively. When considering the environmental properties of these haloes, we must point out that the 4 objects of sample *A* are among the most massive clusters of the volume of the parent simulation while the 5 groups were chosen at random with the only condition to be far away from the 4 clusters. At the end of the resimulations all the haloes of sample *B* appear to be *isolated*, e.g. there is no halo with mass  $M > 10^{13.5} h^{-1} M_{\odot}$  at distance lower than  $5R_{\text{vir}}$ ; on the contrary the big clusters have several small structures inside the volume of their resimulation and all of them underwent significant merging activities. As we will see in Section 6.3, this aspect is important to understand the different properties of the X-ray profiles of the two samples.

### 6.2.1 Preparation of the dataset

Focusing our attention on the cluster outskirts, as said in the previous Sections, we do not consider in our study the effects of the cluster core on the overall properties, avoiding to deal with the theoretical, numerical and observational uncertainties on the physics of the X-ray emitting plasma in the cluster central regions. Furthermore we must take into account that the mass enclosed in a given radial bin in the external regions of clusters ( $r > R_{200}$ ) is dominated by the presence of dense subclumps of the typical dimension of galaxies or small galaxy-groups

<sup>2</sup>Notice that in here we prefer to quote all the temperatures by using the mass-weighted estimator because it is more related to the energetics involved in the process of structure formation. As shown in earlier papers (see, e.g. Mazzotta et al., 2004; Gardini et al., 2004; Rasia et al., 2005), the application of the emission-weighted temperature, even if it was originally introduced to extract from hydrodynamical simulations values directly comparable to the observational spectroscopic measurements, introduces systematic biases when the structures are thermally complex. We verified that the use of the spectroscopic-like temperature of Mazzotta et al. (2004) does not produce significant changes in our results for  $k_B T > 1$  keV.

( $M \lesssim 10^{13} M_{\odot}$ ). Evidences of the existence of these clumps in the regions inside  $R_{200}$  have also been shown by X-ray observations, but it is still not clear whether the frequency and the emission properties of the simulated clumps agree with the observed ones: this is due both to the low surface brightness of these objects that makes them difficult to resolve and to uncertainties in the theoretical modeling (e.g. simulations including cooling tend to produce more clumps and simulations with feedback from SNe end up with smaller clumps than non-radiative ones).

Anyway, since (i) we are interested only in the average properties of galaxy clusters and (ii) these small clumps are generally masked out in observational works, a direct comparison of our simulations with theoretical and observational results requires the introduction of a method to exclude these cold and dense clumps from our analysis.

It is quite difficult to define a precise and unique criterion to identify these condensed regions in the simulation volume from their dynamical and thermodynamical properties, therefore we decided to identify the volumes corresponding to non-collapsed regions. For this purpose we proceed in the following way: for every shell that corresponds to a radial bin of the profile, we sort the gas particles in decreasing volume order (i.e. starting from the more diffuse particles and going up to the denser ones, being the volume associated to the  $i$ -th particle defined as  $V_i = m_{gas}/\rho_{gas,i}$ ) then we compute the profiles calculating the mean of a given quantity considering only the particles summing up to a given percentage of the total volume of the shell.

In order to identify the physical properties of the regions excluded by our analysis, we plot in Fig. 6.1 as an example the maps of the projected density, mass-weighted temperature and soft (0.5–2 keV) X-ray surface brightness of the  $g1$  cluster considering (i) all the particles and (ii) those that are within the 95 per cent volume of each radial shell. We can clearly see from these maps that the volume-selective method actually separates the cold and dense clumps from the rest of the object. Anyway these maps show that this criterion is much more effective in excluding dense regions than cold ones. However, since the X-ray emission is strongly dependent on the density of the gas, we can safely say that it well mimics the observational technique of masking the bright isolated regions.

We also study the shapes of X-ray surface brightness profiles of our simulated clusters. Since we are interested in the outskirts of galaxy clusters we cannot adopt a pure bremsstrahlung emission model because in the corresponding temperature ranges ( $T < 1$  keV) line emission gives a significant contribution. Therefore in order to calculate the profiles we adopt a MEKAL emission model (Mewe et al., 1985; Liedahl et al., 1995) assuming a gas metallicity  $Z = 0.2Z_{\odot}$  (using the solar value tabulated in Anders & Grevesse, 1989) constant for every particle of the simulation: although this value can be an underestimate of the metallicity of the clusters' centre (see De Grandi et al., 2004, for more detail), the chosen model can be considered a good representation of the spectral properties of the clusters' external regions. In the following analyses we consider the objects at redshift  $z = 0$ .

To compute the surface brightness profiles, we adopted the same volume-selection scheme of the density and temperature profiles with the only difference

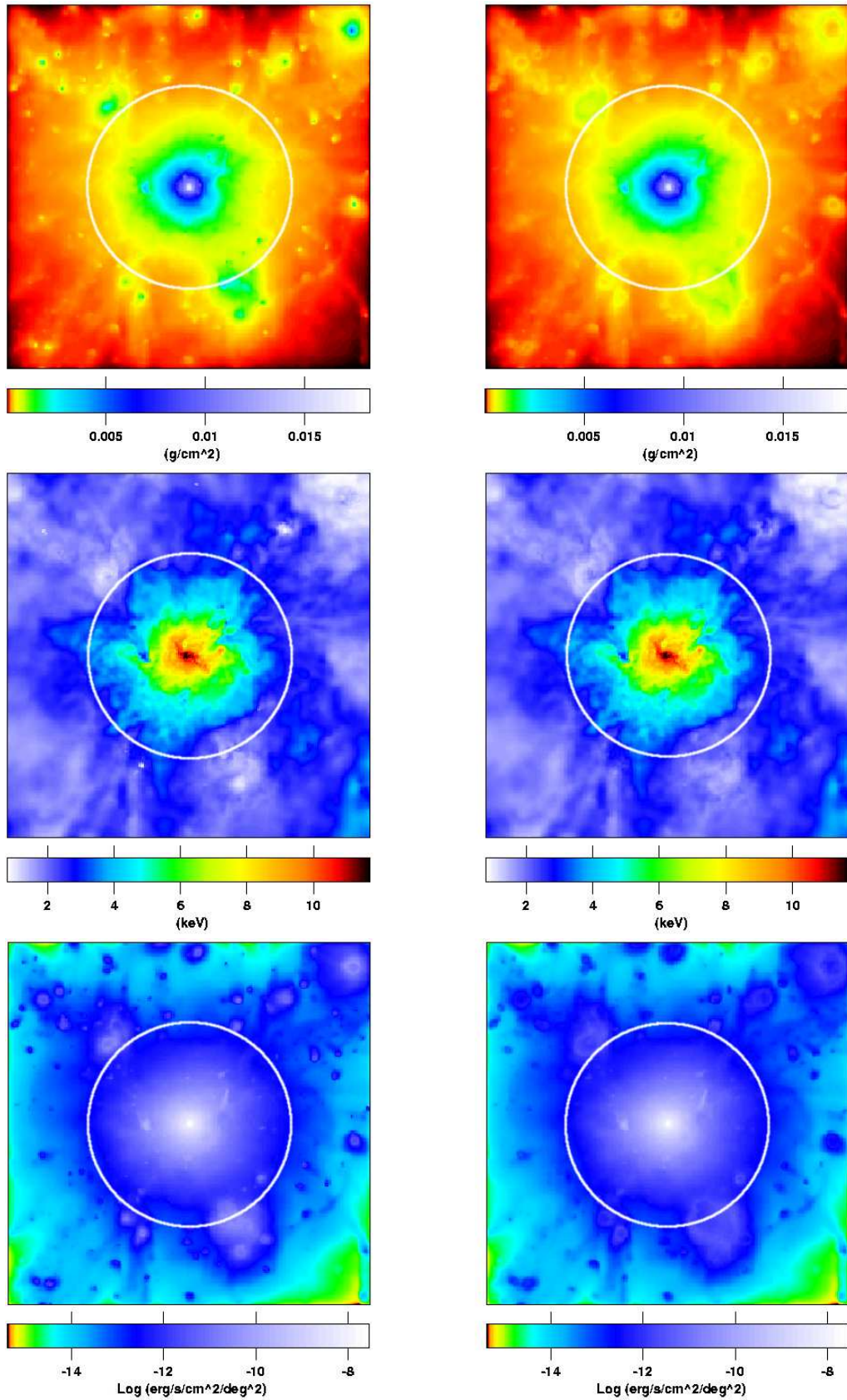


**Figure 6.1.** From top to bottom: maps of the projected gas density, mass-weighted temperature and soft (0.5–2 keV) X-ray emission of the *g1* cluster (*csf* model) for the 100 per cent (left) and 95 per cent (right) volume-selection scheme. The circles indicate the virial radius. The size of the side of each map is 12 Mpc, so they cover roughly up to  $2.5R_{200}$ .

that, since we want to obtain the surface brightness profiles of our objects, we need to take into account the two-dimensional projection on the sky plane. To this purpose, we consider circular ring sections instead of spherical shells: for every ring, we select all the particles that fill a given volume fraction  $f$ , we calculate their luminosity and we obtain  $L_f$  by summing all of them. Finally we normalize it to take into account also for the remaining volume and use the normalized luminosity  $L_{\text{ring}} = L_f/f$  to calculate the surface brightness (see the effects of this method on the 0.5–2 keV X-ray surface brightness shown in the bottom panel of Fig. 6.1).

We checked that this method works efficiently for subtracting almost all the relevant substructures in the surface brightness profiles, except for two massive subhaloes present in the *g1* cluster simulation at a distance of  $(2-3) \times R_{200}$  from the center; only for this cluster we excluded two separate angular regions (45 degrees wide each) from the computation of its X-ray surface brightness profiles.

In Fig. 6.2, we show the gas density, temperature and surface brightness profiles into two different bands for a massive cluster (*g1*) assuming two different physical models: the “ordinary-viscosity non-radiative” (*ovisc*) and the “cooling + star formation + feedback” (*csf*) one. We plot the average profiles together with the ones obtained with different cuts in volume. The profiles in Fig. 6.2 show that eliminating the fraction of mass concentrated in 1 per cent of the volume is sufficient to make the gas density, temperature and surface brightness profiles much more regular than the average ones that consider all the particles in the shell. For these reasons in the following analyses, we will mainly concentrate in fitting the 99 per cent–volume profiles and discuss the results obtained by cutting the volume at different percentages in Section 6.4. By the way we also note that the temperature and density profiles obtained with this method for the *ovisc* model well reproduce the shape of the theoretical profiles obtained by Ascasibar et al. (2006), if we assume a polytropic index  $\gamma \simeq 1.18 - 1.20$ .

In Fig. 6.3 we compare the 99 per cent volume profiles for one of the largest and the smallest cluster of the samples using the four different physical models. As already noted in Borgani et al. (2004), radiative cooling and star formation selectively remove low-entropy gas from high-density regions. Consequently models with cooling tend to produce clusters less dense at the centre ( $r < 0.1R_{200}$ ): in these regions we find that the gas density in non-radiative models is higher by a factor of  $\sim 3.5$  in the most massive clusters and more than 5 in less massive ones. The same cooling processes generate a lack of pressure near the centre of the clusters that heats the infalling gas up to a factor of  $\sim 1.8$  higher than in non-radiative simulations for all mass scales (see also Tornatore et al., 2003). As a result, the X-ray emission in the internal regions is significantly reduced in the *csf* and *csfc* models.

The external regions of the clusters are less affected by the different physics because the low-density gas is less prone to cooling and feedback effects. As we will show later, this makes the results on the external regions of clusters only slightly dependent on the physical model adopted in the simulation (see also Romeo et al., 2006, for influences of other physical processes).

In Fig. 6.4 we compare the 99 per cent volume profiles for the 4 most massive

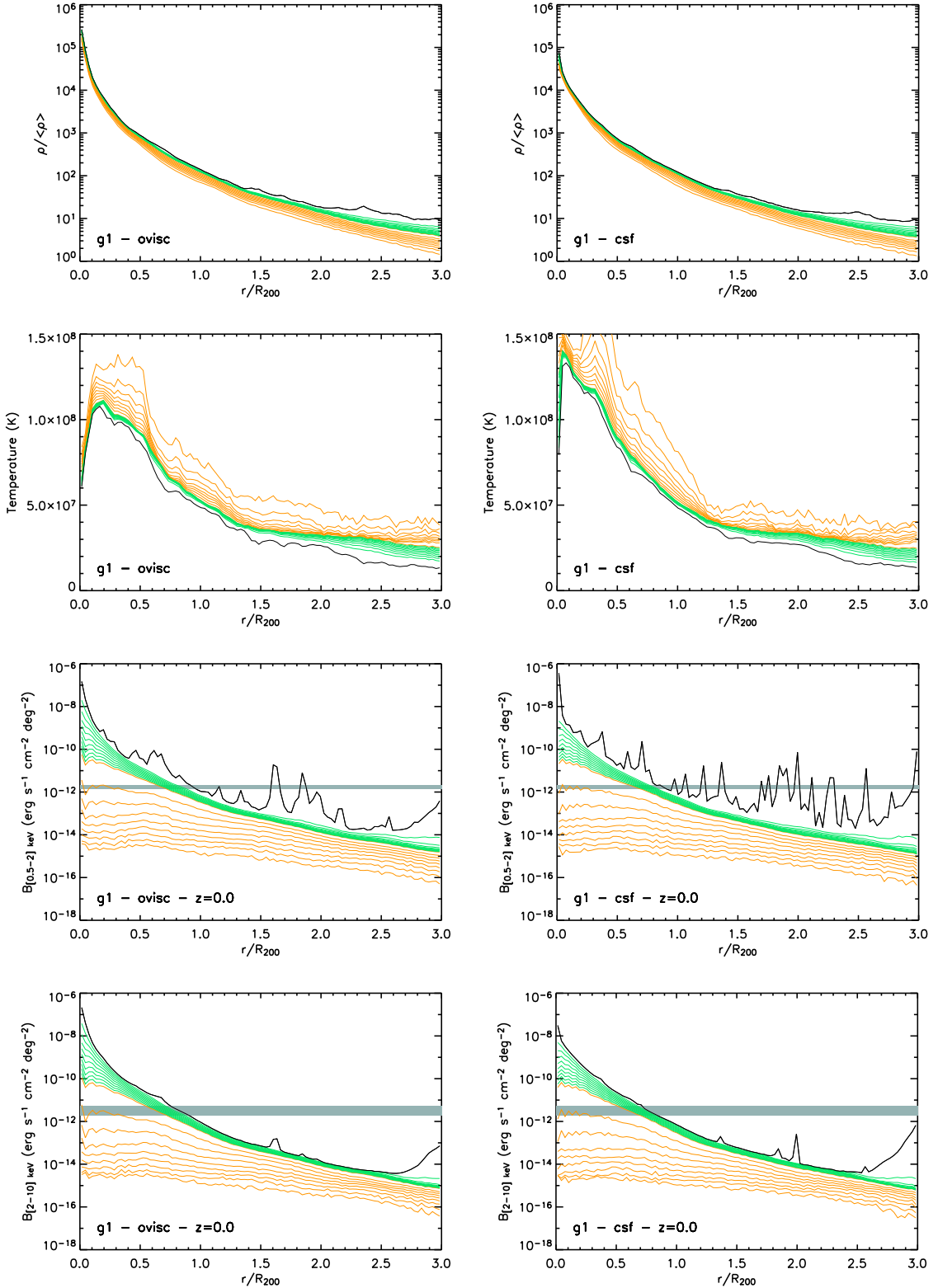


**Figure 6.2.** Radial profiles for different quantities as estimated for the *g1* cluster. From top to bottom: gas density (normalized to the cosmic mean density,  $\langle \rho \rangle \equiv \Omega_b \rho_c$ ), mass-weighted temperature and X-ray surface brightness for the soft (0.5–2 keV) and the hard (2–10 keV) band calculated considering the clusters at  $z = 0$ . Left column: *ovisc* model. Right column: *csf* model. These profiles are obtained from different prescriptions: the black line shows the average of all the gas particles, the orange lines are averages of the different volume percentages from 10 to 90 per cent and the green lines are from 91 to 99 per cent. The extragalactic unresolved background from Hickox & Markevitch (2006) in the 0.5–2 keV and 2–8 keV band is indicated by the shaded region in the soft and hard X-ray surface brightness panels, respectively.

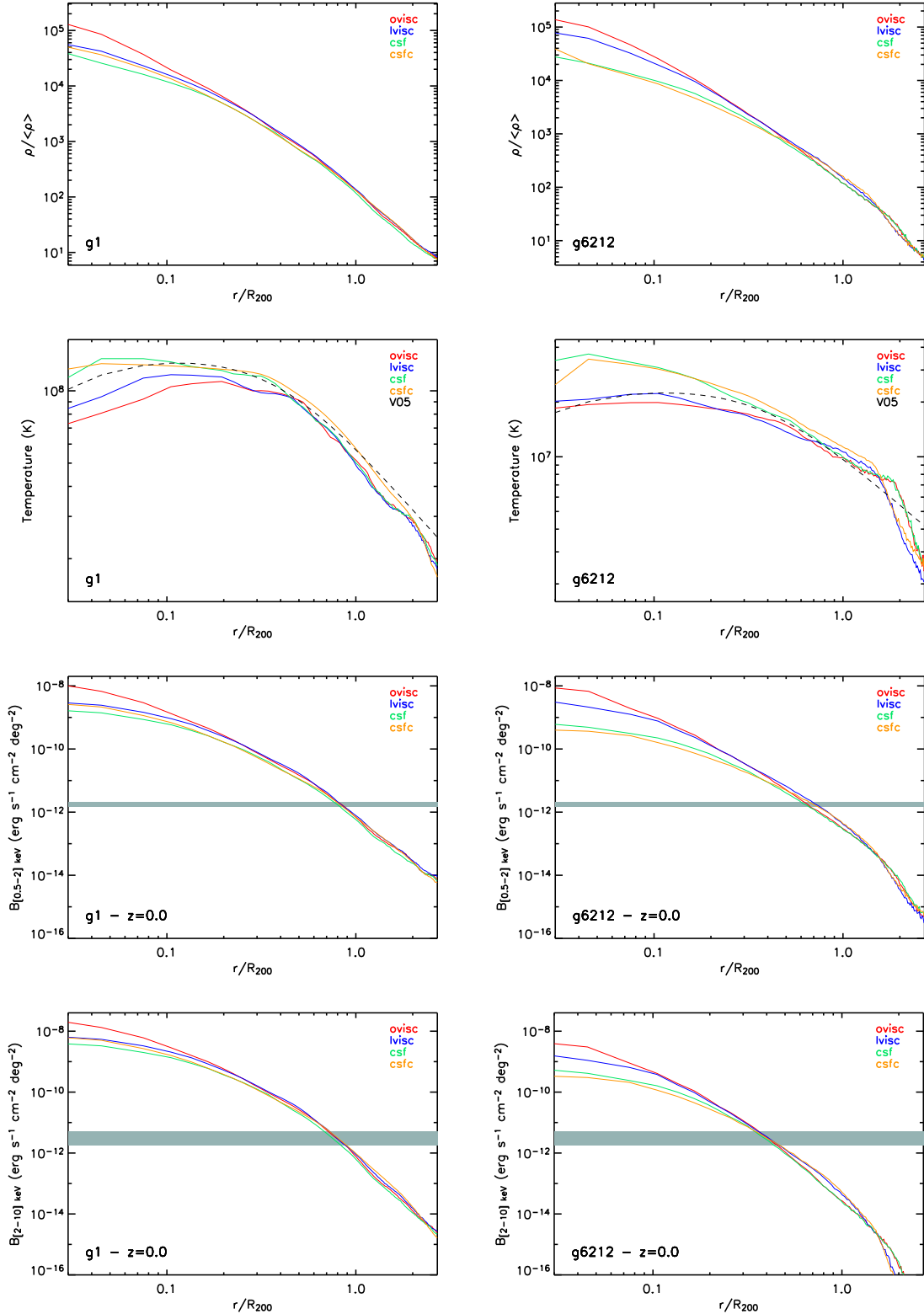


**Figure 6.3.** From top to bottom: comparison between the gas density (normalized to the cosmic mean density,  $\langle \rho \rangle \equiv \Omega_b \rho_c$ ), mass-weighted temperature, soft and hard X-ray surface brightness profiles extracted from the 99 per cent volume of the clusters *g1* (left column) and *g6212* (right column) simulated by using 4 different physical models. A dashed line indicates the functional form from Vikhlinin et al. (2006, eq. 9) that well reproduces the behaviour of the temperature profile of nearby bright galaxy clusters observed with *Chandra*. The functional form is normalized to the average values of the temperature obtained from the 4 models at  $0.5R_{200}$ . The extragalactic unresolved background from Hickox & Markevitch (2006) in the 0.5–2 keV and 2–8 keV band is indicated by the shaded region in the soft and hard X-ray surface brightness panels, respectively.

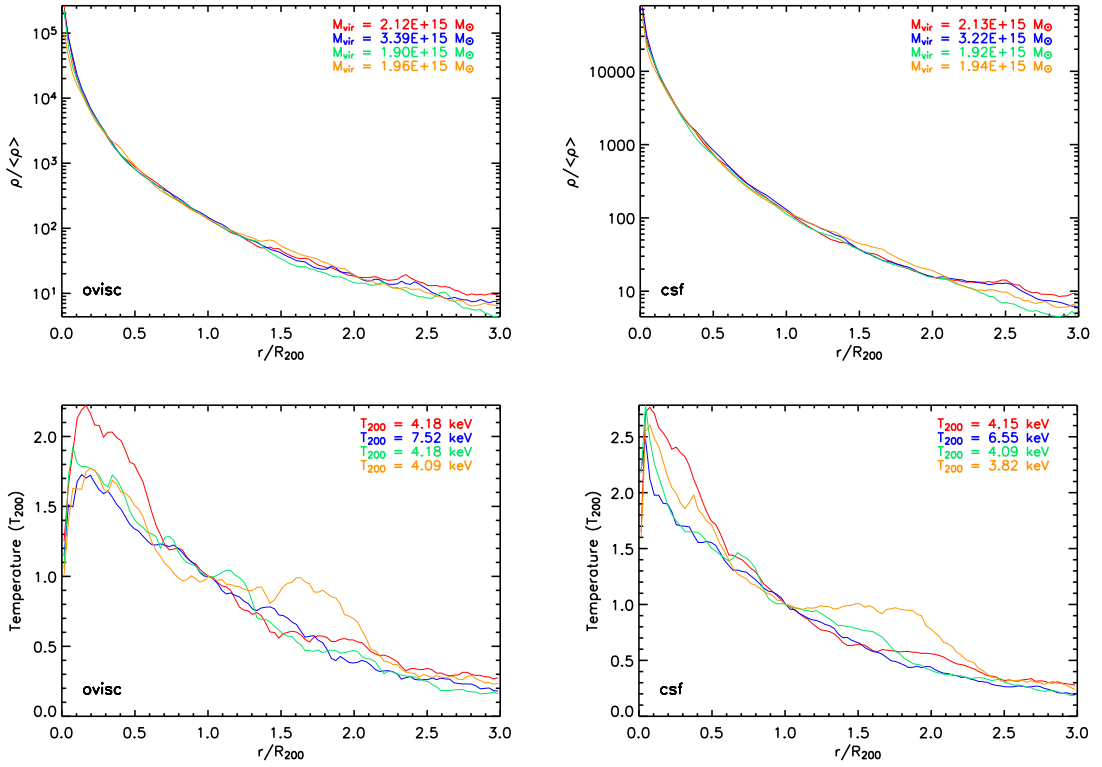


**Figure 6.4.** Comparison between the 99 per cent volume profiles of density (normalized to the cosmic mean density,  $\langle \rho \rangle \equiv \Omega_b \rho_c$ ) (top panels) and mass-weighted temperature normalized to  $T_{200}$  (lower panels) for the clusters *g1* (red), *g8* (blue), *g51* (green), *g72* (orange). Left and right columns refer to the *ovisc* and *csf* model, respectively.

clusters of the dataset (sample A). The density profiles have a very similar shape up to about  $2R_{200}$  indicating a universal function. The regularity of the 99 per cent volume profiles extends also for distances greater than  $3R_{200}$ . The temperature profiles are more irregular (note that the temperatures are normalized using  $T_{200}$ , the temperature at  $R_{200}$ ): the bumps present in the *g1* profile near the centre and in *g72* at  $r \sim 1.7R_{200}$  are an effect of shocks at  $r \sim 0.6R_{200}$  and  $r \sim 2.1R_{200}$ , respectively, due to recent major mergers.

In Table 6.2 we show the ratios between the values of the 99 per cent volume profiles at different radial distances and their values at  $0.3R_{vir}$  obtained with the *ovisc* model. The regularity of these profiles can be seen by the low dispersion between the values of the clusters of the same sample.

**Table 6.2.** Ratios between the profile values at different radial distances and their values at  $0.3R_{200}$ . We show the average and the standard deviation between the two cluster samples for the *ovisc* model.

	Radial distance ( $R_{200}$ )				
	0.5	0.7	1.0	2.0	3.0
SAMPLE A					
$\rho$	$0.31\pm 0.02$	$0.127\pm 0.004$	$0.048\pm 0.002$	$(5.6\pm 0.8)\times 10^{-3}$	$(1.7\pm 0.5)\times 10^{-3}$
$T$	$0.88\pm 0.06$	$0.72\pm 0.06$	$0.60\pm 0.06$	$0.34\pm 0.09$	$0.16\pm 0.03$
$SB_{\text{soft}}$	$0.17\pm 0.03$	$0.040\pm 0.011$	$(8.4\pm 1.2)\times 10^{-3}$	$(2.3\pm 0.9)\times 10^{-4}$	$(6.3\pm 4.3)\times 10^{-5}$
$SB_{\text{hard}}$	$0.15\pm 0.02$	$0.032\pm 0.001$	$(5.5\pm 0.1)\times 10^{-3}$	$(7.1\pm 1.8)\times 10^{-5}$	$(6.4\pm 5.7)\times 10^{-6}$
SAMPLE B					
$\rho$	$0.31\pm 0.02$	$0.13\pm 0.02$	$0.048\pm 0.007$	$(6.0\pm 0.2)\times 10^{-3}$	$(1.6\pm 0.2)\times 10^{-3}$
$T$	$0.84\pm 0.04$	$0.72\pm 0.04$	$0.58\pm 0.03$	$0.29\pm 0.06$	$0.14\pm 0.02$
$SB_{\text{soft}}$	$0.16\pm 0.02$	$0.042\pm 0.011$	$(7.9\pm 1.0)\times 10^{-3}$	$(1.8\pm 0.9)\times 10^{-4}$	$(1.5\pm 1.0)\times 10^{-5}$
$SB_{\text{hard}}$	$0.11\pm 0.01$	$0.021\pm 0.007$	$(2.3\pm 0.4)\times 10^{-3}$	$(1.7\pm 1.4)\times 10^{-5}$	$(5.6\pm 7.2)\times 10^{-7}$

### 6.3 Results on the outer slopes of the radial profiles

To describe the behaviour of the radial density and temperature profiles in the cluster outskirts, we adopt a broken power-law relation given by the expression

$$y(x) = \begin{cases} ax^{-b_1} & \text{if } x \leq R_b/R_{200} \\ a \left(\frac{R_b}{R_{200}}\right)^{-(b_1-b_2)} x^{-b_2} & \text{if } x > R_b/R_{200} \end{cases}, \quad (6.1)$$

in its *logarithmic* form, where  $r$  is the distance from the centre,  $x \equiv r/R_{200}$  and  $a$ ,  $b_1$ ,  $b_2$  and  $R_b$  are the free parameters, representing the normalization, the inner slope, the outer slope and the radius at which the slope changes, respectively. The fit is computed in the interval  $0.3 \leq x \leq 2.7$ . We fit the profiles for the 9 clusters separately and then calculate the average and dispersion for every parameter. The best fit relations for the *ovisc* model are shown together with the profiles of single clusters in Fig. 6.5.

The gas density profiles show a change in the slope of the power law at about  $(1.1-1.3)\times R_{200}$ , with an internal slope of 2.4-2.5 with no significant dependence on the physical model or the volume selection

scheme adopted (see Section 6.4 for details on the effect of different volume cuts) and also a very low dispersion between the different objects. This indicates that the behaviour of the density profiles is well determined from outside the core to more than  $R_{200}$ .

In the outskirts the slope increases up to  $b_2 \sim 3.4$  for all the models showing more dispersion between the 9 haloes due to the fact that in these regions the influence of the environment is becoming more important with respect to the potential well of the cluster itself.

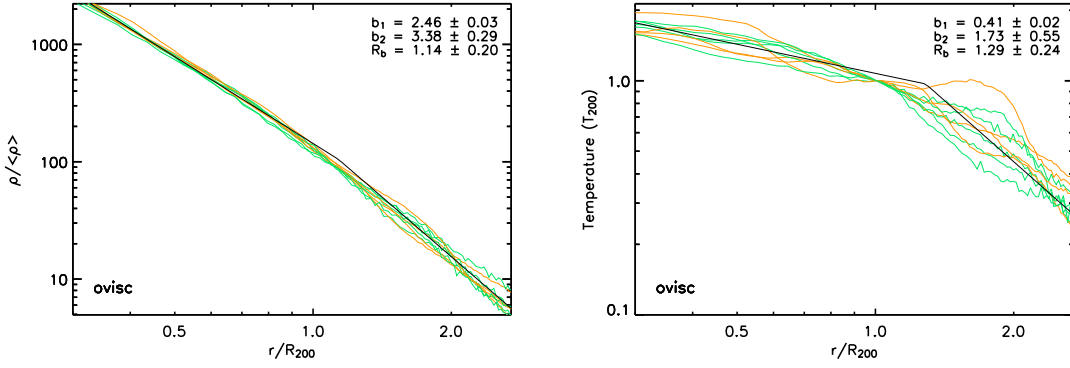


**Figure 6.5.** Profiles (99 per cent volume) of the 9 clusters obtained with the *ovisc* model. The orange lines are for the 4 clusters of sample A, the green lines are for the 5 groups of sample B. We fit the data with a broken power-law relation of equation (6.1) in the interval  $0.3 \leq r/R_{200} \leq 2.7$  and plot (black line) the relation assuming the average of the best-fit parameters between the 9 objects.

In the temperature profiles, the steepening towards the external regions is more prominent and the cutoff is around  $r = 1.3\text{--}1.5 R_{200}$  with significant dispersion between the clusters. The best fit internal slope is significantly

affected by the physics: the profiles obtained with non-radiative simulations have slopes of  $b_1 \sim 0.4$  while *csf* and *csfc* models produce steeper profiles with slopes of  $b_1 \sim 0.6$ .

Also in the outskirts the non-radiative models tend to produce slightly shallower profiles with the difference less significant due to the higher dispersion between the different haloes. The different slopes of the profiles is an effect of the cooling that creates an higher gradient of temperature as can be seen in Fig. 6.3.

In Fig. 6.2, we also show the soft (0.5–2 keV) and hard (2–10 keV) X-ray surface brightness profiles of the *g1* object for the different physical models. These plots indicate that models with cooling produce a higher number of clumps that dominate the soft X-ray emission in the external regions. These clumps are indeed those that are well eliminated by our selection in volume.

We also obtain that the cluster surface brightness at  $z = 0$  reaches the value of the unresolved X-ray background estimated by Hickox & Markevitch (2006) of  $1.76 \pm 0.32$  in the 0.5–2 keV band and  $3.5 \pm 1.7$  in the 2–8 keV band in units of  $10^{-12}$  erg s $^{-1}$  cm $^{-2}$  deg $^{-2}$ , at approximately  $0.8R_{200}$  and  $0.4R_{200}$  in the soft and hard band, respectively; considering the effect of redshift dimming and that, considering the results presented in Chapter 4, a significant fraction of this background can be due to the diffuse gas of non-virialized objects, the perspective of observing the regions around the clusters virial radius is extremely challenging.

Since we observe a steepening of the slope of the X-ray profiles going to the external regions, we fit them with a rolling-index power law function

$$y = ax^{-b_{\max} \frac{x+b_{\min}/b_{\max}}{x+1}}, \quad (6.2)$$

where  $x \equiv r/R_{200}$ , and  $a$ ,  $b_{\min}$  and  $b_{\max}$  are the free parameters, with  $b_{\min}$  and  $b_{\max}$

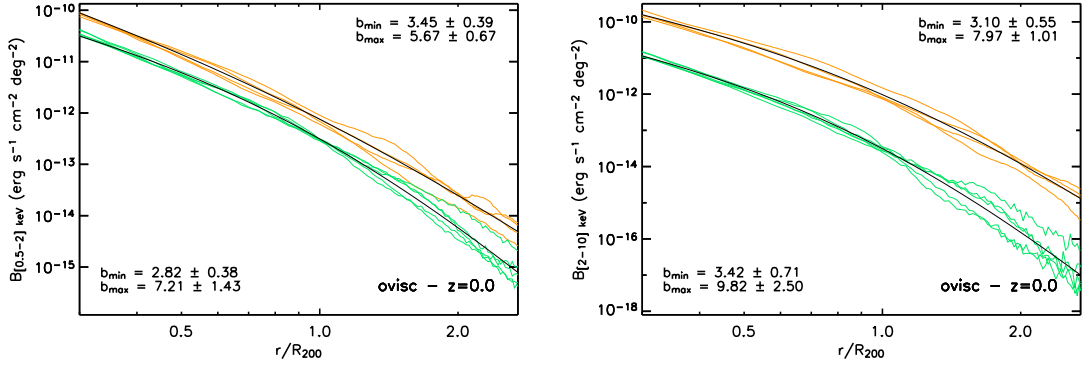


**Figure 6.6.** X-ray surface brightness profiles (99 per cent volume, 0.5–2 and 2–10 keV band) of the 9 clusters for the *ovisc* model. The orange lines are for the 4 clusters of sample A, the green lines are for the 5 groups of sample B. We fit the data of the two samples separately with a rolling-index power-law relation of equation (6.2) in the interval  $0.3 \leq r/R_{200} \leq 2.7$  and plot (black lines) the relations assuming the average of the best-fit parameters between the objects of the samples.

representing the slope in the two asymptotic cases,  $x \rightarrow 0$  and  $x \gg 1$ , respectively. We fit the two samples separately in the interval  $0.3 \leq r/R_{200} \leq 2.7$ . The results for the 4 physical models are quoted in Tab. 6.3. The average best-fit values on the slopes of the surface brightness of the objects simulated with the *ovisc* model are shown in Fig. 6.6.

Overall, the fits well reproduce the shape of the surface brightness in the interval  $0.3 \leq r/R_{200} \leq 2.7$ . Our sample of galaxy “groups” (sample B) presents a soft X-ray profile that is (i) shallower in the centre ( $b_{\min,B} \sim 2.7$ ,  $b_{\min,A} \sim 3.4$ ) and (ii) steeper in the outskirts ( $b_{\max,B} \sim 7.3$ ,  $b_{\max,A} \sim 5.5$ ) than the one estimated in the sample of massive clusters (sample A). The following reasons can be considered to explain this behaviour: (i) the ICM temperature of the objects in sample B at  $R_{200}$  is below 1 keV (see Table 6.1) and decreases at  $r > R_{200}$  to values that becomes comparable to (and less than) the lower end of the 0.5–2 keV band here considered, resulting in a cut-off of the soft X-ray signal. This also explains the steeper slope of the hard X-ray profiles in the less massive objects; (ii) the higher cooling efficiency in groups, with respect to rich clusters, enhances the selective removal of low-entropy gas from the hot phase, thus producing shallower profiles of X-ray emitting gas; (iii) as discussed at the end of Section 6.2, while our clusters are the most massive objects in the volume of the parent simulation and are still accreting material, the “groups” appear to be isolated, thus with less evidence of recent accretion activity. This results in slightly shallower profiles near the centre.

### 6.3.1 Comparison with observational constraints

Our results on the external shape of the gas density, temperature and surface brightness profiles in simulated galaxy clusters can be compared with recent estimates obtained for nearby X-ray bright objects. Neumann (2005) discusses the outer slope of the soft X-ray surface brightness in 14 clusters observed with *ROSAT/PSPC*. In order to compare our results with the ones of that work, we fit the

**Table 6.3.** Distribution of the best-fit values of the rolling-index power-law functions (see equation 6.2) of the soft (0.5–2 keV) and hard (2–10 keV) X-ray surface brightness profiles separated between the two samples *A* and *B* and for different physical models. The profiles are extracted from the 99 per cent volume-selection scheme and fitted over the radial range  $0.3 \leq r/R_{200} \leq 2.7$ .

SOFT X-RAY BAND (0.5–2 keV)				
	Sample A		Sample B	
	$b_{\min}$	$b_{\max}$	$b_{\min}$	$b_{\max}$
<i>ovisc</i>	$3.45 \pm 0.39$	$5.67 \pm 0.67$	$2.82 \pm 0.38$	$7.21 \pm 1.43$
<i>lvisc</i>	$3.36 \pm 0.33$	$5.73 \pm 0.80$	$2.73 \pm 0.79$	$7.72 \pm 1.93$
<i>csf</i>	$3.49 \pm 0.21$	$5.33 \pm 0.57$	$2.50 \pm 0.28$	$7.14 \pm 1.14$
<i>csfc</i>	$2.76 \pm 0.28$	$6.36 \pm 1.09$	$1.99 \pm 0.50$	$7.80 \pm 1.76$
HARD X-RAY BAND (2–10 keV)				
	Sample A		Sample B	
	$b_{\min}$	$b_{\max}$	$b_{\min}$	$b_{\max}$
<i>ovisc</i>	$3.10 \pm 0.55$	$7.97 \pm 1.01$	$3.42 \pm 0.71$	$9.82 \pm 2.50$
<i>lvisc</i>	$3.08 \pm 0.29$	$7.87 \pm 0.90$	$3.36 \pm 1.72$	$10.48 \pm 5.26$
<i>csf</i>	$3.25 \pm 0.41$	$7.56 \pm 0.73$	$3.25 \pm 0.43$	$9.69 \pm 2.66$
<i>csfc</i>	$1.94 \pm 0.36$	$9.31 \pm 2.11$	$2.87 \pm 1.71$	$10.95 \pm 5.79$

99 per cent volume X-ray profiles in different intervals for the two clusters samples with a single power-law function,  $S(x) = ax^{-b}$ , where  $a$  and  $b$  are the two free parameters and  $x \equiv r/R_{200}$ . We avoid to consider the interval  $0.1 \leq x \leq 0.3$ , owing to the fact that this region is very model-dependent and cannot be represented by a single power-law relation.

Our results are listed in Table 6.4 together with the corresponding results ( $b_{\text{obs}}$ ) of Neumann (2005). In the interval  $0.3 \leq x \leq 1.2$ , for the sample of clusters labeled "4" that better matches the virial temperatures of our sample *A*, Neumann (2005) measures a slope of  $3.79 \pm 0.38$  in good agreement with our average values of (3.78, 4.03), being the lower values measured in objects simulated with the inclusion of extra-physics (models *csf* and *csfc*).

In the interval  $0.7 \leq x \leq 1.2$ , the observational constraints are looser and are between  $5.73^{+1.43}_{-1.26}$  for the 7 most massive clusters in the Neumann's sample and  $7.22^{+1.79}_{-1.60}$  for the whole dataset. Our constraint of  $\approx 4.3$ - $4.5$  lays on the lower end of this distribution, but still just  $1\sigma$  away from the results obtained for the hottest sample. The sample *B* shows profiles with mean slopes consistent with those obtained in sample *A* within the measured dispersion (see Table 6.4).

For what concerns the temperature profile, a comparison can be done with the functional form that reproduces the behaviour of the deprojected X-ray temperature profile at  $r \gtrsim 0.05R_{200}$  of 13 low-redshift clusters observed with *Chandra* as

**Table 6.4.** Distribution of the best-fit values of the power-law slopes of the X-ray surface brightness profiles separated between the two samples *A* and *B* ( $b_A$  and  $b_B$ , respectively), the two X-ray bands and different physical models. The profiles extracted from the 99 per cent volume-selection scheme and fitted over the different radial ranges  $x_{\min} - x_{\max}$  (in units of  $R_{200}$ .) Values of  $b_{\text{obs}}$  are the observational constraints in the same radial range from Neumann (2005) (see text in Section 6.3.1).

		SOFT X-RAY BAND (0.5–2 keV)			HARD X-RAY BAND (2–10 keV)	
	$x_{\min} - x_{\max}$	$b_A$	$b_B$	$b_{\text{obs}}$	$b_A$	$b_B$
<i>ovisc</i>	0.3 – 1.2	4.05±0.03	4.09±0.01	3.79±0.38	4.46±0.05	5.23±0.03
<i>lvisc</i>	0.3 – 1.2	4.04±0.04	4.14±0.09		4.47±0.05	5.32±0.17
<i>csf</i>	0.3 – 1.2	3.99±0.00	3.81±0.02		4.50±0.02	5.07±0.04
<i>csfc</i>	0.3 – 1.2	3.79±0.02	3.57±0.04		4.19±0.03	5.03±0.12
<i>ovisc</i>	0.7 – 1.2	4.49±0.19	4.76±0.32	5.73 <sup>+1.43</sup> <sub>-1.26</sub>	5.15±0.41	6.42±0.76
<i>lvisc</i>	0.7 – 1.2	4.54±0.32	4.66±0.19		5.26±0.44	6.20±0.75
<i>csf</i>	0.7 – 1.2	4.31±0.28	4.45±0.11		5.18±0.37	5.92±0.13
<i>csfc</i>	0.7 – 1.2	4.29±0.17	4.35±0.14		4.89±0.24	6.42±0.61
<i>ovisc</i>	1.2 – 2.7	5.15±0.62	6.37±0.93		6.95±0.88	8.43±1.70
<i>lvisc</i>	1.2 – 2.7	5.21±0.59	6.77±0.95		6.88±0.54	9.01±2.72
<i>csf</i>	1.2 – 2.7	4.90±0.53	6.23±0.67		6.70±0.74	8.40±1.52
<i>csfc</i>	1.2 – 2.7	5.67±0.63	6.58±0.88		8.14±1.32	9.14±3.36

presented in Vikhlinin et al. (2006, see their equation 9):

$$T(d) \propto \frac{(d/0.045)^{1.9} + 0.45}{(d/0.045)^{1.9} + 1} \cdot \frac{1}{(1 + (d/0.6)^2)^{0.45}}, \quad (6.3)$$

where  $d \equiv r/R_{500}$ . We overplot this function normalized to the average temperature value at  $0.5R_{200}$  to our profiles in Fig. 6.3.

While it is known that in general hydrodynamical simulations cannot reproduce the steepening of the observed temperature profiles at the centre (see Borgani et al., 2004, 2006, for more detail), we can see that the agreement in the external regions is good for the most massive clusters, as already noted by Markevitch et al. (1998) and De Grandi & Molendi (2002).

The non-radiative models show a good agreement with this form, so that when we normalize the function at  $0.5R_{200}$  the difference between the values quoted in Table 6.2 is less than  $1\sigma$  up to  $2R_{200}$  for both clusters and groups. We only find small deviations from the observed profile that become more significant at  $r < 0.3R_{200}$  for simulations including cooling and at  $r > R_{200}$  where non-thermalized accreting material is dominant. The latter effect is particularly evident in low-mass systems.

### 6.3.2 Implications on X-ray properties of the cluster virial regions

Using our profiles we can predict the steepness of the profiles in the external regions of galaxy clusters. We fit the soft (0.5–2 keV) and hard (2–10 keV) X-ray profiles also in the interval  $1.2 \leq r/R_{200} \leq 2.7$ . The results are shown in Table 6.4. Our

**Table 6.5.** Best-fit results for the inner slope  $b_1$ , outer slope  $b_2$  and break radius  $R_b$  of the gas density profiles fitted with the broken power-law relation of equation (6.1). The profiles are computed considering different cuts in volume, from 50 to 100 per cent.

Model	VOLUME CUT					
	50%	80%	90%	95%	99%	100%
$b_1$						
<i>ovisc</i>	2.47±0.03	2.50±0.03	2.50±0.03	2.47±0.03	2.46±0.03	2.55±0.02
<i>csf</i>	2.42±0.02	2.45±0.01	2.43±0.02	2.37±0.02	2.46±0.03	2.48±0.03
$b_2$						
<i>ovisc</i>	3.86±0.55	3.78±0.43	3.71±0.39	3.60±0.37	3.38±0.29	3.12±0.32
<i>csf</i>	3.85±0.45	3.76±0.37	3.66±0.33	3.53±0.32	3.41±0.19	2.98±0.38
$R_b/R_{200}$						
<i>ovisc</i>	1.12±0.14	1.20±0.14	1.20±0.15	1.14±0.15	1.14±0.20	1.23±0.14
<i>csf</i>	1.15±0.14	1.24±0.12	1.23±0.13	1.10±0.16	1.31±0.28	1.34±0.15

profiles are steeper in the external regions for all the models and for both the cluster samples: the steepening is more evident in sample *B* suggesting a break of self-similarity at the scales around  $2R_{200}$ . As already noted at the end of Section 6.3, this is mainly due to the fact that the temperature in the external regions of the haloes of sample *B* drops below 0.5 keV resulting in a cutoff of the soft X-ray signal. From the fit with a rolling power-law, the values of  $b_{\max}$  can be associated to the asymptotic behaviour at  $r \gg R_{200}$ . We measure a slope of the surface brightness that ranges from about  $\sim 7.5$  in groups to  $\sim 5.8$  in clusters. In terms of the  $\beta$  value of the  $\beta$ -model (e.g. Cavaliere & Fusco-Femiano, 1978),  $\beta \approx (1 + b_{\max})/6$ , it approaches an estimate between 1.4 in groups and 1.1 in clusters, the latter being a 40 per cent steeper than the observed values at  $\sim R_{200}$  (Vikhlinin et al., 1999; Neumann, 2005).

## 6.4 Effects of volume cutting in density and temperature profiles

In this section we will briefly discuss the effects of the volume-selection scheme adopted for the work presented in this Chapter. We show in Table 6.5 and 6.6 the results for the fits of the density and temperature profiles calculated with different cuts in volume using a broken power-law function of equation (6.1) in the logarithmic form.

For the density profiles the internal slope does not depend much on the physics or the volume cutting scheme adopted: this shows that our method does not introduce any bias to the results of density for the internal regions of clusters.

The external slope for the density profiles does not show any significant dependence on the physics but it decreases regularly when we include more and

**Table 6.6.** Best-fit results for the inner slope  $b_1$ , outer slope  $b_2$  and break radius  $R_b$  of the mass-weighted temperature profiles fitted with the broken power-law relation of equation (6.1). The profiles are computed considering different cuts in volume, from 50 to 100 per cent.

Model	VOLUME CUT					
	50%	80%	90%	95%	99%	100%
$b_1$						
<i>ovisc</i>	0.43±0.03	0.43±0.02	0.47±0.02	0.48±0.02	0.41±0.02	0.54±0.03
<i>csf</i>	0.47±0.05	0.55±0.02	0.55±0.02	0.55±0.02	0.57±0.02	0.59±0.02
$b_2$						
<i>ovisc</i>	1.30±0.63	1.22±0.53	1.31±0.54	1.49±0.51	1.73±0.55	2.15±0.65
<i>csf</i>	1.35±0.67	1.38±0.51	1.46±0.47	1.62±0.49	1.90±0.46	2.07±0.64
$R_b/R_{200}$						
<i>ovisc</i>	1.21±0.24	1.19±0.25	1.33±0.21	1.40±0.17	1.29±0.24	1.49±0.18
<i>csf</i>	1.20±0.24	1.44±0.22	1.46±0.20	1.48±0.18	1.56±0.18	1.50±0.17

more cool and diffuse gas: this indicates that to obtain a fair representation of the cluster temperature in the outskirts it is necessary to consider the 99 per cent volume profiles.

If we include all the gas particles the value of  $b_2$  continues to go down, but the profiles begin to show features due to the cold and gas and the  $\chi^2$  of the fit increases. For this reason and since the 99 per cent profiles show a remarkable regularity, as already said in the comments to Fig. 6.2, we can assume these as representative of the global cluster properties, although there may be some small systematic uncertainties due to our method.

As already discussed in Section 6.3, the presence of cooling in the simulations creates steeper temperature profiles at the centre, and this can be seen by the different values of  $b_1$  in Table 6.6. Again, like for the density profiles, the value of the internal slope is not influenced by the volume selection scheme.

On the contrary the values of  $b_2$  are much less affected by the physics but show an increasing trend when adding colder gas, considering also a significant scatter between the 9 clusters. The difference between the 99 and 100 per cent values for  $b_2$  is particularly evident with the *ovisc* model, but, again, given the higher values of the  $\chi^2$  and the regularity of the 99 per cent profiles, we can draw the same conclusions as for the density profiles.

## 6.5 Summary and conclusions

Using the *Hutt* hydrodynamical simulation set (described in Section 3.5.2), performed with the TREE-SPH code GADGET-2, composed of 9 galaxy clusters covering the mass range  $1.5 \times 10^{14} M_\odot < M_{\text{vir}} < 3.4 \times 10^{15} M_\odot$  and adopting 4 different

physical prescriptions with fixed metallicity, we have studied the behaviour in the outer regions of the gas density, temperature, soft (0.5–2 keV) and hard (2–10 keV) X-ray surface brightness profiles paying particular attention to the logarithmic slope.

Outside the central regions, where a not-well defined heating source can partially or totally balance the radiative processes, the physics of the X-ray emitting intracluster plasma is expected to be mainly driven by adiabatic compression and shocks that take place during the collapse of the cosmic baryons into accreting dark matter haloes. These processes are properly considered in cosmological numerical simulations here analysed, allowing us to investigate on solid basis the expected behaviour of the cluster outskirts.

Our main findings can be summarized as follows<sup>3</sup>:

- i* - the behaviour of the profiles in the external regions of clusters ( $r \gtrsim R_{200}$ ) does not depend significantly on the presence or absence of cooling and SN feedback. Only the inclusion of a model of thermal conduction can introduce non-negligible changes in the values of the slopes of the profiles. This shows that the mean behaviour of the X-ray emitting plasma in the cluster outskirts is mainly due to the gravitational force.
- ii* - The gas density profile steepens in the outskirts changing the slope of the power-law from  $\sim 2.5$  to  $\sim 3.4$  at about  $1.2R_{200}$ . The temperature profile varies the slope of the power-law like functional form from 0.4 in non-radiative models and 0.6 in models with cooling and feedback, to about (1.7-1.9) at  $(1.3-1.6) \times R_{200}$ .
- iii* - The surface brightness in the outskirts profiles appears to be dominated by the presence of subclumps of cold and dense material that we exclude from our analyses. After removing these objects, the surface brightness in the 0.5–2 keV band presents a profile with a slope that steepens towards the external regions. Fitting the profiles with a power-law function in different radial ranges between 0.3 and  $2.7R_{200}$  we obtain slopes between 4 and 5.5 in the 4 most massive systems and between 3.8 and 6.5 in the 5 objects with masses  $\approx 10^{14}M_{\odot}$ .
- iv* - We introduce a new rolling-index power-law functional (equation 6.2) which fits well the X-ray surface profiles in the interval  $0.3 \leq r/R_{200} \leq 2.7$ . From the results of these fits, we obtain that our sample of groups of galaxies (sample *B*) has soft X-ray profiles shallower in the centre ( $b_{\min,B} \sim 2.6$ ,  $b_{\min,A} \sim 3.3$ ) and steeper in the outskirts ( $b_{\max,B} \sim 7.4$ ,  $b_{\max,A} \sim 5.8$ ) than our sample of clusters (sample *A*). This is mainly an effect of the drop out from the pass band of the soft X-ray emission, due to the low ICM temperature of the objects in sample *B* at the virial radius.
- v* - We compare our results on the shape of the temperature and soft X-ray surface brightness profiles with the present observational constraints. By using the functional form of Vikhlinin et al. (2006) (eq. 9) extrapolated beyond  $R_{500}$ ,

---

<sup>3</sup>Note that, as in the rest of this Chapter, the values of the slopes here quoted are in fact negative slopes.

we verify that there is a good agreement with the simulated profiles over the radial range  $(0.3-2)\times R_{200}$ . On the surface brightness profile in the 0.5–2 keV band, we measure a slope in the outskirts that is consistent within  $1\sigma$  with the values estimated from *ROSAT/PSPC* data in Neumann (2005).

*vi* - From the overall shape of the simulated profiles, we predict that (see Table 6.2) (1) the ICM temperature profile decreases with radius reaching at  $R_{200}$  average values of 0.60 times the value measured at  $0.3R_{200}$ , (2) the estimated gas density at  $R_{200}$  is  $4.8\times 10^{-3}$  times the gas density measured at  $0.3R_{200}$ , (3) the surface brightness in the soft band is about  $10^{-12}$  erg s<sup>-1</sup> cm<sup>-2</sup> deg<sup>-2</sup> at  $R_{200}$  at  $z = 0$ , that is a factor of few below the extragalactic unresolved X-ray background (see Hickox & Markevitch, 2006).

This last item shows that the perspective to resolve the X-ray emission around the cluster virial regions is extremely challenging from an observational point of view, even at low redshift, unless tight constraints on all the components of the measured background can be reached (see also Molendi, 2004). Considering the similarity of the surface brightness profiles of the objects of the same mass, the observational technique of stacking the images of different clusters (e.g. Neumann, 2005) can help in enhancing the statistics of the profiles in the outer regions.

Overall, our results show how the study of simulated objects can give indications on the requested capabilities of future experiments in order to resolve the cluster virial regions. On the other hand, since the behaviour of the slopes have shown to be mainly independent of the physical models adopted in our simulations, any discrepancy between our results and observations of the clusters virial regions could provide useful hints on the presence of additional physics (e.g. turbulence, magnetic fields, cosmic rays) influencing the thermodynamics of the ICM.

Finally, the work presented in this chapter further demonstrates the complementarity between numerical and observational cosmology in describing the properties of highly non-linear and over dense structures.



## Chapter 7

# THE SUNYAEV-ZEL'DOVICH EFFECTS OF THE LOCAL SUPERCLUSTER

**A**lthough the thermal Sunyaev-Zel'dovich (tSZ) effect is expected to be several orders of magnitudes lower than the primary CMB anisotropies, presence of large structures in the Local Universe can cause significant deviations from the expected values of the power spectrum on the large angular scales. This process could explain the low multipoles anomalies present in CMB data. Using a constrained simulation of the Local Supercluster structure we investigate this possibility and we also study the detectability of the tSZ signal due to these structures with the future *Planck* survey. This chapter is mainly based on “*The imprints of local superclusters on the Sunyaev-Zel'dovich signals and their detectability with Planck*”, Dolag K., Hansen F. K., Roncarelli M., Moscardini L., 2005b, MNRAS, 363, 29.

### 7.1 The low multipoles of the CMB power spectrum and the Local Supercluster

As already said in Section 1.7.2 and in Section 5.1, high-accuracy measurements of the anisotropies of the cosmic microwave background (CMB) are extremely important for cosmology. In fact, by analysing their angular power spectrum,  $C_\ell$ , it is possible to obtain tight constraints on the mechanisms from which the primordial fluctuations originate and on the main cosmological parameters (or combinations of them), like the matter density, the baryonic density and the cosmological constant contribution. For this reason, the astronomical community has been doing a big effort over the last years in order to improve the quality of the CMB data, both in terms of accuracy and resolution.

The best available CMB measurements up to now were provided by the *Wilkinson Microwave Anisotropy Probe* satellite (WMAP; Spergel et al., 2003, 2006). The data obtained in its first three years of activity gave strong support to the so-called concordance model, i.e. a spatially flat universe dominated by dark energy and cold dark matter, with nearly scale-invariant primordial fluctuations, almost gaussianly distributed. The WMAP result is confirming the general picture emerging by the analysis of other different datasets, like high-redshift supernovae Ia, weak lensing, galaxy survey, Lyman- $\alpha$  forest and galaxy clusters.

The statistical analysis and the theoretical interpretation of CMB data of so high quality necessarily require a good understanding of all possible sources of contamination as well as the techniques to separate them from the CMB signal. The most important one is the Sunyaev-Zel'dovich (SZ) effect (refer to Section 5.2 for a brief description of its basic equations), mainly for its thermal (tSZ) component: recent studies allowed several detections of galaxy clusters with this effect (see also the discussion in Section 5.1). For what concerns the detection of the tSZ signal at larger scales, at present only upper limits are available (Diego et al., 2003; Hernández-Monteagudo et al., 2004; Hirata et al., 2004; Huffenberger et al., 2004; Hansen et al., 2005).

In this sense the situation will largely improve in the near future thanks to the capabilities of the *Planck* satellite, whose launch is planned for 2008. In fact the range of frequencies covered by its receivers will be very large, and the noise level is expected to be very low. This will allow to extract the SZ signal for at least 10,000 objects out to redshift  $z \approx 1$  (see, e.g. Bartelmann, 2001).

Despite giving a strong support to the “concordance”  $\Lambda$ CDM cosmology, the CMB data from the WMAP satellite exhibit several anomalies at the lowest multipoles. The most discussed among them is probably the abnormally low value (see the comments on Fig. 1.2) of the quadrupole amplitude (see, however, Efstathiou, 2004) and the fact that the directions of the quadrupole and octopole are unusually well aligned (see, e.g., Gaztañaga et al., 2003; de Oliveira-Costa et al., 2004). There have been some speculation about the possibility that the SZ signal from structures in the local Universe (LU), the so-called Local Supercluster(s), could be the cause of the low quadrupole (Abramo & Sodre, 2003). Further, the quadrupole and octopole directions happen to be pointing toward the Virgo cluster (de Oliveira-Costa et al., 2004), which opens the possibility of contamination from the LU.

The goal of the work presented in this chapter is to investigate the importance of the SZ effects, both thermal and kinetic (kSZ), produced by the local superclusters by comparing it with respect to the cosmological signal and to the contribution of more distant clusters. At this aim we use the results of the *Salacious* constrained simulation of the LU, described in Section 3.5.3, to extract full-sky maps of the two effects in order to discuss the statistical properties of low multipoles in terms of amplitude and alignment.

Moreover, taking advantage of the different set of physical processes treated in the simulations we can assess the uncertainties related to the modelization. Finally we will perform simulations to discuss if the local SZ signal can be detected exploiting the capabilities of the *Planck* satellite.

We present the work as follows. In Section 7.2 we describe the general characteristics of the constrained hydrodynamical simulations of the LU used in the following analysis. Section 7.3 presents our method to produce full-sky maps of the tSZ and kSZ effects. Section 7.4 is devoted to the results of our analysis. In particular we show the statistical properties of the maps in terms of angular power spectra and alignment of lower multipoles and we discuss the possibility of

detecting the local SZ signal with future experiments, like the upcoming *Planck* satellite. Finally we summarize our findings and draw the main conclusions in the final Section 7.5.

## 7.2 The constrained hydrodynamical simulations

We remand the reader to Section 3.5.3 for a detailed description of the *Salacious* constrained simulation. Here we focus on the description of the two different physical implementation used, starting from the same initial conditions, and on the properties of the halos identified in the simulations.

The physical model adopted for the first run, hereafter called *gas*, includes only non-radiative hydrodynamics and has been originally analysed by Dolag et al. (2005a) to study the propagation of cosmic rays in the LU. Hansen et al. (2005) used the gas properties extracted from this simulation to infer a prediction of the SZ effect from diffuse hot gas in the LU. In that paper, the PSCz catalogue was used to map the matter density whereas the simulation was used only to assign a temperature for the gas with a given density. The SZ map realized in this way was cross-correlated to the WMAP data and upper limits were found.

The second run, hereafter called *csf*, exploits all the capabilities of the present version of the GADGET-2 code (see Section 3.4), including cooling, star formation and feedback from SNe. Moreover also the modelization of metal production from the past history of cosmic star formation by Tornatore et al. (2004) was added. The feedback scheme for the *csf* run assumes a Salpeter IMF (Salpeter, 1955) and its parameters have been fixed to get a wind velocity of  $\approx 480$  km/s. In a typical massive cluster the SNe (II and Ia) add to the ICM a feedback of  $\approx 2$  keV per particle in an Hubble time (assuming a cosmological mixture of H and He);  $\approx 25$  per cent of this energy goes into winds. Note that these values can be considered an upper limit because a part of the ICM affected by the star processes could be at the present time out of the cluster virial radius. Moreover such feedback mechanisms cannot avoid the overcooling problem, commonly found in cosmological simulations: the corresponding overproduction of stars, acting mainly in the central regions, tends to amplify by a factor of  $\approx 2$  the effects of the star population. Notice that the metal-dependence of the cooling function does not significantly change the global feedback properties. Another signature that the feedback scheme is not enough efficient is the large amount of metals which is still locked inside the star particles: as a consequence, the resulting ICM metallicity is low, even if still compatible with observed values. A more detailed discussion of cluster properties and metal distribution within the ICM as resulting in simulations including the metal enrichment feedback scheme can be found in Tornatore et al. (2004).

In Table 7.1 we report the main characteristics of the most prominent clusters in our simulations. In particular, we computed the (mass-weighted) temperature within one tenth of the virial radius, and the central Compton  $y$ -parameter. In agreement with previous results in the literature (see, e.g., Tornatore et al., 2003)

**Table 7.1.** Comparison of the properties of the 6 most prominent clusters, listed in Column 1. The observed cluster temperatures  $T_{\text{obs}}$  (Column 2) are taken from Mohr et al. (1999), with the exception of the data for Virgo (Sanderson et al., 2003) and A3627 (Ikebe et al., 2002). Columns 3 and 5 refer to the mass-weighted temperature within  $0.1 \times R_{\text{vir}}$ , as computed in the *gas* and *csf* simulations ( $T_{\text{gas}}^{\text{MW}}$  and  $T_{\text{csf}}^{\text{MW}}$ , respectively). Columns 4 and 6 refer to the spectroscopic-like temperature (Mazzotta et al., 2004) within  $0.1 \times R_{\text{vir}}$ , as computed in the *gas* and *csf* simulations ( $T_{\text{gas}}^{\text{SL}}$  and  $T_{\text{csf}}^{\text{SL}}$ , respectively). In Column 7 we report the value for the Compton  $y$ -parameter, as obtained for Coma by Battistelli et al. (2003). Columns 8 and 9 refer to the values for  $y$  computed in the *gas* and *csf* simulations ( $y_{\text{gas}}$  and  $y_{\text{csf}}$ , respectively). For Coma we averaged the  $y$ -parameter within an area of 450 kpc to be compatible with the beam size of the observational data (Battistelli et al., 2003).

Cluster	Temperatures (keV)					$y$ -parameter ( $10^{-5}$ )		
	$T_{\text{obs}}$	$T_{\text{gas}}^{\text{MW}}$	$T_{\text{gas}}^{\text{SL}}$	$T_{\text{csf}}^{\text{MW}}$	$T_{\text{csf}}^{\text{SL}}$	$y_{\text{obs}}$	$y_{\text{gas}}$	$y_{\text{csf}}$
COMA	$8.21^{+0.16}_{-0.16}$	6.1	5.8	7.3	7.3	$9.6 \pm 1.1$	9.2	6.4
VIRGO	$2.55^{+0.07}_{-0.06}$	3.5	3.0	4.1	3.5		4.8	3.1
CENTAURUS	$3.54^{+0.08}_{-0.08}$	3.8	3.6	4.6	4.5		6.7	4.2
HYDRA	$3.10^{+0.11}_{-0.11}$	3.2	3.2	4.5	4.6		9.3	4.2
PERSEUS	$6.33^{+0.21}_{-0.18}$	5.8	5.2	6.1	5.8		9.5	6.8
A3627	$5.62^{+0.12}_{-0.11}$	3.7	3.6	4.4	4.4		6.6	4.2

and with what we already said in Chapter 6, we find that the temperatures for a given object in the *csf* simulation are always larger than in the *gas* simulation by a factor of approximately 15-20 per cent. Including radiative cooling causes in fact a lack of pressure support, with a subsequent heating of the infalling gas by adiabatic compression. The opposite trend is present for the central Compton  $y$ -parameter, which can be larger by a factor up to 2 in the *gas* simulation than in the *csf* one (see also White et al., 2002; da Silva et al., 2004; Motl et al., 2005).

For completeness, we also list the available observational estimates, which are in rough agreement. Notice that only for Coma we averaged in the simulation the value for the  $y$ -parameter within an area of 450 kpc to be compatible with the beam size of the observational data (Battistelli et al., 2003). Finally we would like to remark that the observed temperatures are not directly comparable with the simulation results, because they are extracted from X-ray spectroscopic data: as shown by Mazzotta et al. (2004) (see also Rasia et al., 2005; Vikhlinin, 2006), there could be a significant bias produced by the complexity of the thermal structure. In Table 7.1 we also added the values for the spectroscopic-like temperature  $T^{\text{SL}}$ , which approximates the spectroscopic temperature better than few per cent (Mazzotta et al., 2004).

### 7.3 Full-sky map making

The integration scheme adopted to compute the maps for this work follows the same strategy than the one described in Section 5.3 for the flat sky approximation. However, since we want to investigate the SZ properties at the lowest multipoles down to  $\ell = 2$ , in this case we need to create full-sky maps. Therefore the difference

is in the pixelization scheme and, consequently, in the distribution of the values associated to the particles into the different pixels.

In principle the integration has to be done over all particles, but in the case of a compact kernel where  $W(r/h)$  becomes null at large  $r/h$  (such as the one we use) it can be restricted to those particles having a distance from the line of sight smaller than their smoothing length.

In practice, however, one would like to obtain the value averaged over all lines of sight crossing the pixel, instead of the value along the line of sight crossing the centre of the pixel only. This can become a problem when the projected size of the structure producing the signal gets smaller than the pixel size. Therefore one usually applies the so-called *gather approximation*, where, given a pixel, all particles - whose projections either overlap or completely fall inside the pixel - are taken into account. In this case the value of the Compton  $y$ -parameter can be written as the sum of the contributions of all relevant particles as:

$$y_{\text{pix}} = \sum_j \frac{m_j}{\rho_j} y_j N_j \frac{A_{\text{pix}}}{A_j} W_{\text{int}}(\tilde{d}_j/h_j), \quad (7.1)$$

where  $\tilde{d}_j$  is the projected distance between the particle and the pixel centre and  $W_{\text{int}}$  is the kernel function described by equation (4.3) integrated along the line of sight. The area  $A_j$  associated to each gas particle can be approximated as the square of the cubic root of the corresponding volume, i.e.  $A_j = (m_j/\rho_j)^{2/3}$ . The normalization factor  $N_j$  is given by

$$\sum_{\text{pix}} N_j A_{\text{pix}} W_{\text{int}}(\tilde{d}_j/h_j) = A_j \quad (7.2)$$

to ensure the conservation of the quantity  $y$  when distributed over more than one pixel.

The method needs two further corrections. First, for pixels which are only partially overlapped by the projected SPH smoothing kernel, we approximate the associated area  $\hat{A}_{\text{pix}}$  as

$$\hat{A}_{\text{pix}} = \sqrt{A_{\text{pix}}} \times (\tilde{d}_j + 0.5\sqrt{A_{\text{pix}}} - h_j). \quad (7.3)$$

To compute the contribution to such a pixel, the weight of the integrated kernel  $W_{\text{int}}$  is then corrected by a factor  $\hat{A}_{\text{pix}}/A_{\text{pix}}$ . This must be taken also into account when normalizing the integrated kernel. We checked that this correction leads to very small changes in the majority of the pixels, but its effect can become substantial in the high-signal regions corresponding to the cluster cores, specially when the particles are distributed over a small number of cells.

Secondly, when a particle contributes to one pixel only, we fix the integrated kernel  $W_{\text{int}}$  to be unity. This is important when the area associated to such a particle is much smaller than the pixel area and ensures that the value corresponding to the particle is completely given to this pixel: in this case the normalization factor  $N_j$  can become significantly smaller than unity to ensure the conservation of the quantities. Finally we notice that, since the SZ effect is independent of distance, no distance factor has to be included into the previous equations.

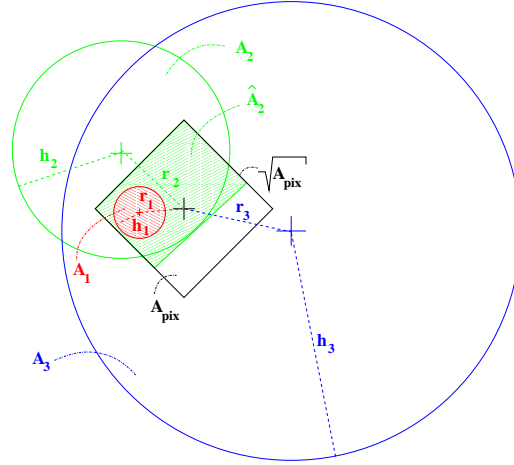


**Figure 7.1.** Sketch of three different geometrical situations for particles contributing to one pixel (represented by the black square). Particle 1 (in red), having a smoothing length  $h_1$  and being at a distance  $r_1$  from the pixel centre, falls completely inside the pixel, but does not overlap the centre. Particle 2 (in green) covers only partially the pixel. For particle 3 (in blue) the whole pixel lies within its projected radius.

Fig. 7.1 exemplifies the three different situations previously discussed by showing how the gas particles can contribute to one pixel (here represented by the square). In such cases, the weight contributed by particle 1 (shown in red) is  $A_1/A_{\text{pix}}$ , the weight for particle 2 (in green) is  $W_{\text{int}}(r_2/h_2)\hat{A}_2/A_2$  and the weight for particle 3 (in blue) is  $W_{\text{int}}(r_2/h_2)A_{\text{pix}}/A_3$ . Note that for particles 2 and 3 the weight needs to be normalized to unity when summed over all pixels to which the particles are contributing.

Our maps have been constructed by applying the previous technique directly to the HEALPIX (Górski & et al., 1999) representation of the full sky. We fix the  $n_{\text{side}}$  parameter to be 1024, which results in an all-sky representation with  $\approx 1.2 \times 10^7$  pixels. In order to avoid spurious effects the line of sight integral has been performed between a minimum and maximum distance ( $r_{\text{min}}$  and  $r_{\text{max}}$ , respectively). In particular we fix  $r_{\text{min}} = 5$  Mpc to be sure that the observer is outside the SPH smoothing radius of all particles, and  $r_{\text{max}} = 110$  Mpc, which represents a conservative limit of our high-resolution region.

## 7.4 Results

### 7.4.1 Full-sky maps

In Fig. 7.2 we show the results of the application of the previous method to obtain a full-sky map of the Compton  $y$ -parameter in supergalactic coordinates. The upper panel corresponds to the signal resulting from our *gas* simulation, covering the LU up to 110 Mpc. It is possible to recognize the most prominent features: Perseus, Virgo, Centaurus, Hydra, A3627 and Coma (very close to the northern pole of the

map). Also the presence of the filamentary structure connecting the largest clusters is still evident.

In the lower panel we show the same map where we add the contribution coming from more distant objects. This has been computed by exploiting the results of Schäfer et al. (2006), who build SZ signal maps by using the *Hubble volume simulation* (Colberg et al., 2000; Jenkins et al., 2001) and suitably inserting the outputs of different hydrodynamic re-simulations of single clusters. Notice that the physical processes considered in these re-simulations, i.e. non-radiative hydrodynamics, are the same included in our *gas* simulation, so no biases are introduced in combining the results. With respect to the Schäfer et al. (2006) work we add only the objects having a distance from the observer larger than 110 Mpc, because the closer ones are already represented in our simulation. The resulting map appears more patchy, having a significant contribution coming from a large number of distant clusters.

The corresponding maps for the kSZ signal, in terms of the  $b$ -parameter, are shown in Fig. 7.3. Again the most important structures of the LU are evident in the upper map and continue to give the dominant contribution in the map including distant objects, shown in lower panel.

It is worth noticing that within the simulation we measure a velocity at the observer position of  $v_x \approx -270$  km/s,  $v_y \approx 420$  km/s and  $v_z \approx -350$  km/s (assuming supergalactic coordinates). This leads to an absolute velocity of  $v \approx 610$  km/s, which is in good agreement with the observed value (see, e.g., the WMAP analysis by Bennett et al., 2003a). Again, the observer velocity points toward a direction which differs from the observed one less than  $10^\circ$ : this emphasizes once more that our simulations are giving a good representation of the large-scale structure in our LU.

By analysing the maps obtained from the results of the *csf* simulation (not shown here) we find only small differences with respect to the previous results, mainly in correspondence of the high-density regions, where the *cfs* simulation tends to give smaller signals. This difference can be quantified by looking at the pixel distribution as a function of  $y$  and  $b$ . This is shown in Fig. 7.4, where the contribution of the LU only is considered. Concerning the tSZ effect (left panel), the histograms are in general very similar, with only a slightly higher frequency for higher values in the *gas* simulation. The differences are more evident in the pixel distributions for the Doppler  $b$ -parameter: again high (absolute) values have higher probability in the *gas* simulation than in the *csf* one.

Analysing the gas bulk motions, we find no significant difference in the *gas* and *csf* runs. Moreover the winds driven by the feedback process are very efficiently stopped short after leaving the star forming region and consequently are not contributing to the kSZ signal. Therefore the difference observed in Fig. 7.4 reflects the fact that the pressure in the *csf* simulation is smaller than in the *gas* one. Again the magnitude of the effect is in good agreement with previous findings (White et al., 2002).

Notice that the distribution for  $b$  is clearly non-gaussian, with a more extended tail toward negative values, produced by the cluster motion inside the LU. Since the

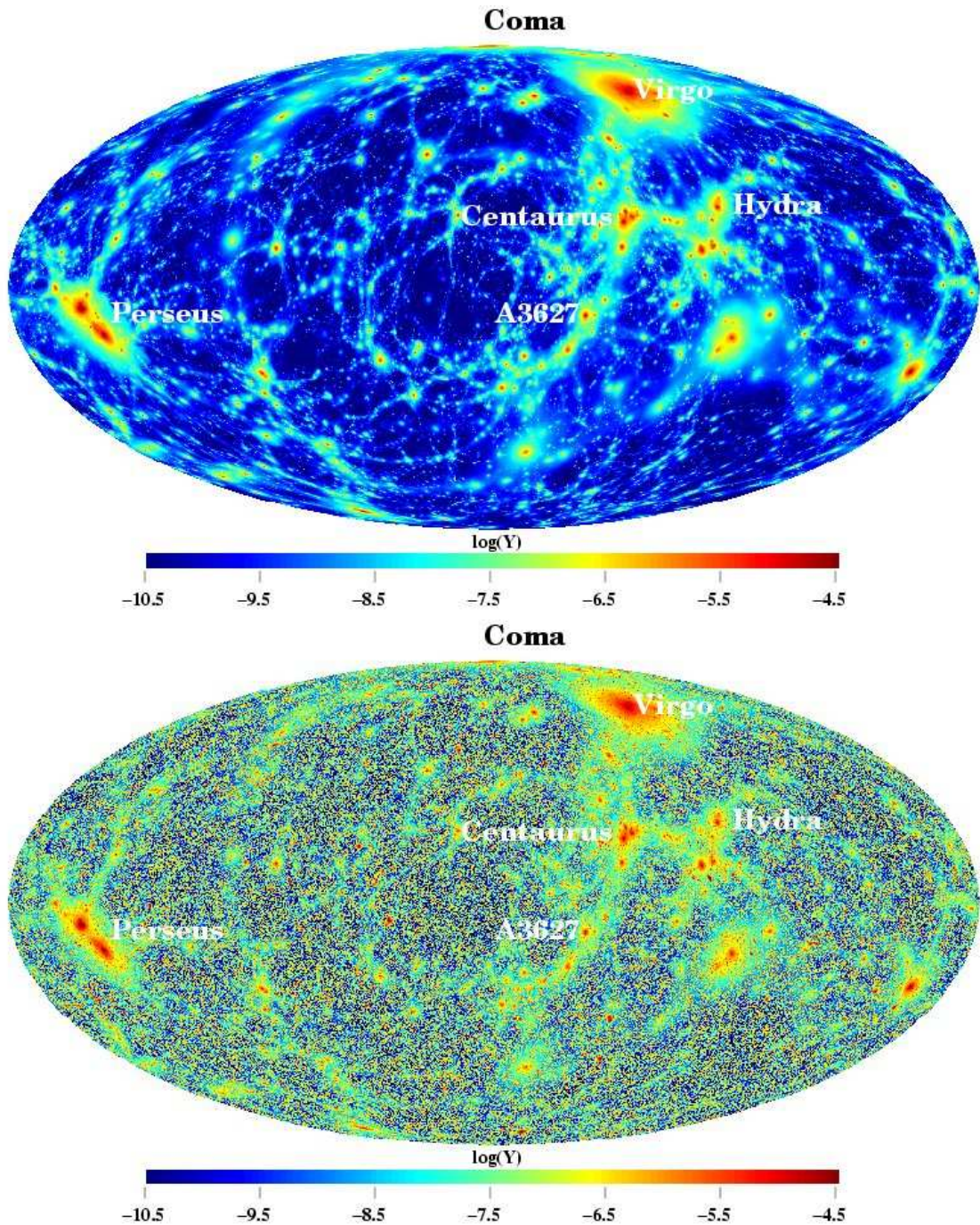


**Figure 7.2.** Full-sky map of the Compton  $y$ -parameter in galactic coordinates. The upper panel shows the results from the *gas* simulation, covering the LU up to 110 Mpc from the Milky Way, while in the lower panel we added the contribution from more distant objects, as estimated by Schäfer et al. (2006). The position of the most prominent structures is indicated in the maps.

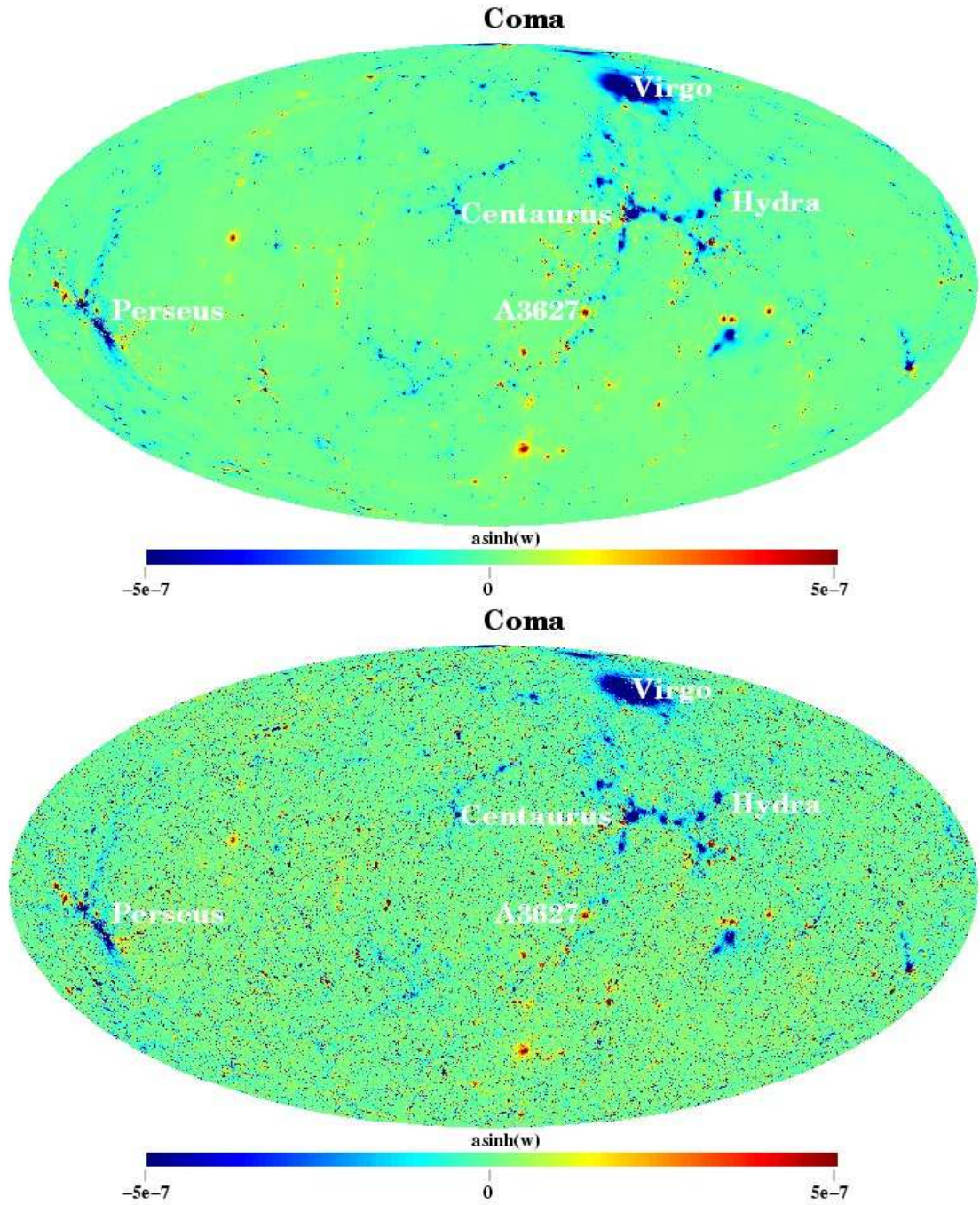


**Figure 7.3.** The same as Fig. 7.2, but for the kSZ effect, shown by using  $\text{asinh}(b)$  to better display positive and negative values.

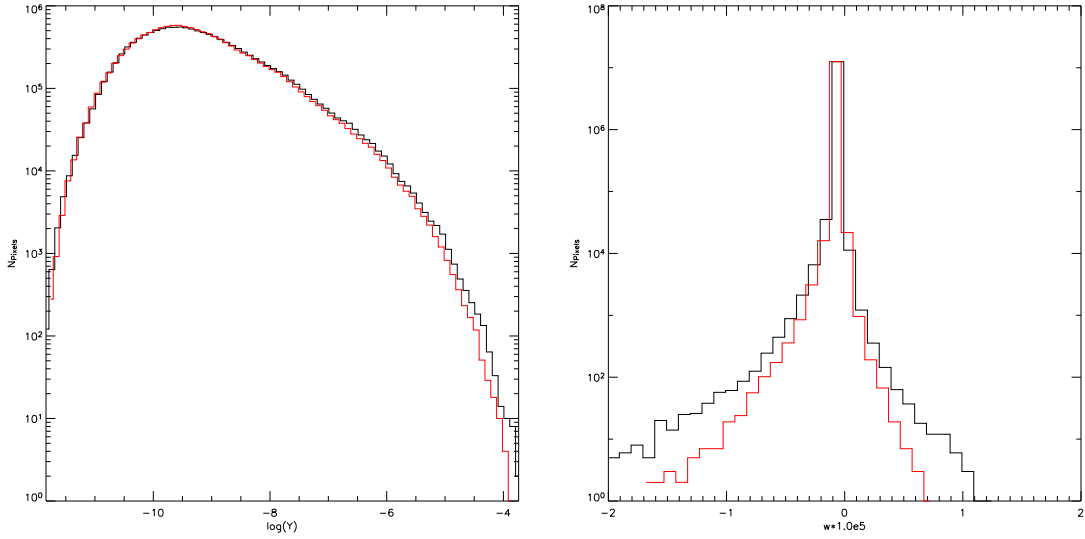


**Figure 7.4.** Comparison between the SZ signals as extracted from the *gas* and *csf* simulations (black and red lines, respectively). The number of pixels having a given value for the Compton  $y$ -parameter and the Doppler  $b$ -parameter are shown in the left and right panels, respectively.

spectral signature of the kSZ effect is the same of CMB, a perfect removal of this contribution could be difficult.

It is also worth to notice that the mean value of the Compton- $y$  parameter computed over the whole sky is dominated by the background map extracted from the *Hubble volume simulation*. For the total map (Fig. 7.2, lower panel) we get a mean value of  $3.3 \times 10^{-7}$ , whereas we find a much smaller mean value ( $4.1 \times 10^{-8}$ ) when considering only the map from the constrained simulation (*gas* run). As discussed before, this value slightly decreases when using the *csf* simulation ( $3.2 \times 10^{-8}$ ). Note that all these values are well below the upper limit derived from *COBE FIRAS* data (Fixsen, 2003).

We can compare the result of the mean value of the total map with the average value of the Compton  $y$ -parameter obtained from the *Keyproject* simulation, and shown in Section 5.4, of  $(1.19 \pm 0.32) \times 10^{-6}$ . This value is significantly higher because it accounts for all the gas up to  $z = 6$ , but when considering the redshift distribution plotted in Fig. 5.6, we can see that the signal up to the distance of  $1500h^{-1}$  Mpc ( $z \simeq 0.6$ , corresponding to half of the size of the *Hubble volume simulation*) corresponds to about 30 per cent of the total value, thus in agreement we the result presented here.

#### 7.4.2 The angular power spectrum

In order to quantify the amount of signal produced by the SZ effects, we compute from our maps the angular power spectrum  $C_\ell$ . In particular we estimate the spectra in the Rayleigh-Jeans regime, where  $\Delta T/T_{\text{CMB}} \simeq -2y$  (see Section 5.2).

The results are shown in Fig. 7.5, where we compare the power spectrum of the primordial CMB radiation (here represented by the upper black line corresponding

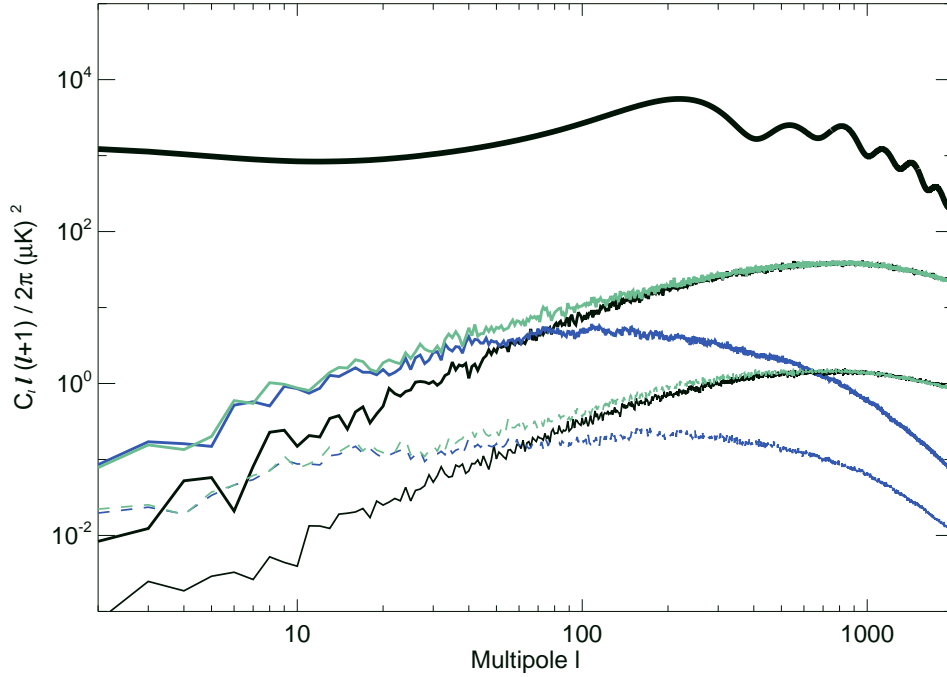


**Figure 7.5.** The power spectra for the SZ effects. Comparison between the cosmological CMB power spectrum (upper black solid lined) and the SZ signals obtained in the different simulations: *Hubble volume simulation* (black lines), local constrained *gas* simulation (blue lines); local constrained *gas* simulation combined with the *Hubble volume simulation* for larger distances (green lines). Upper and lower curves refer to the contributions from tSZ and kSZ effects, respectively. All spectra are taken in the Rayleigh-Jeans regime where  $\Delta T/T_{\text{CMB}} = -2y$ .

to the best fit of the WMAP data obtained by Spergel et al., 2003) to the signals extracted from the numerical simulations here considered. In particular the plot shows  $C_\ell$  for the *gas* simulation and distinguishes the contributions coming from the LU from the one produced by more distant galaxy clusters. Both the tSZ and the kSZ effects are considered. The results confirm that for  $\ell < 2000$  the cosmological signal is dominating the SZ one, being approximately 3-4 orders of magnitude larger. Moreover the kSZ signal is always smaller by a factor of 10-20 than that produced by the tSZ effect.

By comparing the results of our simulation with the estimates obtained by Schäfer et al. (2006), who populated the dark matter only *Hubble volume simulation* (Colberg et al., 2000; Jenkins et al., 2001) with individual, adiabatic cluster simulations, we notice that the SZ effect from the LU (objects with distance smaller than 110 Mpc from the Milky Way) is the most important contribution up to scales corresponding to  $\ell \approx 100$ . This is due to the larger angular size of the Local Supercluster structure. On the contrary, the signal at larger multipoles ( $\ell > 200$ ) seems to be dominated by the more distant sources, which are lying outside of our simulated volume (see also the comments on Fig. 5.7).

In order to quantify the contribution coming from the most prominent clusters, we compute  $C_\ell$  from our maps by applying the galactic cut and masking the regions

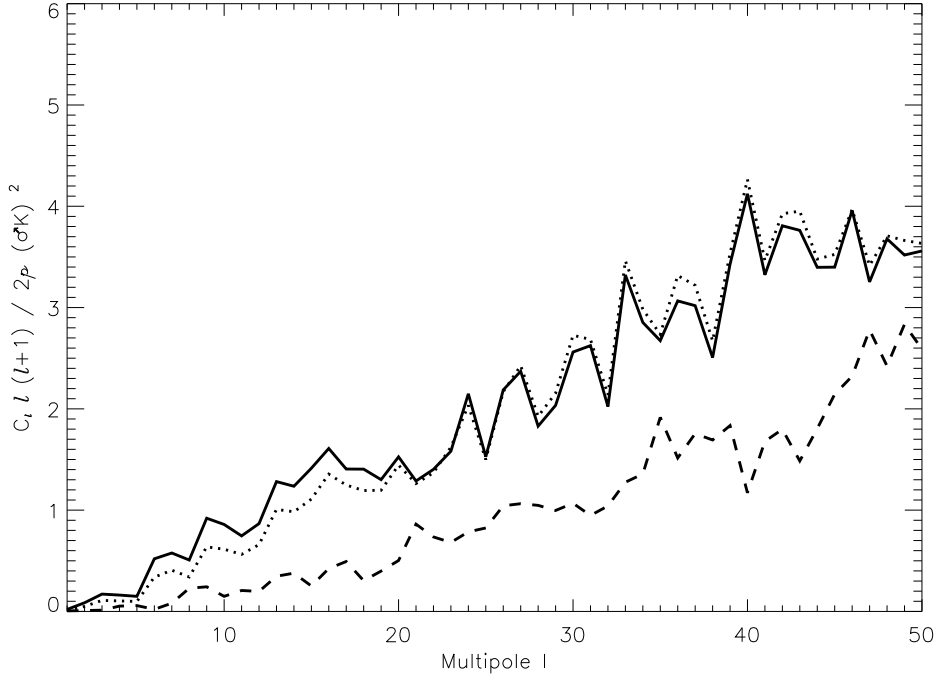


**Figure 7.6.** The large-scale power spectrum of the SZ effect obtained from the constrained simulations including (solid line) and excluding (dotted line) the diffuse gas contribution. The dashed line shows the power spectrum of the *Hubble volume simulation*.

where the 7 largest local galaxy clusters are located. The resulting power spectrum (not shown here) changes drastically for  $\ell > 50$  falling off much more rapidly, while remains unchanged for  $\ell < 50$ . This is an expected result, because the richest clusters are contributing to the power around 2-3 degrees, whereas the total signal from all the rest is dominating the large-scale power.

We further checked the contribution from diffuse gas by masking out in the maps the pixels with Compton  $y$ -parameter smaller than a given value ( $y = 10^{-6}$ ): in such a way only the signal from cluster cores remains. The resulting power spectrum is not strongly affected, showing that the diffuse gas contributes minimally to the observed SZ power. In Fig. 7.6 we show the power spectrum including and excluding the diffuse gas contribution (solid and dotted lines, respectively) along with the power spectrum extracted from the *Hubble volume simulation* (dashed line). Note that the *Hubble volume simulation* gives a lower power spectrum at the largest scales when compared to the constrained simulation, even when the diffuse gas is removed from it.

Having two different constrained realizations of the LU, the first one with adiabatic physics only, the second one including also cooling, star formation and feedback (the *gas* and *csf* simulations, respectively), it is possible to discuss how the previous results depend on the set of the included physical processes. This is done in Fig. 7.7, where we compare directly the power spectra obtained from the two simulations. We find a higher signal in the adiabatic simulation, both for the tSZ

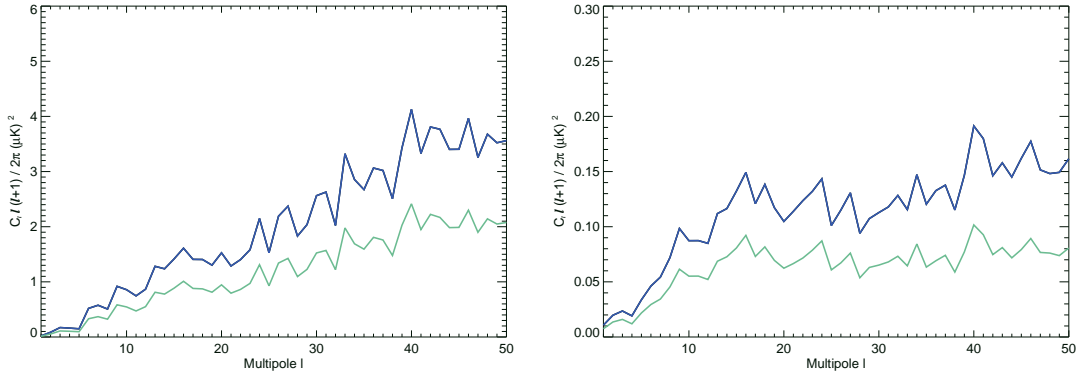


**Figure 7.7.** Effects on the power spectra of the inclusion of different physical processes in the constrained simulations of the LU. Blue and green curves show  $C_l$  as extracted from the *gas* and *csf* simulations, respectively. Left and right panels refer to the tSZ and kSZ effects, respectively. The tSZ spectra are taken in the Rayleigh-Jeans region where  $\Delta T/T_{\text{CMB}} = -2y$ .

and the kSZ effects. The amplitude of this difference is very similar in both cases, being approximately a factor of 2. This is in agreement with the results obtained from individual cluster simulations (see, e.g., White et al., 2002). Therefore we do not expect the signal to get stronger when including additional physical processes and we can take the results obtained from the *gas* simulation as a robust upper bound.

### 7.4.3 Alignment of lower multipoles

Several anomalies have been detected at low multipoles in the WMAP data. In particular Tegmark et al. (2003) and de Oliveira-Costa et al. (2004) find the CMB quadrupole and octopole to have an unusually high degree of alignment, which is significant at the  $2\sigma$  level. Moreover they show that the directions of the quadrupole and the octopole are close to the direction of the Virgo cluster which could suggest a possible link to structures in the LU. By analysing our SZ templates, we find that the directions of the quadrupole and octopole (shown in Fig. 7.8 for the *gas* simulation) are very different from that extracted from the WMAP data: in our maps the quadrupole and octopole point toward  $(b, l) \approx (42.3^\circ, -177.6^\circ)$  and  $(b, l) \approx (32.5^\circ, 88.1^\circ)$ , respectively, while the preferred axes in the WMAP data are in the directions  $(b, l) \approx (58.8^\circ, -102.4^\circ)$  for the quadrupole and  $(b, l) \approx (62.0^\circ, -121.6^\circ)$  for the octopole. Moreover the amplitudes of both quadrupole and octopole are far too small to have such an effect.

Finally it has been claimed by different groups that the quadrupole of the CMB is anomalously low [see the discussion in Efstathiou (2004) and references therein] and that this could be caused by structures present in the LU (Abramo & Sodre, 2003). Again, we find that the amplitude of the SZ effect is far too low to have any relevant effect.

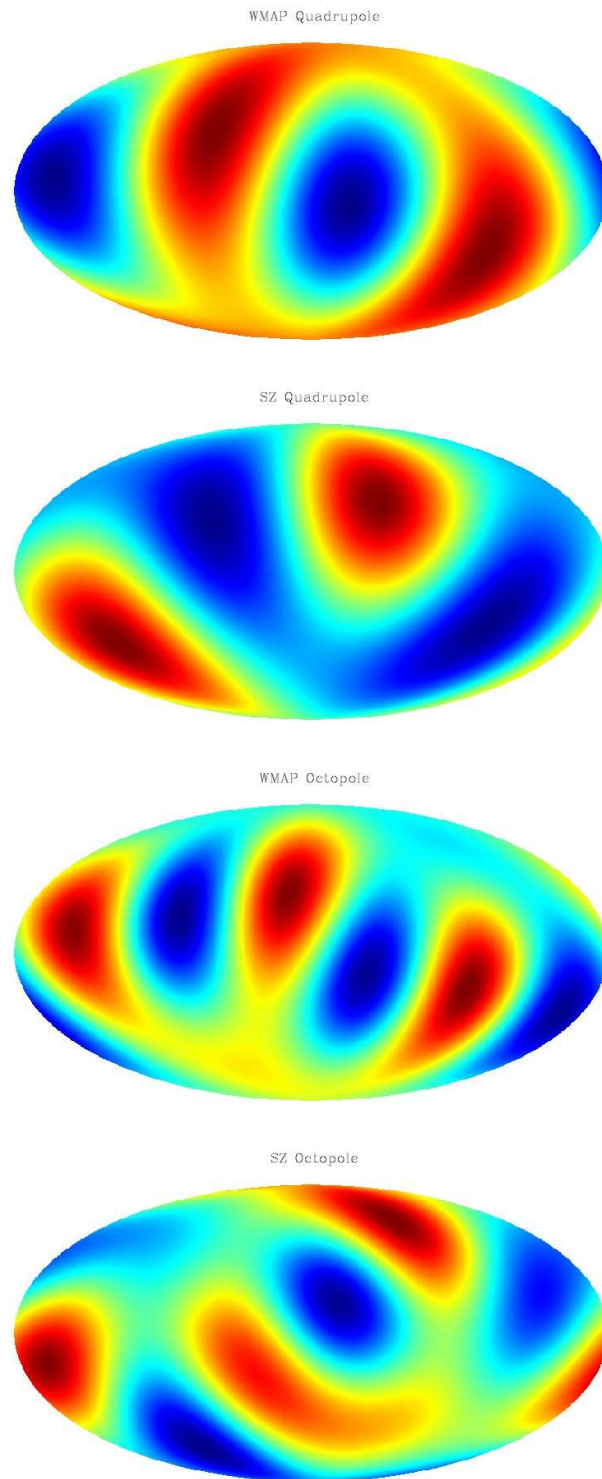


**Figure 7.8.** Upper panels: comparison between the quadrupole maps obtained from the WMAP internal linear combination (first panel) and from the SZ template extracted from the *gas* simulation (second panel). Lower panels: same as the previous panels but for the octopole maps.

#### 7.4.4 Detectability of the local SZ signal with the *Planck* satellite

We investigate now whether the local SZ effect can be observed using the upcoming *Planck* satellite. The very low noise level and the huge frequency range of the *Planck* experiment could make it capable of seeing this effect at large scales. Note that the CMB itself is the most important contamination when trying to look for the SZ effect at large scales (Hansen et al., 2005). As the CMB has the same temperature at all frequencies, using a map produced by computing the difference between two frequency bands could be a promising way of detecting the SZ effect (this strategy was attempted for the WMAP data in Hansen et al., 2005). This makes the observation of the SZ effect limited only by the instrumental noise. Unfortunately galactic foregrounds also have several frequency dependent components, and these need to be eliminated at a very high degree in order to detect the SZ signal. Here we will assume that these have been completely removed outside a conservative galactic cut.

In order to estimate the sensitivity to the local SZ effect for the *Planck* experiment, we simulated *Planck* data for the 70, 100, 143 and 217 GHz channels, by using the technical specifications of *Planck* publicly available. In more detail, we apply the following procedure.

- i* - For each simulation, we generate a CMB sky and smooth it by using the beams corresponding to the 4 channels of interest. The smoothing is performed in the harmonic space by using beams with size of 14, 9.5, 7.1 and 5 arcmin for the channels at 70, 100, 143 and 217 GHz, respectively. As the band width for each frequency channel is expected to be much smaller than the frequency difference between the channels, we approximate the band width to be infinitely narrow.
- ii* - We generate white, non-uniform noise for each channel and add it to the maps. The *Planck* experiment is expected to have highly correlated noise which would affect the noise power spectrum at the largest scales. Since here we are only interested in a rough estimate of the sensitivity of the *Planck* experiment to the SZ effect, we neglect this effect. Consequently our results could be slightly over-optimistic at the largest scales.
- iii* - We add the SZ template to each map by using the frequency dependence of the SZ effect.
- iv* - We construct three different maps, corresponding to the difference between the maps at 217 and 100 GHz (called map A), between 143 and 100 GHz (map B) and between 143 and 70 GHz (map C).
- v* - We apply the Kp0 galaxy and point source mask used by the WMAP team before calculating the power spectrum of the difference maps.

In Fig. 7.9 we show the results of a set of 300 different simulations (the number of simulations has been chosen to obtain error bars correct within a few percent). The solid line corresponds to the power spectrum of the template outside the Kp0 galactic cut. The three shaded areas refer to the  $1\sigma$  spread from simulations of the

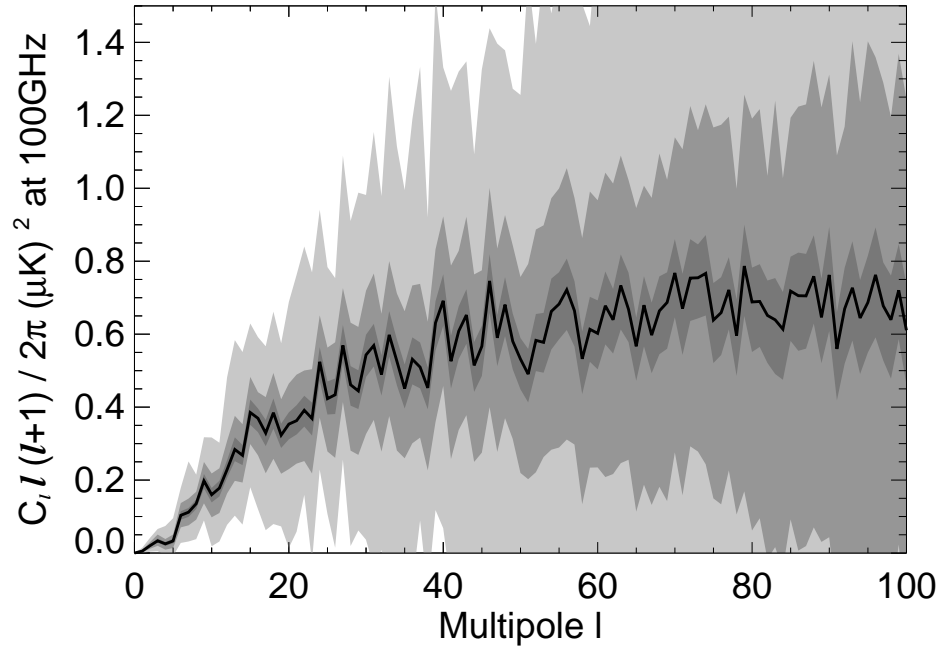


**Figure 7.9.** The estimated power spectra of three difference maps from *Planck* simulations. The solid line shows the power spectrum of the local SZ template. The shaded bands correspond to the  $1\sigma$  spread of the estimated power spectra in 300 simulations for the following difference maps: A = 217-100 GHz, B = 143-100 GHz and C = 143-70 GHz. Map A has the lowest spread and map C has the largest one. The Kp0 galactic cut has been used in these simulations. Note that all spectra are normalized to the expected SZ effect at 100 GHz.

three difference maps, map A having the smallest spread, and map C the largest one. The huge difference between the different pairs comes from two different factors: first, the bigger the frequency difference, the bigger is the SZ effect in the resulting difference map; second, as the CMB is absent in the difference maps, the limiting factor is the noise level which is highly different in different frequency channels.

We notice that assuming white noise and a perfect foreground subtraction outside the Kp0 cut, we can expect the local SZ effect to be detected by the *Planck* satellite. Even if real error bars might be larger than our simulations show, one will still be able to compare data with the predicted local SZ effect.

Finally note that analysing difference maps is a useful tool for checking that foregrounds and other systematic effects of the experiment are well understood. For this purpose it will be of high importance to know well the expected local SZ effect as it will give an important contribution to the difference maps.

## 7.5 Summary and conclusions

We used two hydrodynamical cosmological simulations which are designed to represent the observed large-scale structure of the LU (up to approximately 110 Mpc from the Milky Way) to investigate the imprints of the extended SZ signal caused by Local superclusters onto the cosmological full-sky signal. The two simulations, which assume the standard  $\Lambda$ CDM model, started from the same initial conditions, but included the treatment of a different set of physical processes: the first one assumes adiabatic physics only, while the second one follows also cooling, star formation and supernovae feedback.

We find that the largest and most prominent structures observed in the SZ map constructed from our constrained simulations are caused by local superclusters like Pisces-Perseus or the Centaurus supercluster region. Even Virgo, a relatively poor but nearby cluster, belongs to the most prominent and extended features of the map.

Comparing the power spectra of the tSZ signal with the one derived from the *Hubble volume simulation* (Schäfer et al., 2006), we find that for  $\ell < 100$  these structures lead to an amplitude which is at least twice as high (one order of magnitude for  $\ell < 20$ ). When comparing the derived power spectra for the kSZ this factor is even higher.

However, the overall amplitude of the effect is far too small (3-4 orders of magnitude) to have any significant influence on the lowest multipoles of the CMB. There have been some claims that the anomalously low CMB quadrupole and octopole observed by the WMAP satellite could be explained by the imprints of local superclusters. We have shown that the amplitude of the SZ low multipoles must be considerably much higher in order to produce such an effect as well as to have an influence on the observed quadrupole and octopole.

Moreover, the directions on the sky of the quadrupole and octopole inferred from our simulations do not coincide with the observed direction in the WMAP maps.

Both for our *gas* simulation as well as for the *Hubble volume simulation*, radiative cooling processes and feedback by star formation have been neglected, which could change the absolute amplitude of the inferred SZ signal of galaxy clusters. However, using a simulation which includes all these effects (the *csf* simulation), we even find a slight decrease of the SZ signal, similar to the findings obtained by using isolated cluster simulations. This will make it even more unlikely to explain the abnormal lower multipoles observed in the WMAP data with the SZ signal of the LU.

Nevertheless, we find that when taking advantage of the huge frequency range and low noise level of the *Planck* satellite, an estimate of the SZ power spectrum at large scales could be obtained. We have shown this by producing a set of simulated CMB maps with experimental noise at several frequencies. Analysing the power spectrum of maps obtained by taking the difference of CMB maps at different frequencies, we show that the power spectrum of the SZ effect is limited only by

experimental noise and foreground contamination.

We have found that the predicted noise level of the *Planck* satellite is low enough to allow for the detection of the local SZ power spectrum at low multipoles provided that the galaxy can be removed with sufficient accuracy. It is out of the scope of this work to obtain an accurate estimate of the predicted detection level by the *Planck* satellite, for which correlated noise as well as an accurate study of foreground removal procedures is required.

# CONCLUSIONS

In this Thesis we have presented our work on the modelization of the properties of the cosmic web with hydrodynamical simulations. We have described in detail the connections with the cosmological context of large scale structure (LSS) formation. We have also provided an overview of the numerical methods adopted in cosmology, highlighting their importance and focusing on the ones adopted for our work.

Our study spanned from clusters of galaxies, to filaments and diffuse signals in general, concentrating on the connections with the physical models adopted in our simulations. We described the properties of the intergalactic medium (IGM) as a whole and focused on the warm-hot intergalactic medium (WHIM) component.

For what concerns the observational aspects, we analysed the X-ray emission, comparing our predictions with the large amount of data available and the Sunyaev-Zel'dovich (SZ) effect, both on its thermal (tSZ) and kinetic (kSZ) component, confronting our results mainly with current cosmic microwave background (CMB) anisotropies observations.

Here we conclude the presentation of this Thesis by summarizing our main results in the different topics.

## **Outskirts of galaxy clusters**

- Unlike for the inner regions, the behaviour of the thermodynamical properties in the outskirts results basically independent of the physical modelization of the baryonic component: this indicates that in the external regions the gravitational collapse is by far the dominant component, making these objects highly self-similar.
- The soft (0.5-2 keV) X-ray surface brightness profiles present a clear steepening towards the outskirts: this is more prominent in isolated galaxy groups due to the fact that they are more relaxed and that their low temperature makes their gas emit at energies lower than 0.5 keV.
- At the virial radius the average surface brightness is lower by a factor of few than the measured value of the unresolved X-ray background (XRB). This indicates that in order to observe them a good modelization of the background is required together with the technique of stacking the images of different objects.

### Diffuse X-ray emission

- When studying the emission of the IGM with currently available hydrodynamical models, the total soft X-ray surface brightness due to the IGM is higher than the upper limits imposed by *Chandra* Deep Fields observations. This is mainly due to the presence in the simulations of overluminous groups of galaxies, indicating that the known feedback mechanisms are not able to provide a faithful description of the haloes at the low-mass scales.
- On the contrary, when considering the truly diffuse component due to the WHIM we obtain an estimate which agrees with observational upper limits. We also predict that the majority of the unresolved XRB is due to the cosmic web signal.
- Our results confirm the idea that a further investigation of the diffuse XRB component will probably provide the solution to the “missing baryons” problem.

### The SZ effect

- We provided a detailed statistical description of the large-scale properties of the thermal and kinetic SZ effects. We obtain that more than a half of the total tSZ background comes from the WHIM, but at the angular scales at which the tSZ effect dominates the primary CMB anisotropies ( $\ell > 3000$ ) the signal due to the diffuse component is negligible with respect to the total one.
- The kSZ effect presents a power spectrum which is almost flat at high multipoles (out to  $\ell > 2 \times 10^5$ ), and thus is the dominant component at all frequencies at the angular scales lower than  $\approx 10$  arcsec.
- The two SZ effects are highly correlated between themselves and with the X-ray emission at all angular scales. The correlation factor can be as high as  $r_\ell \approx 0.8 - 0.9$  for the correlation between the X-ray emission and the tSZ effect.
- On the very large angular scales the tSZ effect is dominated by the presence of the structures of the Local Supercluster. Anyway this cannot explain the anomalies measured in the low multipoles of the CMB power spectrum because its signal is much lower than the one due to primary anisotropies.
- However we predict that future low-background observational projects like the *Planck* satellite will probably provide the detection of the local tSZ signal, taking advantage of its different spectral dependence with respect to the primary CMB one.

The work presented in this Thesis further confirms the importance of the interplay between simulations and observations in cosmology. This will be particularly important in the development of new observational projects.

In fact, in the next years the construction of new microwave instruments will provide a series of new observations of galaxy clusters with the SZ effect that will allow a direct comparison with the currently available X-ray data. This will constitute an independent test on the physics of galaxy clusters. The understanding of the properties of the SZ signal with numerical simulations is playing and will play a crucial role in the development of these observational projects and in the future interpretations of the data.

For what concerns X-ray, part of the work presented here is currently being used for the development of a new X-ray instrument, the *Explorer of Diffuse Emission and gamma-ray bursts Explosions (EDGE)* satellite. The main scientific goal of *EDGE* is the detection of the signal of the cosmic web via emission and absorption lines due to the metals present in the WHIM, thus providing a definitive answer on the “missing baryons” problem.

The development of this ambitious project needs a detailed understanding of the physics that regulates the LSS formation. In fact, the study of the instrumentation requirements needs to be based on the most reliable predictions on the cosmic web signal. On the other side the possible future detections of the WHIM signal will be very useful in the understanding of the thermodynamics that regulates the formation of the structures on the large scales, thus providing constraints on the history of the Universe.

This future observational scenario, in which hydrodynamical simulations will play an important part, highlights again the importance of the cosmic web in modern and future cosmology.



## Bibliography

- Abramo L. R., Sodre Jr L., 2003, ArXiv Astrophysics e-prints, astro-ph/0312124
- Alexander D. M., et al., 2003, AJ, 126, 539
- Anders E., Grevesse N., 1989, Geochimica et Cosmochimica Acta, 53, 197
- Ascasibar Y., Sevilla R., Yepes G., Müller V., Gottlöber S., 2006, MNRAS, 371, 193
- Astier P., et al., 2006, A&A, 447, 31
- Babul A., Balogh M. L., Lewis G. F., Poole G. B., 2002, MNRAS, 330, 329
- Balogh M. L., Babul A., Patton D. R., 1999, MNRAS, 307, 463
- Barnes J., Hut P., 1986, Nat, 324, 446
- Bartelmann M., 2001, A&A, 370, 754
- Battistelli E. S., et al., 2003, ApJ, 598, L75
- Bauer F. E., Alexander D. M., Brandt W. N., Schneider D. P., Treister E., Hornschemeier A. E., Garmire G. P., 2004, AJ, 128, 2048
- Bennett C. L., et al., 2003a, ApJ, 583, 1
- Bennett C. L., et al., 2003b, ApJS, 148, 1
- Birkinshaw M., 1999, Phys. Rep., 310, 97
- Birkinshaw M., Hughes J. P., 1994, ApJ, 420, 33
- Birkinshaw M., Hughes J. P., Arnaud K. A., 1991, ApJ, 379, 466
- Boehringer H., et al., 2001, A&A, 369, 826
- Borgani S., et al., 2001, ApJ, 561, 13
- Borgani S., et al., 2004, MNRAS, 348, 1078
- Borgani S., et al., 2006, MNRAS, 367, 1641
- Bower R. G., 1997, MNRAS, 288, 355
- Bower R. G., Benson A. J., Lacey C. G., Baugh C. M., Cole S., Frenk C. S., 2001, MNRAS, 325, 497
- Bryan G. L., 2000, ApJ, 544, L1
- Bryan G. L., Norman M. L., Stone J. M., Cen R., Ostriker J. P., 1995, Computer Physics Communications, 89, 149
- Bryan G. L., Voit G. M., 2001, ApJ, 556, 590
- Carlstrom J. E., Holder G. P., Reese E. D., 2002, ARA&A, 40, 643
- Cavaliere A., Fusco-Femiano R., 1978, A&A, 70, 677

- Cavaliere A., Menci N., Tozzi P., 1998, *ApJ*, 501, 493
- Cen R., Ostriker J. P., 1999, *ApJ*, 514, 1
- Cheng L.-M., et al., 2005, *A&A*, 431, 405
- Cheng L.-M., Wu X.-P., Cooray A., 2004, *A&A*, 413, 65
- Churazov E., Brüggen M., Kaiser C. R., Böhringer H., Forman W., 2001, *ApJ*, 554, 261
- Colberg J. M., et al., 2000, *MNRAS*, 319, 209
- Cole S., et al., 2005, *MNRAS*, 362, 505
- Coles P., Lucchin F., 2002, *Cosmology: The Origin and Evolution of Cosmic Structure*, Wiley-VCH (2nd edition)
- Croft R. A. C., Di Matteo T., Davé R., Hernquist L., Katz N., Fardal M. A., Weinberg D. H., 2001, *ApJ*, 557, 67
- da Silva A. C., Barbosa D., Liddle A. R., Thomas P. A., 2000, *MNRAS*, 317, 37
- da Silva A. C., Kay S. T., Liddle A. R., Thomas P. A., 2004, *MNRAS*, 348, 1401
- da Silva A. C., Kay S. T., Liddle A. R., Thomas P. A., Pearce F. R., Barbosa D., 2001, *ApJ*, 561, L15
- da Silva A. C., Barbosa D., Liddle A. R., Thomas P. A., 2001a, *MNRAS*, 326, 155
- da Silva A. C., Kay S. T., Liddle A. R., Thomas P. A., Pearce F. R., Barbosa D., 2001b, *ApJ*, 561, L15
- Davé R., et al., 2001, *ApJ*, 552, 473
- Davis M., Peebles P. J. E., 1983, *ApJ*, 267, 465
- De Grandi S., Ettori S., Longhetti M., Molendi S., 2004, *A&A*, 419, 7
- De Grandi S., Molendi S., 2002, *ApJ*, 567, 163
- De Luca A., Molendi S., 2004, *A&A*, 419, 837
- de Oliveira-Costa A., Tegmark M., Zaldarriaga M., Hamilton A., 2004, *Phys. Rev. D*, 69, 063516
- Di Matteo T., Springel V., Hernquist L., 2005, *Nat*, 433, 604
- Diaferio A., et al., 2005, *MNRAS*, 356, 1477
- Diego J. M., Majumdar S., 2004, *MNRAS*, 352, 993
- Diego J. M., Silk J., Sliwa W., 2003, *New Astronomy Review*, 47, 855
- Dietrich J. P., Schneider P., Clowe D., Romano-Díaz E., Kerp J., 2005, *A&A*, 440, 453
- Dolag K., Jubelgas M., Springel V., Borgani S., Rasia E., 2004, *ApJ*, 606, L97

- Dolag K., Grasso D., Springel V., Tkachev I., 2005a, JCAP, 1, 9
- Dolag K., Hansen F. K., Roncarelli M., Moscardini L., 2005b, MNRAS, 363, 29
- Dolag K., Vazza F., Brunetti G., Tormen G., 2005c, MNRAS, 364, 753
- Ebeling H., Edge A. C., Bohringer H., Allen S. W., Crawford C. S., Fabian A. C., Voges W., Huchra J. P., 1998, MNRAS, 301, 881
- Efstathiou G., 2004, MNRAS, 348, 885
- Eisenstein D. J., et al., 2005, ApJ, 633, 560
- Eke V. R., Cole S., Frenk C. S., 1996, MNRAS, 282, 263
- Ensslin T. A., Heinz S., 2002, A&A, 384, L27
- Ettori S., et al., 2004, MNRAS, 354, 111
- Ettori S., Fabian A. C., 1999, MNRAS, 305, 834
- Fabian A. C., 1994, ARA&A, 32, 277
- Finoguenov A., Briel U. G., Henry J. P., 2003, A&A, 410, 777
- Fisher K. B., Huchra J. P., Strauss M. A., Davis M., Yahil A., Schlegel D., 1995, ApJS, 100, 69
- Fixsen D. J., 2003, ApJ, 594, L67
- Fujita Y., Suzuki T. K., Wada K., 2004, ApJ, 600, 650
- Fukugita M., 2004, in Ryder S., Pisano D., Walker M., Freeman K., eds, *IAU Symposium*, pp 227–+
- Gardini A., Rasia E., Mazzotta P., Tormen G., De Grandi S., Moscardini L., 2004, MNRAS, 351, 505
- Gaztañaga E., Wagg J., Multamäki T., Montaña A., Hughes D. H., 2003, MNRAS, 346, 47
- Giacconi R., et al., 2002, ApJS, 139, 369
- Gingold R. A., Monaghan J. J., 1977, MNRAS, 181, 375
- Górski K. M., et al. 1999, in Banday A. J., Sheth R. K., da Costa L. N., eds, *Evolution of Large Scale Structure : From Recombination to Garching*, pp 37–+
- Haardt F., Madau P., 1996, ApJ, 461, 20
- Hansen F. K., Branchini E., Mazzotta P., Cabella P., Dolag K., 2005, MNRAS, 361, 753
- Hernández-Monteagudo C., Genova-Santos R., Atrio-Barandela F., 2004, ApJ, 613, L89
- Hernández-Monteagudo C., Verde L., Jimenez R., Spergel D. N., 2006, ApJ, 643, 598

- Hetterscheidt M., et al., 2006, ArXiv Astrophysics e-prints, astro-ph/0606571
- Heymans C., et al., 2005, MNRAS, 361, 160
- Hickox R. C., Markevitch M., 2006, ApJ, 645, 95
- Hickox R. C., Markevitch M., 2007, ArXiv Astrophysics e-prints, astro-ph/0702556
- Hinshaw G., et al., 2006, ArXiv Astrophysics e-prints, astro-ph/0603451
- Hirata C. M., Padmanabhan N., Seljak U., Schlegel D., Brinkmann J., 2004, Phys. Rev. D, 70, 103501
- Hoekstra H., Mellier Y., van Waerbeke L., Semboloni E., Fu L., Hudson M. J., Parker L. C., Tereno I., Benabed K., 2006, ApJ, 647, 116
- Hoffman Y., Ribak E., 1991, ApJ, 380, L5
- Huffenberger K. M., Seljak U., Makarov A., 2004, Phys. Rev. D, 70, 063002
- Ikebe Y., Reiprich T. H., Böhringer H., Tanaka Y., Kitayama T., 2002, A&A, 383, 773
- Iliev I. T., Pen U.-L., Richard Bond J., Mellema G., Shapiro P. R., 2006, New Astronomy Review, 50, 909
- Jenkins A., Frenk C. S., White S. D. M., Colberg J. M., Cole S., Evrard A. E., Couchman H. M. P., Yoshida N., 2001, MNRAS, 321, 372
- Jubelgas M., Springel V., Dolag K., 2004, MNRAS, 351, 423
- Kaastra J. S., Werner N., Herder J. W. A. d., Paerels F. B. S., de Plaa J., Rasmussen A. P., de Vries C. P., 2006, ApJ, 652, 189
- Kaiser N., 1986, MNRAS, 222, 323
- Katz N., Weinberg D. H., Hernquist L., 1996, ApJS, 105, 19
- Kim W.-T., Narayan R., 2003, ApJ, 596, L139
- Kirkman D., Tytler D., Suzuki N., O'Meara J. M., Lubin D., 2003, ApJS, 149, 1
- Kolatt T., Dekel A., Ganon G., Willick J. A., 1996, ApJ, 458, 419
- Lacey C., Cole S., 1993, MNRAS, 262, 627
- Lewis G. F., Babul A., Katz N., Quinn T., Hernquist L., Weinberg D. H., 2000, ApJ, 536, 623
- Liedahl D. A., Osterheld A. L., Goldstein W. H., 1995, ApJ, 438, L115
- Lucchin F., 1998, *Introduzione alla Cosmologia*, Zanichelli
- Lucy L. B., 1977, AJ, 82, 1013
- Mannucci F., Bonoli G., Zappacosta L., Maiolino R., Pedani M., 2007, ArXiv Astrophysics e-prints, astro-ph/0703076
- Markevitch M., Forman W. R., Sarazin C. L., Vikhlinin A., 1998, ApJ, 503, 77

- Massey R., Refregier A., Bacon D. J., Ellis R., Brown M. L., 2005, *MNRAS*, 359, 1277
- Mather J. C., et al., 1994, *ApJ*, 420, 439
- Mathis H., Lemson G., Springel V., Kauffmann G., White S. D. M., Eldar A., Dekel A., 2002, *MNRAS*, 333, 739
- Mathur S., Weinberg D. H., Chen X., 2003, *ApJ*, 582, 82
- Mazzotta P., Rasia E., Moscardini L., Tormen G., 2004, *MNRAS*, 354, 10
- Mewe R., Gronenschild E. H. B. M., van den Oord G. H. J., 1985, *A&A Supp.*, 62, 197
- Miller G. E., Scalo J. M., 1979, *ApJS*, 41, 513
- Mohr J. J., Mathiesen B., Evrard A. E., 1999, *ApJ*, 517, 627
- Molendi S., 2004, in Diaferio A., ed., *IAU Colloq. 195: Outskirts of Galaxy Clusters: Intense Life in the Suburbs*, pp 122–125
- Monaghan J. J., Lattanzio J. C., 1985, *A&A*, 149, 135
- Moretti A., Lazzati D., Campana S., Tagliaferri G., 2002, *ApJ*, 570, 502
- Morris J. P., Monaghan J. J., 1997, *Journal of Computational Physics*, 136, 41
- Motl P. M., Hallman E. J., Burns J. O., Norman M. L., 2005, *ApJ*, 623, L63
- Muanwong O., Thomas P. A., Kay S. T., Pearce F. R., Couchman H. M. P., 2001, *ApJ*, 552, L27
- Murante G., et al., 2004, *ApJ*, 607, L83
- Narayan R., Medvedev M. V., 2001, *ApJ*, 562, L129
- Neumann D. M., 2005, *A&A*, 439, 465
- Nicastro F., et al., 2005a, *Nat*, 433, 495
- Nicastro F., et al., 2005b, *ApJ*, 629, 700
- Parijskij Y. N., 1973, *ApJ*, 180, L47+
- Pearce F. R., Thomas P. A., Couchman H. M. P., Edge A. C., 2000, *MNRAS*, 317, 1029
- Penton S. V., Stocke J. T., Shull J. M., 2004, *ApJS*, 152, 29
- Pointecouteau E., Arnaud M., Pratt G. W., 2005, *A&A*, 435, 1
- Pratt G. W., Arnaud M., 2002, *A&A*, 394, 375
- Rasia E., Mazzotta P., Borgani S., Moscardini L., Dolag K., Tormen G., Diaferio A., Murante G., 2005, *ApJ*, 618, L1
- Rauch M., 1998, *ARA&A*, 36, 267

- Raymond J. C., Smith B. W., 1977, *ApJS*, 35, 419
- Rephaeli Y., 1995, *ARA&A*, 33, 541
- Rephaeli Y., Sadeh S., Shimon M., 2005, in Melchiorri F., Rephaeli Y., eds, *Background Microwave Radiation and Intracluster Cosmology*, pp 57–+
- Riess A. G., et al., 2005, *ApJ*, 627, 579
- Roberts T. P., Warwick R. S., 2001, in Giacconi R., Serio S., Stella L., eds, *ASP Conf. Ser. 234: X-ray Astronomy 2000*, pp 569–+
- Romeo A. D., Sommer-Larsen J., Portinari L., Antonuccio-Delogu V., 2006, *MNRAS*, 371, 548
- Roncarelli M., Moscardini L., Borgani S., Dolag K., 2007, *ArXiv Astrophysics e-prints*, astro-ph/0701680
- Roncarelli M., Moscardini L., Tozzi P., Borgani S., Cheng L. M., Diaferio A., Dolag K., Murante G., 2006a, *MNRAS*, 368, 74
- Roncarelli M., Ettori S., Dolag K., Moscardini L., Borgani S., Murante G., 2006b, *MNRAS*, 373, 1339
- Rosati P., Borgani S., Norman C., 2002, *ARA&A*, 40, 539
- Rosati P., della Ceca R., Burg R., Norman C., Giacconi R., 1995, *ApJ*, 445, L11
- Rosati P., della Ceca R., Norman C., Giacconi R., 1998, *ApJ*, 492, L21
- Ryu D., Ostriker J. P., Kang H., Cen R., 1993, *ApJ*, 414, 1
- Sadeh S., Rephaeli Y., 2004, *New Astronomy*, 9, 373
- Salpeter E. E., 1955, *ApJ*, 121, 161
- Sánchez A. G., Baugh C. M., Percival W. J., Peacock J. A., Padilla N. D., Cole S., Frenk C. S., Norberg P., 2006, *MNRAS*, 366, 189
- Sandage A., Tammann G. A., Saha A., Reindl B., Macchetto F. D., Panagia N., 2006, *ApJ*, 653, 843
- Sanderson A. J. R., Ponman T. J., Finoguenov A., Lloyd-Davies E. J., Markevitch M., 2003, *MNRAS*, 340, 989
- Savage B. D., Sembach K. R., Tripp T. M., Richter P., 2002, *ApJ*, 564, 631
- Schäfer B. M., Pfrommer C., Bartelmann M., Springel V., Hernquist L., 2006, *MNRAS*, 370, 1309
- Seljak U., Zaldarriaga M., 1996, *ApJ*, 469, 437
- Semboloni E., et al., 2006, *A&A*, 452, 51
- Softan A. M., Freyberg M. J., Hasinger G., 2005, *A&A*, 436, 67
- Spergel D. N., et al., 2003, *ApJS*, 148, 175

- Spergel D. N., et al., 2006, ArXiv Astrophysics e-prints, astro-ph/0603449
- Spitzer L., 1962, *Physics of Fully Ionized Gases*, New York: Interscience (2nd edition)
- Springel V., 2005, MNRAS, 364, 1105
- Springel V., Hernquist L., 2003, MNRAS, 339, 289
- Springel V., White M., Hernquist L., 2001, ApJ, 549, 681
- Springel V., Yoshida N., White S. D. M., 2001, New Astronomy, 6, 79
- Sunyaev R. A., Zel'dovich I. B., 1980, ARA&A, 18, 537
- Sunyaev R. A., Zel'dovich Y. B., 1972, Comments on Astrophysics and Space Physics, 4, 173
- Tegmark M., de Oliveira-Costa A., Hamilton A. J., 2003, Phys. Rev. D, 68, 123523
- Tegmark M., et al., 2006, Phys. Rev. D, 74, 123507
- Tormen G., Bouchet F. R., White S. D. M., 1997, MNRAS, 286, 865
- Tornatore L., Borgani S., Matteucci F., Recchi S., Tozzi P., 2004, MNRAS, 349, L19
- Tornatore L., Borgani S., Springel V., Matteucci F., Menci N., Murante G., 2003, MNRAS, 342, 1025
- Tozzi P., Norman C., 2001, ApJ, 546, 63
- Tripp T. M., Savage B. D., Jenkins E. B., 2000, ApJ, 534, L1
- Vikhlinin A., 2006, ApJ, 640, 710
- Vikhlinin A., Forman W., Jones C., 1999, ApJ, 525, 47
- Vikhlinin A., Kravtsov A., Forman W., Jones C., Markevitch M., Murray S. S., Van Speybroeck L., 2006, ApJ, 640, 691
- Voit G. M., 2005, Reviews of Modern Physics, 77, 207
- Voit G. M., Bryan G. L., 2001a, ApJ, 551, L139
- Voit G. M., Bryan G. L., 2001b, Nat, 414, 425
- Voit G. M., Bryan G. L., Balogh M. L., Bower R. G., 2002, ApJ, 576, 601
- Weinberg D. H., Miralda-Escude J., Hernquist L., Katz N., 1997, ApJ, 490, 564
- White M., Hernquist L., Springel V., 2002, ApJ, 579, 16
- Willis J. P., et al., 2005, MNRAS, 363, 675
- Wood-Vasey W. M., et al., 2007, ArXiv Astrophysics e-prints, astro-ph/0701041
- Worsley M. A., et al., 2005, MNRAS, 357, 1281

- Worsley M. A., Fabian A. C., Barcons X., Mateos S., Hasinger G., Brunner H., 2004, MNRAS, 352, L28
- Worsley M. A., Fabian A. C., Bauer F. E., Alexander D. M., Brandt W. N., Lehmer B. D., 2006, MNRAS, 368, 1735
- Xue Y., Wu X., 2003, ApJ, 584, 34
- Yoshida N., Sheth R. K., Diaferio A., 2001, MNRAS, 328, 669
- Yoshida N., Stoehr F., Springel V., White S. D. M., 2002, MNRAS, 335, 762
- Zappacosta L., Mannucci F., Maiolino R., Gilli R., Ferrara A., Finoguenov A., Nagar N. M., Axon D. J., 2002, A&A, 394, 7
- Zel'dovich Y. B., 1970, A&A, 5, 84
- Zhang P., Pen U.-L., Trac H., 2004, MNRAS, 347, 1224
- Zhang T.-J., Liu J., Feng L.-l., He P., Fang L.-Z., 2006, ApJ, 642, 625